Understanding the cantilever dynamics of Atomic Force Microscope and its application to nanomanipulation

A thesis
submitted for the degree of
Doctor of Philosophy
in Jadavpur University

by
Soma Das

Department of Material Sciences
S. N. Bose National Centre for Basic Sciences
Block - JD, Sector - III, Salt Lake, Kolkata - 98
India

March 2009

To my parents……..

Acknowledgment

I would like to express my gratitude to all those who helped me to complete my thesis. Firstly, I would love to give my special appreciation to my research advisor, Professor A. K. Raychaudhuri, who provided a motivating, encouraging, and enthusiastic environment during my pursuit of doctoral research. With his critical assessment and breakthrough ideas he has improved the quality of my work. He allowed me to plan my experiments independently and that has turned out to be very precious at the end. I have learnt the right approach to become a good experimentalist and above all a good physicist from him.

I sincerely thank Dr. P.A. Sreeram for his help and support whenever I asked for. He taught me the basics of numerical simulation.

I am highly indebted to IACS and IUC, Kolkata for providing me access to the facilities like SEM, Zeta potential measurement whenever I needed. I convey my gratitude to Dr. Abhijit Saha for giving me the opportunity to use the Zeta Potential measurement facility. I am thankful to Prof. Harald Fuchs for providing me the opportunity to utilize the UHV-AFM facility in University of Munester, Germany.

I enjoyed the useful discussions and active support from my labmates, Rajesh Neogy, Sudeshna Samanta, Manoranjan Ghosh, M. Venkata Kamalakar, Tapati Sarkar, Subrata Sarkar, Ritwik Bhattacharyaa. Few of my seniors and friends like Achyutda and Sai from IISc, Bangalore have visited our lab and shared views and ideas with me. I thank Dr. Barnali Ghosh, Dr. Anindya Das, Dr. Kuntal Chakraborty, Dr. Kaustuv Das and Dr. Sarathi Kundu for their immediate help and support whenever I asked.

I could not have spent five years in research without the support and encouragement from my parents. I can not express my gratitude towards them in simple words. My brother was always supportive in this long way of research. All of them were in my heart every moment which provided me the courage for carrying out my research.
I would like to thank all of my friends who are always a source of happiness in my life irrespective of my failure or success. I can not name all of them in this limited space but few of them like Bipul, Debu, Badiur, Rupa, Tuhin,..... seniors like Manirulda, Anujda, Monoda, have always given me enough boost in my personal life as well as in research.

Last but not the least, Debmalya has always remained inseparably associated with all the stages of my research work and helped me a lot to complete my thesis. My parents-in-laws and sister-in-law have also provided great support during my thesis writing.
I apologize to all those whose names I could not mention in this limited space but were always supportive in my research work.

List of publications

1. A method to quantitatively evaluate the Hamaker constant using the jump-into-contact effect in atomic force microscopy 2007 Soma Das, P.A. Sreeram and A K Raychaudhuri, *Nanotechnology* , **18**, 035501.

2. Effects of Nonlinear Forces on Dynamic Mode Atomic Force Microscopy and Spectroscopy 2007 Soma Das, P.A. Sreeram and A K Raychaudhuri, *Journal of Nanoscience and Nanotechnology,* **7**, 1-5.

3. Growth of atomically smooth films of Metal-Arachidates by Langmuir-Blodgett technique Soma Das and A. K. Raychaudhuri accepted in *Journal of Nanoscience and Nanotechnology*.

4. Growth of two-dimensional arrays of uncapped gold nanoparticles on silicon substrates 2008 Anindya Das, Soma Das and A. K. Raychaudhuri, *Bulletin of Material Science*, **31,** 1-6.

5. Effect of intrinsic instability of cantilevers on static mode Atomic Force Spectroscopy Soma Das, P.A. Sreeram, A K Raychaudhuri and Dirk Dietzel submitted.

6. Tuning the instability in Static Mode Atomic Force Spectroscopy (AFS) by applying electric field, Soma Das, P.A. Sreeram, A K Raychaudhuri and Dirk Dietzel submitted.

Contents

List of Figures

List of Tables

Chapter 1

Introduction

The thesis is in the general area of Nanoscience and Nanotechnology. The thesis deals with use of Atomic Force Microscope (AFM) in such areas as quantitative force measurements as well as to perform some basic operations of nanomanipulation. The use of AFM in any application depends on our understanding of the nanomechanics of the motion of the microcantilever. The main focus of the thesis is to develop useful and simple quantitative tools that can be used to understand the basic cantilever mechanics as well as doing experiments to validate the calculations. The experimental techniques used in this work are essentially related to atomic force microscopy, which gives a direct access to the topography and forces of the studied systems. The thesis focuses on two specific aspects as stated below. First, to understand the dynamics of microcantilever of Atomic Force Microscope (AFM) moving in a non-linear tip-sample interaction. Second, to modify the interaction by applying an electric field between the tip and the sample to achieve an external control on tip-sample interaction and finally to utilize this understanding for nanomanipulation with precise control in presence of electric field.

The atomic force microscope (AFM) is not only a tool to image the topography of solid surfaces at high resolution. It can also be used to measure force-versus-distance curves. Such curves, briefly called force curves, (often also called “force spectroscopy” curves) provide valuable information on local material properties such as elasticity, hardness, Hamaker constant, adhesion and surface charge densities. For this reason the measurement of force curves has become essential in different fields of research such as surface science, materials engineering, and biology. Another application is the analysis of surface forces.

Some of the most fundamental questions regarding the features seen in the force distance curves taken by AFM: How does tip-sample interaction manifest itself in the force-distance curves taken by AFM? What is the origin of the instabilities show up in AFM spectroscopy? Does the adhesion force have rate dependency? How the tip-sample interaction can be controlled externally? We have tried to answer these questions in detail by experiments and theoretical analysis in this thesis. In this chapter we have first reviewed the past works done in these areas and then mentioned the specific points that we have addressed in this thesis.

1.1 Forces in Atomic Force Microscope

1.1.1 Atomic and intermolecular forces

Basic principle of AFM is based upon the detection of the forces acting between the tip and the sample. Therefore, to understand the data taken using AFM, we have to first know about the different kind of surface forces acting on the tip-sample system. The origin of the surface forces has to be found at the atomic level. Molecular or even macromolecular forces are generally arising from atomic interactions. Let us consider for a first approach a di-atomic molecule formed by two atoms A and B of respective mass m_A and m_B. The frequency of vibration ν of the molecule gives access to an estimation of the force between the two atoms. Indeed, in the case of the harmonic oscillator approximation, the frequency of vibration of the molecular system is given by

$$\upsilon = \frac{1}{2\pi}\sqrt{\frac{k}{m_r}} \qquad (1.1)$$

where k is the spring constant of the system and $m_r = m_A m_B/(m_A+m_B)$ is the reduced mass of the molecule. Wavenumbers (W_n) between 100 – 10,000 cm^{-1} are usually associated to the vibrations of molecules in vibrational spectroscopy studies [1]. Corresponding frequencies are between 3 $X10^{12}$–3 $X10^{14}$ Hz ($W_n.c = \upsilon$, with $c \approx 3X10^{10}$ cm/sec being the velocity of the electromagnetic radiation). As a result, if we take the case of the hydrogen molecule H_2 characterized by $m_A = m_B = 1.673X10^{-27}$ kg and $W_n \approx 4400$ cm^{-1}, we obtain k ≈580 N/m. Then, for small vibrations Δx close to the equilibrium state (Δx ~ 10^{-12} m), the force is roughly given by $F = k\cdot\Delta x \sim 6X10^{-10}$ N. This force is an approximation of the order of magnitude characterizing the force between two atoms. In the case of a surface, the atom is generally an integral part of the crystal lattice and it is bound to its neighboring atoms. Those bonds maintain the atom more rigidly to the surface and increase the total spring constant, as well as the final force.

1.1.2 van-der-Waals forces

The forces relevant to AFM are ultimately of electromagnetic origin. However, different intermolecular, surface and macroscopic effects give rise to interactions with distinctive distance dependencies. In the absence of external fields, the dominant forces are van-der-Waals interactions, short-range repulsive interactions, adhesion and capillary forces. We will discuss about these forces one by one.

Figure 1.1 shows an interatomic force vs. distance curve, which illustrates the force between atoms on a cantilever tip and atoms on a sample surface vs. the separation distance between the tip and the sample. Two distance regimes are labeled on the figure: 1) the “contact” regime (less than a few angstroms), which represents the tip-to-sample spacing for contact AFM, and

2) the "non-contact" regime, ranging from tens of angstroms to hundreds of angstroms, which represents the tip-to-sample spacing for non-contact AFM (NC-AFM). In the contact regime, the interatomic forces are repulsive, while in the non-contact regime they are attractive, and largely a result of long-range van-der-Waals' interactions. It is a long range attractive interaction.

Van-der-Waals bonds are due to electrostatic forces called van-der-Waals (vdW) forces. The origin of vdW forces is generally attributed to electromagnetic forces and one distinguishes three different types of contributions: the electrostatic contributions, the induction contributions and the dispersion contributions.

The Coulomb force F is the basis for the understanding of intermolecular forces. This electrostatic force interacting between two charges Q_1 and Q_2 is given by the formula

$$F = \frac{Q_1 Q_2}{4\pi\varepsilon\varepsilon_0 d^2} \qquad (1.2)$$

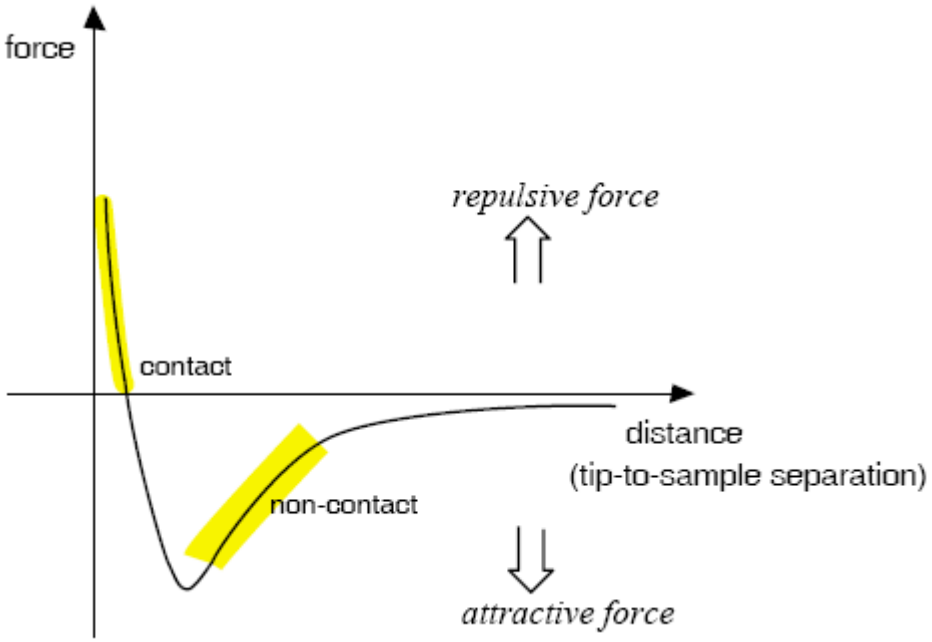

Figure 1.1 Interatomic Force vs. Distance curve.

where d is the distance between the charges. The parameter ε is the dielectric permittivity of the medium and ε_0 is the vacuum permittivity. The corresponding potential energy W is obtained by the negative integration of the previous equation and results in

$$W = \frac{Q_1 Q_2}{4\pi\varepsilon\varepsilon_0 d} \qquad (1.3)$$

As a consequence, opposite charges have a negative potential energy that is reduced when the charges get closer. van-der-Waals forces are based on the same principle. Most of the molecules are not charged, but they present generally a non uniform repartition of the electric charge inducing a dipole in the molecule. This dipole is schematically represented by a vector μ pointing from the negative to the positive side of the molecule (fig.1.2) and called the dipole moment. For two opposite charges Q and −Q separated by a distance D, μ = Q·D. Two effects have an opposed contribution on the dipole. If the dipole is free to rotate, it will point its negative pole towards the positive charge at proximity, whereas thermal activation will drive it away from a perfect orientation. On an average the preferential orientation chosen by the dipole is to point toward the monopole. As a result, two freely rotating dipoles, given by μ_1 and μ_2, attract each other through their opposite charge. Their potential energy, that corresponds in fact to the Helmholtz free energy of interaction, is then given by [2]

$$W = -\frac{C_{orient}}{D^6} = -\frac{\mu_1^2 \mu_2^2}{3(4\pi\varepsilon_0)^2 k_B T D^6} \qquad (1.4)$$

where D>>d is the distance between the dipole and C_{orient} is a parameter independent of the distance between the monopoles. k_BT represents the thermal energy, k_B being the Boltzmann constant and T the temperature. This randomly oriented electrostatic dipole interaction is generally referred to as the Keesom contribution to the van-der-Waals forces.

Another contribution involves the effect of a charge on a molecule having no static dipole moment. In fact, even if the molecule has a homogeneous distribution of the charges, the presence of a monopole induces a charge shift and creates a polar molecule. The induced dipole μ_{ind} interacts then with the charge. In the case of freely rotating dipoles, a molecule

(a) Coulomb interaction. (b) Keesom interaction.

Figure 1.2 Schematic representation of the interaction between charges and dipoles.

with a static dipole moment interacts with a different, but polarisable molecule, giving rise to the Helmholtz free energy expressed as [2]

$$W = -\frac{C_{ind}}{D^6} = -\frac{\mu^2 \alpha}{(4\pi\varepsilon_0)^2 D^6} \qquad (1.5)$$

with α being the polarizability in $C^2m^2J^{-1}$ and defined by the relation $\mu_{ind} = \alpha \cdot E$, where E is the electric field strength. C_{ind} is a term independent of the distance. This effect is called the Debye interaction and corresponds to the randomly oriented induced dipole contribution to the van-der-Waals forces.

The last contribution concerns dispersion interactions. In fact, the two previous explanations fail to explain the attraction between non polar molecules that is experienced in gas condensation at some temperature. To explain such a behavior, we have to refer to quantum mechanical perturbation theory. An illustration is given by considering an atom having its electrons circulating at high frequency around its positive nucleus. If we freeze the atom at a time t, it will show a polarity due to the spatial repartition of its electrons, i.e. we might find more electrons in an area, than in another one. As a result, the direction of the atom polarity changes at high frequency following the rapid movement of its electrons around the nucleus. Now, if one approaches two atoms, referred to as atom 1 and atom 2, they will start to influence each other, and, on average, attractive orientations will dominate. The result is an attractive force, called dispersion or London force, characterized in the case of molecules by the Helmholtz free energy [2]

$$W = -\frac{C_{disp}}{D^6} = -\frac{3}{2}.\frac{\alpha_1\alpha_2}{(4\pi\varepsilon_0)^2 D^6}.\frac{h\nu_1\nu_2}{\nu_1+\nu_2} \qquad (1.6)$$

where the suffixes refer to the corresponding atoms. $h\nu_1$ and $h\nu_2$ are the ionization energies of the molecules, h being the Planck's constant and ν, the respective frequency. Again, the parameter C_{disp} regroups the terms independent of the distance.
The vdW forces are the sum of the Keesom, Debye and London interactions, with generally a domination of the London contribution based on the dispersion forces. Thus, we can add all the terms independent of the distance by writing $C_{vdW} = C_{orient} + C_{ind} + C_{disp}$, with the final potential energy decreasing in accordance with $1/D^6$. From a general point of view, the polarization of the electronic cloud and the presence of dipoles are at the origin of van-der-Waals forces. There is no charge transfer between molecules in the case of van-der-Waals bonding. Resulting solids are generally soft with bad mechanical properties, as solid noble gas.

1.1.3 Hamaker Constant

In order to model the interactions taking place in AFM, it is necessary to consider macroscopic bodies rather than individual atoms or molecules. van-der-Waals energies between macroscopic bodies may be computed via integration only in the approximation that the van-der-Waals force is considered additive and non-retarded. The interaction laws obtained via integration using Derjaguin's approximation [3] are listed in table 1 for common geometries. All interaction laws depend on geometrical features of the bodies and on the Hamaker constant A_H, which includes all physico-chemical information [4]:

$$A_H = \pi^2 C\rho_1\rho_{2,} \qquad (1.7)$$

in which C is the constant in the atom–atom pair potential and ρ_1 and ρ_2 are the number of atoms per unit volume. Typical values of the Hamaker constant of condensed phases in vacuum are about 10^{-19} J.
By assuming the additivity of the van-der-Waals force, the influence of nearby atoms on the couple of interacting atoms is neglected, thus introducing large errors in the

calculation of the Hamaker constant. Lifshitz [5] circumvented this problem via an alternative approach in which each body is considered as a continuum with certain dielectric properties, thus incorporating automatically many-body effects. All expressions in table 1 remain valid. Only the computation of the Hamaker constant changes.

Table 1.1: van-der-Waals interaction laws for most common AFM geometries

Geometry	Force
Two flat surfaces	$f = -\frac{A_H}{6\pi D^3}$ Per unit area
Two spheres	$F = -\frac{A_H}{6D^2}\frac{R_1 R_2}{R_1 + R_2}$
Sphere-flat surface	$F = -\frac{A_H R}{6D^2}$
Cone-flat surface	$F = -\frac{A_H \tan^2\theta}{6D}$
Paraboloid-flat surface	$F = -\frac{A_H l_{xy}^2}{12D^2 l_z}$
Cylinder-flat surface	$F = -\frac{A_H R^2}{6D^3}$

A_H is the Hamaker constant, D is the distance, R is the radius of the sphere or of the cylinder, θ is the semi-aperture of the cone, l is the semi-axis of the paraboloid.

$A_H = \pi^2 C\rho_1\rho_2$, where C is the constant in the atom–atom pair potential and ρ_1 and ρ_2 are the number of atoms per unit volume.

In Lifshitz theory, the Hamaker constant for the interaction of media 1 and 2 across the medium 3 may be expressed as

$$A_H \cong \frac{3}{4}k_B T\frac{\varepsilon_1-\varepsilon_3}{\varepsilon_1+\varepsilon_3}\frac{\varepsilon_2-\varepsilon_3}{\varepsilon_2+\varepsilon_3} + \frac{3h\nu_e}{8\sqrt{2}}\frac{(n_1^2-n_3^2)(n_2^2-n_3^2)}{\sqrt{|n_1^2-n_3^2|}\sqrt{|n_2^2-n_3^2|}[\sqrt{|n_1^2-n_3^2|}+\sqrt{|n_2^2-n_3^2|}]} \quad (1.8)$$

where ε_1, ε_2, ε_3 and n_1, n_2, n_3 are the dielectric constants and the refractive indices of tip, sample, and the medium in between, respectively. υ_e is the mean absorption frequency.
For two identical media ($\varepsilon_1 = \varepsilon_2 \neq \varepsilon_3$, $n_1 = n_2 \neq n3$), eq. 1.8 becomes:

$$A_H \cong \frac{3}{4}k_B T\left(\frac{\varepsilon_1-\varepsilon_3}{\varepsilon_1+\varepsilon_3}\right)^2 + \frac{3h\nu_e}{16\sqrt{2}}\frac{(n_1^2-n_3^2)^2}{\sqrt{(n_1^2+n_3^2)^3}} \quad (1.9)$$

eq. 1.8 reveals two important aspects:

1. The van-der-Waals force between two identical bodies in a medium is always attractive (A_H is positive), whereas the force between two different bodies may be attractive or repulsive.
2. The van-der-Waals force between any two condensed bodies in vacuum or in air ($\varepsilon_3 = 1$ and $n_3 = 1$) is always attractive.

For interactions between conductive bodies such as metals, eq. 1.8 cannot be applied, since ε is infinite. For two metals in vacuum the Hamaker constant is

$$A_H \cong \frac{3}{8\sqrt{2}} h \frac{\nu_{e1}\nu_{e2}}{\nu_{e1}+\nu_{e2}} \cong 4\times10^{-19}\,J \tag{1.10}$$

Here, ν_{e1} and ν_{e2} are the plasma frequencies of the two metals.

1.1.4 Contact and short range repulsive forces: Hertz, JKR, DMT and beyond

In AFM, when the tip touches the surface it deforms the sample by a depth d. For a purely elastic sample, loading and unloading curves, i.e., the approach and withdrawal contact lines, overlap. If the sample is plastically deformed, the sample undergoes a deformation during the loading curve, and, when the tip is withdrawn, it does not regain its own shape as the load decreases, whereas the penetration depth remains the same. Most samples have a mixed behavior. Hence loading and unloading curves seldom overlap. In particular, at a given penetration depth, the force of the unloading curve is lesser than the force of the loading curve. The difference between the approach and the retraction contact lines is called ‘‘loading–unloading hysteresis’’. In the following plastic deformations have been neglected and theories dealing with elastic continuum contact mechanics have been reviewed, in which the tip and sample are assumed to be continuous elastic media.

In the contact part of force curves, both in the approach and in the retraction phase, the elastic deformation of the sample can be related to its Young’s modulus. In order to relate the measured quantities to Young’s modulus, it is necessary to consider the deformation of the sample d. For elastic deformation it is useful to describe the system by means of a potential energy U:

$$U = U_{CS}(D) + U_C(z_C) + U_S(\delta) = U_{CS}(D) + \frac{1}{2}k_C z_C^2 + \frac{1}{2}k_S\delta^2 \tag{1.11}$$

Here, U_{cs} is the tip–sample interaction potential caused by surface forces, U_c the energy due to bending of the cantilever, U_s the elastic deformation energy of the sample, and k_s is the so-called sample stiffness. In general, we can write:

$$D = z_P + z_C + \delta. \tag{1.12}$$

In contact D = 0 and, if the system is in equilibrium, also $k_s\delta = k_c z_c$. Substituting, we obtain

$$k_C z_C = -\frac{k_C k_S}{k_C + k_S} z_P = k_{eff} z_P \tag{1.13}$$

This simple relation shows that the slope of the force–displacement curve is a measure of the stiffness of the sample. If the sample is much stiffer than the cantilever, that is for $k_s >> k_c$, then $k_{eff} \approx k_c$, whereas $k_{eff} \approx k_s$ when $k_s << k_c$, i.e., when the sample is much more compliant than the cantilever. This gives also a rule of thumb for the choice of the cantilever spring constant in experiments dealing with the elastic properties of the sample: If the cantilever spring constant is much lower than the sample spring constant, the force curve will probe primarily the stiffness of the cantilever, and not that of the sample.
The stiffness of the sample is related to its Young's modulus by

$$k_S = \frac{3}{2} a E_{tot} \qquad \text{With} \qquad \frac{1}{E_{tot}} = \frac{3}{4}\left(\frac{1-\nu_S^2}{E_S} + \frac{1-\nu_t^2}{E_t}\right). \tag{1.14}$$

Here, υ_t, E_t, υ_s and E_s are the Poisson's ratio and the Young's moduli of tip and sample, respectively, E_{tot} the reduced Young's modulus, and a is the tip–sample contact radius. Young's modulus of silicon nitride is typically 160–290 GPa, the Poisson's ratio is 0.20–0.27, depending on conditions and precise content of silicon and nitrogen (e.g. [6, 7, 8, 9]). For silicon the values are E = 130–185 GPa and υ = 0.26– 0.28, depending on crystallographic orientation (e.g. [10]). Silicon oxide (fused quartz) has a Young's modulus of 72 GPa and a Poisson's ratio of 0.17; all values at room temperature. In many cases the tip is much stiffer than the sample. If we neglect the deformation of the tip eq. (1.14) can be approximated by

$$k_S = 2a\left(\frac{E_S}{1-\nu_S^2}\right). \tag{1.15}$$

Several theories describe the elastic deformation of the sample. Differences in the relations between the applied load F and the contact radius a or the deformation d is due to the role played by the adhesion in the considered system. Table 2 summarizes the relations between contact radius, the deformation of the sample, and the adhesion force for a spherical tip on a plane surface according to the three most used theories. These theories have been developed by Hertz [11], Johnson–Kendall–Roberts (JKR) [12], and Derjaguin–Müller–Toporov (DMT) [13–15].
In the Hertz model the adhesion of the sample is neglected, whereas the two other theories take account of it outside (DMT) or inside (JKR) the contact area. Hence, Hertz theory can only be applied when the adhesion force is much smaller than the maximum load. In the two other theories, the work of adhesion W can be calculated from the jump-off-contact, if the tip radius R_t is known. Then it is possible to calculate a as a function of the reduced Young's modulus E_{tot} and finally to obtain E_{tot} as a function of d, measured from the contact line. The JKR theory can be applied in the case of large tips and soft samples with a large adhesion, the DMT theory in the case of small tips and stiff samples with a small adhesion. Both theories are only approximations.

Table 1.2 Relation between the contact radius a, the sample deformation δ, and the adhesion force F_{ad} for a spherical tip on a flat surface according to the Hertz, JKR, and DMT theories.

	Hertz	DMT	JKR
a	$\sqrt[3]{\frac{R_t F}{E_{tot}}}$	$\sqrt[3]{\frac{R_t}{E_{tot}}(F+2\pi R_t W)}$	$\sqrt[3]{\frac{R_t}{E_{tot}}(F+3\pi R_t W+\sqrt{6\pi R_t WF+(3\pi R_t W)^2})}$
δ	$\frac{a^2}{R_t}=\left(\frac{F^2}{R_t E_{tot}^2}\right)^{\frac{1}{3}}$	$\frac{a^2}{R_t}=\frac{(F+2\pi R_t W)^{\frac{2}{3}}}{\sqrt[3]{R_t E_{tot}^2}}$	$\frac{a^2}{R_t}-\frac{2}{3}\sqrt{\frac{6\pi Wa}{E_{tot}}}$
F_{ad}	0	$2\pi R_t W$	$\frac{3\pi R_t W}{2}$

R_t is the tip radius and W is the adhesion work per unit area. Often the work of adhesion is replaced by twice the surface energy of the solid. R_t is the radius of the spherical tip, F is the force exerted by the tip on the surface, and E_{tot} is the reduced Young's modulus defined in eq. (1.14).

At this point it is instructive to consider a typical example. For a silicon nitride tip with R_t = 30 nm, E = 200 GPa, υ = 0.3 on silicon nitride we have E_{tot} = 147 GPa. At a load of 1 nN this leads to an indentation of 0.012 nm and a contact radius of 0.59 nm. The mean pressure underneath the tip is thus $P = F/\pi a^2$ = 0.9 GPa or almost 10 kbar.
Maugis [16] has shown that the JKR and DMT models are limits of the same theory, describing the elastic deformations of all samples as a function of the parameter

$$\lambda = \frac{2.06}{D_0}\sqrt[3]{\frac{R_t W^2}{\pi E_{tot}^2}}, \tag{1.16}$$

where D_0 is a typical atomic dimension. In the Maugis theory, the deformation and the contact radius are given by a set of parametric equations:

$$\bar{\delta} = \bar{A}^2 - \frac{4}{3}\lambda\bar{A}\sqrt{m_M^2-1}, \qquad \bar{F} = \bar{A}^3 - \lambda\bar{A}^2(\sqrt{m_M^2-1}+m_M^2\arctan\sqrt{m_M^2-1}) \tag{1.17a}$$

with

$$\bar{A} = \frac{a}{\sqrt[3]{\pi W R_t^{\,2}/E_{tot}}}, \quad \bar{F} = \frac{F}{\pi W R_t}, \quad \bar{\delta} = \frac{\delta}{\sqrt[3]{\pi^2 W^2 R_t/E_{tot}^2}}, \tag{1.17b}$$

and

$$\frac{\lambda\bar{A}^2}{2}[\sqrt{m_M^2-1}+(m_M^2-2)\arctan\sqrt{m_M^2-1}] + \frac{4\lambda^2\bar{A}^2}{3}(1-m_M+\sqrt{m_M^2-1}\arctan\sqrt{m_M^2-1}) = 1 \tag{1.17c}$$

Here, m_M is the ratio between the contact radius a and an annular region, where the adhesion is taken into account. eqs. (1.17) reduce to the respective expressions in Table 2 for $\lambda \to \infty$ (JKR) and for $\lambda \to 0$ (DMT).
The Maugis theory, experimentally verified by Lantz et al. [17], shows that an exact determination of the Young's modulus E and of the work of adhesion W only from force–distance curves is impossible, because the slope of the contact line and the jump-off-contact depend on each other in a way described by the parameterλ, but in order to calculate λ both E and W must be known. All equations given till now are valid for spherical tips. Sneddon [18] has shown that for any punch that can be described as a solid of revolution of a smooth function the load–displacement relationship can be written in the form

$$F = \alpha \delta^n, \tag{1.18}$$

where α and n are constants (n = 1 for flat cylinders, n = 2 for cones, n = 1.5 for spheres and paraboloids).

Plastic deformation

When indenting soft samples, e.g. polymers, plastic deformation may take place. A typical curve with plastic deformation is depicted in fig.1.3 It was acquired on poly (n-butylmethacrylate) (PBMA) at 30^0C. The approach contact-line can be divided in two parts, corresponding to elastic and plastic deformations. Also the fit of the elastic region following the Hertz model ($F \propto \delta^{3/2}$) is shown (dashed line). The two regions are separated by a yielding point. When yielding occurs, the cantilever exerts a critical pressure on the sample, and a plastic deformation is obtained. Please note that the stiffness of the sample after the yielding is lower than before the yielding (the indentation obtained in the plastic region at a certain load is larger than the corresponding elastic deformation, indicated by the dashed line).
In presence of a plastic deformation the contact line of the withdrawal curve does not overlap with the approach contact line. This shows that, upon retracting of the tip, the sample cannot regain completely its shape, as implied by the definition of plastic deformation. As shown in fig. 1.4, we can define the elastic recovery $Z^{max}{}_p$ - p, where p, the permanent plastic deformation, is the intercept between the withdrawal contact line and the axis F = 0. For a totally elastic sample would be p = 0 and the elastic recovery would be equal to $Z^{max}{}_p$; for a totally plastic sample would be $Z^{max}{}_p$ = p and the elastic recovery would be zero. The area between the two contact lines above the axis F = 0, that is A_1, is a measure of the energy needed for the deformation and dissipated into the sample [19], whereas the sum $A_1 + A_2$ is the work done on cantilever and sample, i.e. the maximal energy that could be stored in the sample during the indentation. We can define a plasticity index in the form

$$\psi_P = \frac{A_1}{A_1 + A_2}. \tag{1.19}$$

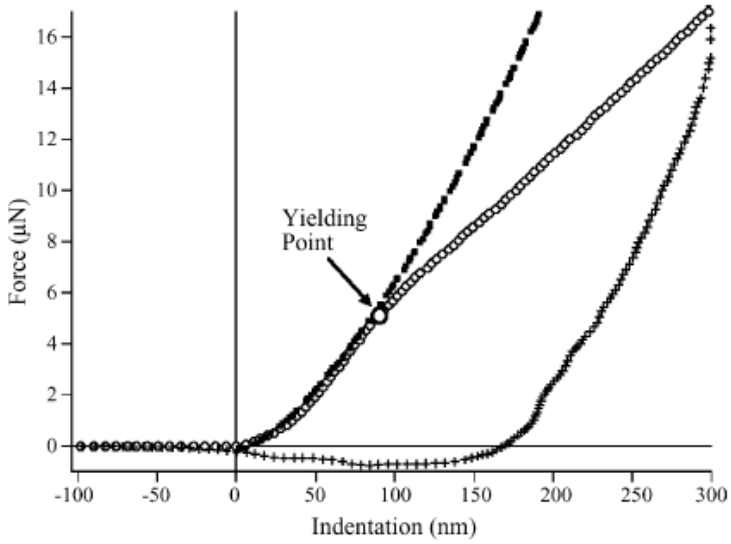

Figure 1.3 Force–distance curves in air on PBMA at 30^0C. The approach curve is drawn with open circles, whereas the retraction curves is drawn with crosses. The contact line of the approach curve can be divided in two parts, i.e., the elastic and the plastic region, divided by a yielding point. Also the fit of the elastic region following the Hertz model ($F \propto \delta^{3/2}$) is shown (dashed line). After the yielding point the sample has become softer, because of the onset of plastic deformations.

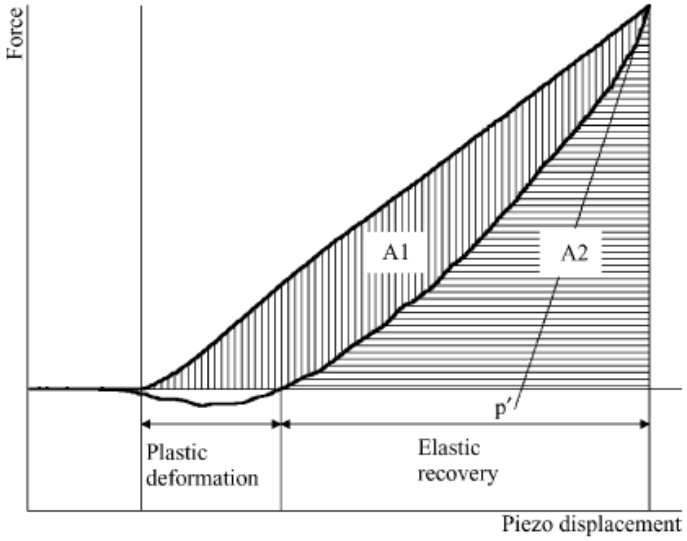

Figure 1.4 Schematic force–distance curves with plastic deformations. The permanent plastic deformation, p, is the intercept between the withdrawal contact line and the axis F = 0; A_1 is the area between the two contact lines above the axis F = 0; A_2 is the area between the retraction contact line and the axis F = 0, p_0 is the intercept between the axis F = 0 and the tangent to the unloading curve for very high loads.

For a totally elastic sample would be $A_1 = 0$ and $\psi_P = 0$, for a totally plastic sample would be $A_2 = 0$ and $\psi_P = 1$.
In several experiments the AFM is used as an indenter in order to measure the Young's modulus and the hardness H of the sample. The basic empirical equations, valid in the plastic regime, are reported by Oliver and Pharr [20, 21]:

$$\frac{dF}{d\delta}\Big|_{\delta_{max}} = \frac{2\beta_1}{\sqrt{\pi}} E_{tot} \sqrt{A_{max}},$$
$$H = \frac{F_{max}}{A_{max}} = \frac{F_{max}}{\beta_2 p'^2}. \quad (1.20)$$

Here, β_1 and β_2 are parameters depending on the indenter geometry, A_{max} the projection of the contact area between the indenter and the sample at the maximal indentation δ_{max}, and p' is the intercept between the axis F = 0 and the tangent to the unloading curve for very high loads. A_{max} can be calculated only if the shape of the tip is exactly known. Alternatively it can be measured by imaging the sample after indentation.
In such experiments the AFM is employed as an indenter and force–displacement curves are not of primary interest. The measurement is focused on the result of a given indentation, i.e., on the shape of the ''imprinted'' hole, and not on the dependence of the deformation on the load.

1.1.5 Lateral forces (Friction)

Another important force presents in the contact regime of AFM operation is lateral force or friction. When scanning in the Constant Force mode perpendicularly to longitudinal axis of the cantilever, besides the cantilever's deflection in the normal direction, an additional torsion bending of the cantilever occurs. It is caused by the moment of forces acting on the tip. With minor deflections, the angle of torsion is proportional to the side (lateral) force. The cantilever's torsion bending is measured by the microscope optical recording system. When moving over a flat surface with zones of different friction factors, the angle of torsion will be changing in every new zone. This allows measuring of the local friction force. If the surface is not absolutely flat, such an interpretation is complicated. To distinguish zones of different friction and relief influence one can utilize second pass on the same line in opposite direction. Nevertheless, this type of measuring allows obtaining images with clearly seen minor relief details and facilitates their search. In addition, the lateral force measuring mode easily provides the atomic resolution on mica and some other laminar materials.
An instrument operating in LFM mode is equipped with cantilever detection scheme that measures both vertical and lateral bending of the cantilever. In contact-AFM mode, only vertical bending of the cantilever is measured, representing changes in sample topography. By measuring lateral bending (or twisting) of the cantilever as well, LFM mode is used to monitor motions arising from forces on the cantilever that are parallel to the plane of the sample surface. Such forces can arise from changes in the frictional coefficient of a region on the sample surface or from onsets of changes in topography. LFM is therefore useful for measuring inhomogeneties in surface materials and producing images with enhanced edges of topographic features.

As with contact-AFM, LFM mode uses a beam-bounce detection scheme, employing a position-sensitive photodetector (PSPD) to measure the bending of the cantilever. In contact-AFM mode, the PSPD is used in a bicell configuration, to detect vertical deflection. In LFM mode, the PSPD is used in a quad-cell configuration in order to detect both lateral and vertical deflection of the cantilever. Figure 1.5 shows both a quad-cell and a bi-cell PSPD.

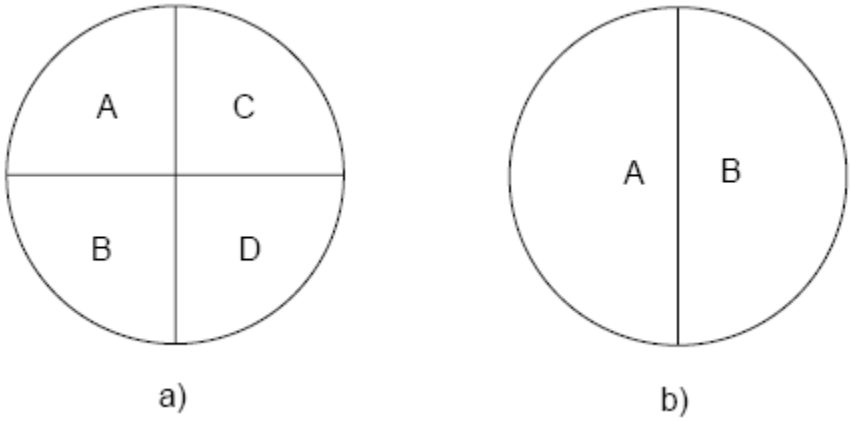

FIGURE 1.5 A quad-cell PSPD (a) and a bi-cell PSPD (b).

LFM mode is used mainly to collect both topographic (AFM) and frictional (LFM) information during a single scan. The topographic information is represented by vertical deflection of the cantilever, which is measured as the difference between signals from the left and right quadrants of the quad-cell PSPD. This signal difference is termed the "A-B" signal, referring to the two halves of a bi-cell PSPD in CAFM, and is represented by:

$$\text{A-B signal} = (A+C) - (B+D) \tag{1.21}$$

Topographic information is also represented by the Topography signal, which is a function of the A-B signal. Frictional information (the LFM signal) is represented by lateral deflection of the cantilever, which is measured as the difference between the upper and lower quadrants of the quad-cell PSPD:

$$\text{LFM signal} = (A+B) - (C+D) \tag{1.22}$$

The PSPD is mounted facing the side of the cantilever. Therefore, lateral twisting of the cantilever is measured as vertical changes in the position of the laser beam on the PSPD. Vertical bending of the cantilever is measured as lateral changes in the position of the laser beam on the PSPD. By acquiring both the Topography and LFM signals, an instrument operating in LFM mode can produce C-AFM and LFM images simultaneously.

LFM tip-sample interaction

This section describes how LFM images correlate with changes in frictional coefficients and topography on a sample surface. Figure 1.6 illustrates how a cantilever responds to

changes in topography, and how that response correlates with the resulting LFM and AFM data. Vertical motion of the cantilever is depicted as a change in the vertical position of the cantilever. Lateral motion of the cantilever is depicted as a change in the angle of the tip with respect to the horizontal.
Figure 1.6a shows that a change in sample topography creates both vertical and lateral changes in cantilever position. The lateral component is not recorded for the AFM image, which monitors only vertical bending of the cantilever. Figure 1.6b shows the AFM signal trace that would result from the topography of fig. 1.6a. Figure 1.6c shows the

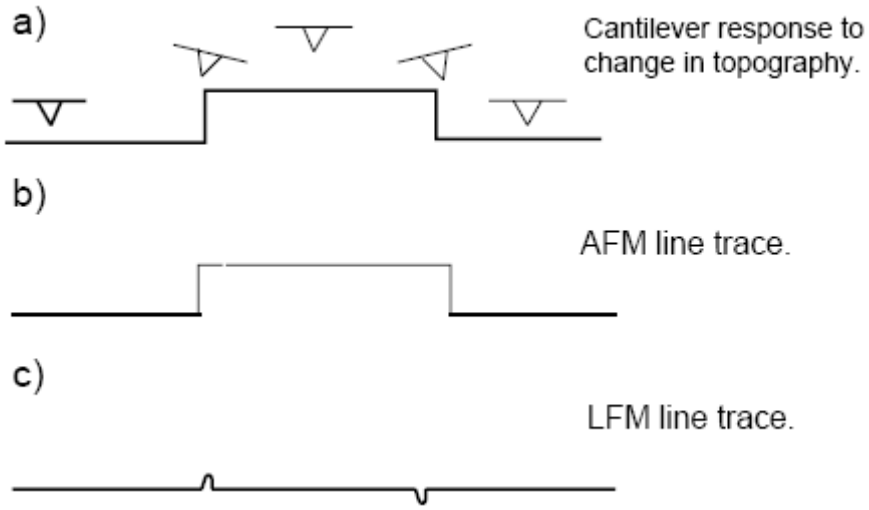

Figure 1.6. Cantilever response to change in topography with the corresponding AFM and LFM signal traces.

LFM signal trace that would result from the topography of fig. 1.6a. As the figure shows, the LFM data reflect only the lateral components of bending (e.g., bending to the right at the rise in topography produces a positive signal and bending to the left at the drop in topography produces a negative signal).
Figure 1.7 illustrates how a cantilever responds to changes in frictional coefficients and how that response correlates with the resulting LFM and AFM data. Figure 1.7a shows a change in frictional coefficient that causes the cantilever to bend to the right for a scan that is taken from left to right. If the scan is taken from right to left, as illustrated in Figure 1.7b, the cantilever bends to the left as it passes over the change in frictional coefficient. A change in topography causes the same type of cantilever bending illustrated in fig. 1.6.
Figure 1.7c shows an AFM signal trace resulting from the surface of fig. 1.7a: the data only reflect the change in sample topography. Figure 1.7d shows the LFM signal trace that would result from a scan taken from left to right. Figure 1.7e shows the LFM signal trace that would result from a scan taken from right to left.
The sign of the LFM signal flips for the change in friction, but not for the change in topography. Changes in topography appear on an LFM image as adjacent dark bright regions. By identifying these adjacent dark/bright regions, and by viewing data from two

scan directions, a user looking at an LFM image can distinguish between contrast changes due to changes in frictional coefficient and those due to changes in topography. Side-by-side AFM and LFM data therefore provide complementary information. By monitoring the LFM signal, you can identify the contribution of lateral cantilever bending to an AFM image. Conversely, having the AFM information available enables you to confirm contrast changes on an LFM image that are due to changes in topography, rather than frictional coefficient.

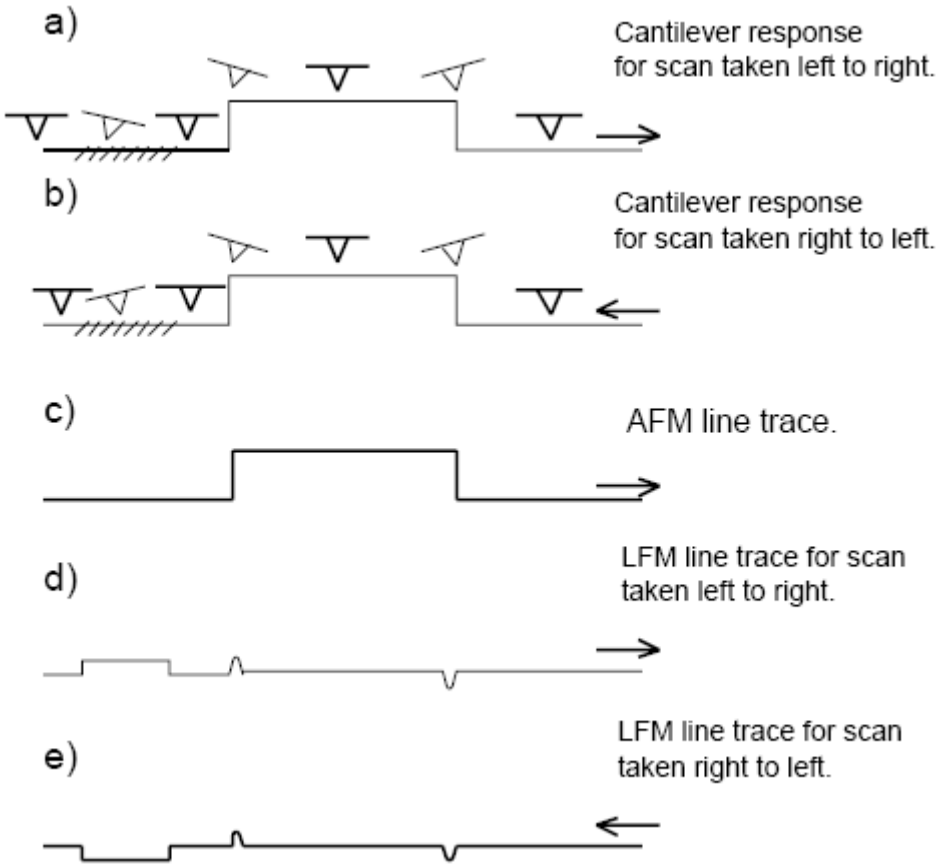

Figure 1.7. Cantilever response to change in frictional coefficient and topography, and corresponding AFM and LFM signal traces.

When operating in LFM mode, it is often useful to view both AFM and LFM data collected from both the forward and reverse sweeps of the scanner in order to distinguish between frictional and topographic information.

1.1.6 Adhesion

In AFM, when retracting the tip from the sample surface, it is believed that the tip stays in contact with the surface until the cantilever force overcomes the adhesive tip–sample interaction. First measurements of this pull-off force or adhesion force F_{ad} were performed by Martin et al. [22] and Erlandson et al. [23]. In the most general case the

adhesion force F_{ad} is a combination of the electrostatic force F_{el}, the van-der-Waals force F_{vdW}, the meniscus or capillary force F_{cap} and forces due to chemical bonds or acid–base interactions F_{chem}:

$$F_{ad} = F_{el} + F_{vdW} + F_{cap} + F_{chem} \tag{1.23}$$

In gaseous environments, significant contributions from electrostatic forces are to be expected mainly on insulators and at low humidity, when charge dissipation is ineffective. In aqueous solutions, most surfaces become charged due to dissociation of surfaces groups and electrostatic forces are important, but their magnitude also depends on electrolyte concentration. The van-der-Waals force always contributes and in most cases it is attractive. At ambient conditions, a water neck forms between AFM tip and substrate due to capillary condensation and adsorption of thin water films at surfaces. This attractive interaction depends on the relative humidity and the hydrophilicity of tip and sample. Depending on the chemical end-groups present on tip and substrate, chemical bonds may form during contact or other specific chemical interactions (e.g. receptor–ligand) may occur and then often dominate the adhesion force.
In many of the AFM studies on adhesion force, conditions were chosen such that the van –der-Waals forces were expected to dominate. In this case F_{ad} should be given by the Hamaker constants of AFM probe and sample and by the contact geometry. Quantitative comparison of such experiments with theoretical predictions is hampered by several factors:
1) Surface roughness has a pronounced influence on adhesion force that is hard to quantify.
2) The precise contact geometry is often hard to determine.
3) Adsorption of contaminants on high energy solid surfaces leads to chemical inhomogeneties of the surfaces.
Nevertheless, AFM force–distance curves have become an important method for studying adhesion properties, especially due to the possibility to detect spatial variations at the nanometer level.

1.1.7 Meniscus force

Under ambient conditions, reduction of forces is limited by the existence of the meniscus force that arises from capillary condensation around the contact sites between tip and surface. One way to avoid the meniscus force is to do imaging in water [24].
The fundamental equation for capillary condensation is the Kelvin equation. It describes the dependence of vapor pressure of a liquid on the curvature of the liquid:

$$RT \ln \frac{P}{P_0} = \gamma V_m \left(\frac{1}{R_1} + \frac{1}{R_2}\right) \tag{1.24}$$

Here R is the gas constant, T the temperature, V_m the molar volume of the liquid, P_0 the vapor pressure of the planar liquid, P the vapor pressure of the liquid with the curved surface, γ the surface tension of the liquid, and R_1 and R_2 are the principal radii of curvature. A consequence of the dependence of vapor pressure on curvature is the phenomenon of capillary condensation. The effective vapor pressure for a curved surface

of a meniscus between a sphere and a planar surface as in fig. 1.8 is reduced compared to a planar surface and therefore condensation can occur already at relative humidity much below 100%, if the radii of curvature are small. The formation of a meniscus by capillary condensation leads to an attractive force between sphere and plate. This so-called meniscus or capillary force is caused by the pressure difference between the liquid and the surrounding vapor phase (additionally, there is also a contribution from the surface tension of the liquid pulling at the three phase contact lines, but this contribution is usually smaller). It is given by the Young–Laplace equation:

$$\Delta P = \gamma\left(\frac{1}{R_1} + \frac{1}{R_2}\right). \tag{1.25}$$

The resulting capillary force F_{cap} between a plate and a sphere with radius R has been calculated by O'Brien and Hermann [25] to be

$$F_{cap} = 2\pi R\gamma(\cos\theta_1 + \cos\theta_2), \tag{1.26}$$

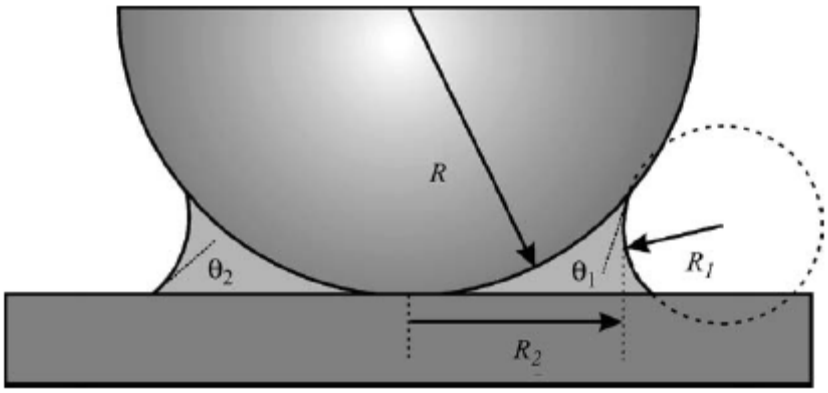

Figure 1.8. Schematic of a water meniscus between a sphere with radius R and a plate. R_1 and R_2 are the two principal radii of curvature for the water meniscus, θ_1 and θ_2 are the contact angles for water on the sphere and the plate, respectively.

where θ_1 and θ_2 are the contact angles between the two surfaces and the liquid. The validity of this equation has been proven for meniscus dimensions of ~1 nm [26, 27]. The total adhesion force in presence of a meniscus will then be given by the sum of the meniscus force and the direct solid–solid contact adhesion. As obvious from eq. 1.26, meniscus forces are expected to be maximal for hydrophilic surfaces (small contact angle) and to vanish for very hydrophobic surfaces. The expected decrease of the adhesion force with increasing hydrophobicity has indeed been observed by several authors [28-34].

An obvious limitation of eq. 1.26 is the fact that it does not contain any dependence on the value of relative humidity, which does not reflect our childhood experience that meniscus forces increase with humidity: building a sand castle will not work with dry sand but very well with wet one. More generally speaking, granular matter is known to become more cohesive with increasing humidity and often a critical humidity is observed

above which handling of the powders gets difficult. Bocquet and Barrat [35] introduced a model that includes effect of surface roughness. Capillary condensation occurs at the small nano-sized contacts of the surface asperities, leading to many small menisci instead of one large (fig. 1.9). Formation of liquid bridges by filling the pores between the asperities would finally result in one large meniscus and a high meniscus force. Assuming that capillary condensation is an activated process (energy barrier to condensate enough liquid to fill the pore volumes from undersaturated vapor) they get a humidity and time-dependent meniscus force:

$$F_{cap}(t) \approx \gamma d \frac{1}{\ln(\frac{P_0}{P})} \ln(\frac{t}{\tau_0}) \qquad (1.27)$$

where P/P_{sat} is the relative humidity, t_0 is a time constant of the order of the time needed to condense one liquid layer, and d is an effective distance taking into account the geometrical characteristics of the contacts. They observed good agreement with this model when looking at the increase in angle of repose of model substances with time and humidity. An analogous experiment on the nanoscale was done by Ando [36]. They used microfabricated silicon arrays of asperities and AFM silicon probes with a flat of 0.7 μm X0.7 μm at the end. Adhesion forces increased with humidity on the arrays but did not on single asperities, indicating that humidity increased the number of asperities contacted by the flat tip. Fuji et al. [37] found a reduced dependence of adhesion on relative humidity for porous silica particles compared to solid ones. This was attributed to the larger roughness/pore size of the porous particles that hindered the formation of capillary bridges. Ata et al. [38] showed by experiments with a smooth spherical particle and flat surfaces of alumina, silver, and titanium-coated Si wafers that surface roughness can lead to an almost complete reduction of the capillary force. This was attributed to an interaction geometry, where the meniscus is formed between a small asperity and the particle. In this case the meniscus is expected to be very thin and will not much affect the adhesion force. Biggs et al. [39] found that forces between a silica sphere and a silica plate increased by a factor of 5–7 for humidity above 60%, but absolute adhesion force

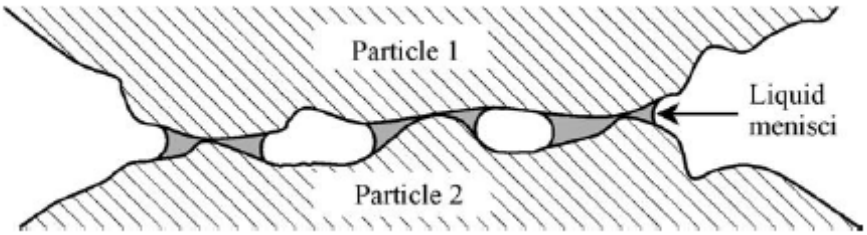

Figure 1.9. Schematic diagram of capillary condensation between rough surfaces. At lower humidity, menisci will form only at the contacts of the asperities.

values were always smaller than expected. This was attributed to surface roughness. Upon retraction of the colloid probe from the surface, long range force indicated neck formation and pooling of liquid between the surfaces immediately after the neck is broken.

It should also be noted, that eq. 1.27 describes the maximum capillary force that is acting when the surfaces are in contact. As soon as the surfaces start to separate, the liquid meniscus has to decrease rapidly in order to maintain its equilibrium radius. Thus, the meniscus force should decrease rapidly leading to a jump-out of the cantilever. However, in the case of nonvolatile liquids, or high enough retraction speeds, the liquid volume would be conserved, leading to a different behavior. Rabinovich et al. [40] studied the meniscus force between glass microspheres and silica substrates in presence of an oil droplet and found good agreement with theoretical predictions using a constant volume boundary conditions. The influence of the retract speed was probed by Wei and Zhao [41] who found an increase of measured meniscus force with tip velocity.
More elaborate theoretical models to describe the meniscus force have been developed in recent years by de Lazzer et al. [42] and Stifter et al. [43] to describe the interaction of an AFM tip with a planar surface. Sirghi et al. [44] extended the model by de Lazzer [42] to include local curvature of the sample surface. It was shown both theoretically and experimentally that the sample local curvature strongly affects the adhesion force. Compared to a flat sample surface, a larger/smaller adhesive force for a concave/convex local curvature is found. Sedin and Rowlen [45] proposed a model where humidity dependence shows a step-like behavior: For humidity below a critical threshold value, the adsorbed amount of water is too small to form a meniscus, above the critical value enough water is always present and adhesion becomes high. Such a steplike behavior was observed for experiments with silica, quartz, mica, and HOPG. Sirghi et al. [46] developed a model for the dependence of the meniscus force on water contact angle (fig. 1.10) to tip and substrate and used it to characterize the hydrophilicity of TiO_2 films. The macroscopically observed changes in contact angle induced by UV treatment were

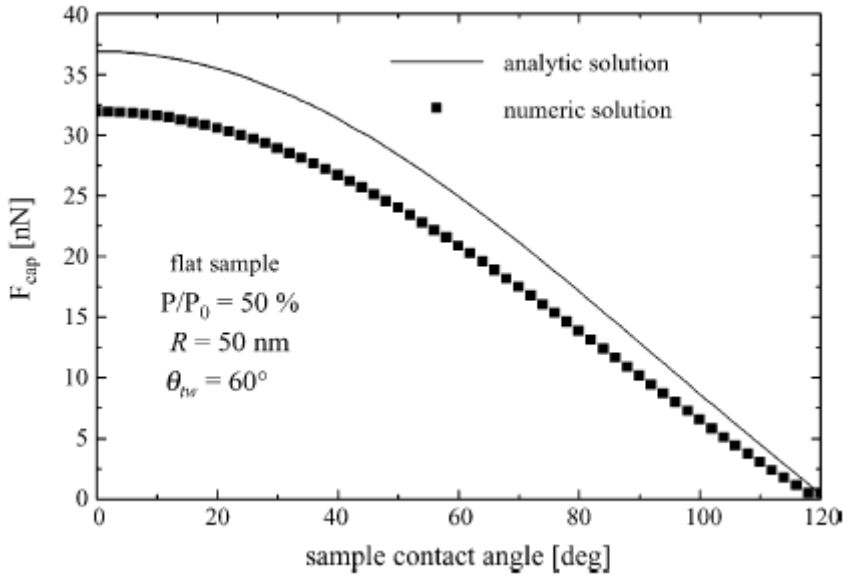

Figure 1.10. Dependence of the AFM tip–sample meniscus force on the sample contact angle as calculated by Sirghi et al. [46] for a tip radius of 50 nm, a tip contact angle of 60^0 and a relative humidity of 50% (from [46]).

reflected in the changes in adhesion force and width of force distributions gave insight in the homogeneity of the surface chemistry. Xiao and Qian [30] developed a theoretical description that includes capillary force, surface tension force, the van-der-Waals force in presence of the meniscus, and takes into account the precise tip shape. The contributions of the different components of the total adhesion force in dependence on humidity are plotted in fig.1.11.

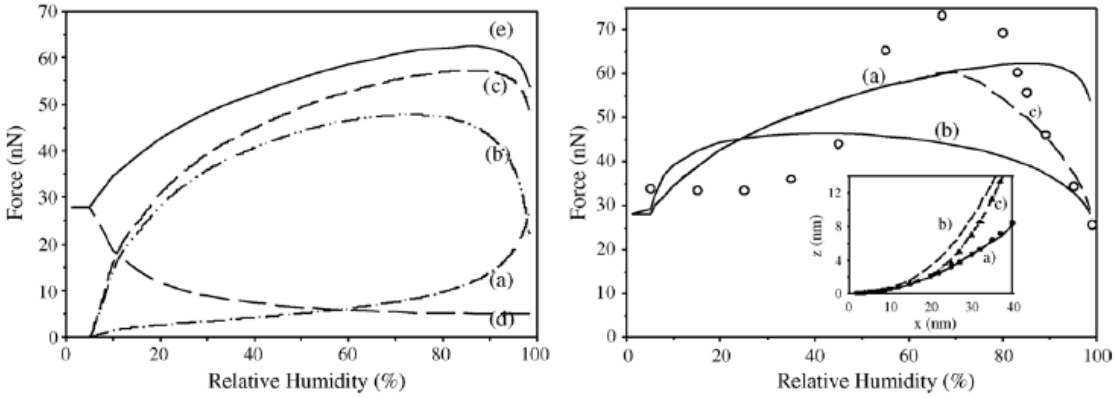

Figure 1.11. Left: contributions of (a) surface tension force, (b) capillary pressure force, (c) total meniscus force, (d) van-der-Waals force, and (e) total (adhesion) force for different values of relative humidity. Parameters used were: tip radius R_t = 100 nm, tip–plane separation 2.5 Å, contact angles $\theta_1 = 60^0$ and $\theta_2 = 0^0$, surface tension γ= 73 mJ/m^2, and volume per molecule 0.03 nm^3. Right: adhesion force between a Si_3N_4 tip and a SiO_2 surface for different tip profiles. The inset shows one half of the symmetric tip profiles, x is the lateral distance from the tip apex. (a) Parabolic tip, (b) and (c) ‘‘dull’’ tips. Lines show calculated values, open circles are experimental results (both figures from [30]).

For strongly hydrophilic surfaces the model predicts an increase followed by a decrease of adhesion with humidity, whereas for hydrophobic materials no significant influence is expected. This was indeed observed for Si_3N_4 tips on a silicon wafer and a N-octadecyltrimethoxysilane SAM, respectively. Furthermore, a strong influence of tip geometry on the humidity dependence was found.
Jones et al. [32] found that adhesion on hydrophobic substrates increased uniformly with humidity and values for small contacts were predicted by simple Laplace–Kelvin theory. For microspheres, values were too small compared to theory, due to surface roughness. For a hydrophobic glass surface, an anomalous behavior was observed: Pull off force was maximal for 20–40% relative humidity and decreased again for higher humidity.
Due to the significant impact of meniscus forces on the flow behavior of powders, several studies have focused on the humidity dependence of adhesion for several commercially relevant powders like hydrated alumina, a silica aerogel, limestone, titania and zeolite [47] or pharmaceutical products like a-lactose monohydrate, salbutamol sulphate, budesonide, triamcinolone acetonide, and disodium cromoglycate [48, 49, 50]. Duong et al. [51] used force–distance curves on 900–1100 μm glass beads that were exposed to different amount of water in a shaker. A clear correlation between amount of water, adhesion force of the AFM tip due to capillary forces and particle size segregation in the shaker was observed.

As a summary, meniscus forces can show a complex and rich behavior depending on surface roughness, interaction geometry and hydrophilicity. Often quite different dependencies of adhesion force on humidity are reported for the same system, e.g. for mica [45, 52, 53], and the increase of adhesion with humidity is either reported to be step-like [39, 45], linearly increasing [32, 54] or exhibiting a maximum at intermediate values [53, 30]. These discrepancies need clarification. Kinetics of neck formation and distribution of water layers at the surface are still open questions. Last but not least, capillary condensation can occur not only from the vapor phase but was also found in binary mixtures [55, 56].

1.1.8 Electrostatic Force

By using conducting tip AFM cantilever and also a conducting substrate one can apply an electrostatic field between the tip and the substrate. A measurement of electrostatic forces is of wide interest for a better understanding of electrostatic force microscopy or Kelvin probe microscopy, and also for understanding charging mechanisms. For this reason a number of experiments and theoretical approaches are described in the literature. Relatively well understood is the interaction between a metallic tip and a metallic sample. For good conductors the electric potential is the same everywhere and identical to the applied potential. In a calculation that implies that the field lines are oriented perpendicular to the surfaces. A calculation of the electrostatic force is straightforward. The energy is given by $CV^2/2$, where C is the capacitance of tip and sample and V is the applied voltage. The force is the derivative of the electrostatic energy. The measure of Coulomb forces until now has been of little interest, but it can be employed in order to study the tip shape. Hao et al. [57] have studied Coulomb forces by modeling the tip-sample system as a sphere on a flat surface and as a sphere-ended conical tip on a fiat sample, as shown in fig. 1.12. In the first case, the force is given by

$$F_0^{SP} = \pi\varepsilon_0 V^2 \frac{R_t}{D} \tag{1.28}$$

for $R_t/D >> 1$ and by

$$F_\infty^{SP} = \pi\varepsilon_0 V^2 \left(\frac{R_t}{D}\right)^2 \tag{1.29}$$

for $R_t/D << 1$. V is the voltage difference between the tip and sample, R_t the radius of the sphere and D is the tip-sample distance.

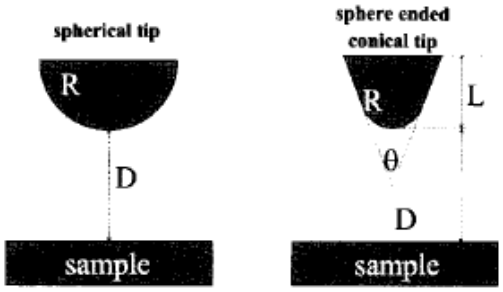

Figure 1.12. The two tip-sample systems employed by Hao et al. [57] for the calculation of Coulomb force. R_t is the radius of the sphere, D the tip-sample distance, L the length of the sphere-ended conical tip, and θ the aperture angle.

In the case of a sphere-ended cone on a flat surface, the force may be calculated by replacing the equipotential conducting surfaces with their equivalent image charges. For small aperture angles ($\theta \leq \pi/9$) the cone may be approximated by a charged line of constant charge density λ_0 given by

$$\lambda_0 = 4\pi\varepsilon_0 V[\ln(\frac{1+\cos\theta}{1-\cos\theta})]^{-1} \qquad (1.30)$$

The resulting force is given by

$$F^c \cong \frac{\lambda_0^2}{4\pi\varepsilon_0}\ln(\frac{L}{4D}), \qquad (1.31)$$

in which L is the cone length ($L << D << R_t$).
Hao et al. have measured the Coulomb forces between a tungsten tip and graphite. By fitting the experimental data, the authors have been able to determine the curvature radius of different tips (270 and 27.5 nm, in good agreement with scanning electron microscope measurements).

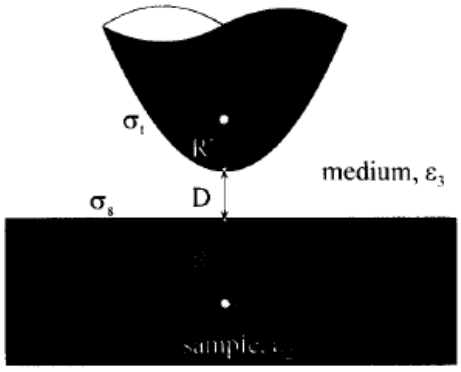

Figure 1.13. The tip-sample system employed by Burnham et al. [58] for the calculation of patch charges force is shown. The tip and sample surface charges are represented by two image charges Q_t and Q_S placed at the distances R' and R". D is the tip sample distance, ε_1, ε_2 and ε_3 are the dielectric constants of the tip, the sample, and the medium, respectively.

Burnham et al. [58] have studied another kind of Coulomb-like force which arises from the patch charges distribution on the tip and sample, i.e., from regions of different surface charge density interacting via a long range force law. The patch charges distribution can be modeled by means of the image charge method, as shown in fig. 1.13. A spherical tip of radius R_t on a flat sample with surface charge densities σ_t and σ_S represented by an image charge Q_t at a distance R' inside the tip and by an image charge Q_s at a distance R" inside the sample are considered. If R >> R' >> D and R" >> D, R, R', then the force is given by

$$4\pi\varepsilon_0 F = -\frac{Q_t}{4R'^2}\left(1-\frac{2D}{R'}\right)\left(\frac{\varepsilon_2-\varepsilon_3}{\varepsilon_2+\varepsilon_3}\right)+\frac{Q_t Q_S}{RR''}\left(1-\frac{2R'}{R}-\frac{4D}{R}\right)\left(\frac{\varepsilon_1-\varepsilon_3}{\varepsilon_1+\varepsilon_3}\right)\left(\frac{\varepsilon_2-\varepsilon_3}{\varepsilon_2+\varepsilon_3}\right), \quad (1.32)$$

where ε_1 and ε_2 are the dielectric constants of the tip and sample and ε_3 is the dielectric constant of the medium.
Patch charge densities are negligible compared to double-layer charge densities. The patch charge force is larger than the van-der-Waals force and has the same dependence on the dielectric constants. Note that, if the geometrical constants R and R' are much larger than D, eq. 1.32 becomes effectively independent on the distance. There is evidence that this occurs when the ratio of the probe radius to the distance is 10^3.
This kind of force has been measured by Burnham et al. [58] and by Agraft et al. [59]. This latter experiment has been performed in vacuum, at liquid helium temperature (4.2 K), using a gold tip on a gold sample. The presence of contaminants can therefore be excluded, allowing the different forces to be distinguished from each other.

1.1.9 Magnetic Force

Like Electrostatic force, one can also map the magnetic force by using magnetized tip (coated with magnetic material) AFM cantilever on a magnetic substrate. This is known as Magnetic Force Microscopy (MFM). In this case, magnetic domains on a surface exert either an attractive or a repulsive force on the magnetized tip, and MFM maps the magnetic domain structure. For examples, MFM can be used to image naturally occurring and deliberately written domain structures of magnetic materials. MFM requires cantilevers that have coated with a ferromagnetic thin film such as sputtered cobalt. The magnetic force between the tip and the sample is often stronger and has a longer range than the van-der-Waals' force which is imaged in non-contact AFM (NC-AFM). Thus it is possible to image only the magnetic domains on a sample by keeping the tip far from the surface, where van-der-Waals' forces are negligible.
The underlying principles of MFM are similar to those of NC-AFM. For the case of MFM, a magnetized tip is used, and forces between this magnetic tip and magnetic domains on the sample surface must be included on the force vs. distance curve.
Fig. shows an interatomic force vs. distance curve for a typical sample and tip used to take an MFM image (e.g., a magnetic storage disk and a cantilever tip coated with

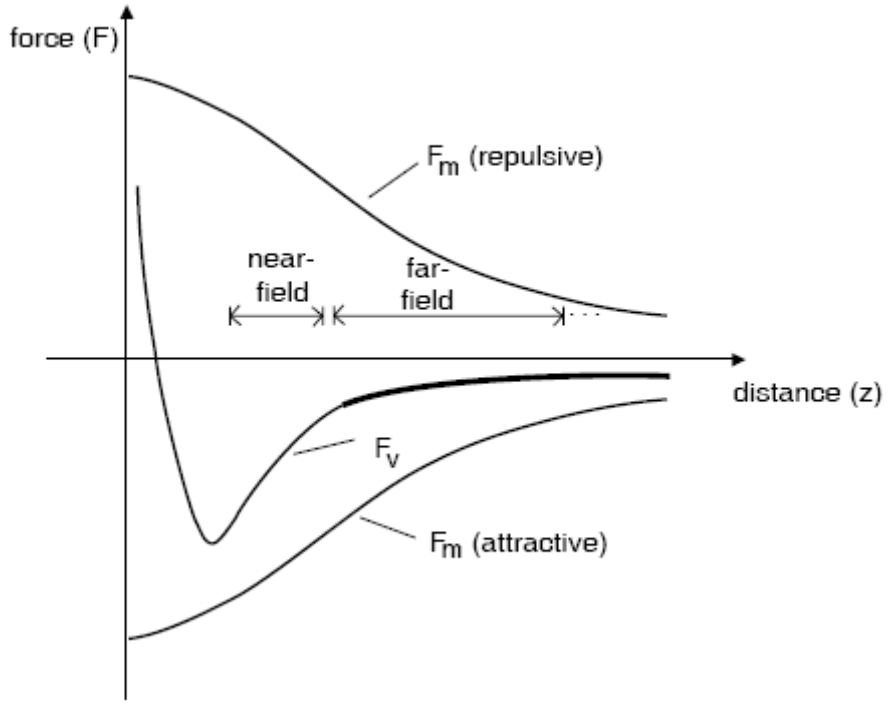

Figure 1.14. Magnetic force and van-der-Waals force.

sputtered cobalt). The figure shows that magnetic forces (F_m) are superimposed upon the van der Waals' forces (F_v), which are still present.
There are two, symmetric magnetic force vs. distance curves: one represents forces acting when the magnetic interaction is attractive (negative F_m values), and the other when it is repulsive (positive F_m values). Both types of forces could be present for a single sample since they could represent different magnetic domains on the sample surface.
The net force between the atoms on the cantilever tip and atoms on the sample surface is the sum of the magnetic force (repulsive or attractive) and the van-der-Waals' force:

$$F = F_m + F_v \tag{1.33}$$

Similarly, the net force gradient experienced by a vibrating cantilever is the sum of the gradient of the magnetic force and the gradient of the van-der-Waals' force:

$$dF/dz = dF_m/dz + dF_v/dz \tag{1.34}$$

where z is the tip-to-sample spacing.
The key to understand MFM methods is to identify the force or force gradient term that is dominant in a given tip-to-sample spacing regime. For MFM, the tip-to-sample spacing typically lies in the range of ten to hundreds of angstroms, or in the non-contact regime. This range of spacing for MFM operation can be further divided into far-field and near-field regimes (as indicated in fig.1.14). The far-field and the near-field regimes are defined based on whether the force gradient is dominated by the magnetic or the van-der-

Waals' force gradient term. Specific distance numbers that define the limits of these regimes depend on the specific tip and sample materials being used.
In the far-field regime, the gradient of the magnetic force is greater than the gradient of the van-der-Waals' force. The dominance of the magnetic force gradient in the far-field regime means that the topography signal, a signal that represents changes in the force gradient, is dominated by the magnetic properties of the sample surface. Thus, if an image is taken using the topography signal one can set the scan parameters to position the tip far enough away from the sample that it is in the far-field regime, and the image will represent magnetic features on the sample surface.
In the near-field regime, the gradient of the van-der-Waals' force is greater than the gradient of the magnetic force. The dominance of the van-der-Waals' force gradient in the near-field regime means that the topography signal that represents the force gradient is dominated by changes in the topography of the sample surface. Thus, if an image is taken using the topography signal, one can set the scan parameters to position the tip close enough to the sample that it is in the near-field regime, and the image will represent topographic features of the sample surface.
The simplest way to take an MFM image to adjust scan parameters such that the tip is far enough away from the sample to position it in the far-field regime. In the far-field regime, the gradient of the van-der-Waals' force is negligible and an image taken using the topography signal represents variations in the gradient of the magnetic force.

1.1.10 Different Modes of AFM

Table1.3 Different modes of AFM and their operating principles

Different modes of AFM	**What is it?**	**Operation regime**
1) Contact Mode	Measurement of probe-surface interaction force (may be van-der-Waals force, or interatomic short range) by deflection of probe cantilever	Contact regime
2) Dynamic Mode (Non-contact and Tapping Mode)	Technique for measurement of forces near a surface by vibrating probe, measuring AC component of force.	Non-contact regime
3) Lateral Force Microscopy (LFM)	Technique for measuring the friction between probe and surface.	Contact regime
4) Conducting AFM	Technique to map different electrical conductivities of the sample surface	Contact regime

Different modes of AFM	What is it?	Operation regime
5) Electrostatic Force Microscopy (EFM)	Measurement of the electric force near a surface, usually associated with permanently polarized materials	Non-contact regime
6) Magnetic Force Microscopy (MFM)	Measurement of the magnetic force near a surface, usually associated with ferromagnetism (permanent polarization)	Non-contact regime
7) Force Modulation Microscopy (FMM)	Technique to map different elastic properties of the sample surface.	Contact regime
8) Scanning Thermal Microscopy (SThM)	Technique to map different thermal conductivities of the sample surface	Contact regime
9) Nanolithography	Technique to create patterns on the surface either by scratching the surface or by anodic oxidation	Contact regime
10) Nanomanipulation	Technique to move the molecules to specific position on the substrate by AFM cantilever	Non-contact regime

Table1.3 Different modes of AFM and their operating principles

1.2 Static mode spectroscopy

In the static mode AFM operation, the static tip deflection is used as a feedback signal. Because the measurement of a static signal is prone to noise and drift, low stiffness cantilevers are used to boost the deflection signal. However, close to the surface of the sample, attractive forces can be quite strong, causing the tip to 'snap-in' to the surface. Thus static mode AFM is almost always done in contact where the overall force is repulsive. Consequently, this technique is typically called 'contact mode'. In contact mode, the force between the tip and the surface is kept constant during scanning by maintaining a constant deflection.

1.2.1 Acquiring Force vs. Distance curves

A force (F) vs. distance (d) curve, which is acquired in contact-AFM mode, is a plot of the force between the tip and the sample as a function of the extension of the piezoelectric scanner tube. Generating an F vs. d curve involves taking an image, then

stopping the raster scan, and then selecting a point on the image to generate an F vs. d curve. It is important to mention here that before acquiring the F vs. d curves we have to calibrate the vertical axis of the F vs. d graph with units of force. If this procedure is not performed, the units of the vertical axis do not correlate correctly with force. This has to be done every time one switches to a different cantilever. The calibration procedure involves taking an F vs. d curve using a hard sample. Using a hard sample ensures that the mechanical properties of the sample do not couple with those of the cantilever and affect the calibration.

1.2.2 Calibration: Methods for the calculation of forces

All AFM whether home made or not, provide the cantilever deflection as a function of the distance between the sample and the rest position of the cantilever. In order to know the tip-sample force, several transformations of the data have to be performed. If the sample is much more rigid than the cantilever and no deformation of the sample occurs, along the contact line the deflection of the cantilever equals the displacement of the piezoactuator, i.e., $\Delta\delta_c = \Delta Z$. Usually, if the optical lever method is employed, the deflection of the cantilever is given by the voltage output of the photodiode. This voltage, however, depends also on laser spot shape and dimensions. Along the contact line, the relation between the voltage output ΔV and the displacement of the piezo is given by

$$\Delta\delta_c = \Delta Z = \Delta V / \Omega, \tag{1.35}$$

where Ω is a proportionality factor. In order to know δ_c the zero deflection value V_0 of the voltage is needed, and can be determined from the zero line. A first problem with this procedure is associated with the hysteresis and the creep of the piezo, affecting the measurement of Z. As a general rule, the response of the piezo should be checked previous to any force-distance curves acquisition and eq. 1.35 should be applied to approach curves. Furthermore, depending on the sample, the relation $\Delta\delta_c = \Delta Z$ might not be correct at low loads. Hence, as a rule of thumb, it is always better to consider in the above procedure the tangent to the loading curve at high loads. The origin of the Z axis is placed at the beginning of the contact line. Because of tip asperities, the contact line may begin prior to intimate true contact. Thus, the asperities on the tip affect the determination of tip-sample distances. Taking into account all these effects, tip-sample distances can be determined by means of the equation:

$$\Delta Z = -\frac{L_p}{w_p} d_{31} \Delta V, \tag{1.36}$$

in which L_p and W_p are the length and the wall thickness of the piezotube, d_{3l} is a proportionality factor characteristic of materials, and V is the voltage applied to the piezo. The factor Ω in eq. 1.35 depends on the dimensions and on the shape of the laser spot on the photodiode, and hence depends on the refractive index of the medium in which the measurements are performed [60]. Furthermore, this factor may change in time due to the thermal drift of the components of the microscope, and should be checked previous to any measurement. Once the deflection of the cantilever in nanometers is known, the product $k_c\Delta\delta_c$, gives the force in newtons:

$$\Delta F = k_c \Delta \delta_c = k_c \Delta V / \Omega. \qquad (1.37)$$

Once the true tip-sample distance is known, and the force has been deduced from cantilever deflections, the curve can be rearranged in order to give a "normalized" representation, i.e., a plot of the force vs. the true tip-sample distance D. This representation is referred to as the "force-distance curve". The main problem in the calculation of forces is given by the knowledge of the cantilever elastic constant.

1.2.3 Understanding Force vs. Distance curves

In F vs. d curve, the vertical force on the cantilever tip is proportional to the cantilever bending, which is measured using a positionsensitive photodetector (PSPD). An F vs. d curve is generated at a single location on a sample surface by measuring how much the cantilever bends during one or more “sweeps” (up and down movements) of the scanner. Variations in the shape of F vs. d curves taken at different locations indicate variations in the local elastic properties of the sample surface. The shape of the curve is also affected by contaminants and surface lubricants, as well as a thin layer of water on the surface, which is usually present when operating a Contact-AFM in air.

A generalized F vs. d curve is shown in fig.1.15 for the case of a Contact-AFM operating in air. It is generated at a specific location on the sample surface by extending

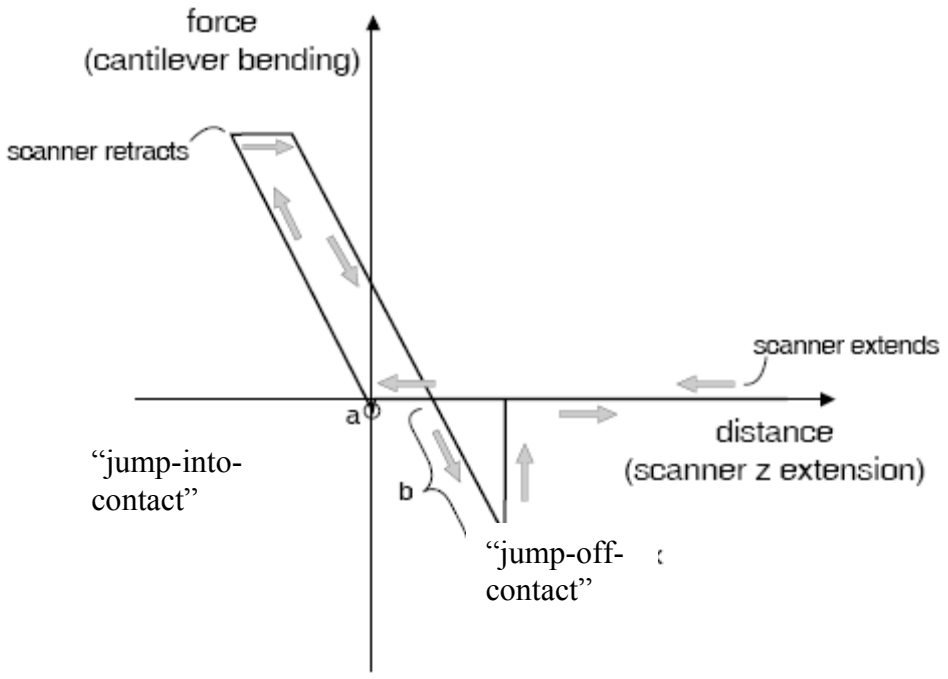

Figure 1.15 A generalized F vs. d curve for an AFM in air.

and then retracting the scanner while measuring cantilever bending. In the figure, the vertical axis (“force”) represents the measured cantilever deflection. The horizontal axis (“distance”) represents the z position of the scanner. The far right side of the curve is

defined to be where the scanner tube is fully retracted, which is the starting point before a curve is taken. The net force on the cantilever at this point should be zero. The tip is not in contact with the sample, and the cantilever is undeflected. As the scanner tube is extended (moving to the left in fig. 1.15), the cantilever remains undeflected until the tip is close enough to the sample to experience the attractive interatomic force. At the "jump-into-contact" point (point a in fig.1.15), the tip snaps into the surface, causing the cantilever to bend toward the surface. The net force on the cantilever is negative (attractive). The scanner continues to extend, until the cantilever is bent away from the surface. The net force on the cantilever is positive (repulsive). After the scanner tube is fully extended, it begins to retract (moving to the right in fig. 1.15).
The force on the cantilever follows a different path. The horizontal offset between the initial and the return paths of fig. 1.15 is due to scanner hysteresis. The additional portion of the curve that shows a negative (attractive) force on the cantilever is generally attributable to a thin layer of water that is usually present on the sample surface when the surface is exposed to air. This water layer exerts a capillary force on the cantilever tip which is strong and attractive. The water layer holds the tip in contact with the surface, pulling the cantilever strongly toward the surface. This deflection of the cantilever is shown in fig. 1.15 as region b, where the net force on the cantilever is strongly negative. The scanner tube eventually retracts far enough for the cantilever tip to spring free of the water layer. This point is called the "jump-off-contact" point. Beyond the "jump-off-contact" point, the cantilever remains undeflected, and the net force on the cantilever should be zero.
Vertical deflection of the cantilever originates from several sources. Attractive van-der-Waals' forces between the tip and the sample pull the cantilever toward the surface. Capillary forces exerted on the tip by liquid layers on the sample surface also pull the cantilever toward the surface. In addition, repulsive interatomic forces between the tip and the sample deflect the cantilever away from the surface. Figure 1.16 shows the effects of positive and negative net forces on cantilever bending.

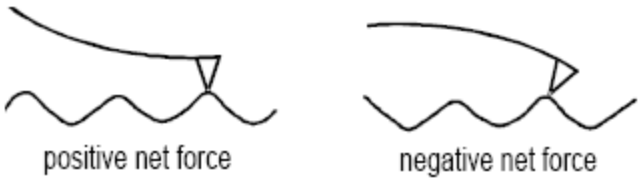

Figure 1.16 Effects of positive and negative net forces on cantilever bending.

1.2.4 Review of static mode spectroscopy

The first study on force-distance curves acquired with an AFM, concerning the characterization of surface forces on LiF and graphite, dates back to 1988 [61]. The first works trying to interpret force-distance curves and related information appeared in 1989-1990. Since the first experiments, it is believed that, when force-distance curves are acquired in air, meniscus forces exerted by thin layers of water vapor dominate any other interactions. Such forces can be eliminated by working in a controlled atmosphere or in a liquid environment. In 1991 several studies of force-distance curves in liquids were

performed, both theoretically and experimentally. Moreover, Mizes et al. [62] performed the first direct measurement of the spatial variation of adhesion. Since then, two different research lines have characterized the research on force-distance curves: on one hand, the study of different interactions in several environments, on the other, the "mapping" of such interactions, drawn from force-distance curves, in order to distinguish materials with different physico-chemical properties (a kind of "surface spectroscopy").
In 1994, a further technique was introduced [63]. This technique employs functionalized tips, i.e., tips covered with particular molecules that selectively adhere to other, in order to study specific forces by means of force-distance curves.

Relation between AFM force-distance curves and tip-sample interaction force

An AFM force-distance curve is a plot of tip-sample interaction forces vs. tip-sample distance. In order to obtain such a plot, the sample (or the tip) is ramped along the vertical axis (Z axis) and the cantilever deflection δ_c is acquired. The tip-sample force is given by Hooke's law:

$$F = -k_C \delta_C \tag{1.38}$$

The distance controlled during the measurement is not the actual tip-sample distance D (fig.1.17), but the distance Z between sample surface and the rest position of the cantilever. These two distances differ because of cantilever deflection δ_c and because of the sample deformation δ_s. These four quantities are related as follows:

$$D = Z - (\delta_C + \delta_S) \tag{1.39}$$

Since one does not know in advance the cantilever deflections and the sample deformations, the only distance that one can control is the Z distance, i.e., the displacement of the piezo. Therefore, the raw curve obtained by AFM should be called

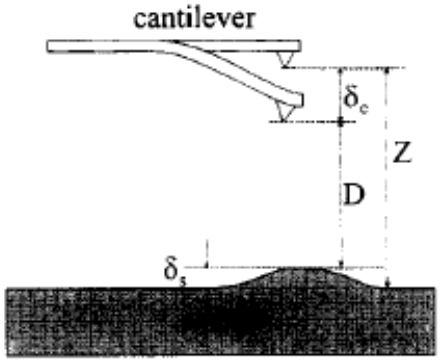

Figure 1.17. The tip-sample system. D is the actual tip-sample distance, whereas Z is the distance between the sample and the cantilever rest position. These two distances differ because of the cantilever deflection δ_C, and because of the sample deformation δ_S.

"force-displacement curve" rather than "force-distance curve". This latter term should be employed only for curves in which the force is plotted versus the true tip-sample distance, that has been previously calculated from raw data. An AFM force-displacement curve does not reproduce tip-sample interactions, but is the result of two contributions:

the tip-sample interaction F(D) and the elastic force of the cantilever, eq. 1.38. Such a result can be intuitively understood by means of the graphical construction shown in fig.1.18.
In fig. 1.18(a) the curve F(D) represents the tip-sample interaction force. For the sake of simplicity, F(D) is chosen to be the interatomic Lennard-Jones force, i.e., $F(D)= -A/D^7 + B/D^{13}$. By expressing tip-sample forces by means of an interatomic Lennard-Jones force, only a simple qualitative description of the mechanisms involved in force-displacement curves acquisition can be provided. In particular, the attractive force between surfaces actually follows a force law $-D^{-n}$ with $n \leq 3$ (and not $n = 7$) and the repulsive part of the force is much more complex than the one modeled by the Lennard-Jones force. The lines 1-3 represent the elastic force of the cantilever, eq. 1.38. In panel (b) of fig. 1.18 the resulting AFM force-displacement curve is shown. At each distance the cantilever deflects until the elastic force of the cantilever equals the tip-sample interaction force, so that the system is in equilibrium. The force values at equilibrium f_a, f_b, f_c are given by the intersections a, b and c between lines 1-3 and the curve F(D), respectively. These force values must not be assigned to the distances D at which the lines intersect the curve F(D), but to the distances Z between the sample and the cantilever rest positions, that are the distances α, β and γ given by the intersections between lines 1-3 and the horizontal axis (zero force axis). Going from right to left, i.e., approaching to the sample, the approach curve is obtained. Making the same graphical construction from left to right, i.e., withdrawing from the sample, gives the withdrawal curve. The result is shown in panel (b) of fig. 1.18. The points A, B, B', C, and C' correspond to the points a, b, b', c, and c', respectively.

Differences between approach and withdrawal curve

In panel (b) of fig. 1.18 two characteristic features of force-displacement curves can be noted: the discontinuities BB’ and CC’ and the hysteresis between approach and withdrawal curve. These features are due to the fact that in the region between b' and c' (panel (a), fig. 1.18) each line has three intersections and hence three equilibrium positions. Two of these positions (between c’ and b and between b' and c) are stable, while the third position (between c and b) is unstable. During the approach phase, the tip follows the trajectory from d to b and then "jumps" from b to b' (i.e., from the force value f_b to $f_{b'}$,).
During retraction, the tip follows the trajectory from b' to c and then jumps from c to c’ (i.e., from f_c to $f_{c'}$). These jumps correspond to the discontinuities BB’ and CC' in panel (b) of fig. 1.18, respectively. Thus, the region between b and c is not sampled. The difference in path between approach and withdrawal curves is usually called "force-displacement curve hysteresis". The two discontinuities in force values are called "jump-to-contact" in the approach curve (BB’ in panel (b) of fig. 1.18) and "jump-off-contact" in the withdrawal curve (CC' in panel (b) of fig. 1.18). This is discussed in detail in chapter 3 and 4.

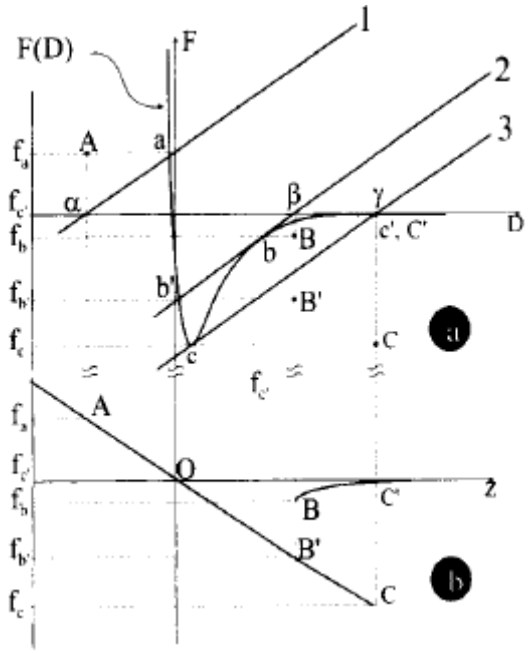

Figure 1.18. Graphical construction of an AFM force-displacement curve. In panel (a) the curve *F(D)* represents the tip-sample interaction and the lines 1, 2, and 3 represent the elastic force of the cantilever. At each distance the cantilever deflects until the elastic force equals the tip-sample force and the system is in equilibrium. The force values f_a, f_b, and f_c at equilibrium are given by the intersections a, b, and c between lines 1, 2, and 3 and the curve *F(D).* These force values must be assigned to the distances Z between the sample and the cantilever rest positions, i.e., the distances α, β, and γ given by the intersections between lines 1, 2, and 3 and the horizontal axis. This graphical construction has to be made going both from right to left and from left to right. The result is shown in panel (b). The points A, B, B', C, and C' correspond to the points a, b, b', c, and c' respectively. BB' and CC' are two discontinuities. The origin O of axis in panel (b) is usually put at the intersection between the prolongation of the zero line and the contact line of the approach curve. The force $f_{c'}$, eventually coincides with the zero force.

In early AFMs, the cantilevers used for force-displacement curves measurements were tungsten wires, curved at one end, with high elastic constants (> 1 N/m) and with large radii of curvature (> 100 nm). The achieved force resolution was usually of the order of hundreds of pN so that the details of the tip sample interaction could hardly be seen. Later, less stiff cantilevers with smaller radii of curvature have been employed, increasing the resolution up to nearly 10 pN. Recently Aoki et al. [64] proved that the force resolution of the AFM can be increased to 0.1 pN. They employed home-made

cantilevers with a spring constant of the order of 10^{-4} N/m. Such flexible cantilevers undergo large brownian motions and hence need to be stabilized by feedback forces. In this case, the feedback force is exerted by means of laser radiation pressure. Besides a first laser beam aimed to the deflections detection, a second laser beam is focused on the cantilever. The intensity of this second laser beam is varied with a fast feedback loop, in order to keep constant the deflection of the cantilever.

1.3 Other methods to measure surface forces

Surface Force Apparatus

The study of surface interactions can be performed with several other tools [65, 66]. Between all these tools the surface force apparatus (SFA) is the leading instrument in surface force measurements. By the end of the 1950s, Spaarnay developed an instrument that could be used to measure forces between two parallel metallic plates that were separated by only a few nanometers distance [67]. Later, Tabor and Winterton, and Israelachvili and Tabor further improved this method and called it the surface force apparatus (SFA) [68, 69]. Two atomically smooth cylindrical surfaces with well-defined radii of curvature are brought in contact under controlled atmosphere. A fluid film separates the bodies. By using optical interferometry techniques, the gap between the bodies can be determined with a resolution of at least 0.1 nm. The SFA was originally developed to measure normal forces between two bodies. Chan and Horn added the lateral displacement option to the SFA [70]. The lateral displacement was introduced by a leaf spring system. During a measurement, the vertical distance, true area of contact, elastic deformation, and lateral force could be registered. Typical sliding velocities were in the range of 0.1-20 μms^{-1} with a stroke length of several hundred micrometers. Van Alsten and Granick implemented a piezoelectric transmitter and receiver, mounted on the lateral springs to excite and measure the lateral displacement [71]. They were able to measure the lateral force with a resolution of 10^{-6} N; the lateral displacement amplitude ranged between several nanometers up to 10 μm. They reported investigations on thin lubricant films of molecular thickness. It was observed that there is a transition from purely viscous to solid-like behaviour with decreasing film thickness [72]. Georges et al. even improved the set-up that required transparent samples in order to measure contact area [73, 74]. With capacitive displacement sensors and piezoelectric transducers, they were able to measure sliding friction between a flat and a sphere in quasi-static and dynamic state.
The SFA employs only surfaces of known geometry, thus leading to precise measurements of surface forces and energies.

Comparisons between Surface Force Apparatus (SFA) and Atomic Force Microscope (AFM)

Although there is a considerable overlap in the force measuring capabilities of the AFM and the SFA, we would like to point out several differences.

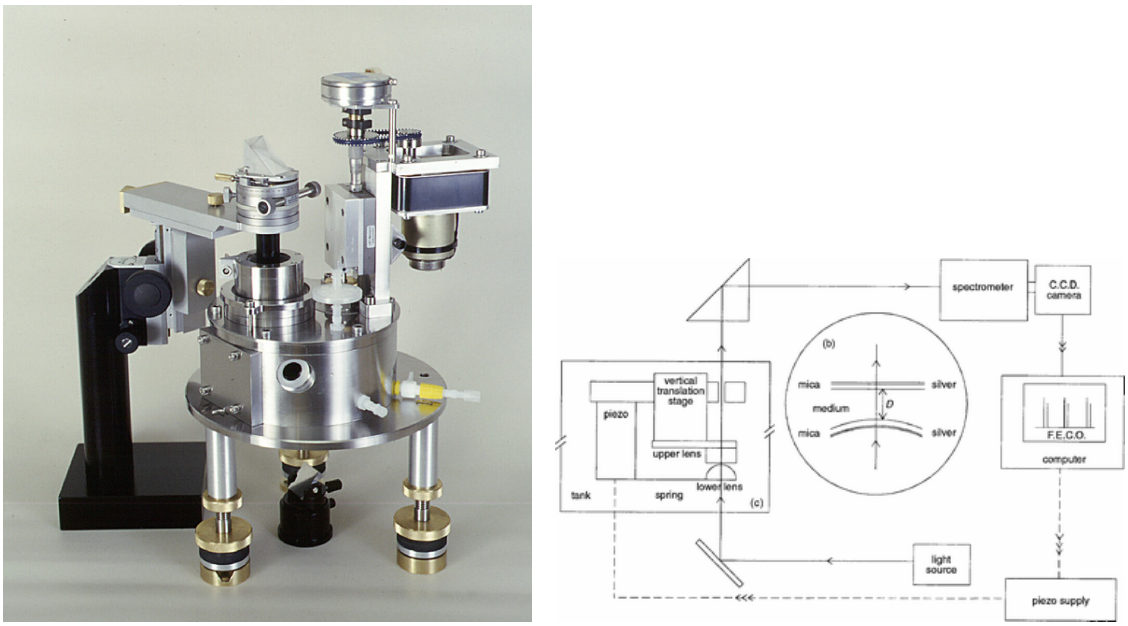

Figure 1.19 Diagram of Surface Force Aparatus

1. Interacting surfaces in AFM are 10^4-10^6 times smaller than those employed in SFA, but in AFM the shape of the surfaces is unknown.
2. When the substrates to be employed are not transparent, the interferometric technique cannot be used to measure forces (ref. [75]).
3. The SFA needs molecularly smooth samples, and therefore it can deal only with mica surfaces or thin layers of materials adsorbed on mica.
4. The SFA cannot characterize indentation or topography.
5. The viscous force on a spherical particle scales with the square of the particle radius. Therefore with an AFM, measurements can be performed at speeds 10^4 times greater while maintaining the same viscous force to surface force ratio [76].
6. Since the interacting surfaces are smaller, and the probability of trapping a contaminant particle is proportional to the square root of the interacting surfaces, the AFM is less subject to contamination [76].

1.4 Dynamic Mode Spectroscopy

While the quantitative interpretation of force curves in contact mode AFM is straightforward using eq. 21, its application to assess short-range attractive interatomic forces is rather limited. The dynamic mode of operation seems to open a variable direction towards achieving this task; however interpretation of the measurement generally appears to be more difficult. Different operational modes are employed in dynamic AFM.
The oscillation trajectory of a dynamically driven cantilever is determined by three parameters: the amplitude, the phase, and the frequency. Tip-sample interactions can influence all three parameters, in the following termed the internal parameters. The

oscillation is driven externally, with excitation amplitude A_d and excitation frequency ω. These variables will be referred to as the external parameters. The external parameters are set by the experimentalist, whereas the internal parameters are measured and contain the crucial information about the force interaction. In scanning probe applications, it is common to control the probe-surface distance z in order to keep an internal parameter constant (i.e., the tunneling current in STM or the beam deflection in contact AFM), which represents a certain tip-sample interaction. In z-spectroscopy mode the distance is varied in a certain range, and the changes of the internal parameters are measured as a fingerprint of the tip-sample interactions.

In dynamic AFM the situation is rather complex. Any of the internal parameters can be used for feedback of the tip-sample distance z. However, in general the tip-sample forces could only be fully assessed by measuring all three parameters. This makes it difficult to obtain images where the distance z is a representative of the surface at one force set-point. A solution to this problem is to establish additional feedback loops, which keeps the internal parameters constant by adjusting the external variables.

In the simplest set-up, the excitation frequency is set to a predefined value, and the excitation amplitude remains constant by a feedback loop. This is called the AM mode (amplitude modulation) or also tapping mode. In principle, any of the internal parameters can be used for feedback to the tip-sample distance; in the AM mode the amplitude signal is used. Certain amplitude (smaller than the free oscillation amplitude) at a frequency close to the resonance of the cantilever is chosen, the tip is approached towards the surface under investigation, and the approach is stopped as soon as the set-point amplitude is reached. The oscillation-phase is usually recorded during the scan; however, the shift of the resonance frequency of the cantilever cannot be directly accessed, since this degree of freedom is blocked by the external excitation at a fixed frequency. It turns out that this mode is simple to operate from a technical perspective, but quantitative information about the tip-sample interaction forces has so far not been reliably extracted from AM mode AFM. Still, it is so far one of the most commonly used modes in dynamic AFM operated in air and even in liquid. The strength of this mode is the qualitative imaging of a large variety of surfaces. The modulated AFM in contrast to the purely static AFM can enhance sensitivity due to the use of lock-in techniques, which allows one to measure amplitude and phase of the oscillation signal with high precision.

As stated before, the internal parameters can be fed back to the external excitation variables. One of the most useful applications in this direction is the self-excitation system. Here the resonant frequency of the cantilever is detected and selected again as the excitation frequency. In a typical set up this is done with a phase shift of 90^0 by feeding back the detector signal to the excitation piezo (i.e., the cantilever is always excited in resonance). Influences of the tip-sample interaction forces on the resonant frequency do not change the two other parameters of the oscillation (i.e., amplitude and phase); only the oscillation frequency is shifted. Therefore it is sufficient to measure the frequency shift between the free oscillation and oscillation with tip-sample interaction. Since the phase remains at a fixed value the oscillating system is much better defined than before, and the degrees of freedom for the oscillation are reduced. To even reduce the last degree of freedom, the oscillation amplitude, another feedback loop can be established to keep the oscillation amplitude (A) constant by varying the excitation amplitude A_d. Now all internal parameters have a fixed relationship to the external excitation variables, the

system is well defined and all parameters can be assessed during the measurement. As it turns out, this mode is the only dynamic mode for which a quantitative relationship between tip-sample forces and the change of the resonant frequency can be established.

1.4.1 Amplitude-modulation/tapping-mode AFM

In tapping-mode or AM-AFM the cantilever is excited externally at a constant frequency close to its resonance. Oscillation amplitude and phase during approach of tip and sample serve as the experimental observation channels. Figure 1.20 shows a diagram of a typical tapping-mode AFM set-up. The oscillation amplitude and the phase (not shown in diagram), detected with the photodiode, are analyzed with a lock-in amplifier. The amplitude is compared to the set-point, and the difference or error signal is used to adjust the z-piezo (i.e., the probe-sample distance). The external modulation unit supplies the signal for the excitation piezo, and at the same time the oscillation signal serves as the reference for the lock-in amplifier. During one oscillation cycle with amplitudes of 10-100 nm the tip-sample interaction will range over a wide distribution of forces, including attractive and repulsive forces. Therefore, a convolution of the force-distance curve with the oscillation trajectory is measured. This complicates the interpretation of AM-AFM measurements appreciably.
At the same time, the resonant frequency of the cantilever will change due to the appearing force gradients. If the cantilever was excited exactly at its resonant frequency before, it will be excited off-resonance after interaction forces are encountered. This in return changes amplitude and phase, which serve as the measurement signals. Consequently, different amplitude will cause a change of the encountered effective force. There is no quantitative theory for the AM-AFM available, which allows the experimentalist to unambiguously convert the experimental data to a force-distance relationship.
The qualitative behaviour for amplitude versus z-position curves is depicted in fig.1.21. At large distances, where the forces between tip and sample are negligible, the cantilever oscillates with its free oscillation amplitude. Upon approach of the probe towards the surface the interaction forces cause the amplitude to change, resulting typically in an amplitude getting smaller with continuously decreasing tip-sample distance. This is expected, since the force-distance curve will eventually reach the repulsive part and the tip is hindered from indenting further into the sample, resulting in smaller oscillation amplitudes.

1.4.2 Self-Excitation Modes/Frequency Modulation

Despite the wide range of technical applications of the AM-or tapping mode of dynamic AFM, historically it was found that it is unsuitable for measurements in an environment extremely useful for scientific research: in vacuum or ultra-high vacuum (UHV) with pressure reaching $1X10^{-10}$ mbar. The STM has already shown how much insight can be gained from some highly defined experiments under those conditions. The time constant τ for the amplitude to adjust to a different tip-sample force scales with 1/Q (where Q is

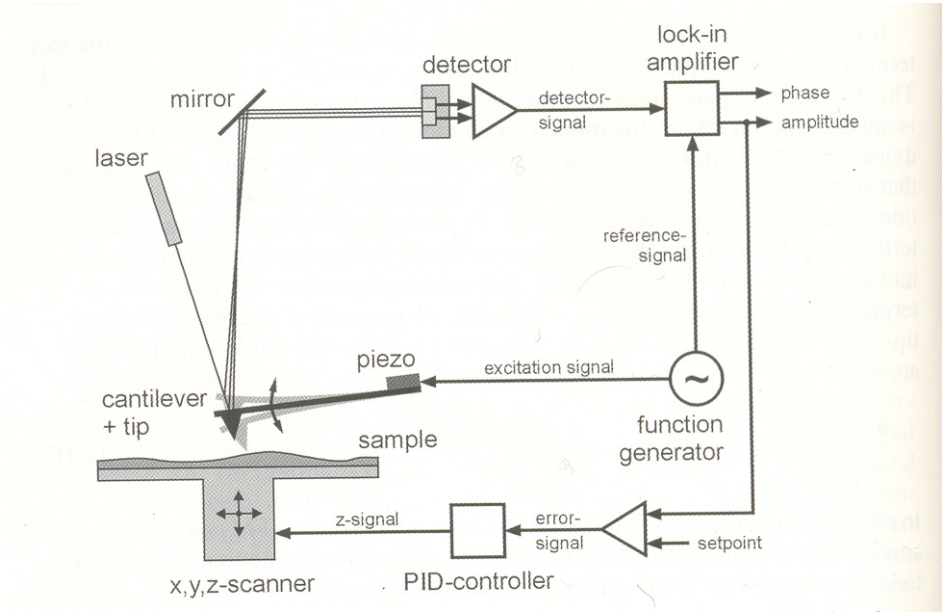

Figure 1.20 Set-up of a dynamic force microscope operated in the AM or tapping mode. A laser beam is deflected by the backside of the cantilever and the deflection is detected by a split photodiode. The excitation frequency is chosen externally with a modulation unit, which drives the excitation piezo. A lock-in-amplifier analyses phase and amplitude of the cantilever oscillation. The amplitude is used as the feedback signal for the probe-sample distance control [77].

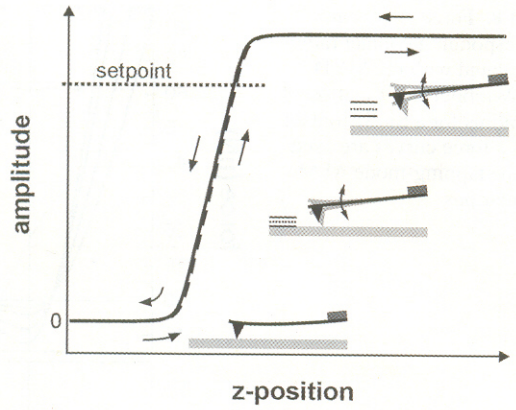

Figure 1.21 Simplified model showing the oscillation amplitude in tapping mode AFM for various probe-sample distances [77].

the quality factor). In vacuum applications Q of the cantilever is of the order of 10,000, which means that τ is in the range of some 10 ms. This is clearly too long for a scan of at least (100X100) data points. The temperature-induced drift of the sample will render useful interpretation of images an impossible task. However, the resonant frequency of

the system will react instantaneously to tip-sample forces. This has led Albrecht et al. [77a] to use a modified excitation scheme.
The system is always oscillated at its resonant frequency. This is achieved by feeding back the oscillation signal from the cantilever into the excitation piezo element. Figure 1.22 pictures the method in a block diagram. The signal from the PSD is phase shifted by 90^0 (and therefore always exciting in resonance) and used as the excitation signal of the cantilever. An additional feedback loop adjusts the excitation amplitude in such a way that the oscillation amplitude remains constant. This ensures that the tip-sample distance is not influenced by changes of the oscillation amplitude. The only degree of freedom of the oscillation system that can react to the tip-sample forces is the change of the resonant frequency. This shift of the frequency is detected and used as the set-point signal for surface scans. Therefore this mode is also called the FM (frequency-modulated) mode.
The sensitivity of the dynamic AFM can be calculated as follows. If electronic noise, laser noise, and thermal drift can be neglected, the main noise contribution will come from thermal excitation of the cantilever. A detailed analysis of a dynamic system yields the following relationship for the minimum detectable force gradient [77a]:

$$\frac{\partial F}{\partial z}\Big|_{MIN} = \sqrt{\frac{4k_c.k_B T.B}{\omega_0 Q\langle z_{osc}^2\rangle}} \qquad (1.40)$$

Here B is the bandwidth of the measurement, T is the temperature, k_c is the spring constant of the cantilever, k_B is the Boltzmann constant, ω_0 is the resonant frequency of the cantilever, and $<z_{osc}^2>$ is the mean-square amplitude of the oscillation. A similar analysis of the AM mode, however, yields virtually the same result [78]. It is found that the minimum detectable force gradient (i.e., the measurement sensitivity), is inversely proportional to the Q-factor of the cantilever. This means, that it should be possible to achieve very high resolution imaging under vacuum conditions. In contrast, AM-or tapping mode AFM cannot be usefully pursued with large Q. Only the FM mode makes it possible to take practical advantage of eq. 1.40.
A breakthrough in high-resolution AFM application was the atomic resolution imaging of the Si(111)-(7X7) surface reconstruction by Giessible [79] under UHV conditions. Today, atomic resolution imaging has become a standard feature guaranteed by industrially produced dynamic AFM systems. While STM has already proven to be an indispensable tool to gain detailed insight into surface structures of conductors with atomic resolution, the dynamic AFM has opened up the avenue into investigating non-conductive surfaces with equal precision (for example on aluminium oxide by Barth et al. [80]).
In this context it is worthwhile to point at a slightly different dynamic AFM method. While in the typical FM-AFM set-up the oscillation amplitude is controlled to stay constant by a dedicated feedback circuit, one could simply keep the excitation amplitude

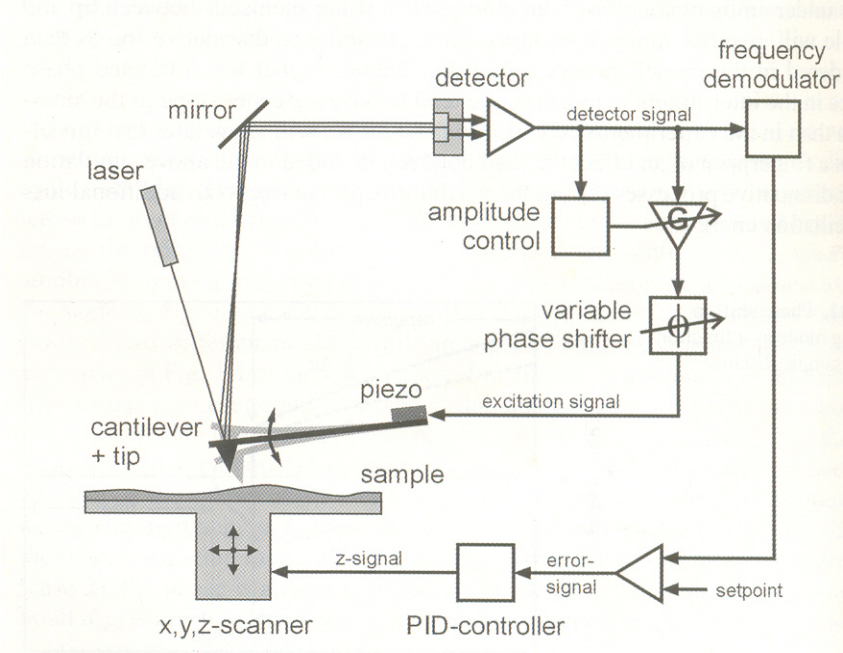

Figure 1.22 Dynamic AFM operated in the self-excitation mode, where the oscillation signal is directly fed back to the excitation piezo. The detector signal is amplified with the variable gain G and phase shifted by phase φ. The frequency demodulator detects the frequency shift due to tip-sample interactions, which serves as the control signal for the probe-sample distance [77].

constant (this has been termed CA=constant amplitude as opposed to the CE=constant excitation mode). It is expected that this mode is gentler to the surface, because any dissipative interaction will reduce the amplitude and therefore increase the tip-sample distance. The tip is prevented from indenting deeply into the surface. This mode has been employed to image soft biological molecules like DNA or thiols in UHV [81]. However, quantitative interpretation of the obtained frequency spectra is more complicated, since the amplitude and tip-sample distance are altered during the measurement. It is difficult to operate the FM-AFM in constant amplitude mode in air, since large dissipative effects make it difficult to ensure constant amplitude; it is indeed possible to use the constant-excitation FM-AFM in air or even in liquid. Still, only few applications of FM-AFM under ambient or liquid conditions have been reported so far.

1.4.3 Review of Dynamic mode spectroscopy

In order to gain some qualitative insight into the complex relationship between forces and oscillation parameters of vibrating cantilevers, numerical simulation has been done and compared with the experimental results. Anczykowski et. al. [82, 83] have calculated the oscillation trajectory of the cantilever under the influence of a given force model. Van-der-Waals interactions were considered the only effective, attractive forces, and the total interaction resembled a Lennard-Jones-type potential. Mechanical relaxations of tip and sample surface were treated in the limits of continuum theory with the numerical

MYD/BHW approach [84, 85], which allows the simulations to be compared to corresponding experiments. Figure 1.23 shows the force-distance curves for different tip radii underlying the dynamic AFM simulations.
The cantilever trajectory was analyzed by solving the equation of motion for the position z(t) of the oscillating cantilever tip

$$m\ddot{z}(t) = -\alpha\dot{z}(t) - kz(t) - kz_d(t) \tag{1.41}$$

extended by the force-distance relationships from fig. 14 using the numerical verlet algorithm [86]. The results of the simulation for the amplitude and phase of the tip oscillation as a function of z-position of the probe are represented in fig. 1.24. One has to keep in mind that the z-position of the probe is not equivalent with the real tip-sample

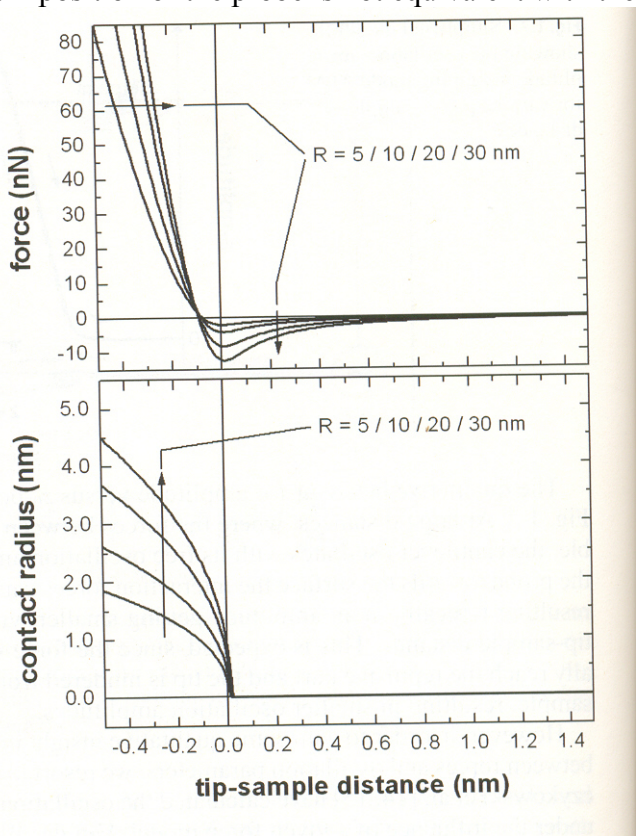

Figure 1.23 Forces curves and corresponding contact radius calculated with the MYD/BHW model as a function of tip-radius for a Si-Si contact. These force curves are used for the tapping mode AFM simulations [77].

distance at equilibrium position, since the cantilever might bend statically due to the interaction forces. The behaviour of the cantilever can be subdivided into three different regimes. We distinguish three cases, where the beam is oscillated below its resonant frequency ω_0, exactly at ω_0 and above ω_0. Figure 1.24 shows that amplitude and phase change rather abruptly at certain points when the z-position is decreased. Additionally, a hysteresis has been found between approach and retraction.
To understand the discontinuous features in the AFM spectroscopy curves of the first case, where the excitation frequency is smaller than ω_0, the oscillation amplitude as a function of excitation frequency (fig. 1.25) is considered. Upon approach of probe and

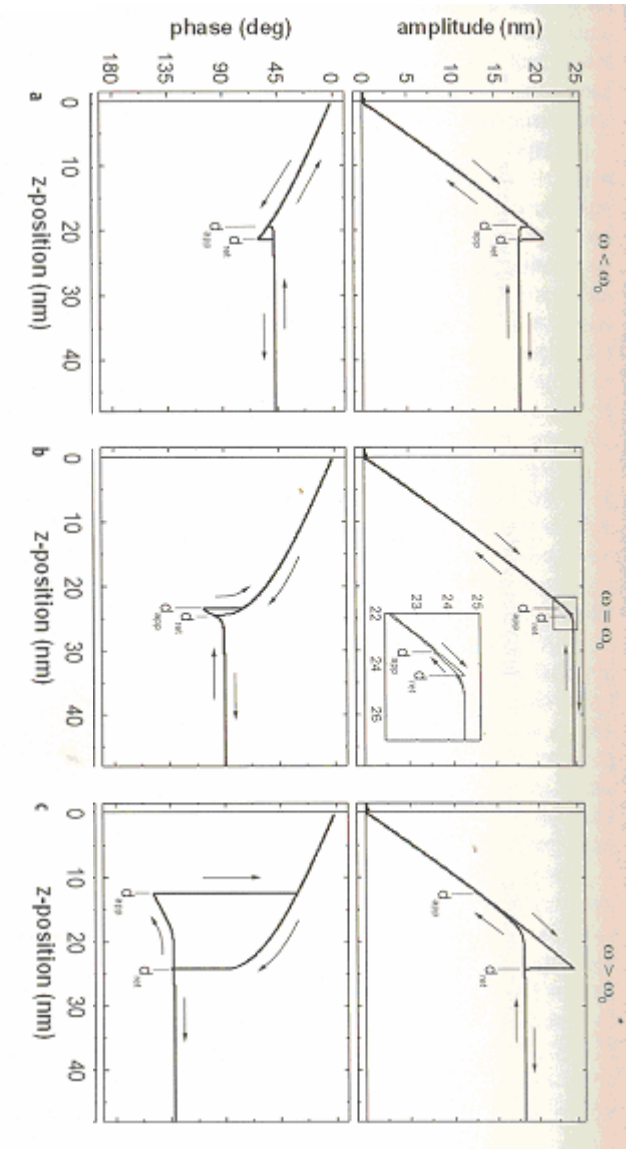

Figure 1.24 Amplitude and phase diagrams with excitation frequency (a) below, (b) exactly at, and (c) above the resonant frequency for the tapping mode AFM from the numerical simulations. Additionally, the botton diagrams show the interaction forces at the point of closest tip-sample distance, i.e., the lower turn-around point of the oscillation [77].

sample, attractive forces will lower the effective resonant frequency of the oscillator. Therefore, the excitation frequency will now be closer to the resonant frequency, causing the vibration amplitude to increase. This is in turn reduces the tip-sample distance, which again gives rise to a stronger attractive force. The system becomes unstable until the point $z=d_{app}$ is reached at which repulsive forces stop the self-enhancing instability. This can be clearly observed in fig. 1.24. Large parts of the force-distance curve cannot be measured due to this instability.

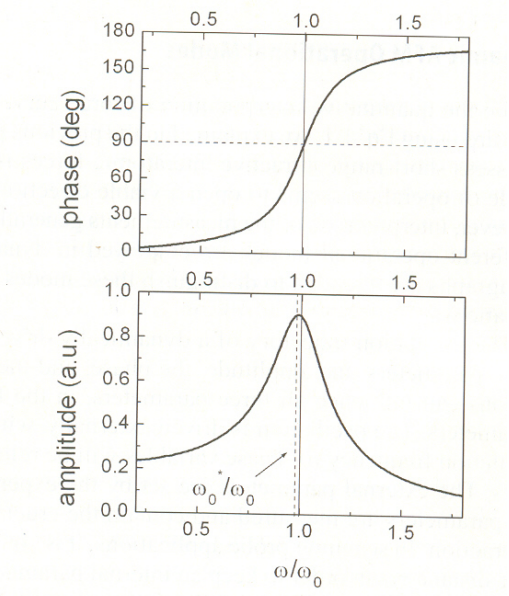

Figure 1.25 Amplitude and phase versus excitation frequency curves for the damped harmonic oscillator, with a quality factor Q=4 [77].

In the second case, where the excitation equals the free resonant frequency, only a small discontinuity is observed upon reduction of the z-position. Here a shift of the resonant frequency towards smaller values, induced by the attractive force interaction, will reduce the oscillation amplitude. The distance between tip and sample is therefore reduced as well, and the self-amplifying effect with the sudden instability does not occur, as long as repulsive forces are not encountered. However, at closer tip-sample distances, repulsive forces will cause the resonant frequency to shift again towards higher values, increasing the amplitude with decreasing tip-sample distance. Therefore a self-enhancing instability will also occur in this case, but here at the crossover from purely attractive forces to the regime where repulsive forces occur. Correspondingly, a small kink in the amplitude curve can be observed in fig. 1.24. An even clearer indication of this effect is manifested by the sudden change in the phase signal at d_{app}.
In the last case, with $\omega > \omega_0$, the effect of amplitude reduction due to the resonant frequency shift is even larger. Again, we find no instability in the amplitude signal during approach in the attractive force regime. Although as soon as the repulsive force regime is reached, the instability occurs due to the induced positive frequency shift. Consequently, a large jump in the phase curve from values smaller than 90^0 towards values larger than 90^0 is observed. The small change in the amplitude curve is not resolved in the simulated curves in fig. 1.24; however, this can be clearly seen in the experimental curves in fig.1.26.
In fig.1.26 corresponding experimental amplitude and phase curves are depicted. The measurements were performed in air with a Si-cantilever approaching a Si-wafer, with a cantilever resonant frequency of 299.95 kHz. Qualitatively, all prominent features of the simulated curves can also be found in the experimental data sets. Hence, the above model seems to capture the important factors necessary for an appropriate description of the experimental situation. The presence of higher harmonics, for small probe–sample

separation (h) has been predicted [87]. In some studies a chaotic behavior of the cantilever has also been observed [88].
Now the question arises what is the reason behind this sudden jump in the amplitude vs. distance curves shown in experiment as well as in the simulation. This has been discussed in detail in chapter 5 of this thesis.

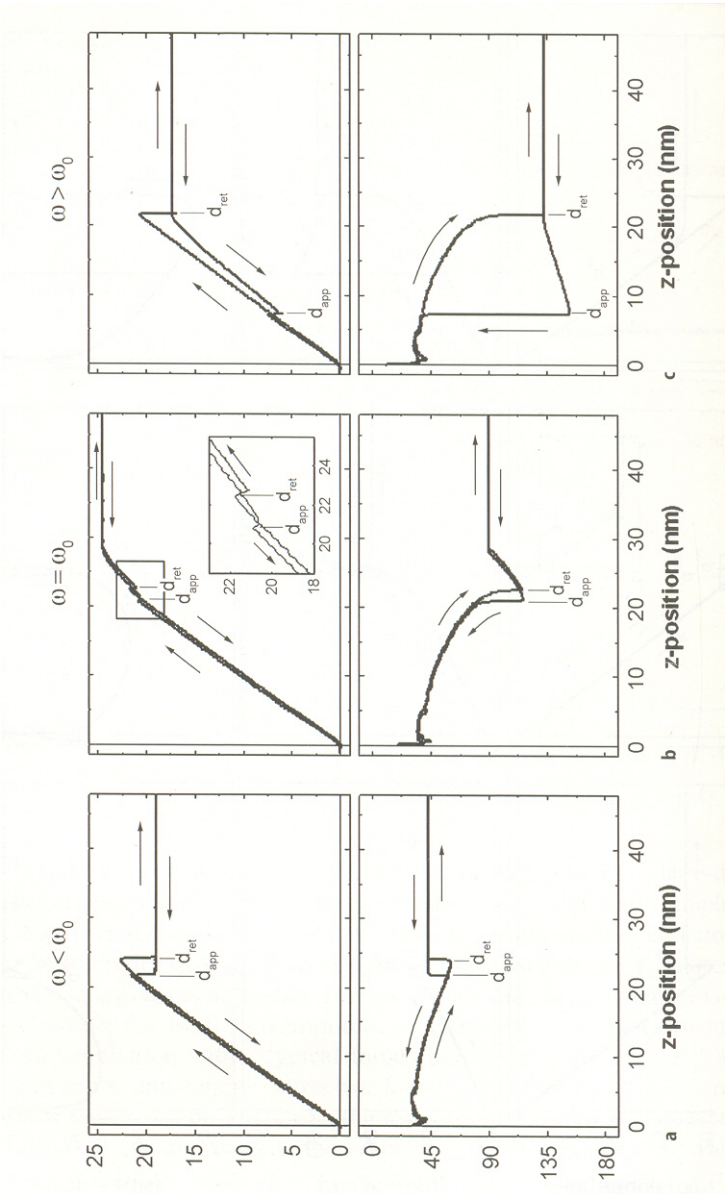

Figure 1.26 Amplitude and phase diagrams with excitation frequency (a) below, (b) exactly at, and (c) above the resonant frequency for tapping mode AFM from experiments with a Si-cantilever on a Si-wafer in air [77].

1.5 AFM Manipulation of Molecules

The linking of our macroscopic world to the nanoscopic world of single molecules, nanoparticles and functional nanostructures is a technological challenge. Researchers in nanobiotechnology face the questions “How to extract and analyze a single nano-object?”, “How to pick and place nanoobjects?” and “How to prototype a functional nanostructure?” Here, nanomanipulation by an atomic force microscope (AFM) offers a practicable solution. In such a system, the AFM can be operated as a nanorobot for manipulation purposes allowing for nanometer precision. AFM technology has the potential not only to observe and evaluate fine structure on a sample but also to manipulate an individual atom or cluster and modify a sample surface. This means that as previous microscope technology such as optical and electron microscopes have been applied to fabricate fine patterns for VLSI devices and storage devices, an application of the AFM technology to fabricate them with atomic and nanometer size can also be expected.

In the early development of techniques, most AFM experiments of molecule systems were limited to observations of their conformational features and physical properties of the sample surface. The achievements to use this technique as a manipulator of individual molecules have appeared in this decade with their recent technical progresses. Although various methodologies to configure the local properties and shapes of materials, such as local scratching, local indentation, anode oxidation, have been attempted, the use of AFM probe techniques to manipulate nanometer scale individual molecules has been the recent focus of innovative nanotechnology research.

Advantages of using AFM probe technique as a precise manipulator for molecules are following:

1) The effective size of an AFM probe is smaller than that of individual molecule units, and the probe can directly access inner parts of molecules.
2) Possibility for manipulation and modification of target molecules via mechanical interaction between the AFM probe and molecules.
3) The results of probe manipulation can be checked in situ using the same AFM scanning system.
4) The electric current flow between the probe and molecules can be used as a parameter of manipulation independently to the AFM feedback motion.
5) More complicated manipulation is possible by using the chemical interaction between molecules and a chemically modified AFM probe.

Especially, it is a versatile feature for nanometer scale manipulation that (1) and (3) is possible. At present, there are only a few successful examples of AFM manipulation of molecules that take full advantage of the benefits of AFM manipulation function, especially its high spatial resolution. The basic idea behind SPM based nanomanipulation is shown in fig. 1.27.

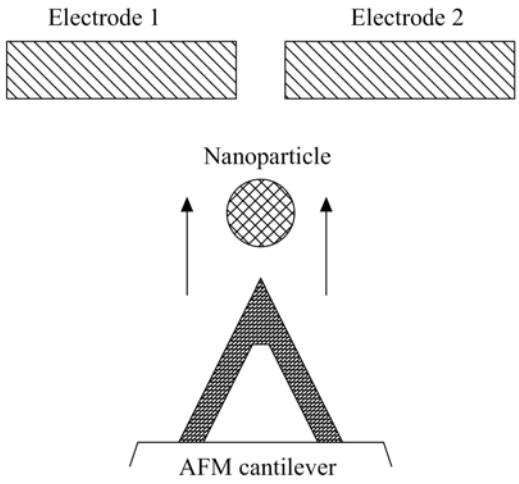

Figure 1.27. Using an AFM tip to place a nanoparticle between two e-beam fabricated electrodes.

1.5.1 Review of Manipulation by AFM

The first atomic level nanomanipulation was done by Scanning Tunneling Microscope (STM) [89]. However, in more recent context by nanomanipulation it is generally implied the use of AFM cantilever to manipulate nano objects. This field however is in its early stages and there is a need to understand the physics of the manipulation in terms of the basic forces that are involved in this process. It is realized that it is different from what one sees in micromanipulation. There are three main road blocks that need to be solved effectively before this field can mature. First, there is need to understand the basic physical and chemical processes that take place in the scale of few nanometers including the mechanics. Second, one needs to develop effective hardware as well as control that have resolution and reproducibility of manipulation at this level. Third, there is need for effective automation and software. Interestingly, these roadblocks not withstanding there are good examples of effective nanomanipulation that has made this field progress. Early stages of AFM based nanomanipulation appeared as far back as 1995 [90, 91], which showed the feasibility of such a process. Subsequent publications also addressed the modeling and simulation of such a process and the issue of manipulation forces [92-95].
The process of nanomanipulation involves control of a number of forces. The main two forces are the force of adhesion (F_a^{tp}) between the AFM tip and the adsorbate particle which will be manipulated and that between the particle and the substrate (F_a^{ps}). These forces are mediated by the surface forces [96] and depend on the formation of meniscus on the substrate. While F_a^{ps} stabilizes the particle on the substrate, F_a^{tp} makes the particle stick to the tip. The contact force between the tip and the particle F_c makes the particle move. The movement of the cantilever from its equilibrium position and the force constant of the cantilever determine the contact force in turn. In addition, since the

experiments are carried out in air ambient, there are capillary forces between the tip and the particle as well as the van-der-Waal forces between the tip and the particle and that between the particle and the substrate. It is the balance of these forces that determines the final dynamics of the particle movement.

As a simple model it is considered that $F_a^{tp} \approx 4\pi R_{eff} \gamma_{sv}$ and $F_a^{ps} \approx 4\pi R_p \gamma_{sv}$ where R_t = Radius of curvature of the tip and R_p= Radius of curvature of the particle and $R_{eff} = (1/R_t+1/R_p)^{-1}$. γ_{sv} = surface energy at the solid vapour interface. In order to move the particle from one place to other it is important to ensure (1) that the particle does not adhere to the tip and also (2) the component of the contact force between the tip and the particle parallel to the surface ($F^c_{||}$) is larger than the force of friction so that the particle can be moved. As a rough estimate of the force of friction is $F^{ps}_{friction} \approx \mu^{ps} (F_a^{ps}+ F^{ps}_{load})$ where F^{ps}_{load}= loading force and μ^{ps} is the coefficient of friction between the particle and the substrate. The tip will "ride" smoothly along the surface of the particle when the tangential component of F_c on the surface of the particle is larger than the frictional force between the two which is determined by F_a^{tp} and the μ^{tp}, the coefficient of friction between the particle and the tip. (The selection of the absorption chemicals is an important issue because it determines the force of adhesion. It depends on the type of the substrate and the particle. For instance, in manipulation of Au on mica Poly-L-Lysine is used.).To meet condition (1), i.e, to ensure the particle does not stick to the tip, one should minimize F_a^{tp}, which for a given γ_{sv} happens for a minimum R_t. This can be achieved by a tip of long aspect ratio. When the tip and the particle have similar size, $R_{eff} \approx R_p/2$ and $F_a^{tp} \approx F_a^{ps}/2$ and the particle is not likely to adhere to the tip. Condition (2) would imply that there is minimum contact force that is needed to move the particle. In order to have a substantial contact force that can make $F^c_{||} > F^{ps}_{friction}$. This would imply that one would need a stiff cantilever (one with a large spring constant typically > 10 N/m) for the manipulation. In fig.1.28 (a) a tentative force diagram for the nanomanipulation is shown.

The scheme to do nanomanipulation can be roughly described as below. Generally noncontact mode mage of the substrate is first taken to mark the particles to be manipulated and the trajectory of its movement. The noncontact mode ensures that $F^c_{||} \approx 0$. The cantilever vibrating at amplitude *A* is then lowered near the particle to be moved. At this stage, the feed back loop of the AFM is put to a hold mode so that the change in vibration amplitude does not make the feed back circuit adjust the tip - particle distance. The contact to the particle is detected by reduction in *A* and an increase in the static deflection. The cantilever carrying the tip is then moved along the desired trajectory. This movement would require a closed loop X-Y scanner for the AFM. At the stop position the tip is again pulled out and the feed back is enabled to start the noncontact mode imaging process again. Sufficient $F_a^{ps} > F_a^{tp}$ will ensure that the particle is parked at the desired spot as described before. This can be made sure by the cantilever oscillating at its previous amplitude again. A schematic of the manipulation process described above is given in figure 22(b). The description given above of the nanomanipulation process as well as the important forces is a simplification of the process that occur which in reality is rather involved.

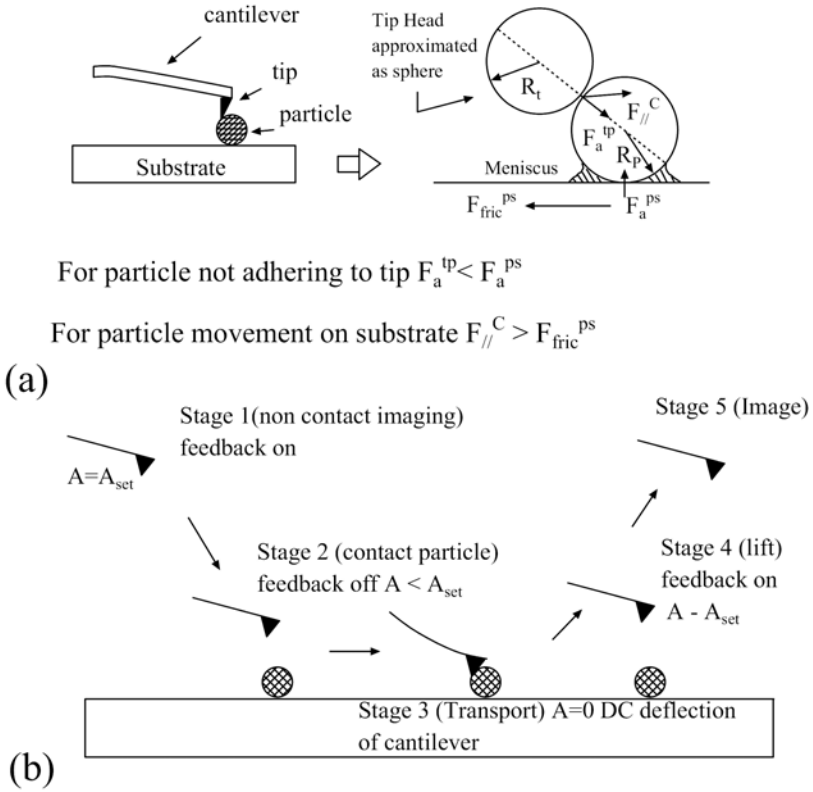

Figure 1.28 (a) Schematic of the forces involved in the nanomanipulation. (b) The scheme for the nano manipulation.

1.6 Motivation of the work

Atomic force microscope is one of the most widely used tools in nanoscience and nanotechnology. Since its discovery, the AFM has emerged as a very powerful tool in the characterization of various properties of materials at the nanometre scale. This is primarily because the AFM can not only image with atomic resolution but it can also measure interatomic forces which are of the order of pico newtons or even much less. These capabilities made the AFM a versatile enabling tool in nanotechnology. It is thus noted that AFM is mainly used for three purposes – i) measuring interatomic forces with spatial resolution ii) imaging and iii) nanomanipulation of nano-objects. **The motivation behind this wok is to first understand the effect of interaction forces (in absence of any external force) as well as electric field on the cantilever dynamics and then use this concept to manipulate nano-objects in presence of electrophoretic force.**
Since the time of the discovery of AFM by Binning et. al., many attempts have been made to explain some of the non-intuitive features seen in these systems. For example, the force versus distance (f-h) curves depend on whether the cantilever is approaching towards the sample or retracting away from it, leading to a hysteresis like behavior. The hysteresis has traditionally been attributed to adhesion due to the layer of water existing on the surface of the sample, or ruptures of molecular bonds, and has indeed been used to measure the "snap off" force. Along with the hysteresis, two instabilities are generally

observed in the (f-h) curves – one when the cantilever is approaching towards the sample (known in literature as "jump-into-contact") and the second one when the cantilever is retracting back from the sample (known in literature as "jump-off-contact"). These instabilities in the (f-h) curves are related to such instabilities like forming or breaking the water bridge and intrinsic instability of the cantilever. Though there are several studies on the static mode spectroscopy as mentioned in section 1.4.4 but none of these studies either provide a quantitative understanding of the effect of these instabilities on (f-h) curves or show how one can separate out these two effects. In case of dynamic mode spectroscopy, one can also observe the instabilities in the amplitude vs. distance (A-h) curves both in the approach part and in the retract part along with the hysteresis. This is also not well understood yet. In this thesis we have revisited these issues of the spectroscopy curves both in static mode and in dynamic mode and tried to answer the questions that we have asked at the beginning of this chapter supported by our experimental data and theoretical calculations.

1.6.1 Specific issues to be addressed

The major aspects of this thesis can be broadly classified into four topics viz.

- **To understand the effect of intrinsic cantilever instability on static mode spectroscopy curves**
- **Control the tip-sample interaction forces at a local level in AFM using an externally applied electric field**
- **To understand the effect of non-linear tip-sample interaction in dynamic mode spectroscopy**
- **Control manipulation of nano-objects in presence of electric field using AFM**

Understanding the effect of intrinsic cantilever instability on static mode spectroscopy curves:

We have shown that the static force spectroscopy curve is significantly modified due to presence of intrinsic cantilever instability. This instability acts in tandem with such instabilities like water bridge or molecular bond rupture and makes the static force spectroscopy curve (including "jump-off-contact") dependent on the step-size of data collection. A model has been proposed to explain the data.
We have also shown that the 'jump-into-contact' of the cantilever in AFM is caused by an inherent instability in the motion of the cantilever. We have shown that the 'jump-into-contact' distance can be used to find the interaction of the cantilever tip with the surface. In the specific context of the attractive van-der-Waals interaction, this method can be realized as a new method of measuring the Hamaker constant for materials. We have also found that the tip to sample separation at the 'jump-into-contact' is simply related to the cantilever deflection at this point, and this provides a method to exactly locate the surface in AFM experiment.

Control the tip-sample interaction forces at a local level in AFM using an externally applied electric field:

We have investigated how an electric field applied between tip and the sample shifts the observed deflection (or force)-vs-distance curves in AFM working in ambient condition and also in Ultra-High vacuum (UHV). The applied electric field allows us to control the effective tip-surface interaction and thus validate our model. We have explained the experimental results using a model and quantitatively established a relation between the observed static mode spectroscopy curves and the electric field which modifies the effective tip- sample interaction in a controlled manner. The investigation establishes a way to quantitatively evaluate the electrostatic force in an AFM using the static mode spectroscopy curves. In AFM the tip-sample interaction mainly arises from the van-der-Waals interaction. In such cases, the use of an electrostatic force, by application of a small voltage between the sample and tip, is an interesting option to change the effective tip-sample interaction in a controlled way. This is because both van-der-Waals and electrostatic interactions have $1/h^2$ (where h is the tip-sample distance) dependence. We have shown that the electric field can be used as a good control parameter to study the micro-cantilever dynamics in an AFM.

Understand the effect of non-linear tip-sample interaction in dynamic mode spectroscopy:

The effects of nonlinear tip–sample forces on dynamic mode atomic force spectroscopy have also been studied both experimentally and by theoretical calculations. The jumps and hysteresis observed in the vibration amplitude (A) versus tip–sample distance (h) curves have been traced to bistability in the resonance curve. A numerical analysis of the basic dynamic equation was used to explain the hysteresis in the experimental curve. It has been found that the location of the hysteresis in the A–h curve depends on the frequency of the forced oscillation relative to the natural frequency of the cantilever. We have also investigated how A-h curve in dynamic mode is related to the static mode spectroscopy curves in the limit of averaging out the sinusoidal driving force.

Control manipulation of nano-objects in presence of electric field using AFM:

Finally, we have utilized the basic understanding of the cantilever dynamics of AFM for the AFM based nanomanipulation. The capability to fabricate or modify nanoscale structures using nanomanipulation is a fundamental step toward realizing the promise and potential of nanotechnology. Not only that, there is need to understand the basic physical and chemical processes that take place in the scale of few nanometers including the mechanics. Very few works have been reported till now to understand the underlying physics of nanomanipulation, i.e., the forces of interaction governing the physical process. To achieve better control, nanomanipulation is done in presence of electric field to study the effect of electrophoretic force.

To start with, PS spheres and silica spheres of 100 nm are used to make a periodic array on patterned silicon substrates (with native oxide layer on it) with the help of standard techniques. These samples are characterized using Optical microscope, Scanning electron Microscope (SEM) and AFM. Next, AFM tip has been used to manipulate a particular sphere (or spheres) in presence of an electric field applied between the tip and sample to study the effect of electrophoretic force during nanomanipulation. The presence of the electric field creates a controllable tip surface interaction that can be utilized for nanomanipulation.
It is noted that the thesis has two very important physics objectives. First understanding the non-linear dynamics of the AFM cantilever in absence and in presence of an electric field and second understanding the basic interaction of the nano-sphere and the tip so that the nanosphere can be effectively manipulated.

1.7 Thesis outline

Due to the varied thematic of this work, each chapter is preceded by a short introduction, and includes a brief conclusion section of the respective chapter to facilitate clarity and readability.
In Chapter two we first discuss in detail about the mathematical model that we have used to understand our experimental results. Then the basic concepts of AFM for its application in spectroscopy, microscopy and nanomanipulation are introduced; the underlying physical principles are also reviewed. We further give a brief overview of the methods of sample preparation and other experimental techniques used for sample characterization and for some control experiments.
In chapter three we have discussed how to evaluate the interaction parameters of van-der-Waals force using the atomic force spectroscopy curves.
Chapter four mainly focuses on the effect of intrinsic instability of cantilever on static mode atomic force spectroscopy. A quantitative understanding of the effect of meniscus force and van-der-Waals force on force-distance curves along with the effect of electric field on static mode spectroscopy has also been discussed in detail in this chapter. Chapter five focuses on the effect of intrinsic instability of cantilever on dynamic mode spectroscopy.
In chapter six we have discussed the controlled manipulation of nano-objects using AFM in presence of electric field.
Chapter seven is the concluding chapter and also gives the future direction of the work.

Bibliography

[1] B. P. Straughan, S.Walker, A. V. Golton, and J. K. Burdett, Spectroscopy (Chapman and Hall, 1976).
[2] G. C. Maitland, Intermolecular Forces: Their Origin and Determination (Oxford: Clarendon Press, 1987).
[3] H.J. Butt, B. Cappella and M. Kappl, Surface Science Reports 59 (2005) 1–152.
[4] H.C. Hamaker, Physica 4 (1937) 1058.
[5] E.M. Lifshitz, Sov. Phys. JETP 2 (1956) 73.
[6] D.A.Walters, J.P. Cleveland, N.H. Thomson, P.K. Hansma, M.A.Wendman, G. Gurley, V. Elings, Rev. Sci. Instrum. 67 (1996) 3583.
[7] J.L. Hazel, V.V. Tsukruk, Thin Solid Films 339 (1999) 249.
[8] A. Khan, J. Philip, P. Hess, J. Appl. Phys. 95 (2004) 1667.
[9] O. Tabata, K. Kawahata, S. Sugiyama, I. Igarashi, Sens. Actuators 20 (1989) 135.
[10] K.R. Virwani, A.P. Malshe, W.F. Schmidt, D.K. Sood, Smart Mater. Struct. 12 (2003) 1028.
[11] H. Hertz, J. Reine Angew. Math. 92 (1882) 156.
[12] K.L. Johnson, K. Kendall, A.D. Roberts, Proc. R. Soc. London A 324 (1971) 301.
[13] B.V. Derjaguin, V.M. Muller, Y.P. Toporov, J. Colloid Interf. Sci. 53 (1975) 314.
[14] V.M. Muller, V.S. Yushchenko, B.V. Derjaguin, J. Colloid Interf. Sci. 77 (1980) 91.
[15] V.M. Muller, B.V. Derjaguin, Y.P. Toporov, Colloids Surf. 7 (1983) 251.
[16] D. Maugis, J. Colloid Interf. Sci. 150 (1992) 243.
[17] M.A. Lantz, S.J. O'Shea, M.E. Welland, K.L. Johnson, Phys. Rev. B 55 (1997) 10776.
[18] I.N. Sneddon, Int. J. Eng. Sci. 3 (1965) 47.
[19] E. Boschung, M. Heuberger, G. Dietler, Appl. Phys. Lett. 64 (1994) 1794.
[20] W.C. Oliver, G.M. Pharr, J. Mater. Res. 7 (1992) 1564.
[21] B.J. Briscoe, L. Fiori, E. Pelillo, J. Phys. D 31 (1998) 2395.
[22]Y. Martin, D.W. Abraham, H.K. Wickramasinghe, Appl. Phys. Lett. 52 (1988) 1103.
[23] R. Erlandsson, G. Hadziioannou, C.M. Mate, G.M. McClelland, S. Chaing, J. Chem. Phys. 89 (1988) 5190.
[24] A.L. Weisenhorn, P.K. Hansma, T.R. Albrecht, C.F. Quate, Appl. Phys. Lett. 54 (1989) 2651.
[25] W.J. O'Brien, J.J. Hermann, J. Adhes. 5 (1973) 91.
[26] L.R. Fisher, J.N. Israelachvili, J. Colloid Interf. Sci. 80 (1981) 528.
[27] H.K. Christenson, J. Colloid Interf. Sci. 121 (1988) 170.
[28] M. Fuji, K. Machida, T. Takei, T. Watanabe, M. Chikazawa, Langmuir 15 (1999) 4584.
[29] B. Bhushan, C. Dandavate, J. Appl. Phys. 87 (2000) 1201.
[30] X. Xiao, L. Qian, Langmuir 16 (2000) 8153.
[31] N. Garoff, S. Zauscher, Langmuir 18 (2002) 6921.
[32] R. Jones, H.M. Pollock, J.A.S. Cleaver, C.S. Hodges, Langmuir 18 (2002) 8045.
[33] E.S. Yoon, S.H. Yang, H.G. Han, H. Kong, Wear 254 (2003) 974.

[34] Y. Kaibara, K. Sugata, M. Tachiki, H. Umezawa, H. Kawarada, Diam. Relat. Mater. 12 (2003) 560.
[35] L. Bocquet, J.L. Barrat, Phys. Rev. Lett. 70 (1993) 2726.
[36] Y. Ando, Wear 238 (2000) 12.
[37] M. Fuji, K. Machida, T. Takei, T. Watanabe, M. Chikazawa, J. Phys. Chem. B 102 (1998) 8782.
[38] A. Ata, Y.I. Rabinovich, R.K. Singh, J. Adhes. Sci. Technol. 16 (2002) 337.
[39] S. Biggs, R.G. Cain, R.R. Dagastine, N.W. Page, J. Adhes. Sci. Technol. 16 (2002) 869.
[40] Y.I. Rabinovich, M.S. Esayanur, K.D. Johanson, J.J. Adler, B.M. Moudgil, J. Adhes. Sci. Technol. 16 (2002) 887.
[41] Z. Wei, Y.P. Zhao, Chin. Phys. Lett. 21 (2004) 616.
[42]A. de Lazzer, M. Dreyer, H.J. Rath, Langmuir 15 (1999) 4551.
[43] T. Stifter, O. Marti, B. Bhushan, Phys. Rev. B 62 (2000) 13667.
[44] L. Sirghi, N. Nakagiri, K. Sugisaki, H. Sugimura, O. Takai, Langmuir 16 (2000) 7796.
[45] D.L. Sedin, K.L. Rowlen, Anal. Chem. 72 (2000) 2183.
[46] L. Sirghi, M. Nakamura, Y. Hatanaka, O. Takai, Langmuir 17 (2001) 8199.
[47] R. Jones, H.M. Pollock, D. Geldart, A. Verlinden, Powder Technol. 132 (2003) 196.
[48] P.M. Young, R. Price, M.J. Tobyn, M. Buttrum, F. Dey, J. Pharm. Sci. 93 (2004) 753.
[49] R. Price, P.M. Young, S. Edge, J.N. Staniforth, Int. J. Pharm. 246 (2002) 47.
[50] P.M. Young, R. Price, M.J. Tobyn, M. Buttrum, F. Dey, J. Pharm. Sci. 92 (2003) 815.
[51] N.H. Duong, E. Shen, T. Shinbrot, F. Muzzio, Powder Technol. 145 (2004) 69.
[52] T. Thundat, X.Y. Zheng, G.Y. Chen, R.J. Warmack, Surf. Sci. 294 (1993) L939.
[53] J. Hu, X.D. Xiao, D.F. Ogletree, M. Salmeron, Science 268 (1995) 267.
[54] W. Gulbinski, D. Pailharey, T. Suszko, Y. Mathey, Surf. Sci. 475 (2001) 149.
[55] H.K. Christenson, J. Colloid Interf. Sci. 104 (1985) 234.
[56] H.K. Christenson, R.G. Horn, J.N. Israelachvili, J. Colloid Interf. Sci. 88 (1982) 79.
[57] H.W. Hao, A. M. Bar, J.J. Saenz, J. Vac. Sci. Technol. B 9 (1991) 1323.
[58] N.A. Burnham, R.J. Colton, H.M. Pollock, Phys. Rev. Lett. 69 (1992) 144.
[59] N. Agraft, G. Rubio, S. Vieira, Phys. Rev. Lett. 74 (1995) 3995.
[60] C.J. Drummond, T.J. Senden, Colloids and Surfaces A 87 (1994) 217.
[61] E. Meyer, H. Heinzelmann, P. Grtitter, Th. Jung, Th. WeisskopL H-R. Hidber, R. Lapka, H. Rudin, J. Gtintherodt, J. Microscopy 152 (1988) 269.
[62]H.A. Mizes, K.-G. Loh, R.J.D. Miller, S.K. Ahuja, E.F. Grabowski, Appl. Phys. Lett. 59 (1991) 2901.
[63] E.-L. Florin, V.T. Moy, H.E. Gaub, Science 264 (1994) 415.
[64] T. Aoki, M. Hiroshima, K. Kitamura, M. Tokunaga, T. Yanagida, Ultramicroscopy 70 (1997) 45.
[65] V.S.J. Craig, Colloids and Surfaces A 129-130 (1997) 75.
[66] P.M. Claesson, T. Ederth, V. Bergeron, M.W. Rutland, Adv. Colloid Interface Sci. 67 (1996) 119.
[67] M.J. Spaarnay, Physica 24 (1958) 751.
[68] D. Tabor, R.H.S. Winterton, Proc. R Soc. London Ser A 331 (1969) 19.

[69] J.N. Israelachvili, D. Tabor, Nature 241 (1973) 148.
[70] D.Y.C. Chan, R.G. Horn, J. Chem. Phys. 83 (1985) 5311
[71] J. Van Alsten, S. Granick, Phys. Rev. Lett. 61 (1998) 2570.
[72] J. Van Alsten, S. Granick, Tribol Trans 33 (1990) 436.
[73] J.M. Georges, S. Millot, J.L. Loubet, A. Tonck, J. Chem. Phys. 98 (1993) 7345.
[74] J.M. Georges, A. Tonck, D. Mazuyer, Wear 175 (1994) 59.
[75] J.N. lsraelachvili, Intermolecular and Surface Forces, Academic Press, London, 1992.
[76] W.A. Ducker, T.J. Senden, R.M. Pashley, Langmuir 8 (1992) 1831.
[77] Applied scanning probe methods edited by B. Bhushan, H. Fuchs, H. Sumio.
[77a] T.R. Albrecht, P. Grütter, D. Horne, D. Rugar, J. Appl. Phys. 69 (1991) 668-673.
[78] Y. Martin, C.C. Williams, H.K. Wickramasinghe, J. Appl. Phys. 61 (1997) 4723.
[79] F.J. Giessible, Science 267 (1995) 68-71.
[80] C. Barth, M. Reichling, Nature 414 (2001) 54-57.
[81] T. Uchihasi, T. Ishida, M. Konoyama, M. Ashino, Y. Sugawara, W. Mizutani, K. Yokoyama, S. Morita, H. Tokumoto, M. Ishikawa, Appl. Surf. Sci. 157 (2000) 244-250.
[82] B. Anczykowski, D Krüger, H. Fuchs, Phys. Rev. B 53 (1996) 15485-15488.
[83] B Anczykowski, D Krüger, K.L. Babcock, H. Fuchs, Ultramicroscopy 66 (1996) 251-259.
[84] B.D. Hughes, L.R. White Quart J Mech Appl Math 32 (1979) 445-471
[85] V.M. Muller, V.S. Yushchenko, B.V. Derjaguin, J Coll Interf Sci 77 (1980) 91-101.
[86] L. Verlet, Phys. Rev. 159 (1967) 98-103; L. Verlet, Phys Rev 165 (1968) 201-214.
[87] Ricardo Garcia and Alvaro San Paulo, Phys. Rev. B 61, (2000) R13381-R
[88] S.I.Lee, S.W .Ho well, A.Raman, and R.Reifenber ger, Phys. Rev. B 66, (2002) 115409-1
[89] J. A Stroscio and D. M. Eigler, Nature 254, (1991)1319-1326.
[90] D. M. Schaefer, R. Reifenberger, A. Patil and R. P. Andreas, Appl. Phys. Letts. 66, (1995) 1012-1014.
[91] T. Junno, K. Deppert, L. Montelius and L. Samuleson , Appl. Phys. Letts. 66, (1995) 3627-3629.
[92] C. Buar, B. C. Gazeu, B. E. Koel, T. R. Ramachandran, A. A. G. Requicha and L. Zini., J. Vac. Sci. Tech. A 15, (1997) 1577–82, T. R. Ramachandran and C. Buar, Nanotechnology 9, (1998), 237-245
[93] R. Resch, A. Bugacov, C. Baur, B. E. Koel, A. Madhukar, A. A. G. Requicha and P. Will, Appl. Phys. A 67, (1998), 265-271.
[94] M. Sitti and H. Hashimoto, Proc. IEEE/ASME (1999), Int. conference on Adv. Intelligent Mechanotronics, (1999) Athens, USA. pp 13-20.
[95] G. Sagvolden, I. Giaever and J. Feder, Rev. Sci. Inst. 70, (1999) 2769-2775.
[96] J. Israelchvili, Intermolecular and Surface Forces, Academic Press, NY, (1992).

Chapter 2

Mathematical Model and Experimental Techniques

I Mathematical Model:

The first section of this chapter describes about the mathematical model that we have developed to understand our experimental data. The interaction between the tip of an atomic force microscope and the sample is modeled as van-der-Waals force. Solutions of the equation of motion of the cantilever in static mode and also in dynamic mode atomic force spectroscopy have been derived. In case of static mode both analytical solution as well as numerical simulation has been done to obtain the cantilever deflection whereas in dynamic mode only numerical simulation has been done. The hysteresis loop observed on approach and retraction of the tip from the sample in both static mode and dynamic mode is presented. It is also shown by analytical calculation that the Hamaker constant of a particular tip-sample assembly can be found out from "jump-into-contact" point in static mode spectroscopy curves.

I a Static mode:

An atomic force microscope consists of a minute cantilever with a sharp tip at its end that is brought into close proximity to a sample. One can fix the position of the sample and mount the cantilever on an x-y-z scanner, a configuration used in "stand-alone" systems aimed at probing large samples. Alternatively, one can mount the sample on a scanner and fix the position of the cantilever, as is conveniently employed in the design of most atomic force microscopes (AFM) that probe small samples. In our system, we use the second configuration. The tip-sample system in an AFM is shown schematically in fig. 2.1. The sample is assumed to be at "ground" level, positioned at h = 0. The base of the cantilever is at a height h as shown in fig. 2.1. The cantilever is approached towards the sample by using a stepper motor. Now the presence of a tip-sample force will bend the cantilever, displacing the position of the tip to z from its position h (when it is free). The deflection of the cantilever, d, will therefore be given by d = z-h. In a real experiment the tip-sample force may involve contributions from atomic, adhesion, and indentation forces, to name only a few. However, the salient features of an AFM can be obtained quite accurately by modeling the attractive tip-sample interaction using a van-der-Waals force and the repulsive interaction by simple Hertzian elastic contact model. The main topic discussed in this section will concern the deflection of the cantilever (d) as a function of the tip-sample distance (h). Note that the value h is computer-controlled via

the stage, while the value of d is measured using optical deflection. Clearly, the tip-sample distance z is determined by both h and d.
The operation of an AFM, in the so-called "contact-mode", will usually start by having the cantilever placed far enough from the sample that the tip does not feel the force from tip-sample interaction. A mechanical drive will then decrease the tip-sample distance until a very slight cantilever deflection is monitored by a photodiode is detected. At this point the coarse mechanical drive will stop, and the computer-controlled bimorph will

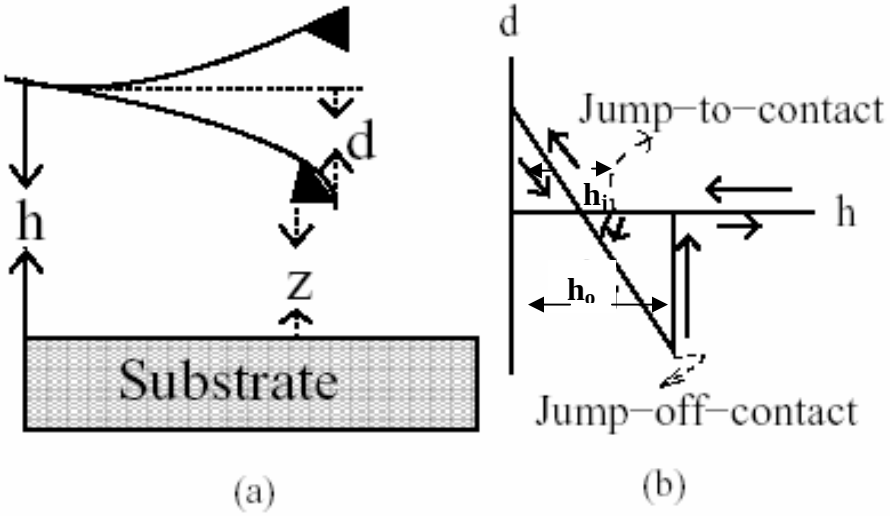

Figure 2.1 A schematic diagram of AFM tip and sample assembly (a) and deflection–distance curves (b). The dotted line in (a) marks the equilibrium position of the cantilever in the absence of an external force. d is positive when measured upwards. The arrows in (b) show the direction of motion of the cantilever.

take over, moving the cantilever closer to the sample. The deflection of the cantilever is continuously monitored as it approaches the sample, showing that for a period of time it is deflected downwards, and then at a particular point (known in literature as "jump-into-contact" (JIC)) denoted by h_j, it will snap into the sample. Moving the cantilever closer to the sample will give rise to a deflection in the opposite direction, indicating that the tip is in contact with the sample. Next the cantilever is pulled away from the sample, and the observed deflection of the cantilever indicates that the tip is still in contact with the sample. At a given point (known in literature as "jump-off-contact" (JOC)) denoted by h_o, tip will snap out from the sample. The cantilever at this point is still bent downward under the influence of tip-sample force. However, when it is retracted further from the sample it will no longer be bent. Tracing the deflection as a function of the tip-sample distance yield a force curve resembling a hysteresis loop that characterizes the operation of the contact-mode AFM. The analysis of the deflection-distance (d-h) curves makes it possible to extract the Hamaker constant of the tip sample assembly. This is discussed in detail in chapter 3 of this thesis.

I a.1 Tip-sample interaction: van-der-Waals force

Of the many forces a tip may encounter when placed in the vicinity of a sample, we consider in the following sections only the one derived from the van-der-Waals force and Derjaguin–Muller–Toporov (DMT) force. The tip–sample force is modeled by a combination of the van-der-Waals force at large tip–sample distances (h) which is essentially attractive and by the Derjaguin–Muller–Toporov (DMT) force which is a combination of the attractive van-der-Waals like force (except that it is h-independent) and the repulsive forces arising due to elastic interaction between the tip and the sample. Thus, formally, the force is given by

$$f_{ts}(h+d) = \begin{cases} -\dfrac{HR_t}{6(h+d)^2} & \text{for } (h+d) > a_0 \\ -\dfrac{HR_t}{6a_0^2} + \dfrac{4}{3}E^*\sqrt{R_t}(a_0 - (h+d))^{\frac{3}{2}} & \text{for } (h+d) \le a_0 \end{cases} \tag{2.1}$$

Here H is the Hamaker constant of the tip sample assembly, R_t is the radius of curvature of the tip, a_0 is the inter-molecular distance and E^* is the reduced Young's modulus. In chapter 1 we have discussed in detail about the importance of Hamaker constant (H) and the various methods of calculating it. E^* is given by

$$\frac{1}{E^*} = \left(\frac{1-\nu_s^2}{E_s} + \frac{1-\nu_t^2}{E_t}\right) \tag{2.2}$$

where, ν_t, E_t, ν_s, E_s are the Poisson's ratio and the Young's moduli of tip and sample respectively. We have also discussed about the short range repulsive forces (Hertzian contact) in chapter 1. Note that the form of the van-der-Waals force is chosen for sphere plate geometry, which is close to the real situation in an AFM experiment. From eq. 2.1 we can see that the force is purely attractive for $(h+d) > a_0$ whereas for $(h+d) \le a_0$, it is a competition between the two terms – the first term is a attractive term and the second one is a repulsive term arising from the indentation of the surface. In case of analytical solution we have only considered the attractive part of the tip-sample interaction, in order to achieve the solutions. Otherwise the equation of motion of the cantilever can not be solved analytically. In case of numerical solution, we have used both the attractive and the repulsive part of the interaction. This is discussed in detail in the following sections. Fig. 2.2 shows the plot of the tip-sample interaction given by eq. 2.1 as a function of the tip-sample distance for HR_t (a) = 2.26×10^{-27} N m^2, a_0 = 0.172 nm and $4/3E^* R_t^{1/2}$ (b) =200.

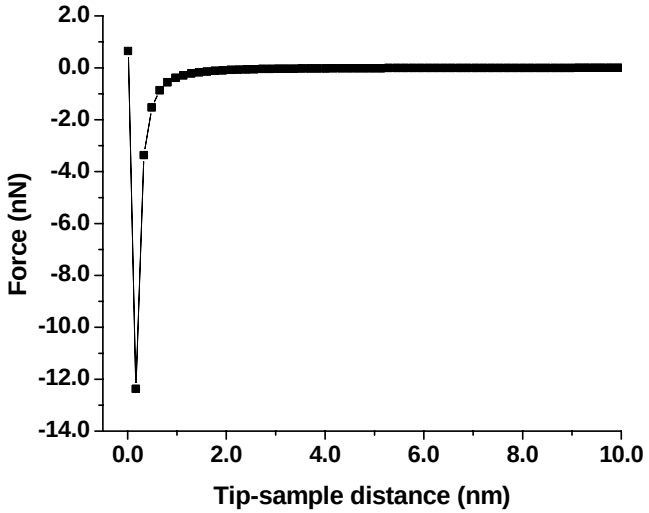

Figure 2.2 A plot of the tip-sample interaction given by eq. 2.1 as a function of the tip-sample distance for the parameters given in the text.

Generally, in AFM the tip-sample force is modeled by van-der-Waals interaction as we have mentioned above but other interactions may also be used. In table 2.1 we have listed some of these interactions.

Tip-sample interaction potential	Form of the tip-sample interaction potential
Lennard-Jones Potential	$V(r) = 4\varepsilon[(\sigma/r)^{12} - (\sigma/r)^{6}]$, where ε is the depth of the potential well and σ is the (finite) distance at which the interparticle potential is zero and r is the distance between the particles.
Morse Potential	$V(r) = D_e(1-e^{-a(r-re)})^2$, where r is the distance between two atoms, r_e is the equilibrium bond distance, D_e is the well depth (defined relative to the dissociated atoms), and a controls the width of the potential.

Table 2.1 Tip-sample interactions potential

Here we have used van-der-Waals force to model the tip-sample interaction. van-der-Waals force is α $1/d^2$ but in other cases the force can have $1/d^n$ dependence, where n is a positive integer. It is important to mention here that whatever the power (n) is, it is always a good approximation to model the tip-sample interaction in AFM as $1/d^2$ because in f-d experiments the system can only probe the two solutions and not more than that.

Therefore, it is more realistic to model the tip-sample interaction force as $1/d^2$ to match the simulated data with experiment.

I a.2 Modeling the cantilever motion:

The AFM is a nonlinear system. Our aim here is to use a simple model which could explain the features seen in experiments. For simplicity, the cantilever is replaced by a small sphere suspended on a spring that is mounted on a vibrating bimorph as shown in fig.2.3. If the curvature of the vibrating cantilever is small enough, one can model its response using an equivalent point-mass suspended by a spring that is mounted on a vibrating bimorph. Therefore, the inherent nonlinearity of the cantilever due to its finite dimensions has not been introduced into our calculation, in order to keep things simple. The characteristics of a damped and linear oscillator model the vibration of the cantilever of an AFM in static mode. Thus, we write the equation of motion of the cantilever as

$$m\ddot{d}(t) + \eta \dot{d}(t) + k_c d(t) = f_{ts}(h + d(t)) \qquad (2.3)$$

Here, m is the mass of the cantilever, η is the friction constant, k_c is the spring constant, d(t) is the deflection of the cantilever measured from its equilibrium position in the absence of any external force, $f_{ts}(h + d)$ is the atomic force between the tip and the sample at the instantaneous position of the tip and t represents time.

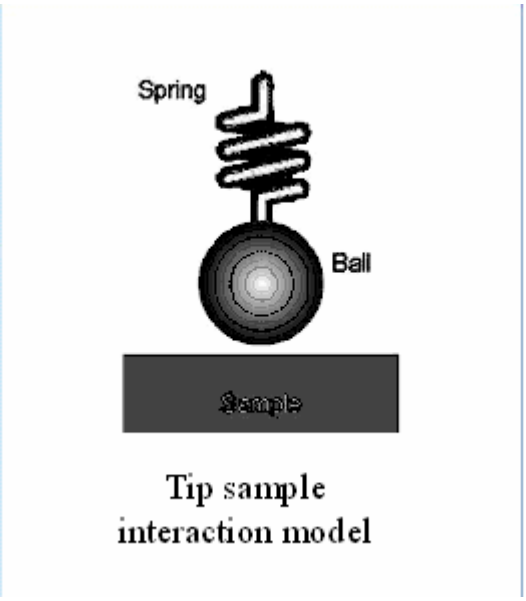

Figure 2.3 A schematic diagram to show that the cantilever of AFM is modeled as a spring-ball system and the sample as a flat surface

In case of the static (or quasi-equilibrium) experiment d(t) = d, where d is the deflection of the cantilever at which it comes to rest. The dynamic equation will reduce to a simple static equation of the form

$$k_c d = f_{ts}(h + d) \qquad (2.4)$$

I a.3 Analytical solutions:

The equation of motion (eq. 2.4) of this system is solved both analytically. First we will discus here about the analytical solution and then the numerical simulation. Finally we have compared both the results with the experimental results. From eqs. 2.1 and 2.4, after some simple manipulations, we obtain the equation for the deflection (d) as (only the attractive part of the tip-sample interaction is considered here for the analytical solution)

$$k_c d = -\frac{HR_t}{6(h+d)^2} \tag{2.5}$$

Rewriting $\tilde{d} = \frac{d}{h}$ and $\tilde{a} = \frac{HR_t}{6k_c h^3}$, we get

$$\tilde{d}(1+\tilde{d})^2 + \tilde{a} = 0 \tag{2.6}$$

Three solutions of this equation are given by

$$\begin{aligned}
\tilde{d}_1 &= -\frac{b_2}{3} + (S+T) \\
\tilde{d}_2 &= -\frac{b_2}{3} - \frac{1}{2}(S+T) + \frac{\sqrt{3}}{2} i(S-T) \\
\tilde{d}_3 &= -\frac{b_2}{3} - \frac{1}{2}(S+T) - \frac{\sqrt{3}}{2} i(S-T)
\end{aligned} \tag{2.7}$$

where

$$\begin{aligned}
S &= (R+\sqrt{D})^{\frac{1}{3}} \\
T &= (R-\sqrt{D})^{\frac{1}{3}} \\
R &= \frac{9b_1b_2 - 27b_0 - 2b_2^3}{54} \\
D &= Q^3 + R^2 \\
Q &= \frac{3b_1 - b_2^2}{9}
\end{aligned} \tag{2.8}$$

and b_0, b_1 and b_2 are the coefficients of $(\tilde{d})^0$, $(\tilde{d})^1$ and $(\tilde{d})^2$ in eq. 2.6. Here we want to mention that eq. 2.7 is valid only for the real values of S and T defined in eq. 2.8. For complex values, the expressions for eq. 2.7 will change. It can be easily seen that b_0 =a, b_1 = 1 and b_2 = 2. The distance $\tilde{d}_1$ has only a real part, while the solutions $\tilde{d}_2$ and $\tilde{d}_3$ are either real or complex conjugates of each other, depending on the parameters of the equation. The actual deflection (d) is obtained by multiplying the solution ($\tilde{d}$) by the corresponding tip–sample distance (h). Figure 2.4 shows the three solutions given by eq. 2.7 as a function of the tip-sample distance (h) for HR_t (a) = 2.26×10^{-27} N m^2, k_c=0.1 Nm^{-1}, a_0 = 0.172 nm and $4/3E^*R_t^{1/2}$ (b) = 200.

The solutions of the cubic equation given by eq. 2.7 have a number of interesting features. For example, let us consider the point where the JIC occurs in our model. At this

point $d_2 = d_3$ and the discriminant D is exactly equal to zero. If we denote the tip–sample distance at this point by h_j and corresponding values of R, Q as R_j, Q_j, we get the equation

$$R_j + \sqrt{Q_j^3 + R_j^2} = R_j - \sqrt{Q_j^3 + R_j^2} \tag{2.9}$$

which leads to the equation

$$Q_j^3 = -R_j^2 \tag{2.10}$$

Replacing the expressions for Q_j and R_j from eq. 2.8, and putting in the values of b_0, b_1 and b_2, we get

$$\frac{HR_t}{6k_c h_j^3} = \frac{4}{27} \tag{2.11}$$

Equation 2.11 can be used to find the Hamaker constant (H) because the tip radius R_t and the cantilever spring constant k_c are known and h_j is experimentally measurable. However, the problem arises because the position of the surface not being known exactly, the absolute value of h_j has a large uncertainty. Below, we show that the magnitude of the jump of the cantilever at the JIC is simply related to h_j. At the JIC, there are only two distinct real solutions to the cubic equation since the solutions corresponding to d_2 and d_3 are degenerate. Subtracting d_3 from d_1, and again putting in the values of b_0, b_1 and b_2, we get the jump of the cantilever (Δd) at the JIC as

$$\Delta d = d_3^j - d_1^j = -h_j \tag{2.12}$$

where $d_1^j$and d_3^j are the deflections at the JIC point corresponding to the two solutions. Eqs 2.11 and 2.12 lead to a practical way of calculating the JIC position and Hamaker constant from the d–h curves. The abovementioned process also indicates that one can obtain a precise method of shifting the raw data obtained from the AFM measurements to properly locate the surface.

I a.4 Simulation:

An important aspect of this thesis is to combine experimental observations with analytical calculations as well as simulation based on simple models. In particular, we have also simulated the d-h curves for the same parameters used for obtaining the analytical solutions. The simulation is essential to solve the equation of motion when both attractive and repulsive parts are present. In case of simulation we have considered both the attractive part and the repulsive part of the tip-sample interaction. Therefore, the simulation is more realistic and matches well with the experimental data. This is discussed in detail later in section 2.1.5. To implement the simulation using a computer we wrote the simulation code in **Mathematica 5** as it automatically selects the best algorithms for each computation. The first step of the simulation is to mention the values of the input parameters like h_s (starting height of the cantilever from the sample), q

(quality factor of the cantilever in air), δh (step size of the motion of the cantilever = (Total distance traversed by the cantilever either in approach part or retract part of the f-d curve)/(total no. of data points)), d_i (initial deflection of the cantilever at t = 0) and v_i (initial velocity of the cantilever at t = 0). The typical values which are most crucial are listed in Table 2.2. Then we have defined the interaction term where the values of a (HR_t), a_0 and b ($4/3E^*R_t^{1/2}$) have been specified. After that we have varied tip-sample separation in specific step and at each step of the simulation we have calculated the force at a particular (h+d) value.

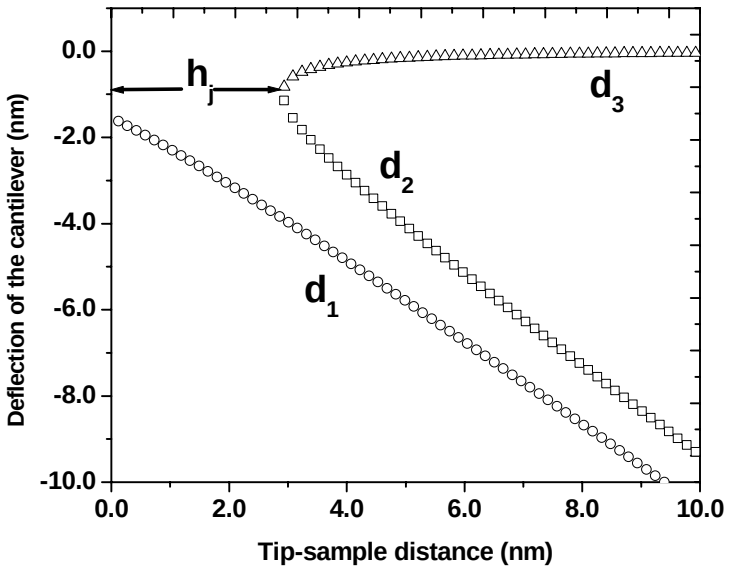

Figure 2.4 Plot of analytical solutions given by equation 2.7 as a function of tip–sample distance (h) for the parameters mentioned in the text. The open circles ($d_1 = \tilde{d}_1 h$) and open triangles ($d_3 = \tilde{d}_3 h$) represent stable solutions. The open squares ($d_2 = \tilde{d}_2 h$) represent the unstable solution. Here only the real part of the solutions is shown.

This force value is then used in the next step of the simulation where we have solved the equation of motion of the cantilever in presence of tip-sample interaction. As can be seen from eq.2.3 that the equation of motion of the cantilever is a second order differential equation in d. Finally, by solving eq.2.3 we get the deflection of the cantilever as a function of h. From the solution we have found out the values of d_{i+1} and v_{i+1} which are the initial conditions for the next simulation step to solve the differential equation. The values of d_{i+1} is fed back to step three of the simulation to calculate the force value at this step of the simulation. Table 2.3 depicts the steps of the simulation. We have considered the deflection values after the system reaches the equilibrium state. To ensure that we have started considering the deflection values in our simulation after 1500 time steps. In the simulation the end point is defined when eq. 2.3 is solved to obtain the deflection of the cantilever for $h = h_s$ at the retraction path of the cantilever. We have done the simulation for different step sizes of the motion of the cantilever, to check the effect of step size on the d-h curves. Figure 2.5 shows the simulated d-h curve for the same parameters used for the analytical solution.

Input Parameters	**Values of the input parameters**
h_s	100.0 nm
q	33.3 (air)
δh	1.6-3.6 nm
d_i	0.0 nm
v_i	0.0 nm/sec
k_c	0.1 N/m
v (for electric field)	2 V and 5 V
ε_0 (for electric field)	$8.8542X10^{-12}$ $C^2N^{-1}m^{-2}$

Table 2.2 Values of the input parameters used in the simulation.

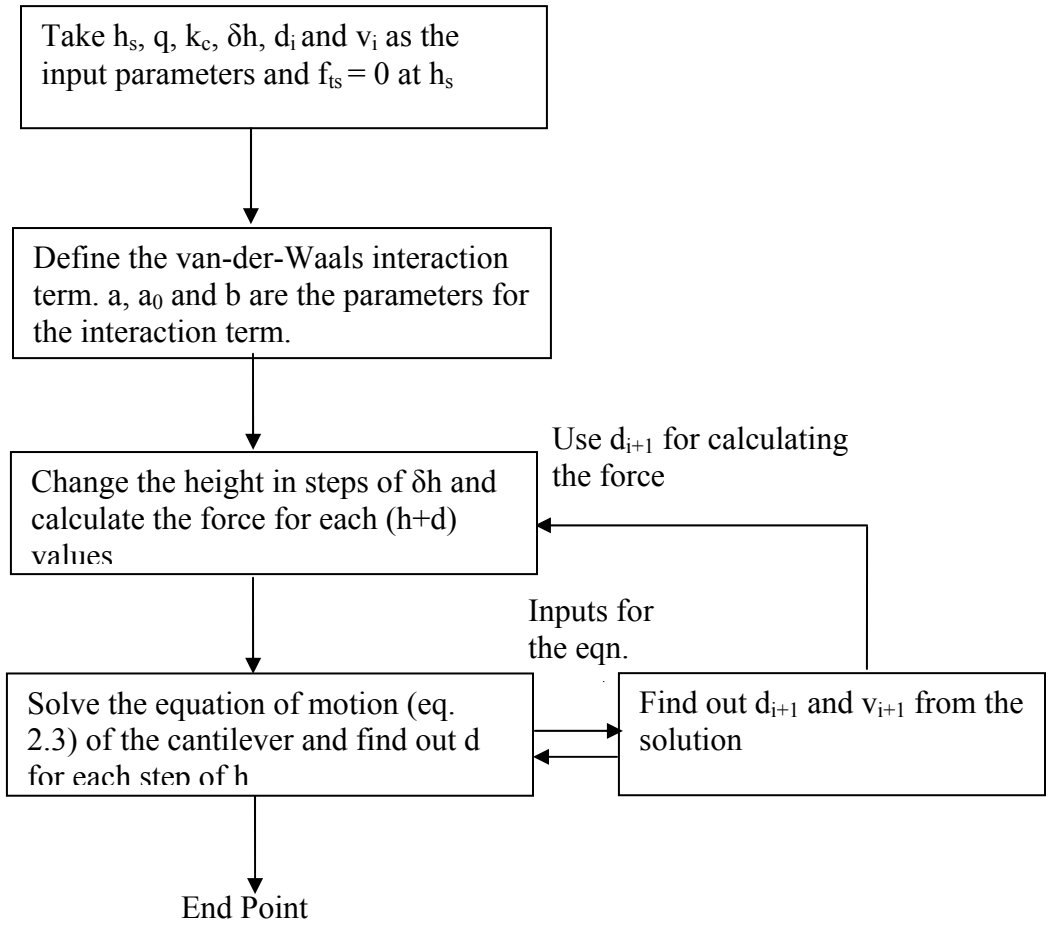

Table 2.3 It shows the steps of the simulation for static mode.

I a.5 Analysis:

In case of analytical solution (shown in fig. 2.4) the first segment, d_3, describes the situation where the bimorph moves the cantilever from a point far away from the sample

toward the sample. Since at large distance the tip-sample force can be neglected, the cantilever does not deflect so that $d_3 \approx 0$. The resultant horizontal curve
will eventually start dropping down as the tip is drawn toward the sample. As the tip–sample distance is reduced, the solutions corresponding to d_2 and d_3 approach each other and they meet at one point (for example, at $h_j \approx 2.9$ nm in fig. 2.4). For tip–sample distances below this, both these solutions become complex (in fig. 2.4 only the real part is shown). It is necessary to note that the solutions d_1 and d_3 are stable solutions, while d_2 is unstable. This has been checked by finding the sign of the derivative of eq. 2.7 with respect to d at each value of h. The derivative of the solutions as a function of h has been shown in fig.2.6. From this figure we can check that d_1 and d_3 are stable solutions whereas d_2 is unstable solution. In the inset of fig.2.6 we have blown up the derivative of the solution d_3 to show that the sign of the derivative is negative in this case. We denote the point where the solutions d_2 and d_3 meet as the "jump-into-contact" (JIC) point. This is the limit of stability for the solution d_3 which defines the motion of the cantilever for the approach curve up to this point. If the tip–sample distance (h) is reduced beyond this point of stability, there is only one real solution available (d_1) and the system will jump into the stable solution given by d_1. This defines the JIC. In chapter 3 we discuss on the experiments on JIC and its usage to find Hamaker constant (H).

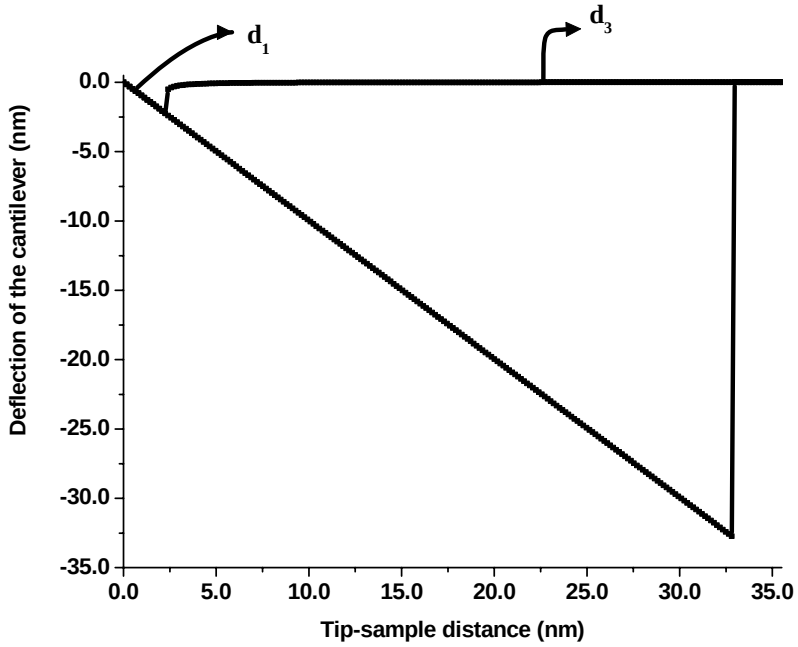

Figure 2.5 Simulated d-h curves for the same parameters used for the analytical solution.

On the retract path the cantilever dynamics follow the solution given by d_1 until it jumps back to the solution given by d_3 at the "jump-off-contact" (JOC) point. The effect of step sizes on the JOC point has been discussed in detail in chapter four. From fig. 2.5 it can be seen that in case of simulation d_1+h is always positive whereas in case of analytical solution it is negative (as can be seen in fig. 2.4) because the repulsive part of the tip-

sample interaction has not been considered. To make it more clear we have solved eq. 2.4 graphically in presence of repulsive interaction and also in absence of it. Fig. 2.7 shows the left side of the equation plotted in red and the right side plotted in black, for the case h = 6 nm (in absence of repulsive tip-sample interaction). The solutions occur at the intersections of these curves, and are labeled as d_1, d_2, and d_3. One can clearly see that for the solution d_1, (d_1+h) is negative in this case as we have not considered the repulsive tip-

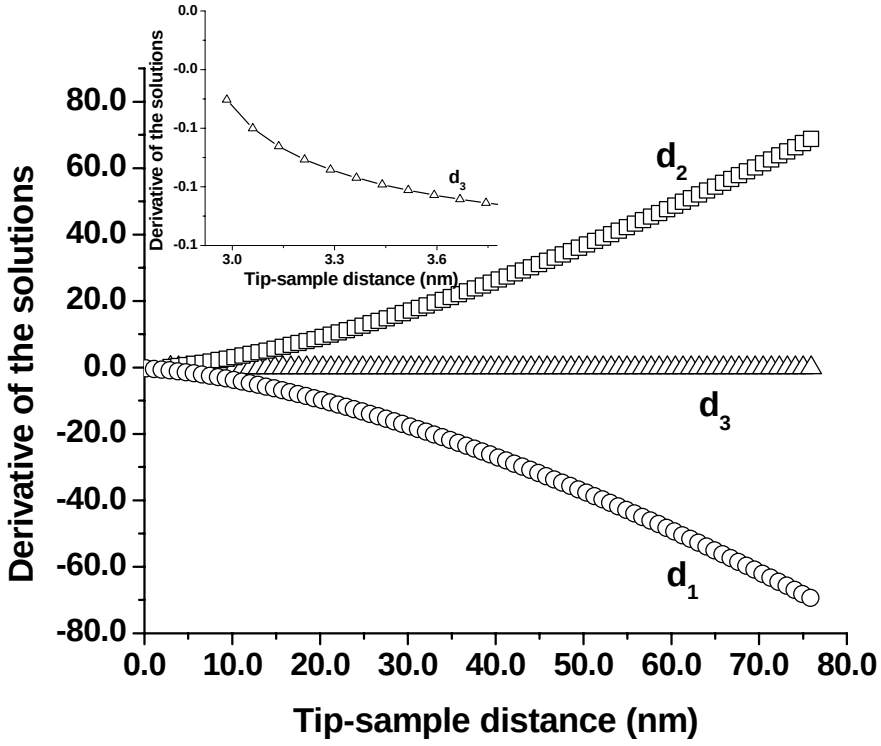

Figure 2.6 The derivative of the solution as a function of h.

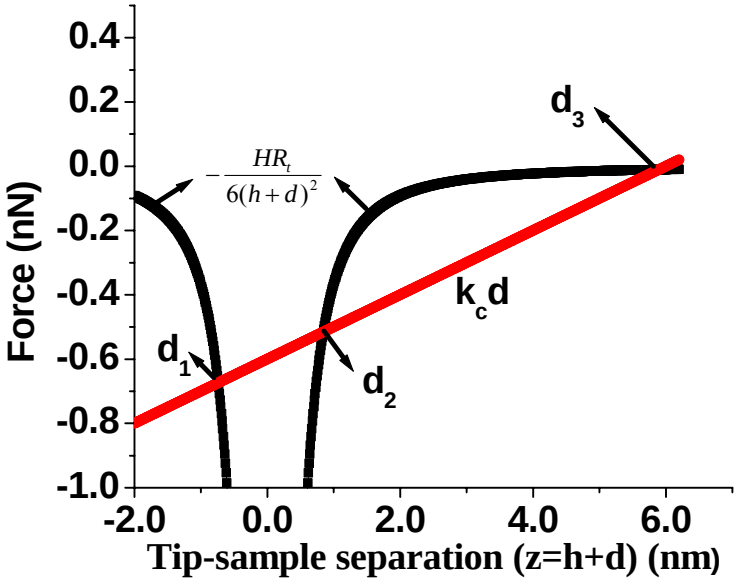

Figure 2.7 Graphical solution of eq. 2.4 (in absence of repulsive tip-sample interaction).

sample interaction in this case. Fig. 2.8 shows the graphical solution of the same but in presence of repulsive tip-sample interaction. From the figure it is clear that in this case (d_1+h) is positive.

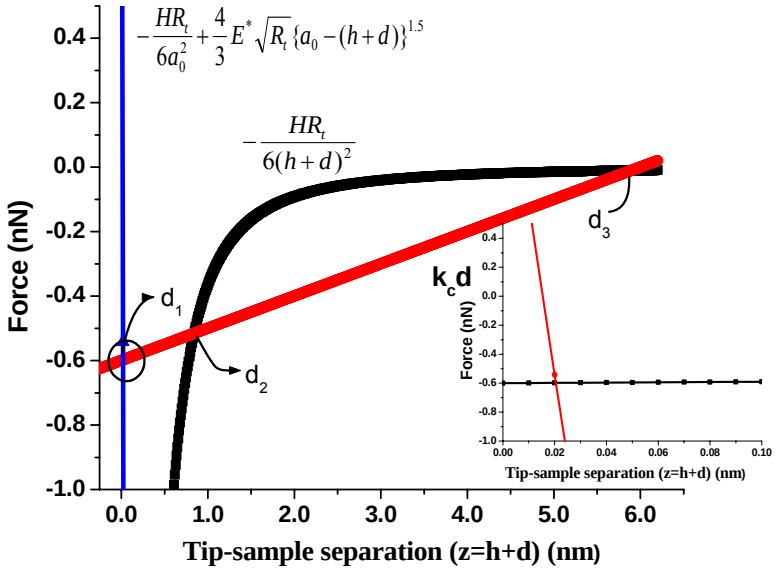

Figure 2.8 Graphical solution of eq. 2.4 (in presence of repulsive tip-sample interaction).

In fig. 2.9 we have plotted the analytical solutions and the simulated graphs together for comparison. To get realistic solution we have to take into account the repulsive part of the tip-sample interaction but for qualitative understanding it is not necessary.

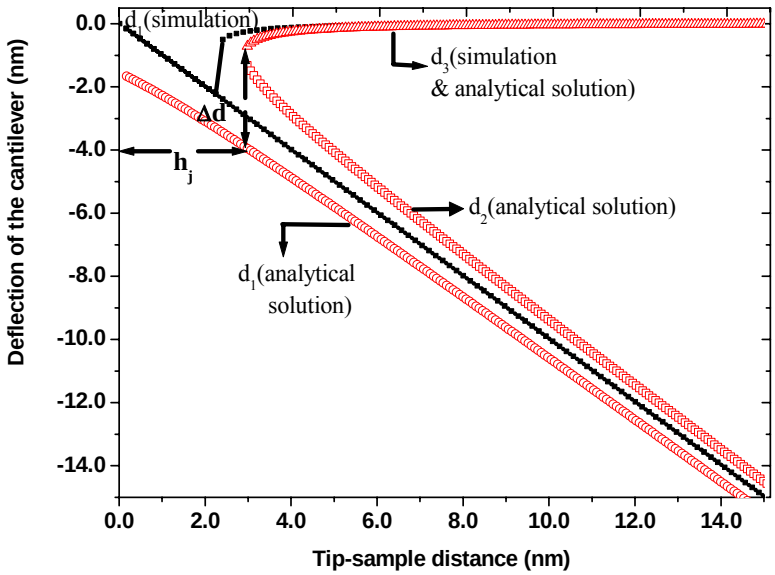

Figure 2.9 It shows the analytical solutions and the simulated d-h curves.

I b Electrostatic interaction:

The application of the electric field allows us to have a controlled handle on the tip-sample interaction which can be changed by the applied field. We have simulated the d-h curves in presence of electrostatic interaction. This has been done to study the effect of the electric field on the intrinsic instability of the cantilever which manifests in the d-h curves as JIC and JOC. This also gives us a controlled way to change the tip-sample interaction, so that its effect on the cantilever dynamics can be studied to validate our analysis process. The effect of the electrostatic interaction on JIC and JOC point has been discussed in detail in chapter four. Here we will mainly focus on how to calculate the electrostatic force between the tip and the sample of AFM and to simulate the d-h curves in presence of electrostatic interaction. It is often convenient to model the apex of a sharp conducting tip of a scanning probe microscope by a sphere and the flat conducting sample by a plane. As discussed in chapter one, Hao et al. have studied Coulomb forces by modeling the tip-sample system as a sphere on a fiat surface. In this case, the force is given by

$$F_{\infty}^{SP} = \pi\varepsilon_0 V^2 \frac{R_t}{(h+d)} \qquad (2.13)$$

for $R_t/(h+d) >> 1$ and by

$$F_{\infty}^{SP} = \pi\varepsilon_0 V^2 \{\frac{R_t}{(h+d)}\}^2 \qquad (2.14)$$

for $R_t/(h+d) << 1$.

V is the voltage difference between the tip and sample, R_t the radius of the sphere and (h+d) is the tip-sample distance. Now this electrostatic force term has been added to the van-der-Waals force term in the simulation and its value has been calculated in each step of the simulation for each (h+d) value along with the van-der-Waals force term. Other steps of the simulation are same as mentioned in section I a.4. The values of the input parameters are given in Table 2.2. Figs. 2.10 (a) and (b) show the simulated and experimental d-h curves in absence and in presence of electric field. From the figures it is clear that on application of electric field JIC and JOC positions shift to higher tip-sample separations and also the deflection of the cantilever increases. Fig. 2.10 also shows that our simulated results match quite well with the experimental results. In table 2.4 we have shown electrostatic forces calculated for other tip-sample geometries. In chapter 1, we have discussed it in detail. In our simulation we have used eq. 2.14 to calculate the electrostatic force between the tip and the sample. This is because we have found that to match our experimental results with the simulation; the best fit is obtained using this sphere-plate geometry which is very close to the real situation in AFM. All the features seen in the experiments can be obtained into our simulated data using this equation.

Tip-sample geometry	**Electrostatic force**	**References**
A sphere-ended cone on a flat surface (the force is calculated by replacing the equipotential conducting surfaces with their equivalent image charges.)	$F^c \cong \frac{\lambda_0^2}{4\pi\varepsilon_0}\ln(\frac{L}{4D})$, where L is the cone length ($L << D << R_t$), R_t is the radius of the sphere, D the tip-sample distance, for small aperture angles ($\theta \leq \pi/9$) the cone may be approximated by a charged line of constant charge density λ_0 given by $\lambda_0 = 4\pi\varepsilon_0 V[\ln(\frac{1+\cos\theta}{1-\cos\theta})]^{-1}$	[57]
Coulomb-like force which arises from the patch charges distribution on the tip and sample, i.e., from regions of different surface charge density interacting via a long range force law.	$4\pi\varepsilon_0 F = -\frac{Q_t}{4R'^2}(1-\frac{2D}{R'})(\frac{\varepsilon_2-\varepsilon_3}{\varepsilon_2+\varepsilon_3}) + \frac{Q_t Q_S}{RR''}(1-\frac{2R'}{R}-\frac{4D}{R})(\frac{\varepsilon_1-\varepsilon_3}{\varepsilon_1+\varepsilon_3})(\frac{\varepsilon_2-\varepsilon_3}{\varepsilon_2+\varepsilon_3})$, For R >> R' >> D and R" >> D, R, R'	[58]

Table 2.4 Electrostatic forces for other tip-sample geometries

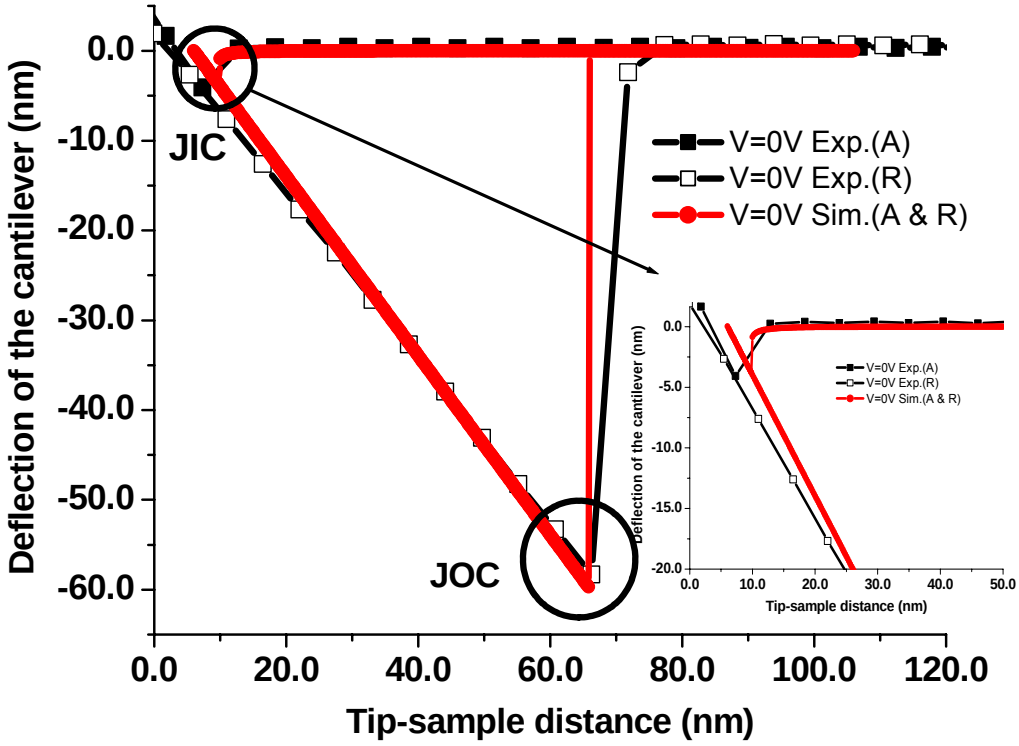

Figure 2.10a It shows the simulated and experimental d-h curves in absence of electric field. The "jump-into-contact" region is blown up in the inset.

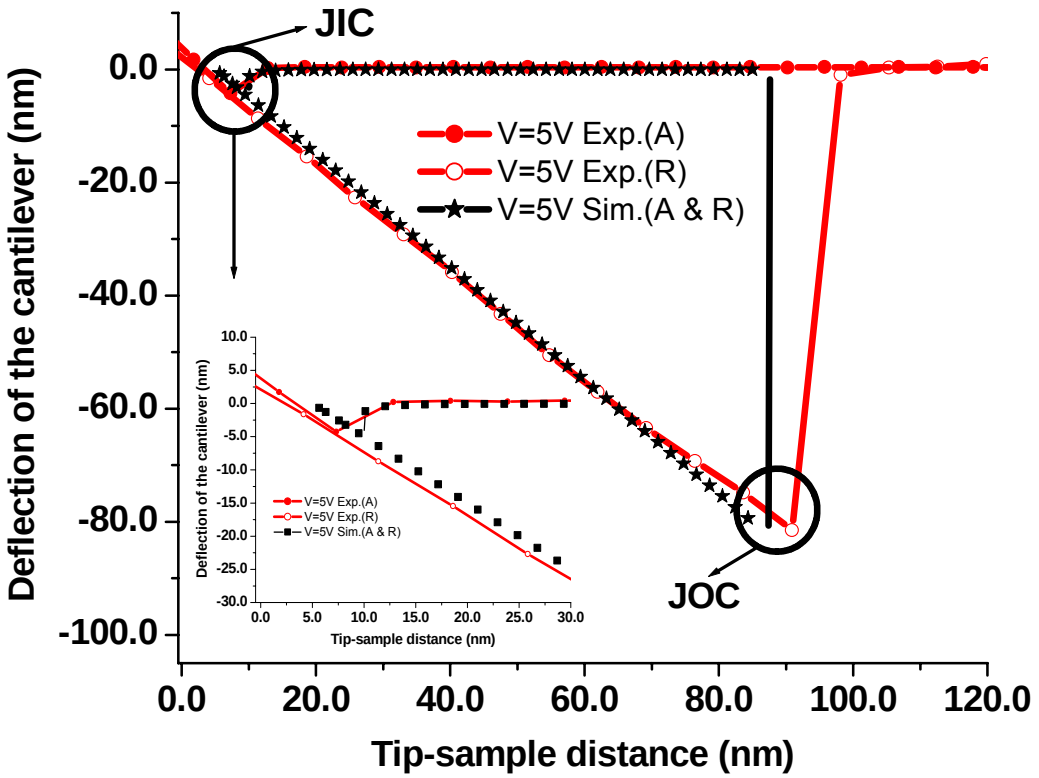

Figure 2.10b It shows the simulated and experimental d-h curves in presence of electric field. The "jump-into-contact" region is blown up in the inset.

I c. Dynamic mode

There are two operational modes employed in dynamic mode AFM known as Amplitude Modulation and Frequency Modulation. These are discussed in detail in chapter 1. We have mainly used the Amplitude Modulation mode. In this mode the cantilever tip either does not come into contact with the sample surface (Non-Contact-AFM) or it comes into contact only at the lowest point in its vibration cycle (Intermittent-Contact-AFM).
For non-contact AFM imaging, the cantilever tip is held about 50 to 100 Å above the sample surface during a scan. It is vibrated at a constant frequency near its mechanical resonant frequency (typically 50 to 400 kHz), with an amplitude of a few tens of angstroms. As the tip is scanned above the surface, the cantilever vibration amplitude changes in response to force gradients that vary with the tip-to-sample spacing. An image representing surface topography is obtained by monitoring these changes in vibration amplitude. Since ideally the cantilever tip never touches the sample surface in non-contact mode, NC-AFM is useful for imaging samples of low moduli, such as soft polymers and biological materials that can be easily damaged by the tip. A further advantage of NC-AFM is that samples such as silicon wafers are not contaminated by contact with the tip, and the tip is not damaged by the sample.

The relationship between the resonant frequency of the cantilever and variations in sample topography can be explained as follows. The resonant frequency of a cantilever is the square root of its spring constant, k, divided by its mass, m:

$$\omega = \sqrt{\frac{k_{eff}}{m}} \qquad (2.14)$$

Here, the spring constant is written as k_{eff}, the effective spring constant, because the spring constant of the cantilever changes as the cantilever moves into close proximity (within a few hundred angstroms) of the sample surface and interatomic forces affect its behavior. Specifically, the spring constant changes when the force between the tip and the sample has a spatial gradient, as it does in the non-contact regime. For a force gradient f', the effective spring constant is given by the following expression:

$$k_{eff} = k - f' \qquad (2.15)$$

In eq. 2.14, k_c is the value of the cantilever's spring constant in free space, i.e., it is the value when the cantilever is far from the sample surface. The value of the cantilever's resonant frequency far from the sample surface is likewise referred to as its free-space resonant frequency (ω_0).

Eqs. 2.14 and 2.15 show that if the cantilever moves into a tip-to-sample spacing regime where the force gradient is positive and increasing, then the effective spring constant of the cantilever, and therefore its resonant frequency, decreases. If the resonant frequency of a cantilever shifts, then the amplitude of cantilever vibration at a given frequency changes. Near a cantilever's resonant frequency, this change is large. Figure 2.11 shows a response curve (vibration amplitude vs. frequency) for a cantilever. If the curve shifts to the left, for example, then there is a change (in this case, a decrease) in the amplitude of cantilever vibration at a given frequency (ω*).

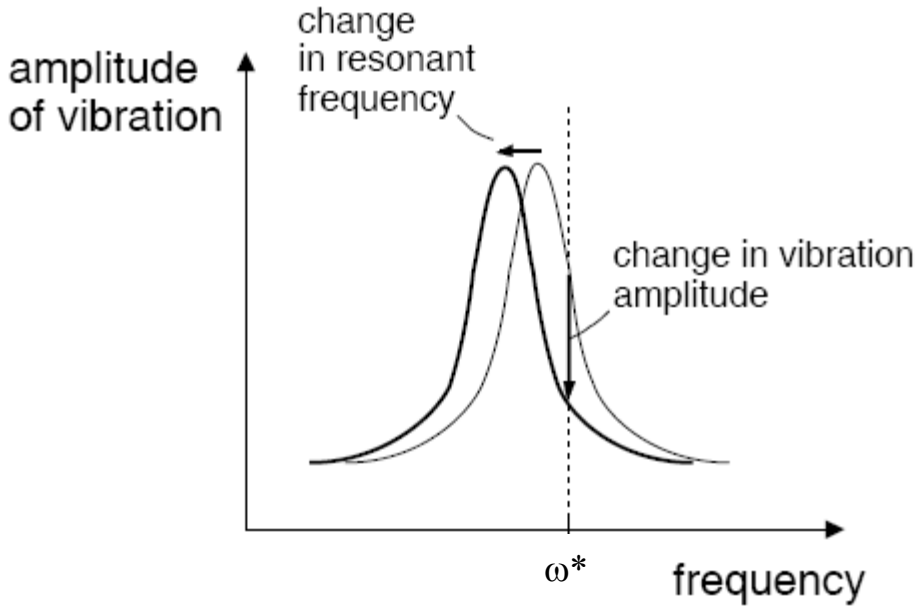

Figure 2.11 Response curves for a cantilever for NC-AFM mode.

This shift in amplitude, associated with a shift in resonant frequency, is the basis for the amplitude modulation (AM) measurement technique to detect changes in a cantilever's resonant frequency.

For AM detection, the cantilever is driven at a fixed frequency near resonance (e.g., ω^* in fig. 2.11), and changes in its vibration amplitude are detected. In non-contact AFM mode, a drive frequency close to, but greater than, the free-space resonant frequency of the cantilever is selected so that the vibration amplitude decreases significantly as the cantilever is brought closer to the sample surface, as illustrated in fig. 2.11. These amplitude changes reflect the change in the force gradient acting on the cantilever, which in turn reflects changes in the tip-to-sample spacing. A feedback mechanism operates to maintain constant cantilever vibration amplitude by adjusting and restoring the tip-to-sample spacing during a scan. As in contact-AFM mode, the amount of scanner z movement necessary to maintain the tip-to-sample spacing (or constant force gradient in the case of NC-AFM) is used to generate an image of topography.

Intermittent-contact AFM (IC-AFM) is similar to NC-AFM, except that in IC-AFM the vibrating cantilever tip is brought closer to the sample, and its vibration amplitude is greater so that at the bottom of its travel, it just barely hits the sample surface. For some samples, this is preferable to full contact AFM because it eliminates lateral forces such as friction and drag that might damage the tip or sample. As with NC-AFM, in IC-AFM the cantilever vibration amplitude changes in response to force gradients that vary with tip-to-sample spacing. An image representing surface topography is obtained by monitoring these changes.

The underlying principles for intermittent-contact AFM are the same as those for non contact AFM. The difference is that for IC-AFM the cantilever is driven (forced to vibrate) at a fixed frequency close to, but less than, its free-space resonant frequency, as shown in fig. 2.12.

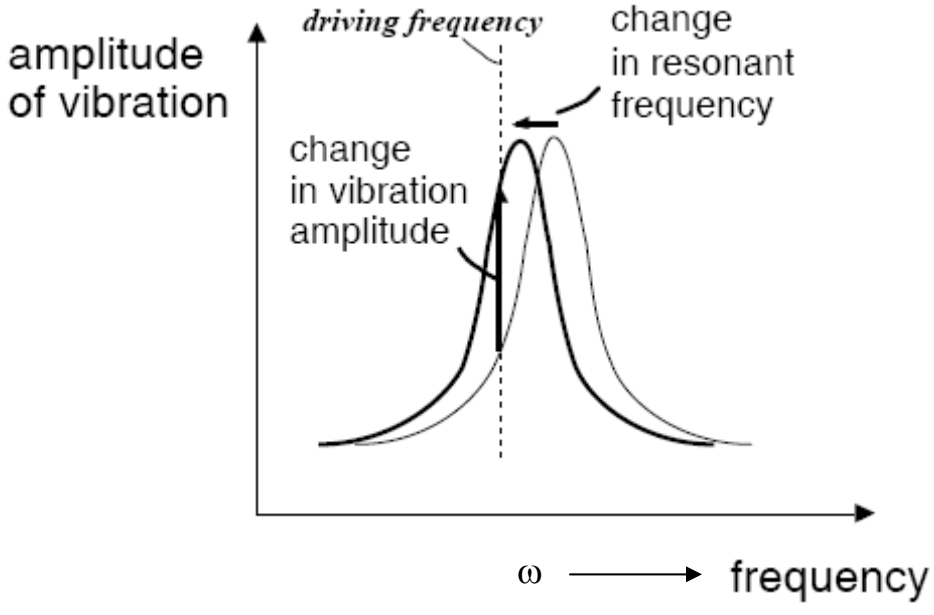

Figure 2.12 Response curve for a cantilever for IC-AFM mode.

Because the drive frequency is just below the free-space resonant frequency, the vibration amplitude of the cantilever increases as the cantilever is brought closer to the sample surface, and intermittent contact is consequently achieved.
While the two methods are similar, NC-AFM tends to outperform IC-AFM when imaging soft samples and samples with low-profile topography requiring maximum lateral resolution. NC-AFM does not suffer from the tip or sample degradation effects which are sometimes observed after taking numerous scans with contact or intermittent-contact AFM.

I c.1 Modeling of the cantilever

In case of dynamic mode the characteristics of a driven, damped and forced oscillator models the vibration of the cantilever of an atomic force microscope in the absence of a tip-sample force. In this case also the cantilever is replaced by a small sphere suspended on a spring that is mounted on a vibrating bimorph. The equation of motion of the microcantilever is generally very complex, since one has to take into account not only the motion of the tip in presence of a medium (air or water) but also the bending of the beam of the microcantilever. In this calculation, we will, however, restrict ourselves to the motion of the tip. While a more sophisticated calculation is necessary to get a better fit for the experimental curves, we find that the approximation of treating only the motion of the tip captures all the generic features obtained in the experiments. The equation of motion of the cantilever in presence of the tip-sample force is given by

$$m\ddot{d}(t) + \eta \dot{d}(t) + k_c d(t) = f_{ts}(h + d(t)) + F\cos\omega t \qquad (2.16)$$

where Fcosωt is the forcing term. F is the amplitude of the oscillating driving force on the microcantilever and ω is the frequency of the oscillating force. The free oscillation frequency of the microcantilever is given by

$$\omega_0 = \sqrt{\frac{k_c}{m}} \qquad (2.17)$$

The general solution of eq. 2.16 is complicated, due to the presence of the nonlinear atomic force $f_{ts}(h+d(t))$. If the atomic forces are absent (e.g., when the microcantilever is far away from the sample surface), eq. 2.16 reduces to the well known equation of a harmonic forced damped oscillator. At small times, this system shows a transient behavior, but at large times, it oscillates with the frequency of the harmonic forcing term i.e., ω. As the microcantilever approaches the surface of the sample, the nonlinear terms begin to make appreciable contribution to the solution of the equation of motion of the microcantilever. Here we have solved this equation numerically as there is no exact analytical solution that exists in this case. We have shown the behaviour of the amplitude of the vibrating cantilever as a function of tip-sample distance. We have also shown how resonance frequency gets shifted and its shape gets modified with the tip-sample distance.

I c.2 Simulation: Amplitude

In dynamic mode, we have simulated the amplitude vs. distance (A-h) curves for the parameters mentioned in Table 2.5. In this case we have considered both the attractive part and the repulsive part of the tip-sample interaction. To implement the simulation using a computer we wrote the simulation code in

Input Parameters	**Values of input parameters**
h_s	100.0 nm
q	50 (air)
k_c	20 N/m
d_i	0.0 nm
v_i	$a_i.\omega$ nm/sec
a_i	75 nm
ω' (ω/ω_0)	1.0, 1.003, 0.997

Table 2.5 Values of the parameters used for the simulation in dynamic mode.

Mathematica 5 as it automatically selects the best algorithms for each computation. The steps of the simulation for obtaining the (A-h) curves in dynamic mode are almost similar to that of calculating the (d-h) curves in static mode. In this case the input parameters are h_s (starting height of the cantilever from the sample), q (quality factor of the cantilever in air), k_c (spring constant of the cantilever), d_i (initial deflection of the cantilever at t = 0), v_i (initial velocity of the cantilever at t = 0), a_i (starting amplitude), $\omega'(\omega/\omega_0$, where ω_0 is the resonance frequency of the cantilever). For calculating the amplitude we have to do one more step which is the calculation of the amplitude from the maximum and the minimum deflection of the cantilever. This is shown in fig. 2.13. The deflection of the cantilever can be obtained by solving eq. 2.16 in this case. Table 2.6 depicts the steps of the simulation. We have simulated the (A-h) curves for both approach and retract path of the cantilever from the sample surface as shown in fig. 2.14. We have also studied the effect of the change in

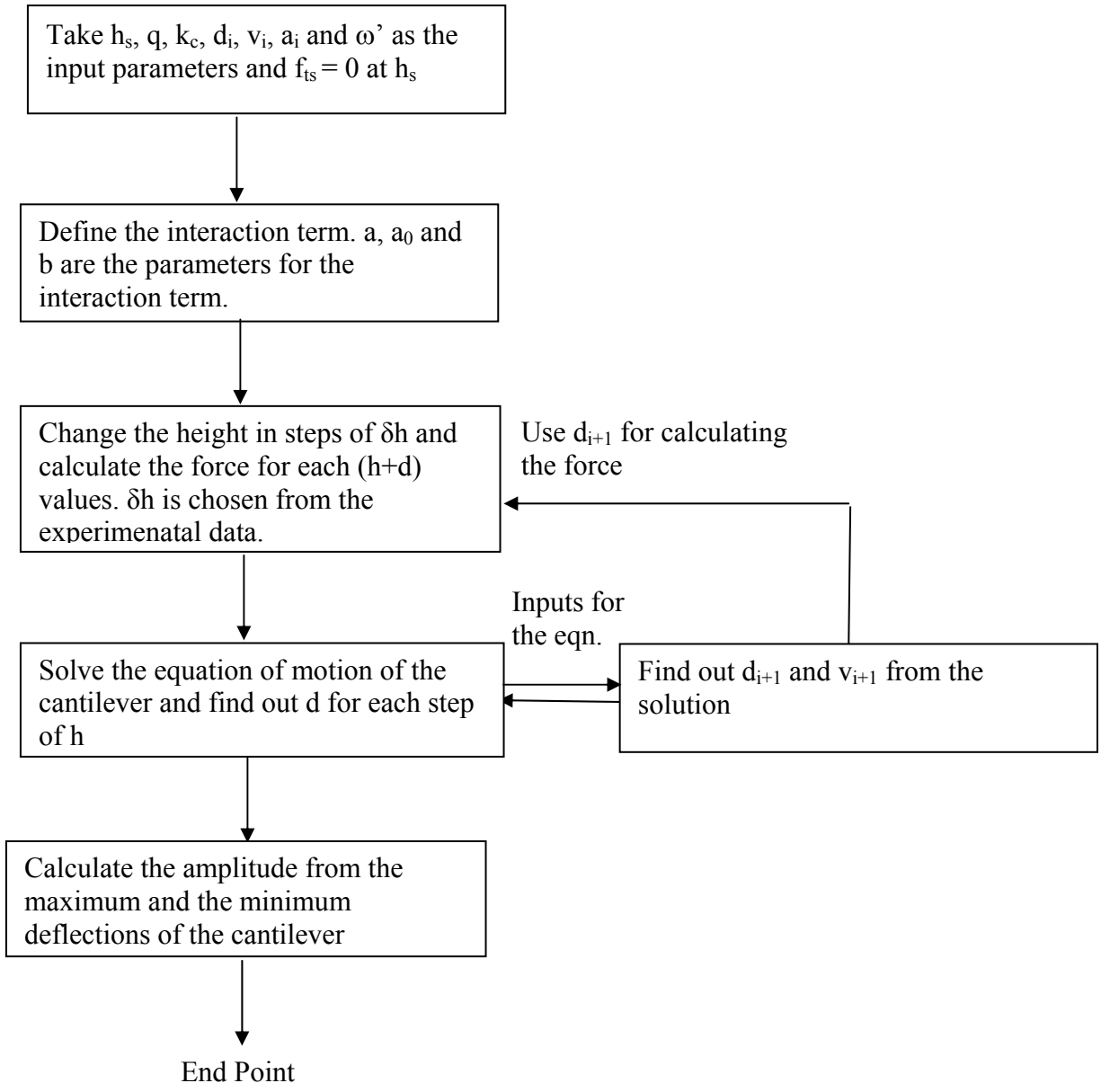

Table 2.6 Steps of the simulation for calculating A-h curves in dynamic mode.

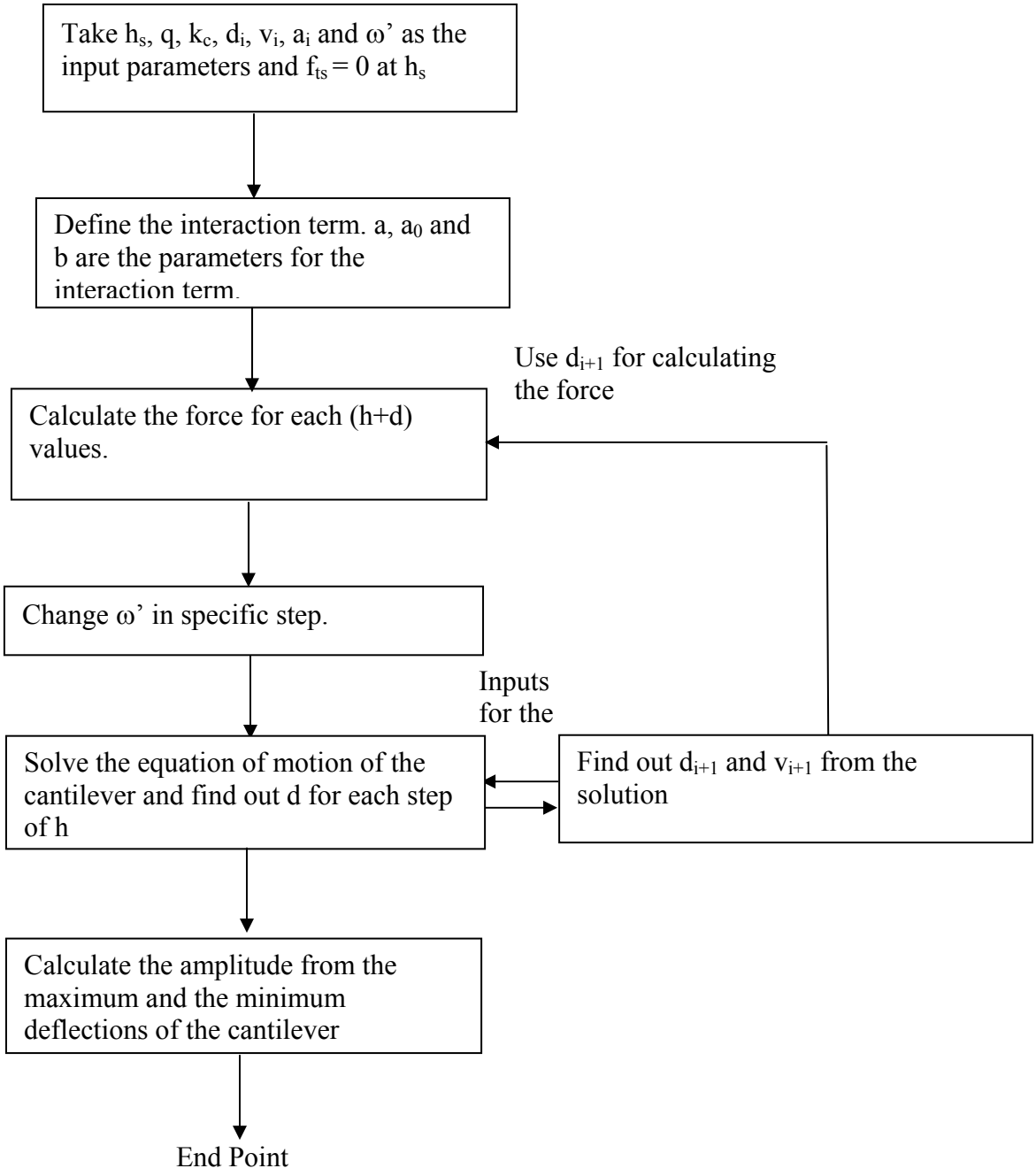

Table 2.7 Steps of the simulation to calculate the resonance curve.

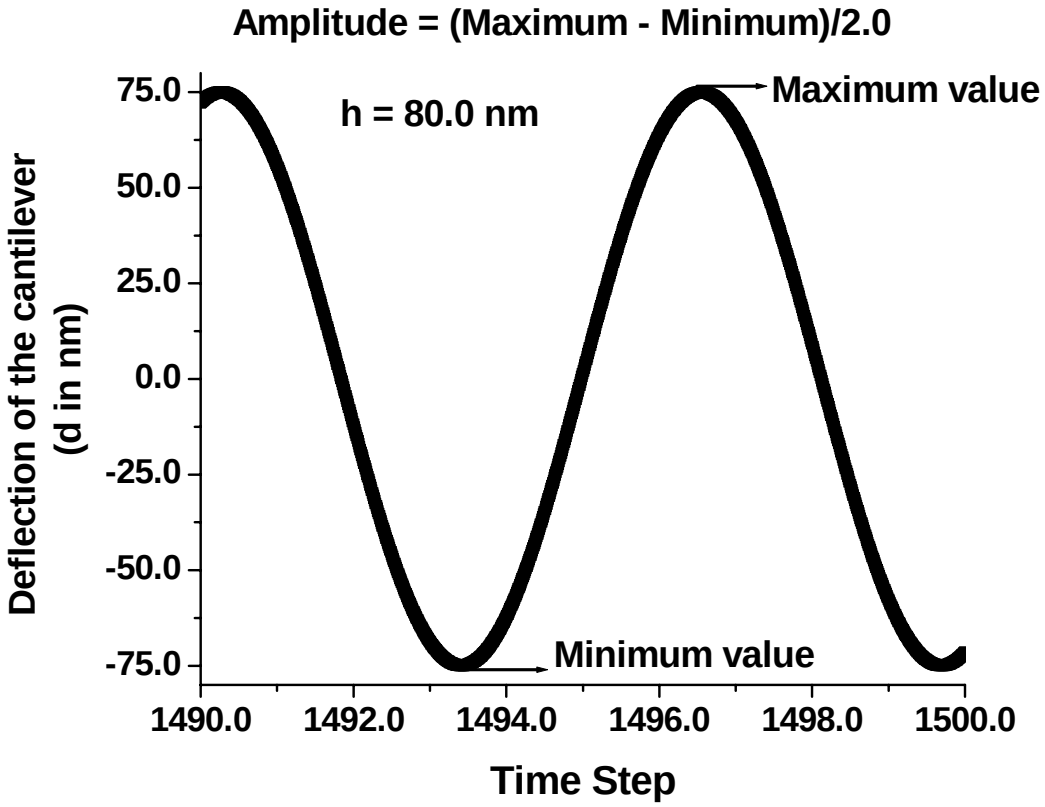

Figure 2.13 It shows the deflection of the cantilever as a function of time. Amplitude at a particular height is calculated from the maximum and the minimum deflection of the cantilever as mentioned in the figure.

set frequency on the (A-h) curves. We have considered three cases – i) $\omega > \omega_0$, ii) $\omega = \omega_0$ and iii) $\omega < \omega_0$. This is discussed in detail in chapter five of this thesis. In figs. 2.15 (a) and (b) we have plotted the deflection of the cantilever as a function of time for two different height values (h = 100 nm and 50 nm) and for three different ω' (0.9, 0.95 and 1.0) values. From these figures we can see that the value of the amplitude, at a particular ω', matches quite well with the value obtained from the resonance curves shown in fig.2.16.

I c.3 Resonance Curves

We have also simulated the resonance curves at different tip-sample separations to understand some features seen in (A-h) curves in dynamic mode. To simulate the resonance curves the following steps are followed. The values of the input parameters used in this simulation are given in Table 2.5. The first step of the simulation is to mention the values of the input parameters like h_s (starting height of the cantilever from the sample), q (quality factor of the cantilever in air), k_c (spring constant of the cantilever), $\omega'(\omega/\omega_0)$, d_i (initial deflection of the cantilever at t = 0) and v_i (initial velocity

of the cantilever at t = 0). Then we have defined the interaction term where the values of HR_t, a_0 and $4/3E^*R_t^{1/2}$ have been specified. After that we have calculated the force at a particular (h+d) value. As here h is fixed, therefore, (h+d) is varied for different d which is obtained by solving the differential eq. 2.16. Then we have varied ω′ for a fixed h value in specific step size. In the next step of the simulation we have solved the equation of motion of the cantilever in presence of tip-sample interaction using the force value and the ω′ (for a fixed h value) values calculated in the previous steps of the simulations.

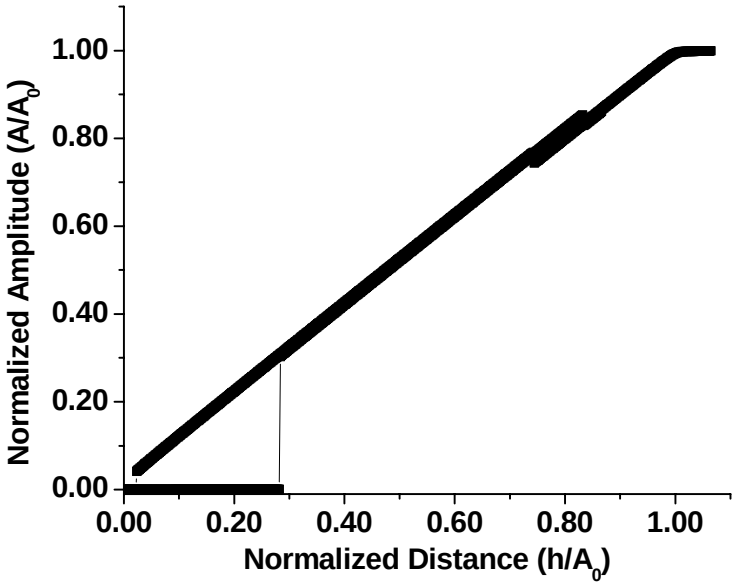

Figure 2.14 Amplitude versus distance curves (simulation).

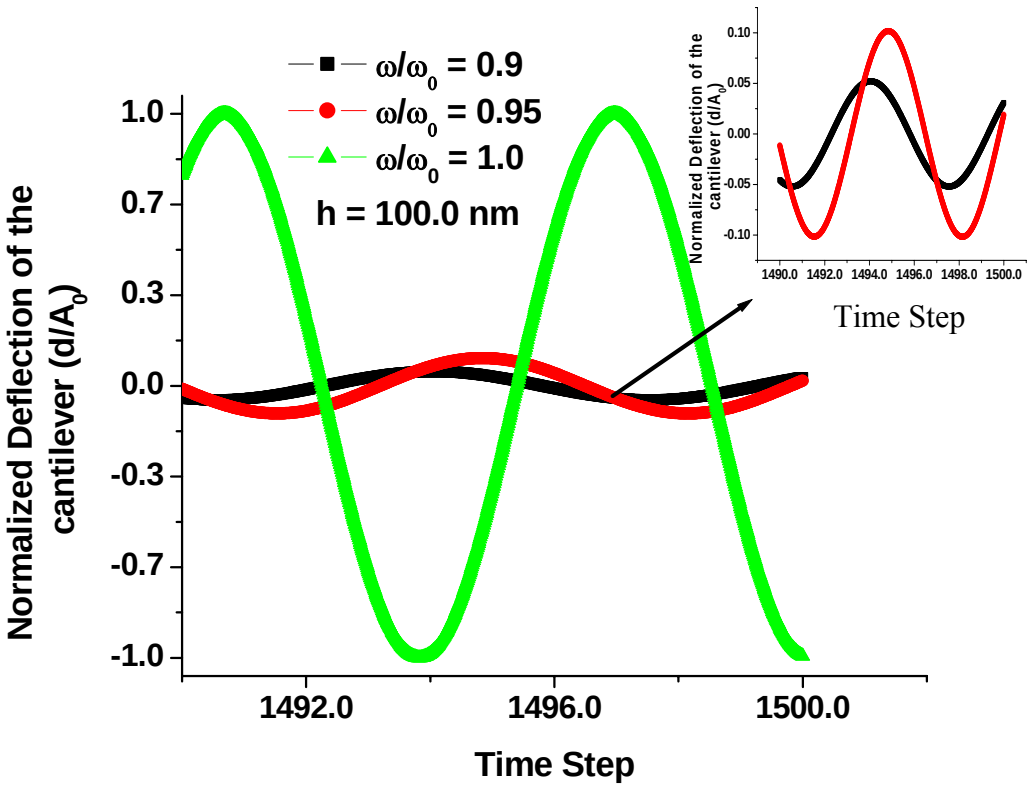

Figure 2.15 (a) It shows the deflection of the cantilever vs. time for h = 100 nm and ω′ = 0.9, 0.95 and 1.0.

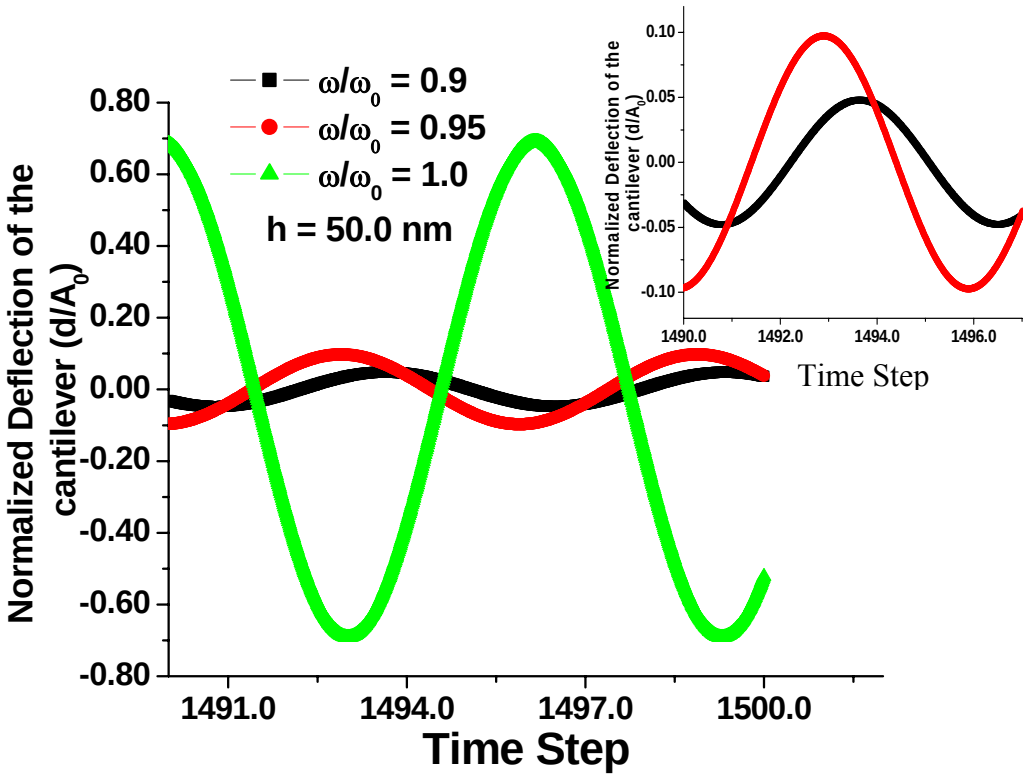

Figure 2.15 (b) It shows the deflection of the cantilever vs. time for h = 50 nm and ω′ = 0.9, 0.95 and 1.0.

Finally, from the solution of eq. 2.16 we have found out the maximum and the minimum values of the deflection and calculated the amplitude value to obtain the resonance curves. From the solution we have found out the value of d_{i+1} and v_{i+1} which are the initial conditions for the next simulation step to solve the differential equation. The values of d_{i+1} is fed back to step three of the simulation to calculate the force value at this step of the simulation. Table 2.7 depicts the steps of the simulation.

I c.4 Analysis:

We have plotted the amplitude versus distance curve (A–h curve) as shown in fig. 2.14. The parameters for the calculation are the same as mentioned above. A prominent outcome of our numerical result is the presence of two jumps in the amplitude distance curve as the cantilever approaches the sample and retracts back. We have studied this aspect in detail, using van-der-Waals forces and the observed features originate from the nonlinear nature of the interaction. These features of the A-h curve are also seen in the experiment. We note the following features. First, there is a flat region for large tip–sample separation in the amplitude versus distance curves. Second, at separations, slightly smaller than the free oscillation amplitude, (h/a_i) =0.95 the cantilever starts to

sense the long-range attractive force. This reduces the effective spring constant and hence the resonance frequency. Third, there is a transition region (h/a_i = 0.73) where the amplitude shows an increase. Fourth, after the transition the amplitude decreases again linearly and finally there is another jump at very small tip-sample distance. Hysteresis loop is observed in the approach—retract curves around these regions.

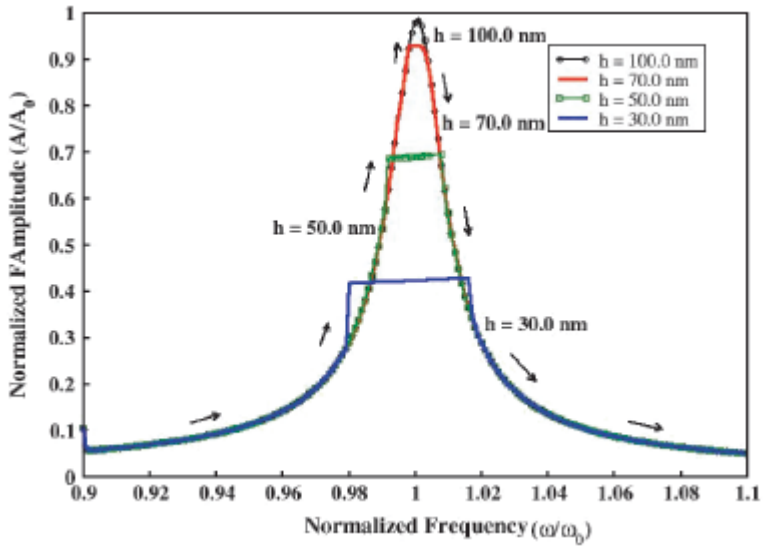

Figure 2.16 Calculated resonance curves for different tip–sample separations. The arrows indicate the direction of the frequency sweep.

II Experimental Techniques

The second part of this chapter presents the experimental techniques used to study the tribology and mechanics at the nanometer scale. A specific emphasis is dedicated to the atomic force microscope, as it is the central pillar for data acquisition in this work. Other tools for probing or imaging the surfaces will be reviewed. This section focuses on the technique of Atomic Force Microscopy (AFM) and Spectroscopy (AFS), sample preparation procedure and other techniques that have been used for sample characterization.

II a Atomic Force Microscope based techniques

Atomic Force Spectroscopy (AFS) i.e. force-distance (f-d) curves have become a fundamental tool in several fields of research, such as surface science, materials engineering, biochemistry and biology. Furthermore, they have great importance for the study of surface interactions from a theoretical point of view. Since 1989, several techniques of acquisition and analysis of f-d curves have arisen. An increasing number of systems, presenting new kinds of forces, have been analyzed. AFM force-distance curves are routinely used in several kinds of measurement, for the determination of elasticity, surface charge densities, and degrees of hydrophobicity. Different forces that can be measured with AFM force-distance curves are Capillary, Coulomb, Van-der-Waals,

double-layer, solvation, hydration, and steric forces. We have utilized this technique to understand the cantilever dynamics both in static mode and dynamic mode in presence of non-linear tip-sample interaction. This also helps to understand the basic interaction of the nanosphere and the tip so that the nano-sphere can be effectively manipulated using AFM.

II a.1. Basic principle of Atomic Force Microscope

The operating principle of AFM is based on measurement of forces of the order of 10^{-13} to 10^{-14} N between the sharp tip attached to one end of a cantilever and the surface of the sample. The probing tip is attached to a cantilever and force acting on the tip causes a small deflection of the cantilever. This deflection is detected and mapped as the tip scans the surface to obtain the image of the surface. The major components of force microscopes are; sharp tip mounted on a soft cantilever, the cantilever deflection detection system, feedback to monitor and control the deflection, mechanical scanning system (piezoelectric tube to raster scan the sample with respect to the tip), tip-sample approach mechanism, and an image display and measurement system via interface. A schematic diagram is shown in fig. 2.17 to explain the basic principle of AFM.

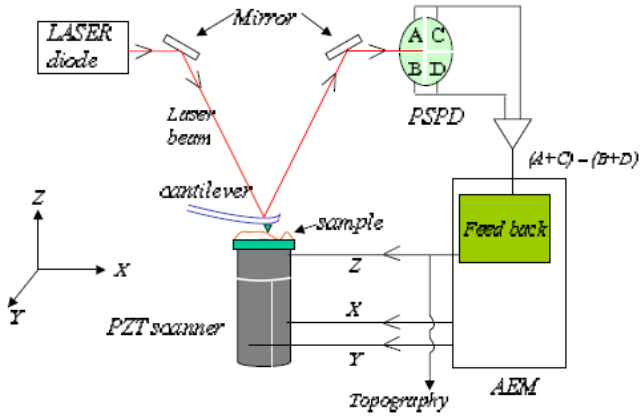

Figure 2.17 A schematic of basic principle of an AFM

The x/y and z piezo that are separately actuated by x/y drive and z-control with extreme precision, so that atomic distances can be measured. The sample is mounted on the xyz piezo, close to a sharp tip under the inclined cantilever with its mount. The diode laser light is focused at the end of the cantilever, reflected via mirror to a split diode that provides the feedback signal (topologic information) for maintaining the force by z-piezo response. Data sampling is made at discrete steps by means of an analog-to-digital converter. Different piezos are used for different xy scan ranges (1 µm X 1 µm upto 200 µm X 200 µm) and z ranges (upto 15 µm). A number of hardware and software linearization facilities are provided for correction of piezo hysteresis that creates stretching at the start of the scan in comparison to the end of the scan, line by line always starting from the same side.

In AFM, the interaction force is dependent on the relative separation between the tip and the sample as shown in fig. 2.18. If the tip is brought from a distance of hundreds of

angstrom to few tens of angstroms towards the sample, it is acted upon by an attractive long range van-der-Waals force or chemical interaction force, gradually increasing in magnitude until a maximum is reached. At this point there occurs onset of a repulsive force between the tip and the sample due to electrostatic repulsion between the electron clouds of atoms at the tip and sample and a turnover in the curve appears. As the tip is brought more and more close to the sample the repulsive force increases and it weakens the attractive force gradually and finally the force becomes completely repulsive and the tip just touches the sample. At this part the slop of the curve is very steep and further reduction of tip to sample separation is not possible and even if the cantilever is moved more towards the sample, the repulsive force deflects the cantilever resulting an upward bend. The amount of deflection of the cantilever gives an estimation of the inter-atomic force. The repulsive regime of the curve is also known as contact regime and the attractive one beyond the turning point is known as non-contact regime and AFM can be operated at the both regimes. Again in contact mode operation the imaging of the sample can be done either by keeping the positions of the cantilever and the sample at fixed z-positions while one of them scans over the sample in xy-plane or by keeping the force between the tip and the sample at a fixed value or in other word keeping the sample to tip separation fixed by moving the cantilever or the sample up and down in z-direction during the scanning in xy-plane. The first one is called “constant height mode” and second one is known as “constant force” mode. In the constant height mode the deflection of the cantilever follows the topography and in another one movement in the cantilever is required to compensate the height variation of the sample follows the topography of the sample. Thus an AFM image gives three dimensional (3D) informations of sample’s microscopy through the topography.

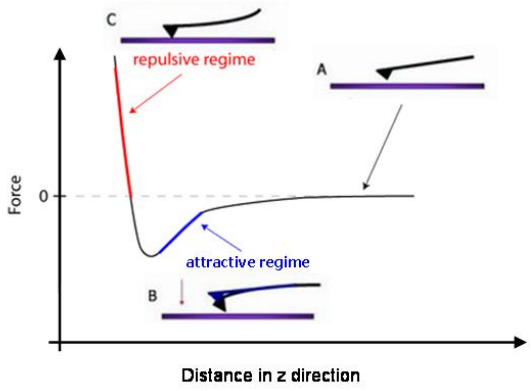

Figure 2.18 Interatomic interaction forces between the tip and the sample.

The movement of the cantilever or the sample in z-direction is controlled by a feedback loop consisting of a proportional integral-differential (PID) controller. For relatively rough sample, constant force mode is generally preferred to avoid any scratching on the sample by the tip even though it is little bit slower than the constant height mode due to extra time required for the feedback operation. It can be noted that these basic requirements are common for non-contact mode operation also. The deflection of the

cantilever can be measured by optical method or using piezo-resistive transducer or by using scanning tunneling microscope. Optical deflection detection method using a laser diode is commonly used in most of the commercial AFMs since it offers very high force resolution (~10^{-12}N), compactness and operational simplicity. The optical stage consists of a laser diode, position sensitive detector (PSPD), reflecting cantilever and collimating lenses. The position sensitive detector is a quadrant photodiode, which gives a signal proportional to the position of a spot of light. For maximum sensitivity, the laser spot on the PSPD should move as much as possible for given cantilever deflection. To maximize the spot movement the concept of the optical lever is generally used. This is achieved by adding a reflecting mirror (M) in the optical path from cantilever to PSPD. Optical lever ratio = (length of the laser path/length of the cantilever). In this method a beam of light from a laser source is made to fall on the cantilever which when bounces back is made to fall on a four quadrant position sensitive photodiode detector (PSPD) as shown in figure 2.17. The signal of (A+C)−(B+D) of the PSPD measures the vertical movement of the beam over the PSPD which is directly related to the amount of the cantilever's deflection. Frictional information (the LFM signal) is represented by lateral deflection of the cantilever, which is measured as (A+B)-(C+D). In our experiment we used this method of deflection detection.

The quality of topography image can be badly affected by external vibrations. These vibrations have lowest resonance of typically 20Hz with amplitude of several micrometers. To minimize the vibrational influence in our experiment the AFM was placed on a "pnumetic vibration isolation system" consisting of a platform over four pnumetic vibration isolator legs, designed by Technical Manufacturing Corporation (model no: model no. 63-32453-01) [1]. The design of this is shown in fig. 2.19. Each leg has one "Gimbal type piston" in an air column. The piston takes the load of the table and the air column acts as vibration damper. Out of the four isolator legs, three are master having height control valve along with pressure gauge and one slave whose height is controlled by the master one in the diagonally opposite to it. From an automatic turn on-off compressor, set for 80 psi, was used to supply clean air to the air column.

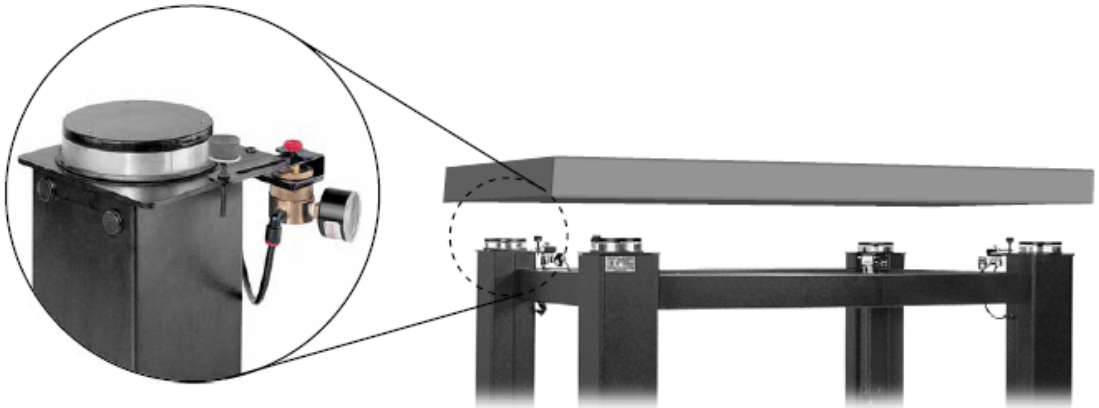

Height Control Valve
attached to master piston isolator.

M = Master Isolator with Height Control Valve (V)
S = Slave Isolator (no valve).

(a)

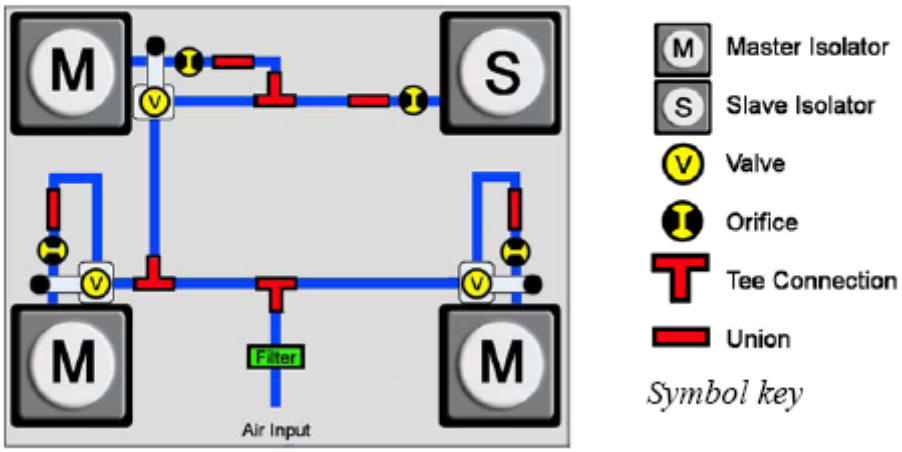

(b)

Figure 2.19 a) The vibration damper used in the experiments b) the air supply scheme [1]

In our setup, the sample was placed on a sample stub over a five-sectored piezo tube whose movement in all three directions independently was controlled by an electronic module called"Autoprobe electronic module" (AEM), a part of the AFM setup. The cantilever was fixed on a probe carrier. AEM uses one 20-bit digital-to analog and analog-to-digital converter (DAC) card for x-y-z scan and imaging and one 16 bit DAC for system control. The maximum scan range was ~ 90 µm in x-y direction and 7.5 µm in the vertical direction. The resolution of DAC in the lateral direction was 0.25 Å and that in the vertical direction was 0.025 Å. In this setup we could choose any direction, x or y as fast scan direction while the other as slow scan direction. Images taken in the both direction should match. Typical scan resolution at which we took the images was 256 × 256 pixels. The operation of the AFM was done by software namely "ProScan Data Acquisition Software", supplied along with the AFM by the manufacturer. For acquiring image with complete informations, selection of the scan rate is a crucial parameter. The scan rate represents the number of lines scanned per sec (lps) along the fast-scan direction or in other word the waiting time of the probe for acquiring data at each pixel. The selection of scan rate depends mainly on two factors, response time of the z-feedback circuit and the response time of the probe which is limited by the response of the probe to reach a new thermal equilibrium. We usually used a scan rate ≤ 1lps to give the tip a minimum acquiring time of 3.9 m sec per pixel which sufficiently long for the tip to reach the thermal equilibrium.
There are different modes of AFM, like Contact Mode, Non-contact Mode or Tapping Mode, Electrostatic Force Microscopy (EFM), Conducting AFM, Magnetic Force Microscopy (MFM), Scanning thermal Microscopy (SThM), Force Modulation Microscopy (FMM). AFM can also be used for Oxidation Lithography, Dip-pen lithography and Nanomanipulation. In our experiments we have mainly explored Contact

mode, Non-contact mode (both spectroscopy and microscopy), Nanomanipulation and Force Modulation.

II a.2. Atomic Force Spectroscopy in Contact Mode

AFM is able to acquire f-d curves on every kind of surface and in every kind of environment. The entire f-d curves can be collected. Moreover, force measurements can be correlated with topography measurements. The AFM is the only tool able to measure the interactions between nanometer sized surfaces, allowing local forces and sample properties to be compared. In a force measurement the sample is moved up and down by applying a voltage to the piezoelectric translator, onto which the sample is mounted, while measuring the cantilever deflection (fig. 2.20). When acquiring f-d curves, the piezo must be ramped along the Z axis, i.e., the axis perpendicular to the surface. In static mode, the sample is displaced along the Z axis in discrete steps and the variations in cantilever deflection are collected.

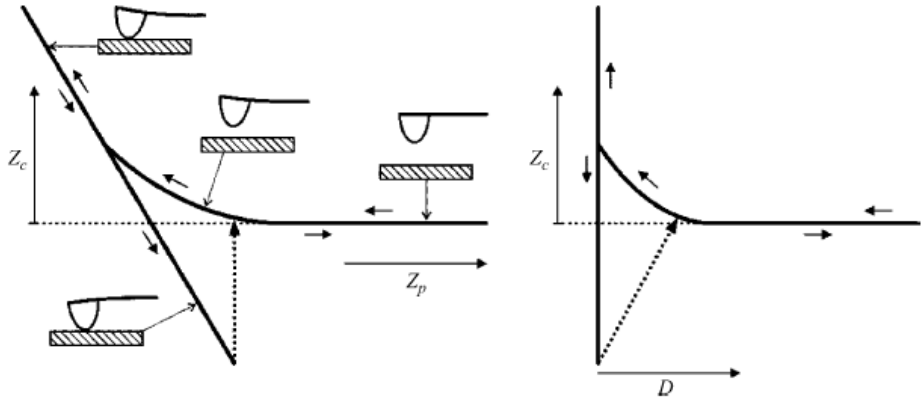

Figure 2.20 Schematic of a typical cantilever deflection-vs.-piezo height (Z_c-vs.-Z_p) curve (left) and corresponding Z_c-vs.-D plot, with $D = Z_c + Z_p$.

The most convenient geometry is a planar surface. Problems due to sample roughness are greatly reduced in the AFM compared to other surface force techniques since the sample only needs to be smooth on a scale comparable to the radius of curvature at the end of the tip. The result of a force measurement is a measure of the cantilever deflection, Z_c, versus position of the piezo, Z_p, normal to the surface. To obtain a f vs. d curve, Z_c and Z_p have to be converted into force and distance. The force F is obtained by multiplying the deflection of the cantilever with its spring constant k_c: $F = k_c Z_c$. The tip–sample separation D is calculated by adding the deflection to the position: $D = Z_p + Z_c$.
When a force is applied to the probe, the cantilever bends and the reflected light-beam moves through an angle equal to twice the change of the end slope dZ_c/dX. For a cantilever with a rectangular cross-section of width w, length L, and thickness t_c, the change of the end slope (fig. 2.21) is given by

$$\frac{dZ_C}{dX} = \frac{6FL^2}{Ewt_C^3} \qquad (2.18)$$

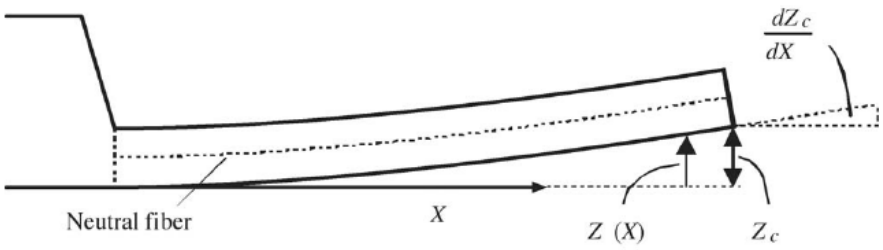

Figure 2.21 Schematic side view of a cantilever with a force at its end. X is the horizontal coordinate originating at the basis of the cantilever; Z(X) is the cantilever deflection at the position X, Z_c being the cantilever deflection at its end.

Here, E is the Young's modulus of the cantilever material. F is the force applied to the end of the cantilever in normal direction. The signal detected with the optical lever technique is proportional to the end slope of the cantilever. The deflection of the cantilever is given by

$$Z_C = \frac{4FL^3}{Ewt_C^3} = \frac{2}{3}L\frac{dZ_C}{dX} \qquad (2.19)$$

Hence, the deflection is proportional to the signal. These relations only hold under equilibrium condition. If the movement of the cantilever is significantly faster than what is allowed by its resonance frequency Eqs. (2.18) and (2.19) are not valid anymore and the signal is not necessarily proportional to the deflection. The position of the sample is adjusted by the piezoelectric translator. Piezoelectric crystals show creep and hysteresis which affects the accuracy of the distance determination [2]. Usually the piezoelectric translator moves with constant velocity up and down so that its position versus-time can be described by a triangular function. A constant approaching and retracting velocity is the simplest boundary condition when analyzing dynamic effects in a force experiment. A problem might arise for high velocities because then the cantilever might vibrate each time the direction of the movement changes. No useful deflection signal can be obtained until this vibration is damped. Typically, the frequency is 0.1–1 kHz, significantly below the resonance frequency of the cantilever and the cantilever assumes its equilibrium deflection at all times. External vibrations, such as vibrations of the building, the table, or noise, which are usually in the low frequency regime, are less transmitted to the cantilever, when the resonance frequency of the cantilever is as high as possible. A high resonance frequency is also important to be able to scan fast because the resonance frequency limits the time resolution [3, 4].

II a.3. Specifications of the cantilevers

The specifications of the cantilevers that we have used for our experiments are given below. For static mode spectroscopy we have used non-conductive Si_3N_4 cantilevers with Au-Cr coated on the back side of the cantilever. We have used two different cantilevers having spring constant and resonance frequency values 0.03 N/m, 0.1 N/m and 10-20 KHz, 26-50 KHz respectively. The radii of curvatures of the tips are 25 nm and 30 nm

respectively. Figure 2.22 shows the SEM image of the cantilevers mounted on a chip used for contact mode.
For studying the effect of electric field on static mode spectroscopy we have used conducting cantilevers made of Antimony doped silicon with PtIr coated on the front side and the back side of the cantilevers. The spring constant of the cantilever is 0.2 N/m and resonance frequency is 10-16 KHz. The radius of curvature of the tip is 35 nm. The radii of curvatures of the tips are found by direct imaging of the cantilevers using SEM. Figure 2.23 shows the SEM image of the tip. For dynamic mode spectroscopy we have used cantilevers made of Phosphorus doped silicon cantilevers coated with aluminum on the back side of the cantilever. The spring constant of the cantilever is 20-80 N/m and the resonance frequency is 270-320 KHz. For Force modulation microscopy we have also used silicon cantilevers having spring constant 3 N/m and resonance frequency 71-90 KHz.

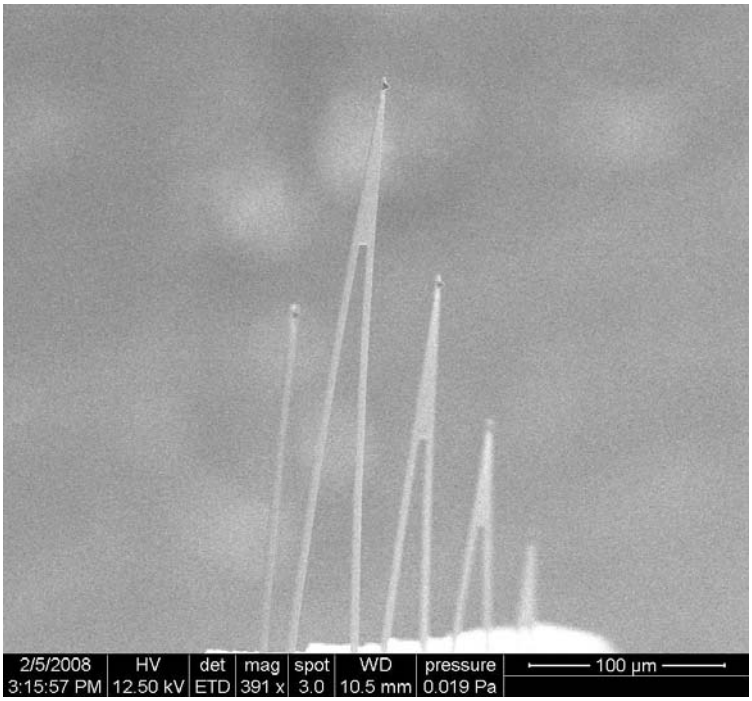

Figure 2.22 It shows the cantilevers mounted on a chip used for contact mode AFM.

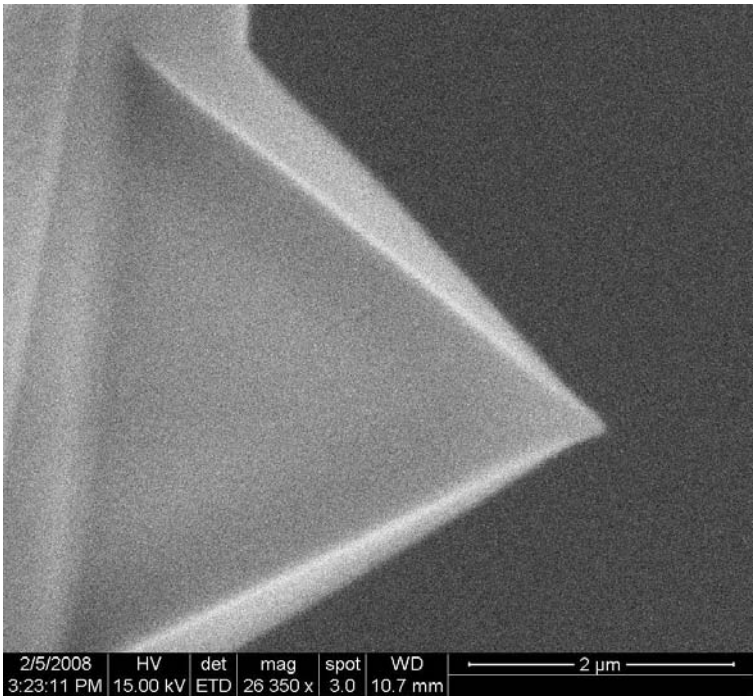

Figure 2.23 It shows the SEM image of the tip.

Table 2.8 shows a list of special cantilevers used for different modes of AFM.

Modes of AFM	**Specifications of the cantilevers used**
Contact Mode	Cantilevers are made of silicon or Si_3N_4 with Au reflective coating on the backside of the cantilever. These cantilevers are generally softer cantilevers. The spring constant varies from 0.01 N/m to 0.9 N/m
Non-contact Mode	Cantilevers are made of silicon with aluminum reflective coating on the backside of the cantilever. These cantilevers are stiffer than the cantilevers used for contact mode. The spring constant can be varied from 0.9 N/m to 40 N/m.
Conducting AFM (C-AFM)	Cantilevers are made of silicon with doped diamond coating at the front side and aluminum reflecting coating at the back side of the cantilever. The doped diamond coating is used to harden the tip in applications that require both increased wear resistance and a conductive tip.
Electrostatic Force Microscopy (EFM)	Cantilevers are made of silicon with PtIr

	coated both on the front side and the back side of the cantilever to make it conducting. These cantilevers can also be used for Conducting AFM.
Magnetic Force Microscopy (MFM)	Cantilevers are made of silicon with magnetic Co-Cr coated on the tip and the back side of the cantilever. The Co coating is protected from oxidation by a Cr layer, resulting in longer cantilever performance.
Scanning Tunneling Microscopy (STM)	These tips are formed from a Pt/Ir wire and cut at the end to form the tip. STM tips are meant to be used with a conductive sample.
Scanning Thermal Microscopy (SThM)	Cantilevers are made of silicon. Active element is a 5μm Platinum/Rhodium thermal resistor which works as the tip.

II a.4. Atomic Force Spectroscopy in Dynamic mode

There are two principal modes of acquisition of force-distance curves. One is called the static mode which is described above. In the second mode, called the non-contact mode, the cantilever is vibrated by an extra piezoelectric transducer while the sample is approached and withdrawn, and the amplitude (Amplitude modulation) [5, 6] or the resonance frequency (FM, frequency modulation) [7, 8] of the cantilever oscillations are collected as a function of tip-sample distance. The non-contact mode was introduced by Martin et al. [9]. When the tip approaches the sample and the distance becomes so small that tip and sample start to interact, the cantilever is not free anymore and the interaction has to be taken into account. It leads to a shift of the resonance frequency. For an attractive force the resonance frequency is reduced, for a repulsive force it is increased. This change of the resonance curve can be used to analyze surface forces [10]. A potential advantage of dynamic force measurements is the high sensitivity. This allows using stiffer cantilevers and thus avoiding the jump-in which often prevents an accurate measurement of attractive forces. The amplitude Z_0 can either be small or large. For small amplitudes the interaction potential does not change significantly over a distance Z_0 and the tip feels the same force independent of the specific phase. Then the resonance frequency shifts according to where $D = Z_p + Z_c$ is the tip–sample distance. In large amplitude dynamic AFM the jump-into-contact is avoided by using stiff cantilevers. The cantilever is vibrated at amplitudes much larger than the inter-atomic spacing, typically 1–100 nm. Interaction forces cause a phase shift between the excitation and the response of the cantilever. This phase shift is measured versus distance. One problem is that the theoretical analysis is not straightforward and the method is not really used for quantitative measurements of surface forces but it is mainly used for imaging in non-contact mode [11, 12].

We have used Atomic Force spectroscopy (both in contact mode and in dynamic mode) for understanding the dynamics of the AFM (CP II from Veeco [13]) cantilever in presence of non-linear tip-sample interaction. We have also studied the f-d curves in presence of an external electric field to have better control over the tip-sample

interaction. In our setup, a bias can be applied either to the sample or to the cantilever. Sample bias can be applied through software and for applying the bias to the cantilever we have used a lock-in-amplifier.

II a.5. Nanomanipulation

In nanomanipulation generally a preformed nanoparticle, nanotube or a nanowire is manipulated to place it at a predetermined site. The most widely used tool for nanomanipulation is the cantilever of the AFM that provides a "robotic" arm to place the nano objects in predetermined sites. AFM technology has the potential not only to observe and evaluate fine structure on a sample but also to manipulate an individual atom or cluster and modify a sample surface. This means that as previous microscope technology such as optical and electron microscopes has been applied to fabricate fine patterns for VLSI devices and storage devices, an application of the AFM technology to fabricate them with atomic and nanometer size can also be expected. Nanomanipulation, in principle, should also include "manipulation" using forces of self-assembly or other chemical forces and manipulations using optical tweezers. However, the word “nanomanipulation” is often used in a limited context where a SPM tip is used for manipulation of a nano object.

Nanomanipulation is generally done in dynamic mode. The manipulation mechanism, that is generally used, is based on the mechanical pushing of an object by the tip. Since the imaging mode is based on the opposite mechanism, that is, a feedback loop that works to prevent mechanical contact between the tip and sample, the software takes control of the imaging process by using various manipulation protocols. These manipulation protocols differ in their approach to achieve physical contact between the tip and the object. All the protocols are based on dynamic mode operation, but some work in contact mode as well. Each of these mechanisms can be used independently; however a combination of two may be used in some cases (some combinations are not allowed by the software due to logical conflicts). The forces acting during manipulation has been discussed in detail in chapter 1. Figure 2.24 shows an example of nanomanipulation using AFM.

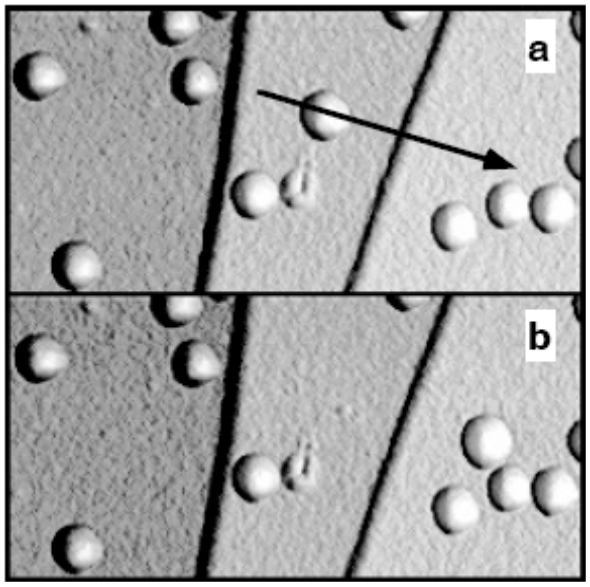

Figure 2.24 A 30 nm Au particles before (a) and after (b) being pushed over a 10 nm high step along the direction indicated by the arrow. Image sizes are both 1X0.5 μm [14].

We have performed Nanomanipulation using AFM on monolayer of polystyrene spheres coated on silicon surface by spin-coating and evaporation method.

II a.6. Force Modulation

Force Modulation Microscopy (FMM) operates in contact atomic force microscopy mode and is used to detect variations in the mechanical properties of a surface, such as surface elasticity, adhesion, or friction. Like Lateral Force Microscopy and Magnetic Force Microscopy, FMM allows simultaneous acquisition of both topographic and material-properties data as has been discussed below. For FMM, t he cantilever tip is scanned in contact with the sample surface. Just like contact AFM, the z feedback loop uses the DC cantilever deflection signal to maintain a constant force between the tip and the sample and to generate a topographic image. Additionally, either the tip or the sample is oscillated in z with a sine wave. The amplitude of the cantilever modulation that results from this applied signal varies according to the elastic properties of the sample's surface, as shown in fig.2.25.

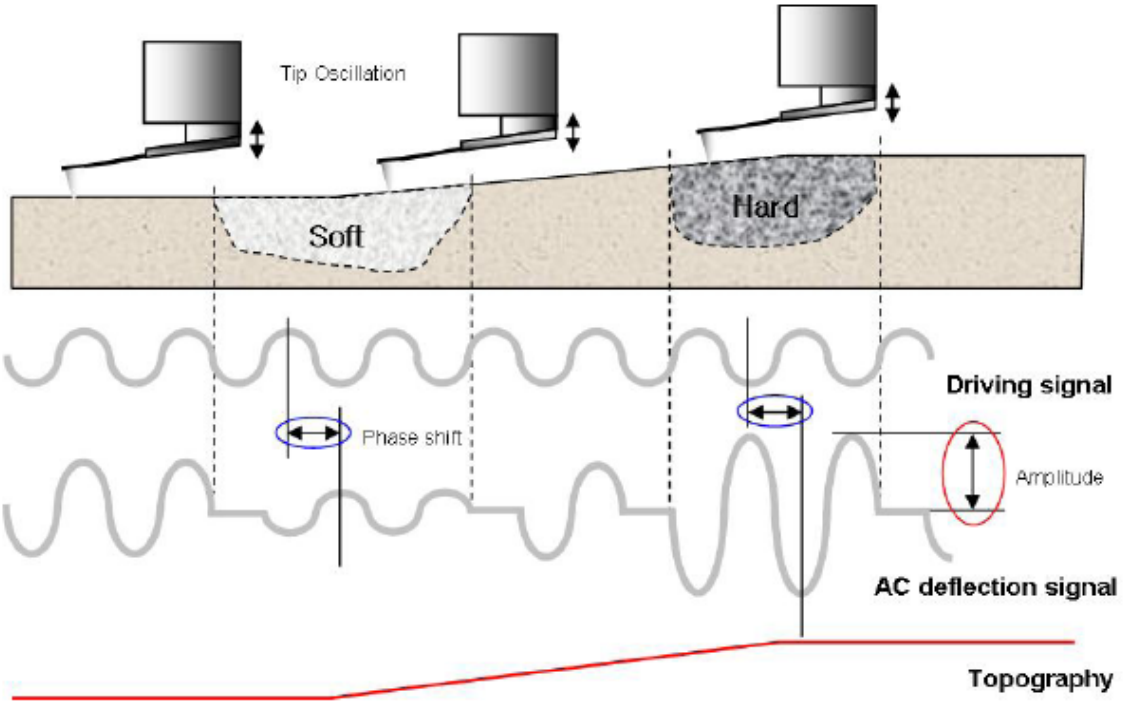

Figure 2.25 The amplitude of the cantilever oscillation signal varies according to the mechanical properties of the sample's surface.

The system generates an FMM image, which is a measure of the sample's elastic properties, from changes in the amplitude of the cantilever modulation. A hard sample transmits the oscillation directly to the cantilever; a soft ample absorbs the oscillation. For a hard area the measured tip oscillation amplitude is large, for a soft area it is small.
Shift in the phase of the oscillation can be detected as well. This technique is known as phase detection microscopy (PDM), and provides an additional contrast mechanism within a region of homogeneous hardness. The frequency of the oscillation ranges from tens to hundreds of kilohertz, substantially faster than the z feedback loop is set up to track. This means the force on the sample is modulated such that the average force on the sample is equal to that in contact mode. Thus, topographic information can be separated from local variation in the sample's elastic properties, and multiple images can be collected simultaneously.
Two modes of FMM operation can be defined depending on whether the modulation signal is applied to the tip or to the sample: 1) tip modulation mode; or 2) sample modulation mode. In tip modulation mode, a driving signal is sent to the cantilever. The driving oscillates the cantilever at a constant frequency. The amplitude of the resulting cantilever oscillation signal varies according the sample's mechanical properties and is used to generate an FMM image. In sample modulation mode, the sample is placed on the sample actuator. A driving signal is sent to the sample actuator to oscillate the sample at a constant frequency. When the sample oscillates, the cantilever oscillates as well, since the tip and the sample are in contact. As in tip modulation mode, the amplitude of the

cantilever oscillation signal varies according to the sample's mechanical properties and is used to generate an FMM image.
We have shown two examples of FMM below. Figure 2.26 [15] shows images of a carbon black deposit in a section of automobile tire rubber. The force modulation image (right) clearly differentiates the stiffer carbon black area in the center from the surrounding rubber. Figure 2.27 [15] shows the contact mode topography and force modulation images of a two-phase block copolymer. This set of images illustrates the resolving power of the force modulation imaging technique — while the topography image provides very little indication of the heterogeneous nature of the sample, the force modulation image clearly maps the two phases of the material, resolving features as small as 10nm wide.

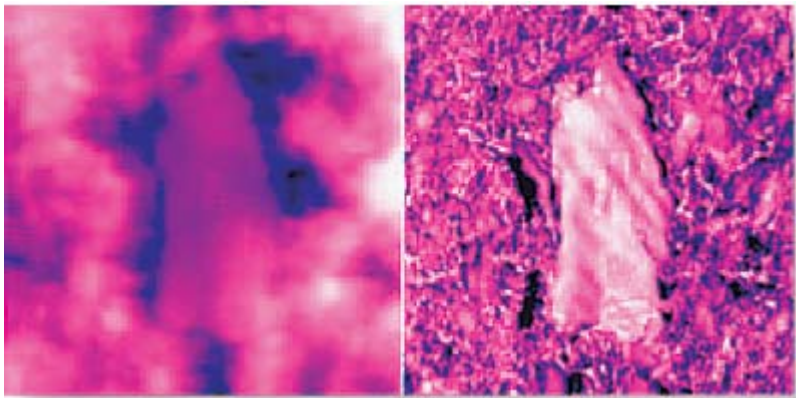

Figure 2.26 Contact mode topography (left) and force modulation image (right) of carbon black deposit in automobile tire rubber 15μm scan.

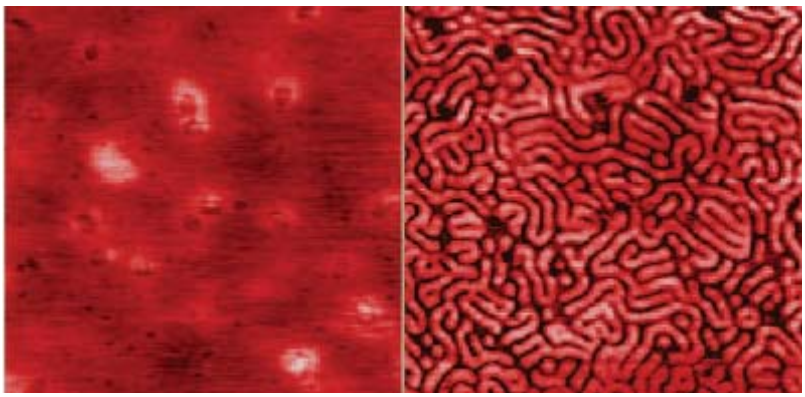

Figure 2.27 Contact mode topography (left) and force modulation image (right) of a two-phase block copolymer. The softer, more compliant component of the polymer maps in black. 900nm scans.

We have used Force Modulation technique for imaging the dewetted uncapped Gold nanoparticles filled polymer thin films. It helps to understand how the gold nanoparticles orient themselves within the dewetted polymer structures. Force Modulation is performed on a single droplet forming due to dewetting of a 15 nm thick PS film, with 0.1 % nano particle concentration. The image reveals that each droplet has a core–shell structure.

II b Sample preparation

II b.1 Preparation of Silicon surface

The first and crucial step of sample preparation is the cleaning of the substrate and the surface treatment according to the need of sample preparation. For our experiments we have mainly used silicon substrates. Here we will first mention about the cleaning procedure of silicon surface and then the surface treatment to make it hydrophobic or hydrophilic. The silicon wafer has been cleaned in the following way. Firstly, the silicon wafer was ultrasonicated in Tri-chloro-ethylene (TCE), acetone and propanol (Iso-propyle alcohol) at room temperature for 5 min, to remove contamination from organic grease. Then, the degreased silicon substrate was heated in boiling Piranha solution (4:1 (v/v) H_2SO_4/H_2O_2) and RCA solution (1:1:5 (v/v/v) $NH_3/H_2O_2/H_2O$) for 1 hour each. Subsequently, the silicon substrate was rinsed several times with MQ water. Another function of the Piranha solution is to increase the thickness of the oxide layer on top of the silicon surface which makes the surface hydrophilic.
We have used the following procedure to make the silicon surface hydrophobic. The cleaned silicon substrates were kept in a solution of diluted HF ($HF:H_2O$ = 50:1) for 30 seconds. This solution etched the oxide layer on top of the substrate and silicon wafer becomes hydrophobic. The substrates then washed thoroughly using MQ water.

II b.2 Hard-sphere Lithography

There are two major routes for nanofabrication: “bottom-up” and “top-down”. The “top-down” approach utilizes various techniques to scale down bulk materials and to create nano-devices. This approach uses very sophisticated preparation methods and provides the most control over composition and geometry of the manufactured structures. On the other hand, it is costly and time consuming. Examples of this approach are photolithography (PL) and electron beam lithography (EBL). The “bottom-up” approach refers to the manipulation of atoms, molecules, or larger building blocks and their assembly into bigger structures. This can be achieved by the use of powerful microscopes, which allow nanomanipulation. Also, natural selfassembly properties of matter are used for the fabrication of more complex structures. It is inherently parallel, time-efficient and low-cost, but it does not provide the same precision as the “top-down” approach. Several important criteria determine the usability of nanofabrication methods that are utilized in the preparation of arrays of nanoparticles, namely: control of the geometry of the nanoparticle arrays, spatial resolution, cost, and time consumption. Block copolymer lithography and shadow nanosphere lithography (SNSL) [16, 17] are the cheapest technologies. Several methods are reported for hardsphere lithography like evaporation method [18, 19], electrostatic deposition [20, 21], dip-coating [22], Langmuir-Blodgette coating [23], electrophoretic deposition [24], self-assembly on pre-patterned subatrates [25], spin-coating [26], self-assembly at the interface of two different media [27]. We have mainly used two methods- 1) evaporation method and 2) spin-coating method.

Evaporation method

As is well-known, the production of a latex particle monolayer film is usually realized by the evaporation of a solution on a substrate [28]. The quality of the results depends strongly on the properties of the substrate as well as on how homogeneous the process of evaporation is. Polystyrene latex beads (Bangs Laboratories) [29], with a diameter of 100 nm and 30 nm were used. The concentration of the solution used was 1 wt%. This solution was mixed with ethanol (1:1volume ratio). The reason for this is two-fold. Ethanol has about 79% of the density of water. Therefore, it is directed towards the water surface. Once the mixture reaches the surface, it is dispersed over a large area due to the amphiphilic ethanol molecules, which preferentially tends to cover the entire interface. Due to good solubility of ethanol in the water, some nanospheres might penetrate into the bulk water.A droplet (~10 μl) of this mixture, with an opportune ratio of water/particles, was deposited on a properly cleaned silicon surface. The proper water/particles ratio was calculated depending on the deposition area and on the size of the spheres. The whole system was enclosed in a small plastic box of volume around 30 cm^3. We believe that the small volume helps to slow down the evaporation process, which takes approximately 5 hours to take place completely. The box also protects the surface from the external air flow, which can disturb it. The whole system was tilted about 9^0. In this way the evaporation starts from the top of the sample on a horizontal border where evaporation takes place. This border moves then to the bottom of the sample until it is completely dry. The speed of evaporation and the quality of the resulting sample depends on this angle. Figure 2.28 shows a schematic view of the setup. Our depositions covered an area of about 1 cm^2, but in any sample only around half of the area was covered by monolayers. The other half is the one where the evaporation takes place at last, at the bottom of the sample. We believe that in such regions the remaining of water concentrates impurities and the excess particles, creating multilayers and clusters.

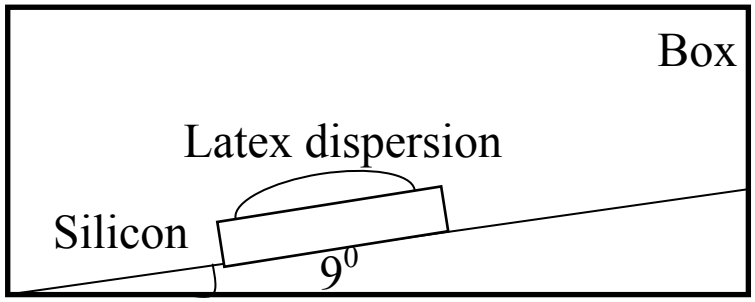

Figure 2.28 A schematic view of the experimental setup.

Effect of different parameters on evaporation

Particle Concentration:

In a typical experiment the volume (10 μl) and concentration (1wt %) of the latex suspension have been chosen to provide (approximately) a dense monolayer of particles. In another set of experiments we have varied the latex concentration (keeping constant the overall volume of 10 μl) from 0.5 to 5.0 wt %. Although the concentration varied for over 1 order of magnitude, there is no substantial difference in the occurrence of the processes. One should notice only that when the particle concentration is higher, the area occupied by bilayers is larger. Oppositely, when the particle concentration is lower, large areas free of particles are formed between the parcels covered with a particle monolayer.
Electrolyte Concentration: The polystyrene latex particles in aqueous solution bear a negative surface electrical charge due to dissociation of surface ionizable groups. This prevents the tendency for formation of transient aggregates, which is certainly due to the screened electrostatic repulsion, at the stage of Brownian motion. Adding opposite charges to the solution allows the attractive van-der-Waals interaction between the particles to become operative. In our case we did not use any electrolyte solution.
Presence of Surfactants: It is known that the surfactant solutions exhibit a slower evaporation rate than pure water at the same conditions. In our case we have used anionic sodium dodecyl sulfate (SDS). The concentration of SDS in the solution was.

Tilt angle:

The basic idea behind the inclination of the box is a deformation of the suspension droplet such that nucleation starts at the upper edge of the droplet and crystal growth proceeds downwards in a defined direction. The droplet deformation gives a lower limit of the inclination angle. An upper limit is given by the following: in the case of a contact angle hystereses, capillary forces compete with gravity and a droplet can remain stuck on a tilted surface without sliding [30]. Between these two limits, which were 3^0 and 15^0 in our experiments, we could not find any dependence of crystal quality and size on the tilt angle.

Evaporation rate:

Another physical parameter is the evaporation rate of the dispersion medium which is assumed to be water from here on. It is directly proportional to the vapour pressure and depends exponentially on temperature: $p \sim \exp(W/k_B T)$, where W denotes the molar evaporation energy. In general, lower evaporation rates, i.e., lower temperatures, favours larger crystallites. This dependency was extensively studied in [31]. Rapid evaporation shortens the interval during which the particles are mobile and leads to smaller crystallites.

Interactions in colloids:

Forces acting on colloids in solutions have been studied over several decades and are described in detail in the literature [32]. Despite the good understanding of individual forces in simple two-body systems, overall complex interactions in many-body systems are still too difficult to be precisely calculated, especially if long-range forces, i.e. acting on distances several times bigger than dispersed media, are involved. The behavior of spheres on the water surface is determined by the interaction potential of the spheres. The interactions of PS spheres at the interface arise due to attractive and repulsive forces and the interaction potential is determined by the sum of all potentials acting in the system (van-der-Waals, electrostatic, double layer, capillary etc.) The forces acting on the PS spheres are influenced by the following factors:

• Residual surfactant, initiator, monomer or other impurities, adsorbed on the PS latex after synthesis.
• Charge on the surface (i.e. type and surface density of functionalities on the PS sphere).
• The degree of diffusion of the dispersing medium into PS spheres.
• PS latex surface roughness.
• Ionic strength.
• Surface tension.

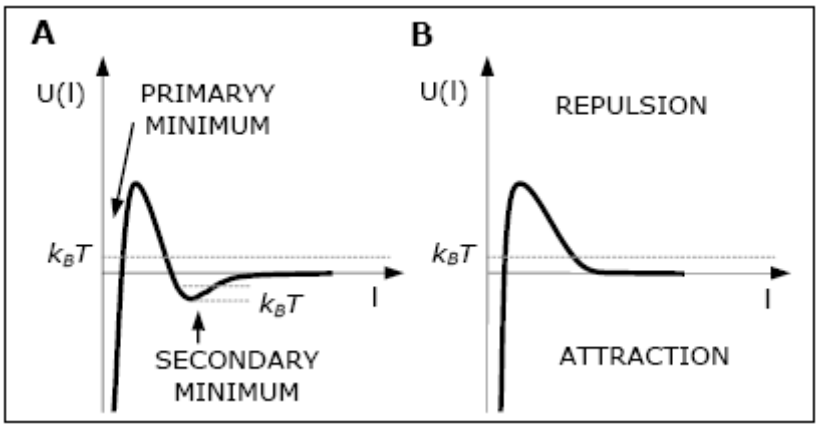

Figure 2.29 Examples of interaction energy potentials U versus separation l between two spheres trapped at air-water interface. A) Potential with two energy minima, B) Potential with one energy minimum. (k_BT is thermal energy at room temperature).

Crystallization and increase of the density of monolayer require the interaction potential to have deep potential minimum, marked as primary minimum, and one big energy barrier (figure 2.29). The interaction potential presented in figure 2.29A has the secondary shallow minimum, which can trap a sphere weakly. The primary energy minimum is many times deeper than the Boltzmann energy k_BT at room temperature. Therefore, when interfacial spheres approaching each other overcome the energy barrier between the two minima, they will experience strong attractions and coagulate. If spheres are to be arranged into a weakly bound colloidal crystal described by the interaction potential in figure 2.29A or a "two-dimensional gas of spheres" described by the

interaction potential in figure 2.29B, the energy barrier in both cases has to be bigger than the kinetic energy carried by the momentum of the dispersing spheres. In case of interaction potential (A) floating spheres self-assemble due to attraction caused by the secondary shallow energy minimum creating loosely packed crystal. In case of potential interaction (B), floating spheres repel each other creating "2D gas of spheres" which can be compressed into a monolayer by continuous distribution of spheres until the entire area of the interface is covered. Situations described by interaction potentials (A) and (B) are suitable for mask preparation, because the spheres can move relatively and rearrange themselves from multicrystalline structure into single crystal. If the energy barrier is surmounted by the PS spheres due to collisions and Brownian motion, they end up in a stable state described by the primary minimum. The monolayer is then multicrystalline and dense, and recrystallization step cannot be realized.

Spin coating:

We have also used spin-coating technique for preparing monolayer of latex spheres of 100 nm polystyrene spheres onto the Si substrate using a spin coater. The speed of the spin-coater was 2500-3000 r.p.m and the time was 30 seconds. We have used spin-coating technique because in this case most of the area of the substrate is covered by single or by few numbers of polystyrene spheres and in rest multilayer is formed. This is well-suited for doing nanomanipulation of single sphere using Atomic Force Microscope.

II b.3 Catalytic Etching for making patterned surface

This technique is actually a deposition of metal plus wet chemical etching method [33]. Metal particles are usually deposited on the silicon wafer with oxide layer on it, and then silicon substrates covered with metal clusters are immersed into the etching solution. An etching mixture consisting of MQ water, HF, and H_2O_2 was used at room temperature. The detailed experimental procedure is given below.

(100)-oriented silicon wafers were used in the experiments. This dry deposition plus wet chemical etching method mainly consists of four steps:

(1) Silicon wafers were sequentially cleaned with acetone (5 mins), ethanol (5 mins), MQ water and boiling Piranha solution (H_2SO_4:H_2O_2 = 4:1; V/V, 1 h), rinsed thoroughly with MQ water and then RCA solution (1:1:5 (v/v/v) $NH_3/H_2O_2/H_2O$) for 1 h. Subsequently, the silicon substrate was rinsed several times with MQ water.

(2) Metal films (thickness ~ 30 nm) were deposited via thermal evaporation onto the clean silicon surface in a vacuum evaporator with degree of vacuum 1×10^{-6} mbar.

(3) Silicon wafers covered with metal clusters were immersed into the etching solution of mixed MQ water, HF and H_2O_2 in a sealed Teflon vessel, and treated for a certain time (room temperature). The concentrations of HF and H_2O_2 were 4.6 and 0.44 M, respectively.

(4) Finally, the silver film was removed by immersion in boiling aqua regia (3:1 (v/v) HCl/HNO_3) for 15 mins.

However, the role of the metal (Ag) particles and the exact mechanism of the catalytic etching process are still unclear and controversial but it is believed that microscopically local anode (Si) and cathode (metal) sites form on the etched surface with local cell

currents flowing between the sites during etching. In analogy with the pioneering studies of Si etching, [34, 35] the following mechanism is proposed:
Cathode reaction (at metal):
$H_2O_2+2H^+ \rightarrow 2H_2O+2H^+$,
$2H^++2e^- \rightarrow H_2\uparrow$,
Anode reaction:
$Si+4H^++4HF \rightarrow SiF_4+4H^+$,
$SiF_4+2HF \rightarrow H_2SiF_6$,
Overall reaction:
$Si+H_2O_2+6HF \rightarrow 2H_2O+H_2SiF_6+H_2\uparrow$.
A critical feature of this reaction scheme is the generation of H^+ from H_2O_2 and the reduction of H^+ to form H_2, both of which are facilitated by the metal particles. The observation of much higher etching rates for Ag suggests a catalytic role. Finally, it is well to note that H_2O_2 is but one possible oxidant, and others may work as well or better—the key feature being the ability to generate mobile holes at the metal-solution interface.
We have used this technique to make periodic trenches on silicon surface. For this, we have first written the pattern on silicon surface by e-beam lithography (described in detail in section 2.6.2). After developing the resist was present everywhere on the substrate except on the patterns. Then a thin silver film (~ 30 nm) has been evaporated on top of it. Then the substrate has been immersed into the chemical etching solution to get the trenches. The depth of the trenches depends on the concentration of echants and how long the substrate has been immersed into the solution. Finally the silver film has been removed as stated above. Fig. 2.30 shows a SEM image of these trenches made on silicon surface by the abovementioned technique and fig. 2.30a shows the magnified SEM image of one of such trenches.

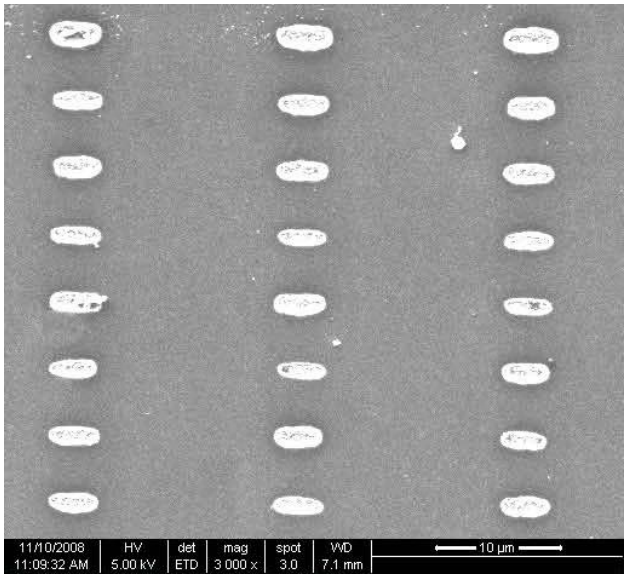

Figure 2.30 SEM image of the trenches made on silicon surface.

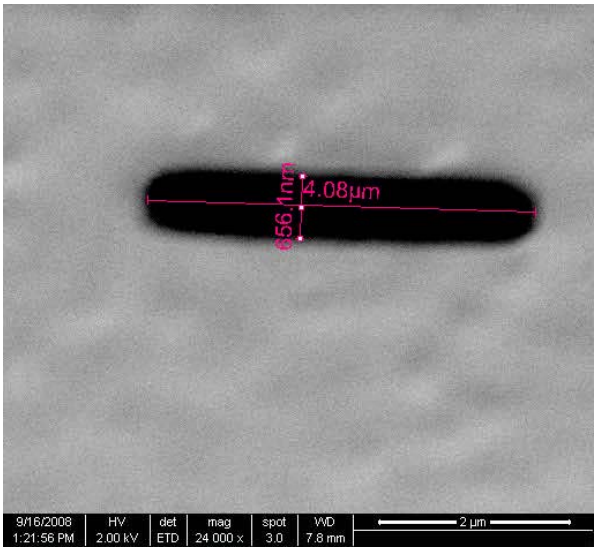

Figure 2.30 (a) Magnified SEM image of one of such trenches made on silicon surface.

II b.4 Langmuir-Blodgett Technique for Thin film preparation

The Langmuir-Blodgett (LB) technique, first introduced by Irving Langmuir and applied extensively by Katharine Blodgett, involves the vertical movement of a solid substrate through the monolayer/air interface. The surface pressure and temperature of the monolayer are first controlled so that the organic film is in a condensed and stable state. If the surface pressure versus area measurements is undertaken at several temperatures, and the points corresponding to the same phase transitions are plotted on a pressure versus temperatures diagram, the resulting diagram will show the range of temperature and pressures over which the various phases exist. The phase diagram (different states) of n-docosanoic acid (behenic acid) is shown in fig. 2.31.

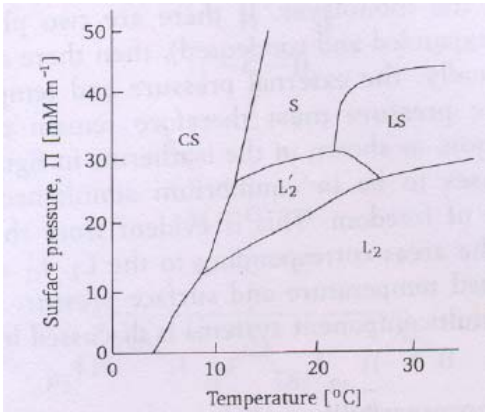

Figure 2.31 Surface pressure versus temperature phase diagram for n-docosanoic acid

The nature of phase diagrams for monolayer-forming materials has very important implications for the control of variables such as temperature and surface pressure in

monolayer experiments (and for the transfer of monolayer to solid supports). For instance, if a monolayer is controlled so that it is in a condensed phase that is very close to a phase boundary in the phase diagram, a small change in either temperature or surface pressure may alter the state of the floating layer, affecting the deposition characteristics of the monolayer on solid supports. For fatty acid type materials, deposition generally proceeds from either the L_2', LS or S phase (with surface pressures in the range 20-40 mNm^{-1} and temperatures 15-20^0C). However, it is also possible to start from one of the other monolayer states. The molecular organization in the resulting LB film will depend on these initial conditions.

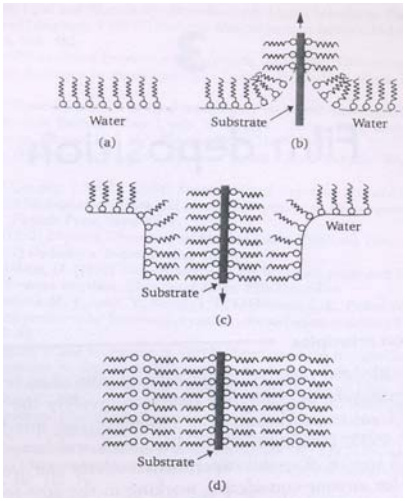

Figure 2.32 Y-type Langmuir-Blodgett film deposition

Fig.2.32 shows the commonest form of LB film deposition. The substrate is hydrophilic and the first monolayer is transferred as the substrate is raised through the water. The substrate may therefore be placed in the subphase before the monolayer is spread. Subsequently, a monolayer is deposited on each traversal of the monolayer/air interface. As shown, these stack in a head-to-head and tail-to-tail pattern; this deposition mode is called the Y-type. Although this is the most frequently encountered situation, instances in which the floating monolayer is only transferred to the substrate as it is being inserted into the subphase, or only as it is being removed, are often observed. These deposition modes are called X-type (monolayer transfer on the downstroke only) and Z-type (transfer on the upstroke only) and are illustrated in fig 2.33.

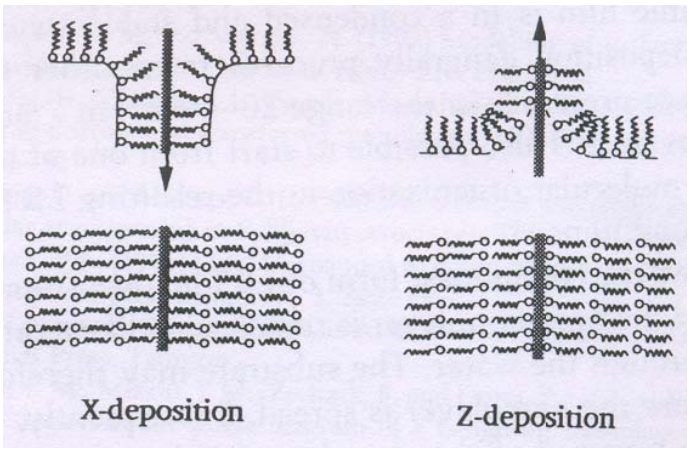

Figure 2.33 X-type and Z-type Langmuir-Blodgett film depositions.

Film transfer is characterized by measurement of the deposition ratio τ (also called the transfer ratio). This is the decrease in the area occupied by the monolayer (held at constant pressure) on the water surface divided by the coated area of the solid substrate, i.e., $\tau=A_L/A_S$, where A_L is the decrease in the area occupied by the monolayer on the water surface and A_S is the coated area of the solid substrate.

Langmuir-Blodgett Trough and Compression System

In the simplest type of equipment, the trough forms an integral part of the monolayer barrier. The principle of operation is shown in fig. 2.34(a). The barrier may be moved via a suitable gearing system to an electric motor. Most of the trough need not be very deep (a few millimeters) as a 'well' can allow for the transfer of the floating layer onto a

(a)

Figure 2.34 (a) Simple LB trough with a single movable barrier.

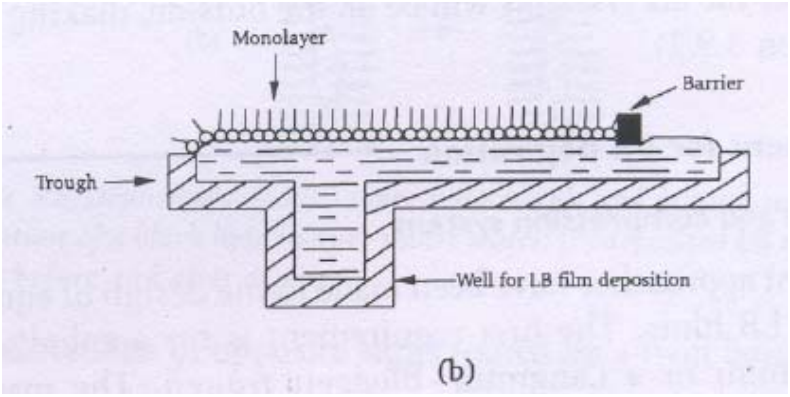

Figure 2.34 (b) Cross-section of a trough with a well to facilitate LB film deposition.

substrate (fig.2.34 (b)). Most LB troughs are based on rectangular geometries, but systems designed in a circular fashion are also used. The material (PTFE) used for all parts of the trough that come into direct contact with the subphase should be inert and able to withstand the organic solvents used for monolayer spreading and cleaning.
The most common method for monitoring the surface pressure is the Wilhelmy plate. The sensitivity of this method is ~10^{-3} mNm^{-1}. An absolute measurement of π is made by suspending a plate from a sensitive balance in the monolayer. Fig. 2.35 shows the experimental arrangement. The forces acting on the plate are due to gravity and surface tension downwards and buoyancy, due to displaced water, upwards. For a rectangular plate of dimensions l, w and t and of material of density ρw immersed to a depth h in a liquid of density ρL, the net downward force F is given by

$$F=\rho wgl\omega t+2\gamma(t+\omega)\cos\theta-\rho Lgt\omega h \qquad 2.20$$

where γ is the surface tension of the liquid, θ is the contact angle on the solid plate and g is the gravitational constant. The usual procedure is to choose a plate that is completely wetted by the liquid (i.e., $\theta=0$) and measure the change in F for a stationary plate. The change in force ΔF is then related to the change in surface

$$\Delta\gamma=\Delta F(t+\omega)/2 \qquad 2.21$$

If the plate is thin, so that $t<<\omega$

$$\Delta\gamma=\Delta F\omega/2 \qquad 2.22$$

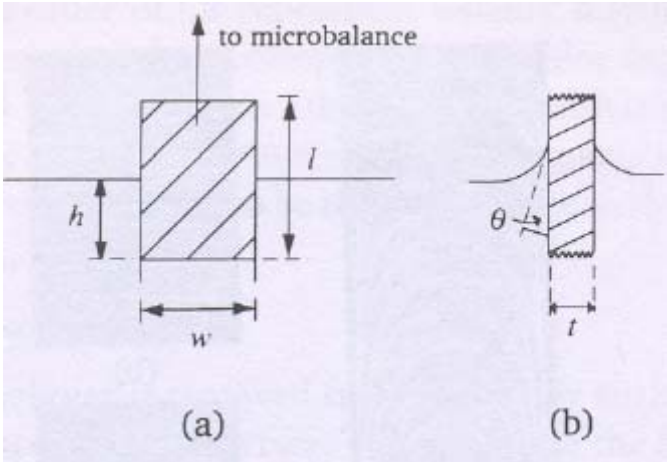

Figure 2.35 A Wilhelmy plate (a) front view (b) side view

We have used Langmuir-Blodgett trough from Apex Instruments Co. [36] for preparing atomically smooth thin films of metal arachidates (Ni^{2+}, Cd^{2+}, Zn^{2+}).

II b.5 Thermal evaporation

This section focuses on the deposition of thin films by evaporation in vacuum as the means. The objective of this deposition process is to controllably transfer atoms from a heated source to a substrate located a distance away, where film formation and growth proceed atomistically. Quite simply, thermal energy is imparted to atoms in a liquid or solid source such that their temperature is raised to the point where they either efficiently evaporate or sublime. Advances in the development of vacuum pumping equipment and the fabrication of suitable Joule heating sources, first made from platinum and then tungsten wire, spurred the progress of evaporation technology. Scientific interest in the phenomenon of evaporation and the properties of thin metal films was soon followed by industrial production of optical components such as mirrors and beam splitters, and later of antireflection coatings. Higher deposition rates, better vacuum and cleaner environments for film formation and growth, and general applicability to all classes of materials were among the reasons for the ascendancy of evaporation methods.

Evaporation Rate

Early attempts to quantitatively interpret evaporation phenomena are associated with the names of Hertz and Knudsen and, later, Langmuir [37]. Based on experimentation on the evaporation of mercury, Hertz in 1882 observed that evaporation rates were:
1. Not limited by insufficient heat supplied to the surface of the molten evaporant.
2. Proportional to the difference between the equilibrium pressure, P_e, of Hg at the given temperature and the hydrostatic pressure, P_h, acting on the evaporant.
He concluded that a liquid has a specific ability to evaporate at a given temperature. Furthermore, the maximum evaporation rate is attained when the number of vapor molecules emitted corresponds to that required to exert the equilibrium vapor pressure

while none return. These ideas led to the basic equation for the rate of evaporation from both liquid and solid surfaces, namely,

$$\varphi_e = \frac{\alpha_e N_A (P_e - P_h)}{(2\pi MRT)^{\frac{1}{2}}} \qquad 2.23$$

where φ_e is the evaporation flux in number of atoms (or molecules) per unit area, per unit time, and α_e is the coefficient of evaporation, which has a value between 0 and 1. When $\alpha_e = 1$ and P_h is zero, the maximum evaporation rate is realized. An expression for the maximum value of φ_e is

$$\varphi_e = \frac{3.513X10^{22}}{(MT)^{\frac{1}{2}}} P_e \quad \text{molecules/cm}^2\text{-s} \qquad 2.24$$

When P_e is expressed in torr, a useful variant of this formula is

$$\Gamma_e = 5.84X10^{-2}(M/T)^{\frac{1}{2}} P_e \quad \text{gm/cm}^2\text{-s}, \qquad 2.25$$

where Γ_e is the mass evaporation rate. At a pressure of 10^{-2} torr, a typical value of Γ_e for many elements is approximately 10^{-4} grams per second per cm^2 of evaporant area. The key variable influencing evaporation rates is temperature since it has a profound effect on equilibrium vapor pressures.

Vapor Pressure of the Elements

A convenient starting point for expressing the connection between temperature and vapor pressure is the Clausius-Clapyeron equation, which for both solid-vapor and liquid-vapor equilibria can be written as

$$\frac{dP}{dT} = \frac{\Delta H(T)}{T\Delta V} \qquad 2.26$$

The changes in enthalpy, $\Delta H(T)$, and volume, ΔV, refer to differences between the vapor (v) and the particular condensed phase (c) from which it originates, while T is the transformation temperature in question. Since $\Delta V = V_v — V_c$, and the volume of vapor normally considerably exceeds that of the condensed solid or liquid phase, $\Delta V \cong V_v$. If the gas is assumed to be perfect, $V_v = RT/P$, and eq. 2.26 may be rewritten as

$$\frac{dP}{dT} = \frac{P\Delta H(T)}{RT^2} \qquad 2.27$$

As a first approximation, $\Delta H(T) = \Delta H_e$, the molar heat of evaporation (a constant), in which case simple integration yields

$$\ln P \cong -\frac{\Delta H_e}{RT} + I \qquad \text{or} \qquad P = P_0 \exp -\frac{\Delta H_e}{RT} \qquad 2.28$$

where I (or P_0 = expI) is the constant of integration. Through substitution of the latent heat of vaporization ΔH_v for ΔH_e, the boiling point for T, and 1 atm for P, the value of I can be determined for the liquid-vapor transformation. For practical purposes eq. 2.28 adequately describes the temperature dependence of the vapor pressure in many materials. It is rigorously applicable over only a small temperature range, however. To extend the range of validity, the temperature dependence of $\Delta H(T)$ must be taken into account. For example, careful evaluation of thermodynamic data reveals that the vapor pressure of liquid Al is given by [37]

$$\log P(\text{torr}) = -15{,}993/T + 12.409 - 0.999\log T - 3.52X10^{-6}T \qquad 2.29$$

The Arrhenius character of log P vs 1/T is essentially preserved by the first two terms on the right-hand side while the remaining terms are small corrections.
Vapor-pressure data for many other metals have been similarly obtained and conveniently represented as a function of temperature in fig. 2.36 [38]. Similarly, vapor-pressure data for elements important in the deposition of semiconductor films are presented in fig. 2.37 [39]. Many of the data represent direct measurements of the vapor pressures. Other values are inferred indirectly from thermodynamic relationships

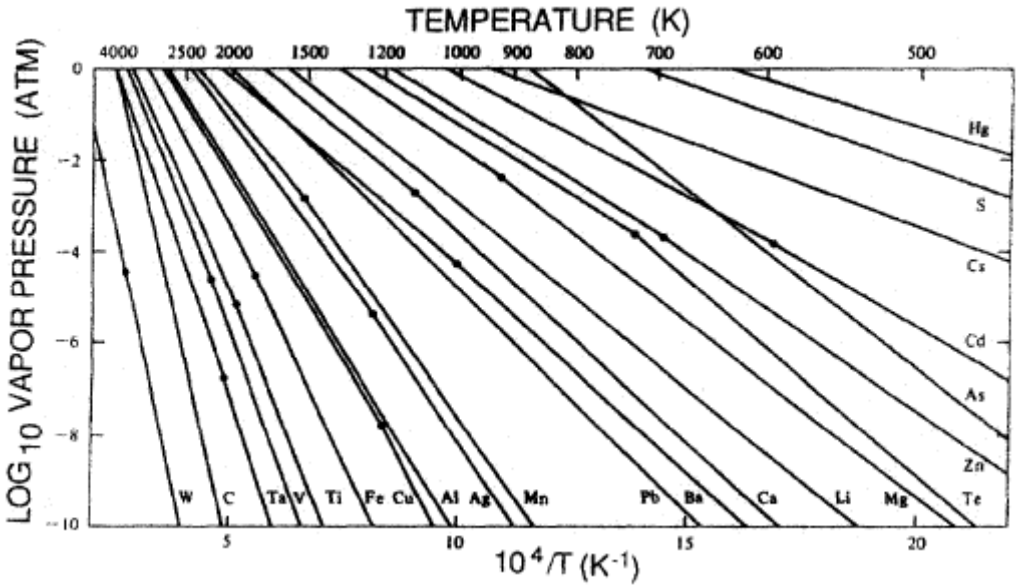

Figure 2.36 Vapor pressures of selected elements. Dots correspond to melting points [38].

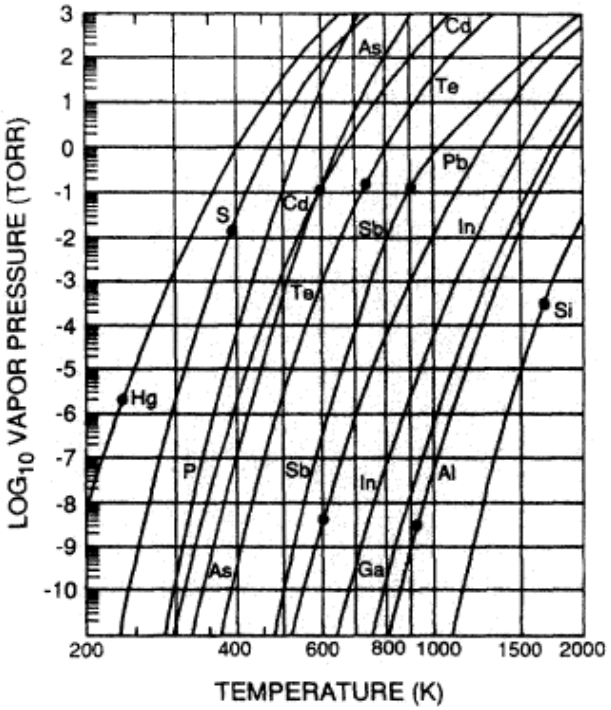

Figure 2.37 Vapor pressures of elements employed in semiconductor materials. Dots correspond to melting points [39].

and identities using limited experimental data. Thus the vapor pressures of many refractory metals can be unerringly extrapolated to lower temperatures even though it may be impossible to measure them directly. For this to be practical the thermodynamic data that are available must be accurate.

Two modes of evaporation can be distinguished in practice depending on whether the vapor effectively emanates from a liquid or solid source. As a rule of thumb, a melt will be required if the element in question does not achieve a vapor pressure greater than 10^{-3} torr at its melting point. Most metals fall into this category and effective film deposition is attained only when the source is molten. On the other hand, elements such as Cr, Ti, Mo, Fe, and Si reach sufficiently high vapor pressures below the melting point and, therefore, sublime.

Deposition Geometry

Deposition of thin films involves consideration of both the source of evaporant atoms and the substrates upon which they impinge. Source-substrate geometry, in turn, influences film uniformity, a concern of paramount importance that will be treated subsequently. Evaporation from a point source is the simplest of situations to model. In this case evaporant particles are imagined to originate from an infinitesimally small region (dA_e) of a spherical source of surface area A_e with a uniform mass evaporation rate as shown in fig. 2.38a. The total evaporated mass M_e is then given by the double integral

$$M_e = \int_0^t \int_{A_e} \Gamma_e \, dA_e \, dt \qquad 2.30$$

Of this amount, mass dM_s falls on the substrate of area dA_s. Since the projected area dA_s on the surface of the sphere is dA_e, with $dA_c = dA_s \cos\theta$, the proportionality holds that $dM_s:M_e = dA_c:4\pi r^2$. Finally,

$$\frac{dM_s}{dA_s} = \frac{M_e \cos\theta}{4\pi r^2} \qquad 2.31$$

is obtained where θ is the angle between the vector from the origin to the planar substrate and the vector representing the substrate normal. On a per-unit time basis the film deposition rate R (atoms/cm^2-s) is a term that has the same units as φ. The deposition

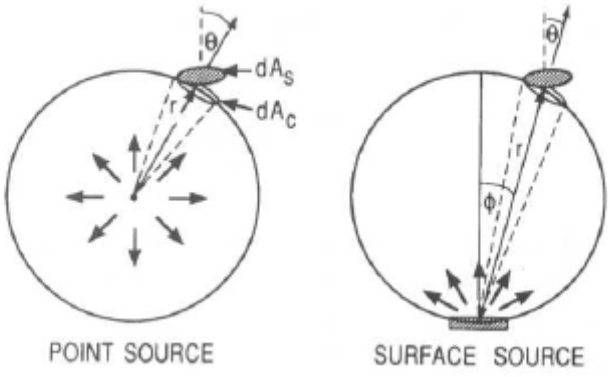

Figure 2.38 Evaporation from (a) point source, (b) surface source.

varies with the geometric orientation of the substrate and with the inverse square of the source-substrate distance. Substrates placed tangent to the surface of the receiving sphere would be coated uniformly irrespective of placement since θ = 0 and cosθ=1.

An evaporation source employed in the pioneering research by Knudsen made use of an isothermal enclosure with a very small opening through which the evaporant atoms or molecules effused. These effusion or Knudsen cells are frequently employed in molecular-beam epitaxy deposition systems where precise control of evaporation variables is required. Kinetic theory predicts that the molecular flow of the vapor through the hole is directed according to a cosine distribution law, and this has been verified experimentally. The mass deposited per unit area is therefore given by

$$\frac{dM_s}{dA_s} = \frac{M_e \cos\phi\cos\theta}{\pi r^2} \qquad 2.32$$

and is now dependent on two angles that are defined in fig. 2.38b. These correspond to the evaporant emission angle ϕ and the deposition or receiving angle θ. Evaporation from an extended area or surface source is also modeled by eq. 2.32. Physically, the extended source is a superposition of many point sources that strongly contribute to the vapor stream where ϕ is close to zero degrees, accounting for the vertically directed lobe-shaped emission; however, in the ϕ= 90° direction there is no emission. Boat filaments

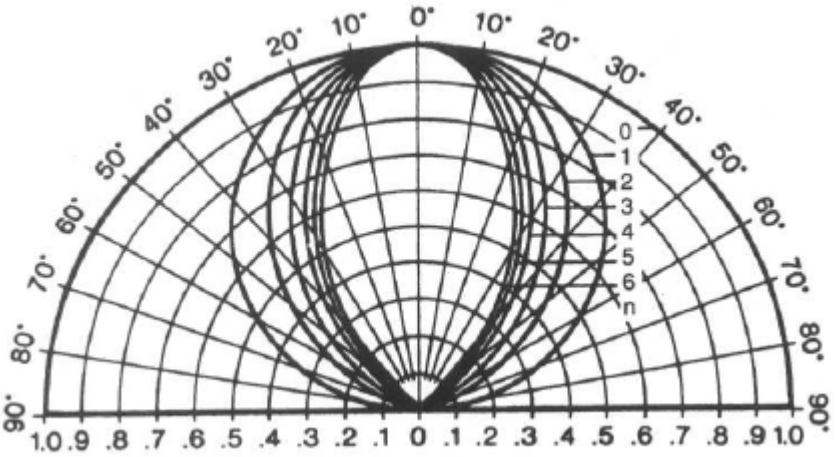

Figure 2.39 Calculated lobe-shaped vapor clouds with various cosine exponents. [46]

and wide crucibles containing a pool of molten material to be evaporated approximate surface sources in practice.

From careful measurements of the angular distribution of film thickness, it has been found that rather than a $\cos\phi$ dependence, a $\cos^n\phi$ evaporation law is more realistic in many cases. As shown in fig. 2.39, n is a number that determines the geometry of the lobe-shaped vapor cloud and the angular distribution of evaporant flux from such sources. When n is large, the vapor flux is highly directed. Physically n is related to the evaporation crucible geometry and scales directly with the ratio of the melt depth (below top of crucible) to the melt surface area. Deep, narrow crucibles with large n have been employed to confine evaporated radioactive materials to a narrow angular spread in order to minimize chamber contamination. The corresponding deposition equation for such sources is [40]

$$\frac{dM_s}{dA_s} = \frac{M_e(n+1)\cos^n\phi\cos\theta}{2\pi r^2}, \qquad n \geq 0 \qquad 2.33$$

As the source becomes increasingly directional, the receiving surface area effectively exposed to evaporant shrinks (i.e., $4\pi r^2$, πr^2, and $2\pi r^2/(n+1)$ for point, $\cos\phi$, and $\cos^n\phi$ sources, respectively).

Electrically Heated Evaporation Sources

This section describes some of the hardware and techniques used to electrically heat sources for the efficient evaporation of thin films. Discussed are the widely used resistance, induction, and electron-beam heating methods. The overwhelming bulk of evaporated thin films deposited commercially for electrically, optically, and mechanically functional applications are deposited by these methods or variants of them. The first sources used to heat evaporants relied on the Joule heating of metal filaments. Clearly, such heaters must reach the temperature of the evaporant in question while having a negligible vapor pressure in comparison. Ideally, they should not contaminate, react with, or alloy with the evaporant, or release gases such as oxygen, nitrogen, or hydrogen at the evaporation temperature. These requirements have led to the development and use of

resistance-heated evaporation sources used singly or with inert oxide or ceramic-compound crucibles. Some of these are shown in fig. 2.40. They can be divided into the following important categories.

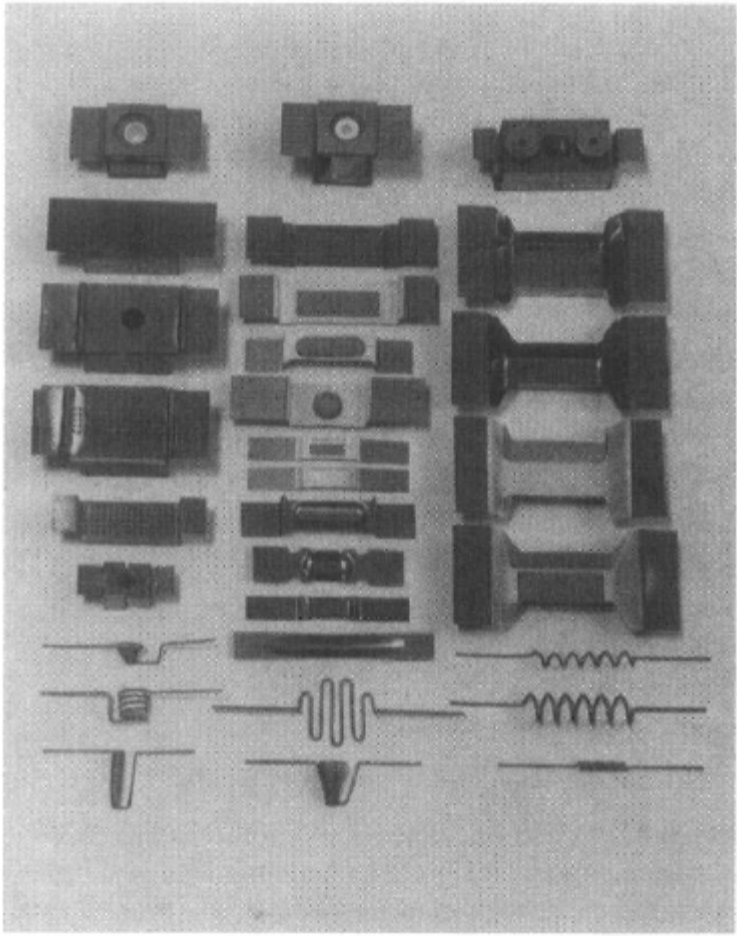

Figure 2.40 Assorted resistance heated evaporation sources. (Courtesy of R. D, Mathis Company)

Tungsten Wire Sources

These sources are in the form of individual or multiply stranded wires twisted into helical or conical shapes. Helical coils are used for metals that wet tungsten readily; the conical baskets are better adapted to contain poorly wetting materials. In the former case, metal evaporant wire is wrapped around or hung from the tungsten strands and the molten beads of metal are retained by surface tension forces. Tungsten filaments can be operated up to about 2200 K before they begin to fail rapidly.

Refractory Metal Sheet Sources

Tungsten, tantalum, and molybdenum sheet metal sources, like the wire filaments, are self-resistance heaters that require low-voltage, high-current power supplies. These sources have been fabricated into a variety of shapes including the dimpled strip, boat, canoe, and deep-folded configurations. Deep-folded boat sources have been used to evaporate MgF_2 and powder mixtures of metals and metal oxides for coating ophthalmic lenses in batch-type evaporators. Other than the abovementioned sources there are sublimation furnaces and crucible sources which are used as evaporation sources.
We have used evaporation system from Hind High Vacuum Co. (P) LTD. [41] (Model – 12" MSPT) to evaporate silver and gold on silicon substrate and glass substrate for making conducting surfaces.

II c. Other Techniques used

II c.1 Scanning Electron Microscope

Basic principle of Scanning Electron Microscope:

The scanning electron microscope (SEM) is a type of electron microscope that images the sample surface by scanning it with a high-energy beam of electrons in a raster scan pattern. The electrons interact with the atoms that make up the sample producing signals which contain information about the sample's surface topography, composition and other properties such as electrical conductivity. An electron microscope uses a focused beam of electrons to obtain much higher magnification than is possible on conventional light microscopes. This increase in magnification is possible because the wavelength of a high-speed electron is much lower than that of visible light, and so much higher resolution can be obtained. Of course, optics must be employed to reach this magnification, just like the light microscope. Basic physics explains how a magnetic field will bend the path of an electron, so electromagnets are used to focus the beam. A schematic diagram of the Scanning Electron Microscope column, electron beam formation and ray path are shown in fig. 2.41(a), (b) and (c) respectively.

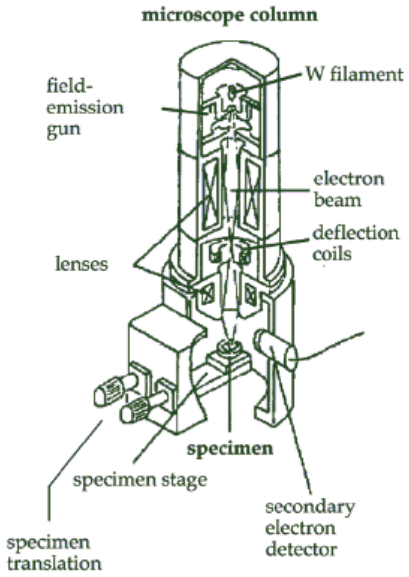

Figure2.41(a) A schematic diagram of Scanning Electron Microscope column

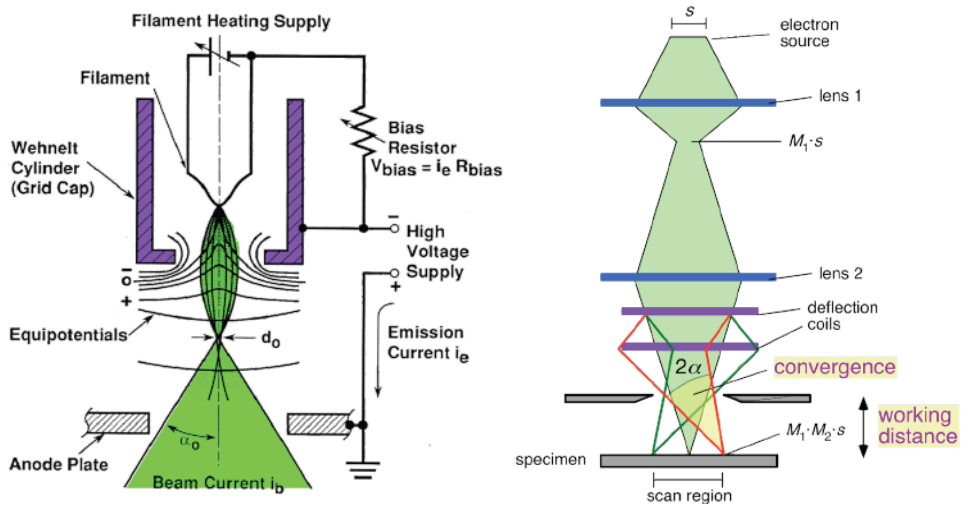

Figure2.41 (b) A schematic diagram of electron beam formation and (c) ray path.

The types of signals produced by an SEM include secondary electrons, back scattered electrons (BSE), characteristic x-rays, light (cathodoluminescence), specimen current and transmitted electrons. These types of signal all require specialized detectors for their detection that are not usually all present on a single machine. The signals result from interactions of the electron beam with atoms at or near the surface of the sample. In the most common or standard detection mode, secondary electron imaging or SEI, the SEM can produce very high-resolution images of a sample surface. A wide range of magnifications is possible, ranging from about x 25 (about equivalent to that of a powerful hand-lens) to about x 250,000, about 250 times the magnification limit of the best light microscopes. Back-scattered electrons (BSE) are beam electrons that are

reflected from the sample by elastic scattering. BSE are often used in analytical SEM along with the spectra made from the characteristic x-rays. Because the intensity of the BSE signal is strongly related to the atomic number (Z) of the specimen, BSE images can provide information about the distribution of different elements in the sample. Characteristic X-rays are emitted when the electron beam removes an inner shell electron from the sample, causing a higher energy electron to fill the shell and release energy. These characteristic x-rays are used to identify the composition and measure the abundance of elements in the sample.
We have used Scanning Electron Microscope from FEI [42] (Model No. Quanta 200) for characterizing the samples prepared by hard-sphere lithography. We have also used it for the dimensional analysis of the cantilevers that we have used for our experiments for Atomic Force Spectroscopy. Figure 2.42 shows a SEM image of the 100 nm PS sphere spin-coated on Si surface.

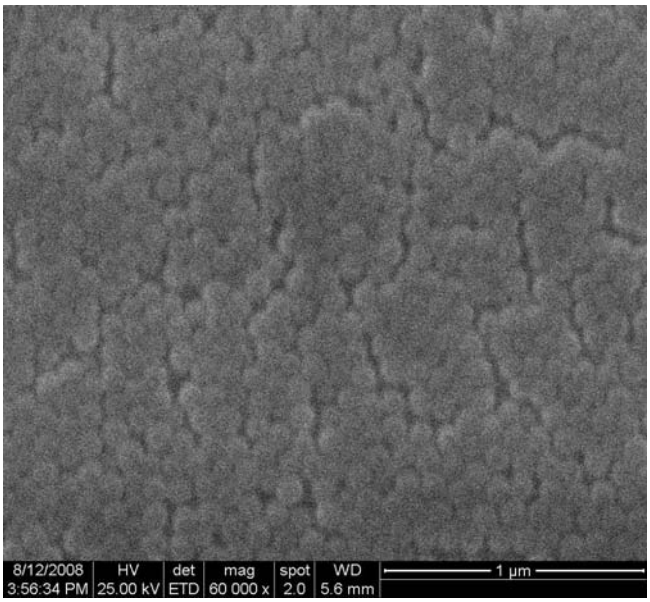

Figure 2.42 SEM image of the 100 nm PS spheres spin-coated on Si surface

II c.2 Electron Beam Lithography:

Electron beam lithography (often abbreviated as e-beam lithography) is the practice of scanning a beam of electrons in a patterned fashion across a surface covered with a film (called the resist), ("exposing" the resist) and of selectively removing either exposed or non-exposed regions of the resist ("developing"). The purpose is to create very small structures in the resist that can subsequently be transferred into another material f or a number of purposes, for example for the creation of very small electronic devices. The primary advantage of electron beam lithography is that it is one of the ways to beat the diffraction limit of light and make features in the nanometer regime. This form of maskless lithography has found wide usage in mask-making used in photolithography, low-volume production of semiconductor components, and research and development. On the other hand, the key limitation of electron beam lithography is throughput, i.e., the

very long time it takes to expose an entire silicon wafer or glass substrate. A long exposure time leaves the user vulnerable to beam drift or instability which may occur during the exposure. Also, the turn-around time for reworking or re-design is lengthened unnecessarily if the pattern is not being changed the second time. The minimum time to expose a given area for a given dose is given by the following formula:

Dose * exposed area = beam current * exposure time = total charge of incident electrons

For example, assuming an exposure area of 1 cm^2, a dose of 10^{-3} Coulombs/cm^2, and a beam current of 10^{-9} Amperes, the resulting minimum write time would be 10^6 seconds (about 12 days). This minimum write time does not include time for the stage to move back and forth, as well as time for the beam to be blanked (blocked from the wafer during deflection), as well as time for other possible beam corrections and adjustments in the middle of writing. To cover the 700 cm^2 surface area of a 300 mm silicon wafer, the minimum write time would extend to $7X10^8$ seconds, about 22 years. This is a factor of about 10 million times slower than current optical lithography tools. It is clear that throughput is a serious limitation for electron beam lithography, especially when writing dense patterns over a large area.

Patterning of Electron Sensitive Resists

Electron beam lithography is carried out on electron-sensitive resist materials such as the polymer, PMMA. Solutions of the resist are spin-coated onto a sample and baked to leave a hardened thin-film on the surface of sample. The EBL system is then used to move a focused electron beam across the sample to selectively expose a pattern in the resist previously designed with the system´s in-built CAD tools. Exposure of a positive tone resist such as PMMA to electrons causes fragmentation of the polymer chain into smaller molecular units in a process known as chain-scission. A suitable developer solution can then be used to selectively dissolve the fragmented polymer chains in the exposed areas of resist, whereas as the unexposed resist remains insoluble in the developer solution. The process therefore leaves a patterned resist mask on the sample that can be used for further processing on the sample. The resulting pattern in the resist can be transferred into the sample using either metal lift-off or etching. Reactive ion etching (RIE) or inductively coupled plasma (ICP) etching is generally preferred over wet chemical etching for e-beam lithography applications since it maintains the small feature sizes produced in the resist.

Electron trajectories in resist:

An incident electron (purple in fig. 2.43) produces secondary electrons (blue in fig. 2.43). Sometimes, the incident electron may itself be backscattered as shown here and leave the surface of the resist (amber).

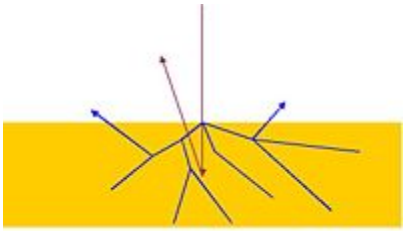

Figure 2.43 Electron trajectories in resist

The primary electrons in the incident beam lose energy upon entering a material through inelastic scattering or collisions with other electrons. In such a collision the momentum transfer from the incident electron to an atomic electron can be expressed as $dp = 2e^2 /bv$, where b is the distance of closest approach between the electrons, and *v* is the incident electron velocity. The energy transferred by the collision is given by $T = (dp)^2 / 2m = e^4 / Eb^2$, where m is the electron mass and E is the incident electron energy, given by $E = (1 / 2)mv^2$. By integrating over all values of T between the lowest binding energy, E_0, and the incident energy, one obtains the result that the total cross section for collision is inversely proportional to the incident energy E, and proportional to $1/E_0 - 1/E$. Generally, $E >> E_0$, so the result is essentially inversely proportional to the binding energy.

By using the same integration approach, but over the range $2E_0$ to E, one obtains by comparing cross-sections that half of the inelastic collisions of the incident electrons produce electrons with kinetic energy greater than E_0. These secondary electrons are capable of breaking bonds (with binding energy E_0) at some distance away from the original collision. Additionally, they can generate additional, lower energy electrons, resulting in an electron cascade. Hence, it is important to recognize the significant contribution of secondary electrons to the spread of the energy deposition.

Resolution capability

With today's electron optics, electron beam widths can routinely go down to a few nm. This is limited mainly by aberrations and space charge. However, the feature resolution limit is determined not by the beam size but by forward scattering (or effective beam broadening) in the photoresist while the pitch resolution limit is determined by secondary electron travel in the photoresist. This point is driven home by the 2007 demonstration of double patterning using electron beam lithography in the fabrication of 15 nm half-pitch zone plates. Although a 15 nm feature was resolved, a 30 nm pitch was still difficult to do, due to secondary electrons scattering from the adjacent feature. The use of double patterning allowed the spacing between features to be wide enough for the secondary electron scattering to be significantly reduced. The forward scattering can be decreased by using higher energy electrons or thinner photoresist, but the generation of secondary electrons is inevitable. The travel distance of secondary electrons is not a fundamentally derived physical value, but a statistical parameter often determined from many experiments or Monte Carlo simulations down to < 1 eV. This is necessary since the energy distribution of secondary electrons peaks well below 10 eV. Hence, the resolution

limit is not usually cited as a well-fixed number as with an optical diffraction-limited system. Repeatability and control at the practical resolution limit often require considerations not related to image formation, e.g., photoresist development and intermolecular forces.

Proximity effect

The smallest features produced by electron beam lithography have generally been isolated features, as nested features exacerbate the proximity effect, whereby electrons from exposure of an adjacent region spill over into the exposure of the currently written feature, effectively enlarging its image, and reducing its contrast, i.e., difference between maximum and minimum intensity. Hence, nested feature resolution is harder to control. For most resists, it is difficult to go below 25 nm lines and spaces, and a limit of 20 nm lines and spaces has been found. Proximity effects (due to electron scattering) can be reduced by solving the inverse problem and calculating the exposure function that leads to a dose distribution as close as possible to the desired dose when convolved by the scattering distribution point spread function.

Charging

Since electrons are charged particles, they tend to charge the substrate negatively unless they can quickly gain access to a path to ground. For a high-energy beam incident on a silicon wafer, virtually all the electrons stop in the wafer where they can follow a path to ground. However, for a quartz substrate such as a photomask, the embedded electrons will take a much longer time to move to ground. Often the negative charge acquired by a substrate can be compensated or even exceeded by a positive charge on the surface due to secondary electron emission into the vacuum. The presence of a thin conducting layer above or below the resist is generally of limited use for high energy (50 keV or more) electron beams, since most electrons pass through the layer into the substrate. The charge dissipation layer is generally useful only around or below 10 keV, since the resist is thinner and most of the electrons either stop in the resist or close to the conducting layer.

The range of low-energy secondary electrons (the largest component of the free electron population in the resist-substrate system) which can contribute to charging is not a fixed number but can vary from 0 to as high as 50 nm. Hence, resist-substrate charging is not repeatable and is difficult to compensate consistently. Positive charging is more tolerable than negative charging, because the latter can deflect the electron beam away from the desired exposure location.

We have used Scanning Electron Microscope from FEI [48] (Model No. Quanta 200) for electron beam lithography also. We have used two positive photoresists PMMA (350K) and PMAA (950K) for our work. First we have spin cast PMAA (350K) at 3000 r.p.m. for 40 seconds on cleaned silicon surface and baked it at 180^0C for 3 mins. Then on top of it we have spin cast PMMA (950K) at 6000 r.p.m. for 40 seconds and baked it at120^0C

for 1 hour. Figure 2.44 shows the SEM image of the patterned generated by E-beam lithography. The parameters for writing the patterns using electron beam are mentioned below:

Filament voltage: 30 KV

Filament current: 50 µAmp

Area dose: 300 µAmp/cm^2

Spot size: 1 pico Amp.

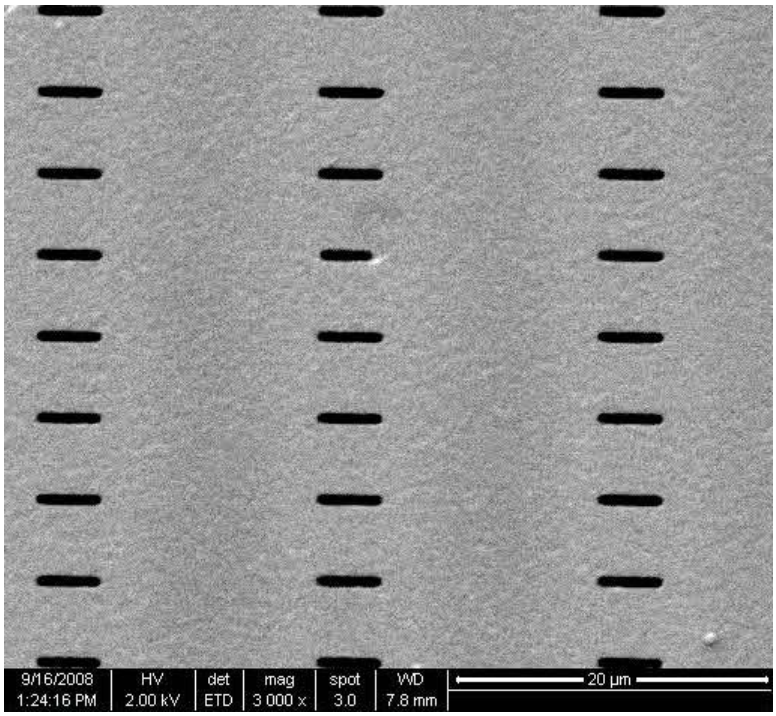

Figure 2.44 SEM image of the pattern generated by E-beam lithography

II c.3 Zeta Potential Measurement:

The zeta potential is the overall charge a particle acquires in a specific medium. It is the electrical potential that exists at the "slipping plane" of a particle, which is some small distance from its surface. In colloidal solution development of a net charge at the particle surface affects the distribution of ions in the surrounding interfacial region, resulting in an increased concentration of counter ions (ions of opposite charge to that of the particle) close to the surface**.** Thus an electrical double layer exists round each particle. Zeta Potential is a very good index of the magnitude of the interaction between colloidal particles and Zeta Potential measurements are used to assess the stability of colloidal systems. Fig. 2.45 shows a schematic diagram of Zeta potential as a function of distance from the surface.

If all the particles have a large negative or positive zeta potential they will repel each other and there is dispersion stability. If the particles have low zeta potential values then there is no force to prevent the particles coming together and there is dispersion instability. A dividing line between stable and unstable aqueous dispersions is generally taken at either +30 or -30mV. Particles with zeta potentials more positive than +30mV and more negative than -30 mV are normally considered stable as shown in fig.2.46.

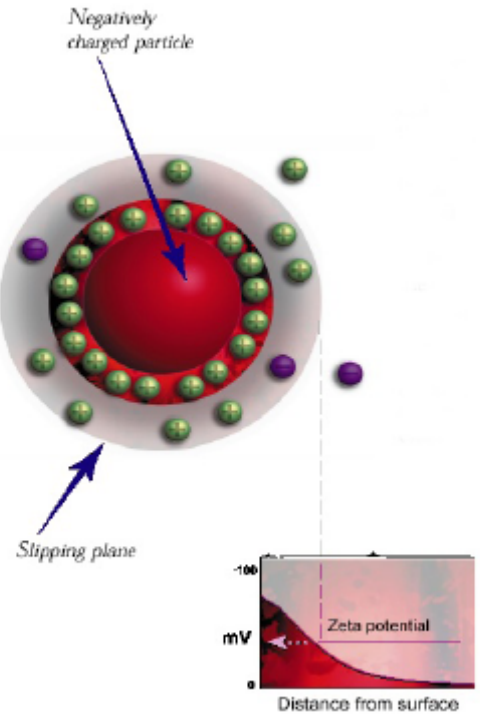

Figure 2.45 A schematic diagram of Zeta potential as a function of distance from the surface.

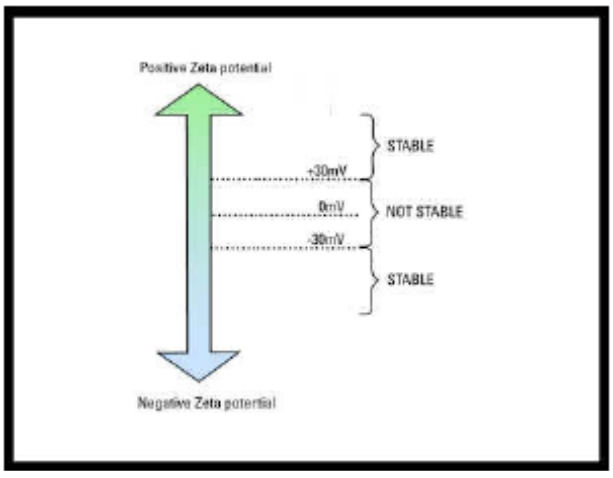

Figure 2.46 A schematic diagram of Zeta potential as a function of distance from the surface.

The most important factor that affects zeta potential is pH. A zeta potential value quoted without a definition of it's environment (pH, ionic strength, concentration of any additives) is a meaningless number. Fig. 2.47 shows the dependence of Zeta potential on pH of the solution.

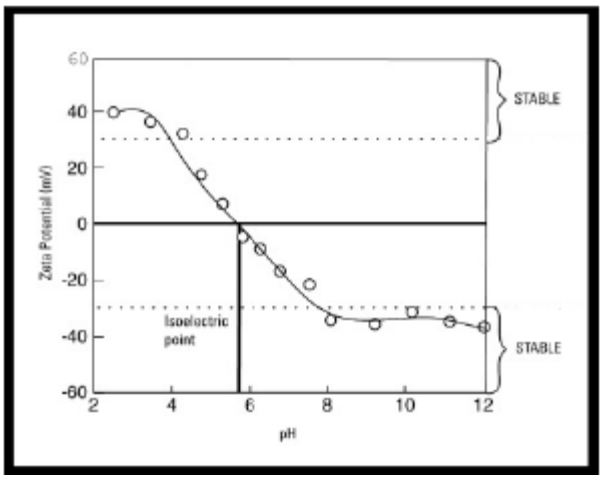

Figure 2.47 Dependence of Zeta potential on pH of the solution.

Measuring Zeta Potential:

Zeta Potential is derived from measuring the mobility distribution of a dispersion of charged particles as they are subjected to an electric field. Mobility is defined as the velocity of a particle per electric field unit and is measured by applying an electric field to the dispersion of particles and measuring their average velocity.

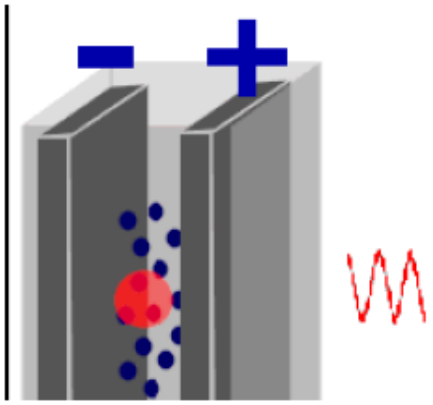

(particles and laser beam not to scale)

Figure 2.48 Charged particles in a liquid suspension can be made to move by applying an electric field to the liquid through two electrodes. By alternating the charge between the electrodes, the particles move back and forth between the electrodes at a velocity relative to their surface charge and the electrode potential. This velocity can be determined by measuring the doppler shift of laser light scattered off of the moving particles.

Depending on the concentration of ions in the diluent, either the Smoluchowski (for high ionic strengths) or Huckel (for low ionic strengths) equations are used to obtain the Zeta potential from the measured mobilities. Electrophoretic Light Scattering (ELS) is used to measure Zeta potential. To make a measurement, a small aliquot of sample is typically placed in a disposable plastic cuvette. Then the platinum electrodes are inserted. The entire cell is placed into the system. Because of the unique cell design, there is no need to align the cell to the stationary plane. After the cell is in place, a simple click of the mouse starts the measurement. Since ELS requires the use of heterodyned light, the scattered light must be properly mixed with a reference beam (split off from the incident light beam) prior to entering the detector. The software will begin a measurement by automatically adjusting the incident light intensity to optimize the mixing between the scattered light and the reference beam. Once this is completed, a reference power spectrum is measured while the electric field is off. Then the electric field is applied and another power spectrum is measured. The change in the frequency of the peak in this power spectrum when compared to the reference spectrum is the Doppler shift. The Doppler shift is used to calculate the average mobility. Using the Smoluchowski equation, the zeta potential is determined.

We have used Zeta potential measurement system Malvern Instruments Zetasizer Systems (Model No. Nano ZS [43]) for measuring the zeta potential of the Polystyrene sphere solutions. We have taken measurements on three solutions i) 1wt% of 100 nm PS solution (in water and 0.1% of SDS), ii) 1wt% of 100 nm PS solution (in water and 0.1% of SDS) mixed with methanol (1:1 volume ratio) iii) 1wt% of 30 nm PS solution (in water and 0.1% of NAN3).

Bibliography

[1] Technical Manufacturing Corporation, *http://www.techmfg.com/*
[2] S.M. Hues, C.F. Draper, K.P. Lee, R.J. Colton, Rev. Sci. Instrum. 65 (1994) 1561.
[3] T.R. Albrecht, S. Akamine, T.E. Carver, C.F. Quate, J. Vac. Sci. Technol. A 8 (1990) 3386.
[4] H.-J. Butt, P. Siedle, K. Seifert, K. Fendler, T. Seeger, E. Bamberg, A.L. Weisenhorn, K. Goldie, A. Engel, J. Microsc. 169 (1993) 75.
[5] M.A. Lantz, S.J. O'Shea, M.E. Welland, Appl. Phys. Lett. 65 (1994) 409.
[6] M.C. Friedenberg, C.M. Mate, Langmuir 12 (1996) 6138.
[7] T.R. Albrecht, P. Gru¨ tter, D. Horne, D. Rugar, J. Appl. Phys. 69 (1991) 668.
[8] H. Ueyama, Y. Sugawara, S. Morita, Appl. Phys. A 66 (1998) S295.
[9] Y. Martin, C.C. Williams, H.K. Wickramasinghe, J. Appl. Phys. 61 (1987) 4723.
[10] W.A. Ducker, R.F. Cook, Appl. Phys. Lett. 56 (1990) 2408.
[11] F. Giessibl, Science 267 (1995) 68.
[12] Y. Sugawara, M. Ohta, H. Ueyama, S. Morita, F. Osaka, S. Ohkouchi, M. Suzuki, S. Mishima, J. Vac. Sci. Technol. B 14 (1996) 953.
[13] Veeco Metrology Inc.,112 Robin Hill Road, Santa Barbara, CA 93117.
[14] C Baur, A Bugacov, B E Koel, A Madhukar, N Montoya, T R Ramachandran, A A G Requicha, R Resch and P Will, Nanotechnology (1998), **9,** 360–364.
[15] http://www.veeco.com.
[16] A. Kosiorek, W. Kandulski, P. Chudzinski, K. Kempa, and M. Giersig, Nano Letters **4,** 1359 (2004).
[17]. U. C. Fischer and H. P. Zingsheim. *Sub-Microscopic Pattern Replication with Visible-Light*. Journal of Vacuum Science & Technology **19,** 881 (1981).
[18] P. N. Bartlett, P. R. Birkin, and M. A. Ghanem. *Electrochemical deposition of macroporous platinum, palladium and cobalt films using polystyrene latex sphere templates*. Chemical Communications **,** 1671 (2000).
[19] T. R. Jensen, G. C. Schatz, and R. P. Van Duyne. *Nanosphere lithography: Surface plasmon resonance spectrum of a periodic array of silver nanoparticles by ultraviolet-visible extinction spectroscopy and electrodynamic modeling*. Journal of Physical Chemistry B **103,** 2394 (1999).
[20] H. W. Deckman and J. H. Dunsmuir. *Applications of Surface Textures Produced with Natural Lithography*. Journal of Vacuum Science & Technology B **1,** 1109 (1983).
[21] H. W. Deckman and J. H. Dunsmuir. *Natural Lithography*. Applied Physics Letters **41,** 377 (1982).
[22] R. C. Rossi, M. X. Tan, and N. S. Lewis. *Size-dependent electrical behavior of spatially inhomogeneous barrier height regions on silicon*. Applied Physics Letters **77,** 2698 (2000).
[23] K. U. Fulda and B. Tieke. *Langmuir Films of Monodisperse 0.5-Mu-M Spherical Polymer Particles with A Hydrophobic Core and A Hydrophilic Shell*. Advanced Materials **6,** 288 (1994).
[24] A. L. Rogach, N. A. Kotov, D. S. Koktysh, J. W. Ostrander, and G. A.

Ragoisha. *Electrophoretic deposition of latex-based 3D colloidal photonic crystals: A technique for rapid production of high-quality opals*. Chemistry of Materials **12,** 2721 (2000).
[25] J. P. Hoogenboom, C. Retif, E. de Bres, M. V. de Boer, A. K. van Langen-Suurling, J. Romijn, and A. van Blaaderen. *Template-induced growth of close-packed and non-close-packed colloidal crystals during solvent evaporation*. Nano Letters **4,** 205 (2004).
[26] J. C. Hulteen and R. P. Vanduyne. *Nanosphere Lithography - A Materials General Fabrication Process for Periodic Particle Array Surfaces*. Journal of Vacuum Science & Technology A-Vacuum Surfaces and Films **13,** 1553 (1995).
[27] D. Marczewski and W. A. Goedel. *The preparation of submicrometer-sized rings by embedding and selective etching of spherical silica particles*. Nano Letters **5,** 295 (2005).
[28] R. Micheletto, H. Fukuda, and M. Ohtsut, Langmuir,11, 3333-3336 (1996).
[29] Bangs Laboratories, Inc., 9025 Technology Dr., Fishers, IN 46038.
[30] D. Quere, M.-J. Azzopardi, L. Delattre, Langmuir 14,1998, 2213.
[31] S. Rakers, L.F. Chi, H. Fuchs, Langmuir 13, 1997,7121.
[32] Israelachvili J. Intermolecular & surface forces, second edition**,** Elsevier Academic Press, London (1991).
[33] Z. Huang, H. Fang, and J. Zhu, Adv. Mater., 19, 744–748, 2007.
[34] X. Li and P. W. Bohn, Appl. Phys. Lett., 77, 2572, 2000.
[35] T. Unagami, J. Electrochem. Soc. 127, 476, 1980.
[36] Apex Instruments Co., 82D Ibrahimpur Road, Kolkata 700032, India.
[37] B. Chapman, Glow Discharge Processes**.** John Wiley & Sons, New York, 1980.
[38] A. Grill, Cold Plasma in Materials Fabrication. IEEE Press, New York, 1994.
[39] J. E. Mahan, Physical Vapor Deposition of Thin Films**,** John Wiley & Sons, New York, 2000.
[40] D. M. Mattox, J. Vac. Sci. Technol. A7(3), 1105 (1989).
[41] Hind High Vacuum Co. (P) LTD. Bangalore, India.
[42] North America Nnaoport, 5350 NEDawson Creek Drive, Hillsboro, Oregon, 97124, USA.
[43] Malvern Instruments Ltd., Enigma Business Park, Grovewood Road, Malvern, Worcestershire WR14 1XZ, United Kingdom.

Chapter 3

A method to quantitatively evaluate the van-der-Waals interaction in atomic force microscopy using cantilever instability

The force vs. distance (f-d) curve that we measure in an AFM has a dominant contribution arising from microcantilever instability as it moves in a non-linear force field. This is a principal theme of the thesis. In this chapter we demonstrate that how do the dominant features of the (f-d) curve like the “jump-into-contact” and the “jump-off-contact” get determined by the microcantilever instability and give us a way to study quantitatively the tip-sample interaction like the van-der-Waals interaction.
We show that the ‘jump-into-contact’ and “jump-off-contact” of the cantilever in the atomic force microscope (AFM) is caused by an inherent instability in the motion of the AFM cantilever. This instability acts in tandem with such instabilities like water bridge or molecular bond rupture and makes the static force spectroscopy curve (including ``jump-off-contact'') dependent on the step-size of data collection which is discussed in detail in chapter four. We also show that the ‘jump-into-contact’ distance can be used to find the interaction of the cantilever tip with the surface. A model has been proposed to explain the data. In the specific context of the attractive van-der-Waals interaction, this method can be realized as a new method of measuring the Hamaker constant for materials. The Hamaker constant is determined from the deflection of the cantilever at the ‘jump-into-contact’ using the force constant of the cantilever and the tip radius of curvature, all of which can be obtained by measurements. The results have been verified experimentally on a sample of cleaved mica, a sample of Si wafer with natural oxide and a silver film, using a number of cantilevers with different spring constants. We emphasize that the method described here is applicable only to surfaces that have van-der-Waals interaction as the tip–sample interaction. We also find that the tip to sample separation at the ‘jump-into-contact’ is simply related to the cantilever deflection at this point, and this provides a method to exactly locate the surface.

3.1 Introduction

Atomic force microscope (AFM) is one of the most widely used tools in nanoscience and nanotechnology. Since its discovery, the AFM [1] has emerged as a very powerful tool in the characterization of various properties of materials at the nanometre scale. This is primarily because the AFM can not only image with atomic resolution but it can also

measure inter-atomic forces which are of the order of piconewtons or even much less. These capabilities made the AFM a versatile enabling tool in nanotechnology [2]. One of the standard experiments performed with an AFM is the measurement of the force distance curves [3, 4], i.e. measurement of the force of interaction between the tip and the substrate. In this measurement, the cantilever deflection (d) is measured as a function of the separation of the tip and the sample (z) and the force of interaction is the product of the deflection d of the cantilever and the spring constant k_c of the cantilever. (Note: The force obtained in this manner is not exactly the force between the tip and the sample, since the effective spring constant of the cantilever can be modified by the elastic deformation of the surface of the sample and the tip when they are in contact with each other. Hence, in our study, we will consistently use the concept of deflection of the cantilever instead of the force). In the measurement of the force–distance curve, d is measured from its equilibrium position (in the absence of any external force), when it is at a distance h from the sample (the substrate), as shown in fig. 3.1(a). The measured force–distance curve, shown schematically in fig. 3.1(b), generally shows hysteresis. The approach curve shows a 'jump-into-contact' (JIC) and the retraction part of the curve shows the 'jump-off-contact' (JOC). The concept of JOC has been used extensively in the past as a quantitative measure of the adhesion force [5, 6]. The hysteresis has traditionally been attributed to adhesion due to the layer of water existing on the surface of the sample [7, 8], or rupture of molecular bonds [9, 10], and has indeed been used to measure the ``snap off'' force. In contrast, however, not much attention has been paid to the phenomenon of JIC, except for early papers that pointed out the basic causes for the existence of such a phenomenon [3, 11]. In this chapter we will first revisit the issue of JIC and present a new approach to the JIC phenomenon in the force–distance curves of an AFM. This is done in order to investigate whether it can be used to obtain quantitatively some of the microscopic parameters of tip–sample interaction and thus can

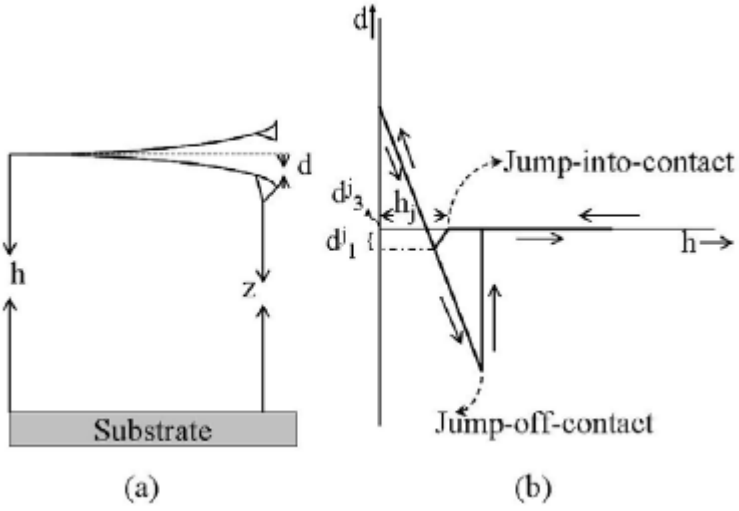

Figure 3.1 Schematic diagram of AFM tip and sample assembly (a) and force–distance curves (b). The dotted line in (a) marks the equilibrium position of the cantilever in the absence of an external force. d is positive when measured upwards. The arrows in (b) show the direction of motion of the cantilever.

be made a useful tool. A simple model is used to understand this instability and obtain a quantitative measure of not only the distance h_j at which the JIC should occur but also how much the magnitude of the deflection of the cantilever at the JIC should be. These measures are directly related to parameters of the force field. We have performed experiments to verify some of the predictions of our theory. We investigate this phenomenon in the specific context of the van-der-Waals interaction, and from the measured deflection of the cantilever at the JIC we determined the Hamaker constant using the known parameters such as the radius of curvature of the tip (R_t) and the cantilever spring constant (k_c). We also discuss the extent of uncertainty in the data and compare the relative merits of this method vis-a-vis other methods of determining the Hamaker constant. We note here that in chapter 4 the effective Hamaker constant has been controlled by an electric field and the ideas elaborated in this chapter has been quantitatively discussed.

3.2 Theoretical Modeling

The AFM is a nonlinear system. Our aim here is to use a simple model which could explain the feature seen in experiments. We model the motion of a cantilever by a spring-ball system. The inherent nonlinearity of the cantilever due to its finite dimensions has not been introduced into our calculation, in order to keep things simple [12]. Thus, we write the equation of motion of the cantilever as

$$m\ddot{d}(t) + \eta\dot{d}(t) + kd(t) = f_{ts}(h + d(t)) \qquad 3.1$$

Here, m is the mass of the cantilever, η is the friction constant, k_c is the spring constant, d(t) is the deflection of the cantilever measured from its equilibrium position in the absence of any external force, h is the distance between the sample and the tip when the tip is in the equilibrium position (in the absence of any external force), $f_{ts}(h + d)$ is the atomic force between the tip and the sample at the instantaneous position of the tip and t represents time. In case of the static (or quasi-equilibrium) experiment $d(t) = d$, where d is the deflection of the cantilever at which it comes to rest. The dynamic equation will reduce to a simple static equation of the form

$$k_c d = f_{ts}(h + d) \qquad 3.2$$

One can take a generalized force field for $f_{ts}(h + d)$ and obtain a solution to eq. 3.2 that will give the parameters of the interaction potential. In order to have a definite result that can be verified by experiment, we investigated the specific case of van-der-Waals interaction between the tip and the surface and an elastically deformable surface for the contact force. The subsequent results obtained are thus specific to the van-der-Waals interactions. The tip–sample force is modeled by a combination of the van-der-Waals force at large tip–sample distances (h) which is essentially attractive and by the Derjaguin–Muller–Toporov (DMT) [13, 14] force which is a combination of the attractive van-der-Waals like force (except that it is h-independent) and the repulsive forces arising due to elastic interaction between the tip and the sample. Thus, formally, the force is given by

$$f_{ts}(z) = \begin{cases} -\dfrac{HR_t}{6z^2} \\ -\dfrac{HR_t}{6a_0^2} + \dfrac{4}{3}E^*\sqrt{R_t}(a_0 - z)^{\frac{3}{2}} \end{cases} \qquad 3.3$$

Here, $z = h + d$, a_0 is an intermolecular distance, and H is the Hamaker constant, which depends on the material of the tip and the sample and also on the intervening medium. E^* is the effective elastic modulus between the tip and the sample. E^* is given by

$$\frac{1}{E^*} = \left(\frac{1-\nu_s^2}{E_s} + \frac{1-\nu_t^2}{E_t}\right) \qquad 3.4$$

where, ν_t, E_t, ν_s, E_s are the Poisson's ratio and the Young's moduli of tip and sample respectively. Note that the form of the van-der-Waals force is chosen for sphere plate geometry, which is close to the real situation in an AFM experiment1. Here we will only concentrate on the regime where $z > a_0$, where the force is purely a van-der-Waals force. We will see below that the JIC is mainly determined by the attractive part of the interaction. For the observation of the JIC, we work in the region of attractive interaction and take the force on the right-hand side of eq. 3.2 to be the van-der-Waals force. This is justified because we will see below that the JIC distance is usually much larger than a_0. We want to mention here that the attractive force is the only force present when $h + d >$ the intermolecular distance (a_0), whereas when $h + d < a_0$ the force has a repulsive component, which increases with reducing h. The repulsive component typically ensures that $h + d > 0$. It is interesting to note that, while the repulsive force is essential, the qualitative understanding of the f-h curves, comes even when the repulsive force is taken to be absent. Here we have ignored the repulsive interaction for obtaining the exact solutions to the equation of motion of the cantilever. This will produce a slight deviation from the actual results; however, this will not change the conclusion.
From eqs. 3.2 and 3.3, after some simple manipulations, we obtain the equation for the deflection (d) as

$$k_c d(h+d)^2 + \frac{HR_t}{6} = 0 \qquad 3.5$$

Rewriting $\tilde{d} = \dfrac{d}{h}$ and $\tilde{a} = \dfrac{HR_t}{6k_c h^3}$, we get

$$\tilde{d}(1+\tilde{d})^2 + \tilde{a} = 0 \qquad 3.6$$

The three solutions of these equations are given by

$$\begin{aligned} \tilde{d}_1 &= -\frac{b_2}{3} + (S+T) \\ \tilde{d}_2 &= -\frac{b_2}{3} - \frac{1}{2}(S+T) + \frac{\sqrt{3}}{2}i(S-T) \\ \tilde{d}_3 &= -\frac{b_2}{3} - \frac{1}{2}(S+T) - \frac{\sqrt{3}}{2}i(S-T) \end{aligned} \qquad 3.7$$

where

$$S = (R + \sqrt{D})^{\frac{1}{3}}$$
$$T = (R - \sqrt{D})^{\frac{1}{3}}$$
$$R = \frac{9b_1b_2 - 27b_0 - 2b_2^3}{54} \qquad 3.8$$
$$D = Q^3 + R^2$$
$$Q = \frac{3b_1 - b_2^2}{9}$$

and b_0, b_1 and b_2 are the coefficients of $(d)^0$, $(d)^1$ and $(d)^2$ in eq. 3.6. Here we want to mention that eq. 3.7 is valid only for the real values of S and T defined in eq. 3.7. For complex values, the expressions for eq. 3.7 will change. It can be easily seen that $b_0 = a$, $b_1 = 1$ and $b_2 = 2$. The distance $\tilde{d}_1$ has only a real part, while the solutions $\tilde{d}_2$ and $\tilde{d}_3$ are either real or complex conjugates of each other, depending on the parameters of the equation. The actual deflection (d) is obtained by multiplying the solution by the corresponding tip–sample distance (h). Figure 3.2 shows the simulated d-h curves (approach and retract) in presence of both attractive and repulsive part of the tip-sample interactions and also the analytical solutions of eq. 3.5 as a function of the tip-sample distance (h) for $HR_t = 2.26 \times 10^{-27}$ N m^2, k_c=0.1 Nm^{-1} and $a_0 = 0.15$ nm. In simulated d-h curves we get realistic d_1 (= $\tilde{d}_1$.h) as in this case both attractive and repulsive part of the tip-sample interactions are present. One can find out from fig. 3.2 that d_1+h, obtained from simulation, is always positive whereas in case of analytical solution it is negative because the repulsive part of the tip-sample interaction has not been considered. It can be noted that the JIC position also matches quite well in these two cases. Of the three solutions, the solution given by the open circles corresponds to $d_1 = \tilde{d}_1 h$ while the open square and triangle correspond to $d_2 = \tilde{d}_2 h$ and $d_3 = \tilde{d}_3 h$ respectively. Note that as the tip–sample distance is reduced, the solutions corresponding to d_2 and d_3 approach each other and they meet at one point (for example, at $h \approx 2.9$ nm in fig. 3.2). For tip–sample distances below this both these solutions become complex (in fig. 3.2 only the real part is shown). It is necessary to note that the solutions d_1 and d_3 are stable solutions, while d_2 is unstable. This has been checked by finding the sign of the derivative of eq. 3.2 with respect to d at each value of h. We denote the point where the solutions d_2 and d_3 meet as the JIC point. This is the limit of

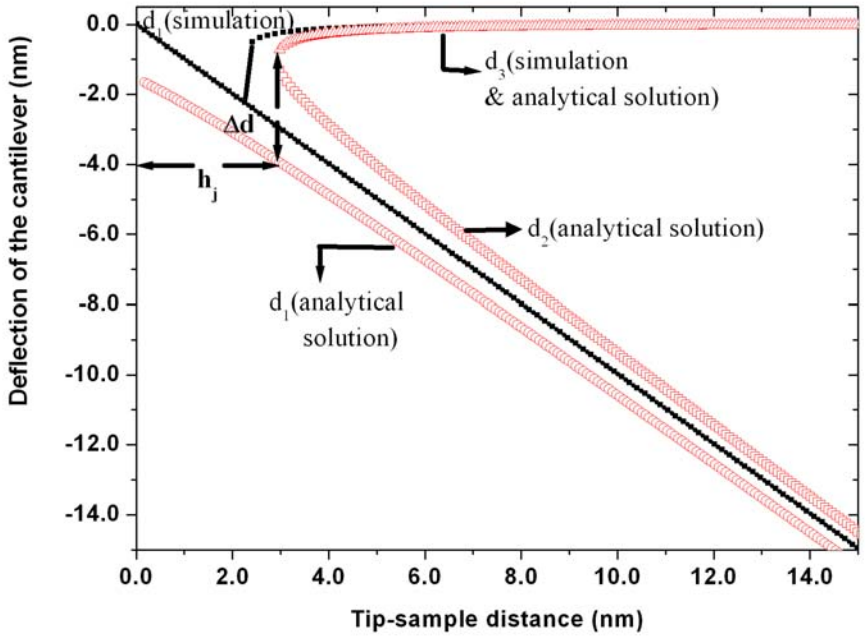

Figure 3.2 Plot of solutions given by eq. 3.7 as a function of tip–sample distance (h) for the parameters mentioned in the text. The open circles ($d_1 = \tilde{d}_1 h$) and open triangles ($d_3 = \tilde{d}_3 h$) represent stable solutions. The open squares ($d_2 = \tilde{d}_2 h$) represent the unstable solution. Here only the real part of the solutions is shown.

stability for the solution d_3 which defines the motion of the cantilever for the approach curve up to this point. If the tip–sample distance (h) is reduced beyond this point of stability, there is only one real solution available (d_1) and the system will jump into the stable solution given by d_1. This defines the JIC. It must be noted here that this jump has occurred in the attractive regime and we do not take recourse to any adhesion forces for explaining the phenomenon. We also emphasize here that on the retract path the cantilever dynamics follow the solution given by d_1 until it jumps back to the solution given by d_3 at the JOC point. The solutions of the cubic equation given by eq. 3.7 have a number of interesting features. For example, let us consider the point where the JIC occurs in our model. At this point $d_2 = d_3$ and the discriminant D is exactly equal to zero. If we denote the tip–sample distance at this point by h_j and corresponding values of R, Q as R_j, Q_j, we get the equation R_j

$$R_j + \sqrt{Q_j^3 + R_j^2} = R_j - \sqrt{Q_j^3 + R_j^2} \qquad 3.9$$

which leads to the equation

$$Q_j^3 = -R_j^2 \qquad 3.10$$

Replacing the expressions for Q_j and R_j from eq. 3.8, and putting in the values of b_0, b_1 and b_2, we get

$$\frac{HR_t}{6k_c h_j^3} = \frac{4}{27} \qquad 3.11$$

Equation 3.11 can be used to find the Hamaker constant (H) because the tip radius R_t and the cantilever spring constant k_c are known and h_j is experimentally measurable. However, the problem arises because the position of the surface not being known exactly, the absolute value of h_j has a large uncertainty. Below, we show that the magnitude of the jump of the cantilever at the JIC is simply related to h_j and this fact can be used to calculate the Hamaker constant (H) with a high degree of confidence which is limited by the magnitude of the uncertainty in determination of k_c and R_t, both of which,
however, are experimentally measurable [15, 16]. At the JIC, there are only two distinct real solutions to the cubic equation since the solutions corresponding to d_2 and d_3 are degenerate. Subtracting d_3 from d_1, and again putting in the values of b_0, b_1 and b_2, we get the jump of the cantilever (Δd) at the JIC as

$$\Delta d = d_3^j - d_1^j = -h_j \qquad 3.12$$

where $d_1^j$and d_3^j are the deflections at the JIC point corresponding to the two solutions. Eqs 3.11 and 3.12 lead to a practical way of calculating the Hamaker constant from the deflection–displacement curves. Determination of the Hamaker constant from eqs. 3.11 and 3.12 will need knowledge of k_c and R_t of a given cantilever which can be obtained from experiment. Alternatively, we note that if h_j is measured for a material with known Hamaker constant, this can be used to calibrate the k_c/R_t ratio of a given cantilever, which in turn can be used to find an unknown Hamaker constant. Given the practical difficulties in knowing k_c and R_t exactly, this may be a more practical method. Note also that eq. 3.12 is itself independent of the material of the tip, sample and the intervening medium. The abovementioned process also indicates that one can obtain a precise method of shifting the raw data obtained from the AFM measurements to properly locate the surface.

3.3 Experimental Details

The data have been taken using an atomic force microscope (Model CP II) from Veeco on freshly cleaved mica, on Si wafer with natural oxide and on a silver metal film. We have used three different cantilevers for taking data for a given surface in order to vary the k_c/R_t ratio. The cantilevers used had Si_3N_4 tips and spring constants (radius of curvature) of 0.03 N m^{-1} (R_t = 30 nm), 0.1 Nm^{-1} (R_t = 35 nm) and 0.9 Nm^{-1} (R_t = 50 nm). We have found the radius of curvature of the tip from the images taken by a field emission gun scanning electron microscope (FEG-SEM). The medium between the tip and sample for all the experiments was air at room temperature and the rates of data collection were 0.5 and 0.1 Hz. We have repeatedly taken the force–distance curves using the same three cantilevers mentioned above. The reproducibility of the data confirms that there was no damage of the tip of the cantilever during the experiment, and this is also corroborated by the FEG-SEM images. While all possible efforts have been made to eliminate the effects of additional extraneous interactions, the possibility of electrostatic forces due to space charges cannot be completely ruled out. However, as we show below that our results are in good agreement with earlier work, [17–19], we do not expect a substantial electrostatic presence in our experiments, since electrostatic forces are

expected to modify the results by a large amount. It would, however, be interesting to observe the effect of electrostatic interactions.

3.4 Results

Figure 3.3 shows a typical AFM deflection (d) versus displacement (h) curve for a freshly cleaved mica sample and a Si_3N_4 tip of spring constant 0.1 Nm^{-1} in air. The data have been plotted as deflection versus distance. The arrows in fig. 3.3 indicate the direction of motion of the cantilever (approach and retract). The JIC region is highlighted in the inset of fig. 3.3. From fig. 3.3 we can see that the JIC occurs at a tip–sample separation (h) of approximately 2.9 nm, which is the attractive regime of the force–distance curves, since $a_0 \approx 0.15$ nm [13, 14]. The JIC occurs at larger values of h for smaller k_c. For instance, for $k_c \approx 0.03$ N m^{-1}, the jump occurs at $h_j \approx 3.5$ nm. Thus the parameters of the attractive potential are good enough to determine the JIC. In fig. 3.4 we plot the observed h_j^{-3} (h_j is the JIC distance) as a function of the quantity k_c/R_t. The quantities k_c/R_t are the physical parameters of the cantilevers used. We have taken three cantilevers of the same composition but with different k_c and R_t to achieve three different (k_c/R_t) ratios for a given surface material. The main uncertainty in the determination of H from the experiment arises from these two parameters. One can use the parameters given by the manufacturer's data but a better alternative is to experimentally determine them. From eq. 3.11, it can be seen that since the Δd or $h_j \propto k_c^{-1/3}$, thus it is advisable to use a softer cantilever (low k_c) so that Δd or h_j are larger, leading to less uncertainty in determination of these quantities. The graph according to eqs. 3.11 and 3.12 gives a straight line and the inverse of the slope gives the Hamaker constant H. The data have been taken in ambient

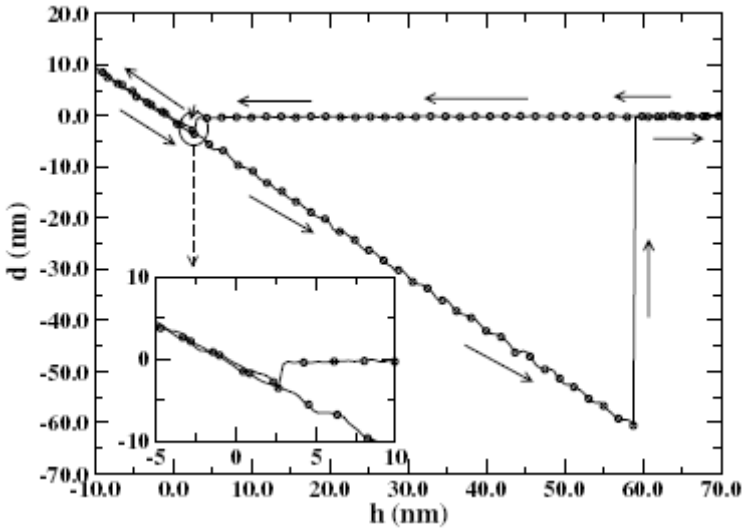

Figure 3.3 Approach and retract curves of the deflection (d) versus the displacement (h) of the tip of the microcantilever for mica using a Si_3N_4 tip (free motion spring constant *k* = 0.1 Nm^{-1}) in air. The arrows indicate the direction of motion of the cantilever (approach and retract). The JC region is highlighted in the inset.

conditions within a glove chamber. The error bars in the data have been obtained by repeated data taking on the same surface and with the same tip, and they show the extent of variance one would expect in such experiments. The reproducibility of the data also indicates that the tip, used in the experiment, did not get damaged during the collection of the data. From our experiment we obtain $H \approx (0.64 \pm 0.07) \times 10^{-19}$ J for mica, $H \approx (0.66 \pm 0.27) \times 10^{-19}$ J for SiO_2 and $H \approx (3.73 \pm 0.89) \times 10^{-19}$ J for silver. A summary of results obtained is shown in table 3.1. This can be compared with calculated values of 1.28×10^{-19} J for mica [20], 1.21×10^{-19} J for SiO_2 [20] and 2.9×10^{-19} J for silver [17], using Si_3N_4 as the tip material with vacuum as the intervening medium. A similar calculation with water as the intervening medium gives 0.245×10^{-19} J for mica [20], 0.207×10^{-19} J for SiO_2 [20] and 1.39×10^{-19} J for silver [19] with Si_3N_4 as the tip material. These values have been obtained from calculations using full Lifshitz theory [21–23] for the individual materials.

3.5 Discussions:

The values we have obtained experimentally lay between the Hamaker constant values for vacuum as the intervening medium and water as the intervening medium, suggesting the influence of the relative humidity of air in calculating the Hamaker constant. The relative humidity in the glove chamber during measurement was typically ~55% (for mica and SiO_2) and ~33% for silver. Since the JIC data are routinely obtained while one measures the force–distance curve, it is easy to obtain a very important physical parameter from the same experiment. We point out that the utility of the JIC data to obtain a quantitative measure of a physical parameter such as the Hamaker constant is

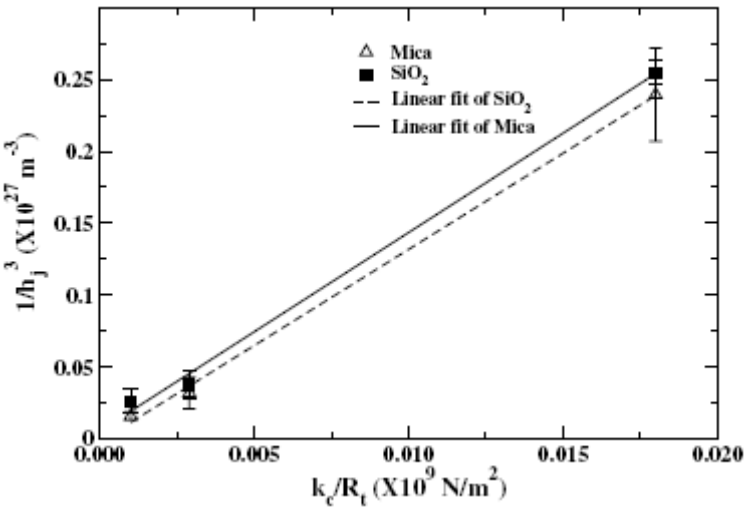

Figure 3.4 Plot of the observed 'jump-into-contact' distance h^{-3}_j as a function of the quantity k_c/R_t . The solid line and the dashed line are the best fits of the experimental data on mica and Si wafer with natural oxide respectively.

novel, and the uncertainty in the determination of h_j can be eliminated by measurement of Δd and the (k_c/R_t) ratio. As mentioned before, a known tip–surface system (known Hamaker constant) can be used to calibrate a given cantilever (k_c/R_t) ratio using eq. 3.11 and 3.12 if no direct measurements of k_c and R_t are available. This calibration can also be used to find the Hamaker constant for unknown surface. We also emphasize that since, for a given cantilever, the (k_c/R_t) ratio is fixed, a map of the JIC on an inhomogeneous surface can generate a map of the Hamaker constant. There are quite a few methods of measuring the Hamaker constant [24]. These methods include direct force measurements using a surface force apparatus [25] and an atomic force microscope [4, 26–28] where the full force–distance curve is fitted to a model of the van-der-Waals equation. The other methods are based on measuring physical properties of materials, such as the dielectric

Materials	Atomic Force Microscope (using 10^{-19} J)	Surface Force Apparatus (10^{-19}J)	Full Lifshitz theory (10^{-19}J)
Mica	0.64±0.07 (Air, RH~55%)	1.35 (vacuum), 0.22 (water) [24]	1.28 (vacuum), 0.245 (water) [18]
SiO_2	0.66±0.27 (Air, RH~55%)	0.5-0.6 (vacuum) [24]	1.21 (vacuum), 0.207 (water) [18]
Silver	3.73±0.89 (Air, RH~33%)	2.9 (air) [17]	2.4 (vacuum) [18], 1.39 (water) [19]

Table 3.1 Values of Hamaker constant obtained by our method and its comparison with Lifshitz theory. We also show experimental values obtained by a surface force apparatus.

constant [29, 30]. In general, Lifshitz theory [21–23] is widely used for calculating Hamaker constants from the dielectric constant of materials. We note that the reported values of Hamaker constants for the same material obtained from different methods showed considerable variations [24]. The earlier works in obtaining Hamaker constant from an atomic force microscope were mainly based on fitting the attractive part of the approach curve with the expression for the van-der-Waals force. In that method the main problem was the presence of the JIC. In our method we have actually used the JIC to find the interaction constant. The advantage of measuring the Hamaker constant using the method described in this paper is that we can find the JIC distance from experimental force–distance curves using eq. 3.12 easily. No numerical fit to the complete force–distance curve is necessary. Here we also want to emphasize that this method has the advantage of mapping the Hamaker constant in an inhomogeneous system whereas this is not possible using a surface force apparatus because it does not have the spatial resolution. Two important points have to be noted in this context: first, the experimental force–distance curves should be taken properly for approach of the cantilever motion with close measurements near the JIC, and second, the radius of the tip (R_t) and the spring constant of the cantilever (k_c) have to be found with least uncertainty if absolute data have to be obtained. We point out that eq. 3.12 is also a very important outcome of this work. This gives us a way to determine the actual position of the surface. In AFM

measurements there is indeed a problem in evaluating the absolute value of the tip–sample separation (h). The JIC is a special point at which the distance (h) is equal to $|\Delta d|$, which thus can be appropriately fixed. Once this is fixed the position of the origin of h (the sample) can be located. We emphasize that the analysis above is applicable only to surfaces that have van-der-Waals interaction as the tip–sample interaction because of the specific type of tip–sample interaction used. However, the method is general enough and can be used with other tip–sample interactions as well. The fact that a nonlinear force field introduces an instability that leads to JIC is a conclusion of general validity.
In addition, our investigation also gives us a practical way to locate the actual distance of the cantilever from the surface. The phenomenon is completely governed by the attractive part of the tip–sample interaction. An important outcome of the investigation is the observation of the independence of the JIC on the actual elastic forces that make the tip–sample contact interaction. Since the JIC can be measured at different spots on a given surface, this method gives us a tool to obtain a map of the tip–surface interaction as measured by a parameter such as the Hamaker constant (in the context of van-der-Waals interaction) with a spatial resolution offered by a typical AFM. The spatial resolution is an added advantage over other methods of determining the Hamaker constant, such as the surface force apparatus.

3.6 Conclusions

We have studied the static deflection–distance curves for an atomic force microscope using a simple model that gives the "jump-into-contact" often observed in force–distance curves of an AFM as an instability of the cantilever moving in a nonlinear force field. The model provides a unique method of determining the tip–sample interaction parameters. We have developed the concept specially for van der Waals interaction for definiteness. In this case the method gives the Hamaker constant. We find values that are comparable to the Hamaker constant measured by other methods. The model also provides a reliable criterion for locating the sample and thus shifting the raw deflection–distance data obtained from AFM by locating the distance at which the "jump-into-contact" occurs. This process removes the arbitrariness of locating the sample in the AFM. The method also gives us a way to map the Hamaker constant over a surface, that may be inhomogeneous, by mapping the JIC with an AFM, for hard samples (i.e. samples with small deformations due to tip–sample interactions). It must be noted here that this is one of the problems which has to be addressed in the case of soft samples (polymers, biological molecules, etc), where tip–sample forces can dramatically modify the effective tip–sample distance. In such cases, the JIC will not provide an accurate measurement of the tip–sample distance. One possibility is to use cantilevers of very small spring constant (k_c), so that the JIC occurs at large enough distances, where the deformation of the sample may become less important. This is, however, a problem to be investigated further.

Bibliography

[1] Binning G, Quate C F and Gerber Ch 1986 Phys. Rev. Lett. **56** 930.
[2] Giessbl F J 2003 Rev. Mod. Phys. **75** 949.
[3] Cappella B and Dietler G 1999 Surf. Sci. Rep. **34** 1.
[4] Butt H J, Cappella B and Kappl M 2005 Surf. Sci. Rep. **59** 1.
[5] Cappella B, Baschieri P, Frediani C, Miccoli P and Ascoli C 1997 IEEE Eng. Med. Biol. Mag. **16** 58.
[6] Hao H W, Bar´o AMand S´aenz J J 1991 J. Vac. Sci. Technol. B **9** 1323.
[7] B. Cappella, P. Baschieri, C. Frediani, P. Miccoli and C. Ascoli, 1997 Engineering in Medicine and Biology Magazine IEEE **16**, 58.
[8] H. H. Wen, A.M. Baró and J.J. Sáenz, 1991 Jour. Vac. Sci. Tech.B **9**, 1323.
[9] M. He, A.S. Blum, D.E. Aston, C. Buenviaje, R.M. Overney and R. Luginbühl, 2001 Journal Of Chemical Physics **114**, 1355.
[10] J. Grobelny, N. Pradeep, D.-I. Kim and Z.C. Ying, 2006 Applied Physics Letters **88**, 091906.
[11] Burnham N A and Colton R J 1989 J. Vac. Sci. Technol. A **7** 2906.
[12] For a recent review on theories of SFM, see, Hofer W A, Foster A S and Shluger A L 2003 Rev. Mod. Phys. **75** 1287.
[13] Israelachvili J 1991 Intermolecular and Surface Forces (London: Academic).
[14] Derjaguin B V, Muller V M and Toporov Y P 1975 J. Colloid Interface Sci. **53** 314.
[15] Cook S M, Schäffer T E, Chynoweth K M, Wigton M, Simmonds R W and Lang K M 2006 Nanotechnology **17** 2135.
[16] Charlles C A and Seah M P 2005 Nanotechnology **16** 1666.
[17] Parker J L 1992 Langmuir **8** 551.
[18] Coakley C J and Tabor D 1978 J. Phys. D: Appl. Phys. **11** L77.
[19] Visser J 1976 Adv. Colloid Interface Sci. **3** 331.
[20] Bergstr¨om L 1997 Adv. Colloid Interface Sci. **70** 125.
[21] Lifshitz E M 1956 Sov. Phys.-JETP **2** 73.
[22] Dzyaloshinskii I E, Lifshitz E M and Pitaevskii L P 1961 Adv. Phys. **10** 165.
[23] Ninham B W and Parsegian V A 1970 J. Chem. Phys. **52** 4578.
[24] Ackler H D, French R H and Chiang Y-M 1996 J. Colloid Interface Sci. **179** 460.
[25] Horn R G, Clarke D R and Clarkson M T 1988 J. Mater. Res. **3** 413.
[26] Burnham N A, Dominguez D D, Mowery R L and Colton R J 1990 Phys. Rev. Lett. **64** 1931.
[27] Ederth T 2001 Langmuir **17** 3329.
[28] Seog J, Dean D, Plaas A H K, Wong-Palms S, Grodzinsky A J and Ortiz C 2002 Macromolecules **35** 5601.
[29] Tabor F R S D and Winterton R H S 1969 Proc. R. Soc. **312** 435.
[30] Hough D B and White L R 1980 Adv. Colloid Interface Sci. **14** 3.

Chapter 4

Effect of intrinsic instability of cantilevers on static mode Atomic Force Spectroscopy

We show that the static force spectroscopy curve is significantly modified due to presence of intrinsic cantilever instability. This instability acts in tandem with such instabilities like water bridge or molecular bond rupture and makes the static force spectroscopy curve (including "jump-off-contact") dependent on the step-size of the movement of sample stage. A model has been proposed to explain the data. This has been further validated by applying an electric field between tip and substrate which modifies the tip-substrate interaction. We have investigated the role of cantilever instabilities in determination of the AFS curves in an Atomic Force Microscope (AFM) working in Ultra-High vacuum (UHV). We also showed how an electric field applied between tip and the sample shifts the observed deflection (or force) –vs.-distance curves in the AFM. We explained the experiment using a model and quantitatively established a relation between the observed AFS curves and the electric field which modifies the effective tipsample interaction in a controlled manner. The investigation establishes a way to quantitatively evaluate the electrostatic force in an AFM using the static AFS curves.

4.1 Introduction:

Atomic Force Microscopy (AFM) has emerged as a powerful tool, having a wide variety of applications, from understanding the atomic level forces, Casimir force [1], friction at nanometer length scales [2, 3] to controlled manipulation of atoms [4]. This relatively simple instrument has revolutionized our understanding of structures at the nanometer scale and hence the ability to manipulate systems at atomic scales in a wide variety of subjects including material science, soft matter and biology [5, 6]. The cantilever deflection, if analyzed properly, can give us a quantitative measure of the tip-sample interaction.

Since the time of its discovery by Binning et. al. [7], many attempts have been made to explain some of the non-intuitive features seen in these systems. For example, the force versus distance (f-h) curves [8] depend on whether the cantilever is approaching towards the sample or retracting away from it (henceforth referred to as the " approach" and the "retract", respectively), leading to a hysteresis like behaviour as shown in fig.4.1. The

hysteresis has traditionally been attributed to adhesion due to the layer of water existing on the surface of the sample [9, 10], or rupture of molecular bonds [11, 12], and has indeed been used to measure the "snap off" force. In UHV-AFM, there is no such water layer present on the tip and the sample yet the f-h curves taken in UHV-AFM shows hysteresis with distinct "jump-into-contact" (JIC) and "jump-off-contact" (JOC). In this chapter we mainly focus on the fact that widely used practice of determining the "snap off" force from the (f-h) curves can be erroneous because intrinsic instability in cantilevers can actually modify the (f-h) curves. We also show how one can properly acquire data and interpret the (f-h) curves in the context of these instabilities. In an actual experiment the quantity measured is the cantilever deflection (d) as a function of the distance between the sample and the cantilever tip when the tip is in the equilibrium position (in absence of any external force) (h). The force $f = k_c d$, where k_c is cantilever spring constant. It is important to note that although the steps in which the sample approaches or retracts from the cantilever (the z-controller resolution) can be very small ≈ 0.025 Å), the cantilever deflection d is only measured at discrete points in the whole path. In all our discussions below we will define "step size" (δh) as the distance between two such neighboring points, and assume that the distance between these points is covered smoothly without any noticable change to the deflection. This assumption will be discussed in more details later in the paper. If the maximum distance between the cantilever and the surface is h_{max} and the number of data points acquired is N, then $h_{max} = N.\delta h$. In case of experiments done in ambient condition, N has been kept fixed at 500 (in one direction) and hence δh can be varied by varying h but for the experiments done in UHV, h has been kept fixed while N has been varied to vary the step size.

The two important parameters that one obtains from the experimental f-h curves are the "jump-into-contact" (JIC) distance obtained from the approach part and the "jump-off-contact" (JOC) from the retract part. The force, defined by $f^* = k_c d^*$, where d^* is the cantilever deflection at JOC, has traditionally been attributed to adhesion or molecular bond rupture. whole path. In all our discussions below we will define "step size" (δh) as the distance between two such neighboring points, and assume that the distance between these points is covered smoothly without any noticable change to the deflection. However, we observe experimentally that d^* and h^* (the tip-sample separation at JOC) depend on step size (δh) as shown in fig. 4.2. In this paper we show both experimentally and through theoretical analysis that these observed dependencies of d^* and h^* on δh arise due to an intrinsic instability in the cantilever dynamics which manifests itself mainly due to the procedure of data acquisition in most AFM. We show, in particular, that both the instabilities (the intrinsic instability and the "snap off" instability) occur in tandem. We also find that in UHV-AFM where the "snap-off" instability is absent, one observes the JIC and JOC arising solely from the intrinsic instability. The intrinsic instability arises mainly due to the motion of the cantilever in a non-linear force field and the two instabilities can be separated out in a real AFM experiment by acquiring data as a function of δh. We support our inference by varying the tip-surface force and thus the instability in a controlled manner by applying an electric field between them. In many cases the tip–sample interaction arises from the van-der-Waals interaction. In such cases, the use of an electrostatic force, by application of a small voltage between the sample and tip, is an interesting option to change the effective tip-sample interaction in a controlled way. This is because both van-der-Waals and electrostatic interactions have $1/h^2$ (where h

is the tip-sample distance) dependence. We show that the electric field can be used as a good control parameter to study the micro-cantilever dynamics in an AFM. We find that the shift of the observed d^* and h^* on δh can be cleanly explained by our model.

The quantitative measurement of electrostatic forces by an AFM is of wider interest because a better understanding of the charging mechanisms in the nanometer scales can be obtained. Investigation of the tip-sample (substrate) interaction under an applied field is not only an important exercise in understanding the microcantilever dynamics but also a necessary ingredient in doing controlled nanomanipulation using electrophoretic force in an AFM. The necessary quantitative information on the tip-sample interactions can be obtained from these parameters using the model analysis presented here. We have also shown that d^* and h^* are not unique for a tip-substrate pair but depends on the step size

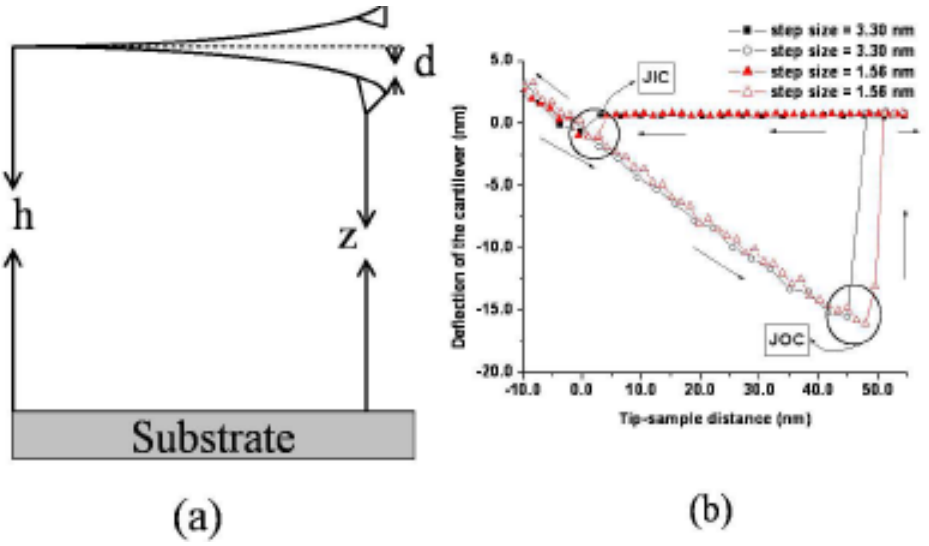

Figure 4.1 Schematic diagram of AFM tip and sample assembly (a) and deflection-distance curves at different step sizes taken on Si (b). The dotted line in (a) marks the equilibrium position of the cantilever in the absence of an external force. d is positive when measured upwards. The arrows in (b) show the direction of motion of the cantilever.

(δh) which also gives a measure of tip sample interaction that leads to the instability. We specifically study the dependence of d^* and h^* on an applied electric field. We also study the dependence of these quantities on δh in presence of an electric field. From the data and the analysis we establish quantitatively how the tip-sample interaction and the resulting AFS are affected by the applied field.
Different theoretical models have been provided to calculate the electrostatic force between the tip and the sample for different geometries and also have been verified experimentally through study of cantilever deflection under field in static mode [10]. However, no attention has been paid to understand how electric field modifies the tip-sample interaction parameters and the resulting AFS curves.

4.2 Experimental details:

The experiments were carried out using a commercial AFM (Model CP II,Veeco) [13] using cantilevers (k_c ~ 0.1N/m) with Si_3N_4 tip on cleaned Si wafers with natural oxide layer on it unless otherwise stated. The cantilever tip had a radius of curvature, R_t ~ 30 nm as determined by direct imaging. The experiments were carried out using an UHV-AFM (Omicron) [14] with a base pressure of 10^{-8} mbar. For experiment using applied electric field, the substrates were gold film and conducting Indium-Tin oxide (ITO) coated glass. A Si cantilever (k_c~0.2 N/m) with tip coated with PtIr was used. A d.c. bias was applied to the tip from an external source and the sample was grounded. For UHV-AFM system, a d.c. bias was applied to the sample and the tip was the ground. Experiments were carried out in a glove box with controlled R_H using flow of Ar gas at a temperature controlled environment at 28^0 C. In case of UHV-AFM system, the sample and the cantilever were baked in vacuum before placing into the UHV

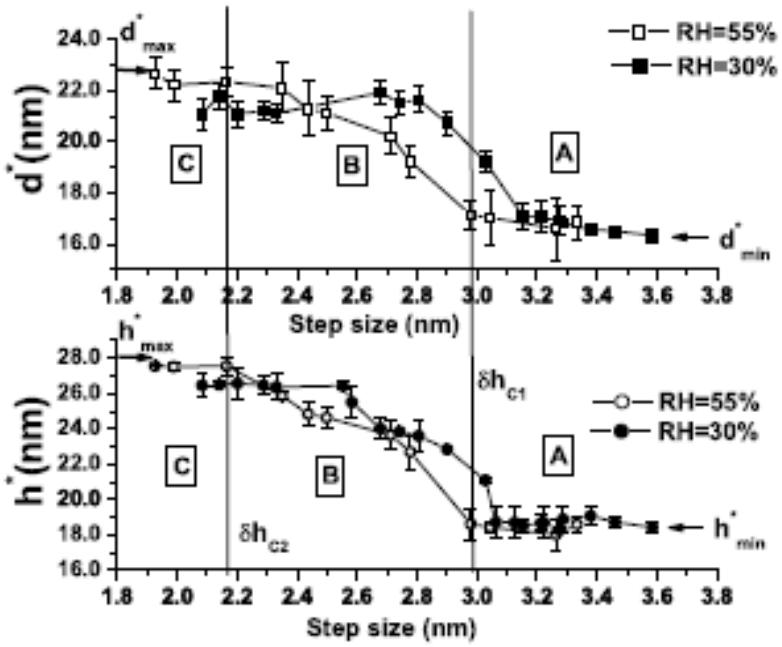

Figure 4.2 Variation of $|d^*|$ and h^* with step size. The closed squares and closed circles show the experimental curves for RH = 30% and the open squares and the open circles for RH = 55%. The lines indicating δh_{c1} and δh_{c2} are for RH=55%

chamber to ensure the absence of water layer. The rate of data collection was 0.1 Hz for all the experiments presented here.

4.3 Discussions:

4.3.1. van-der-Waals interaction:

Fig. 4.2 shows a set of h^* and d^* data plotted as a function of h. The data have been obtained from the typical (d-h) curves as shown in fig. 4.1. The data taken with two representative humidities (R_H=30% and 55%) are taken on Si surface with oxide (hydrophilic). Another set of data (fig. 3) are taken on a hydrophobic surface (created by etching the oxide layer using 50:1 (v/v) HF solution for 30 seconds). All the data show a definite trend. There are three regions in the data (barring the data taken on the hydrophobic surface). In region A, occurring at highest step size, we find that for $\delta h \geq \delta h_{c1}$, both h^* and d^*, reach a limiting value which is

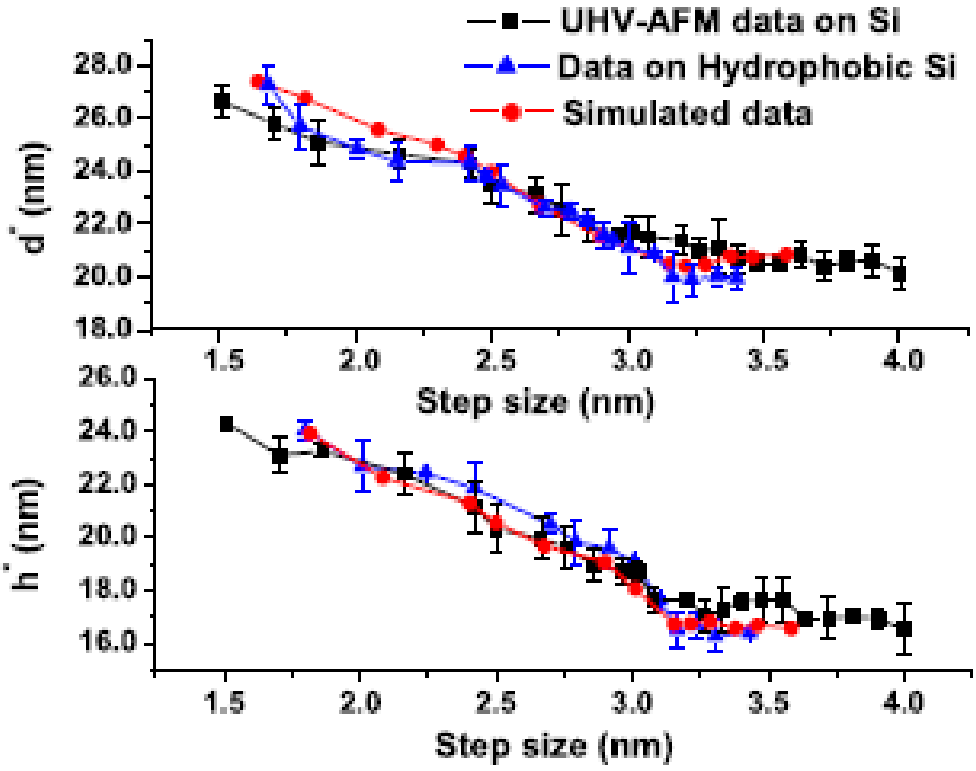

Figure 4.3 Variation of d^* and h^* with step size. The closed squares show the experimental curves on Si taken in UHV-AFM, the closed triangles show the experimental curves on hydrophobic Si and the closed circles show the simulated curves. The parameters used for the simulation are mentioned in the text.

independent of δh. We call these limiting values h^*_{min} and d^*_{min}, and they are almost independent of the R_H values. In the region C, that occurs for smaller δh the h^* and d^*

again reach a limiting value h^*_{max} and d^*_{max} for $\delta h \le \delta h_{c2}$ for hydrophilic surface. For $\delta h \le \delta h_{c2}$ both h^* and d^* become independent of δh and h^*_{max}, d^*_{max} and δh_{c2} all depend strongly on R_H. In particular δh_{c2} is most sensitive to R_H and it increases as R_H is decreased along with the decrease in h^*_{max}, d^*_{max}. For the hydrophobic surface (fig. 4.3), there is no δh_{c2} and h^* and d^* go on increasing as δh is reduced. Data taken in an UHV-AFM is similar to that taken on a hydrophobic surface (there is no δh_{c2}). The data shown here are representative of a large number of data collected in the controlled experiment. In the region B which is the transition region, both h^* and d^* increase as δh is reduced. We propose that the two limiting regions in the data (region A and C) are due to the two instabilities that determine the cantilever motion. The instability at lower step size (region C) which depends on the humidity is due to the "snap-off" phenomena arising from the breaking of the water bridge at the tip-substrate interface. A strong proof in favour of this is the observation that it is absent in the data taken on a hydrophobic surface and in the data taken using UHV-AFM. The instability at higher step size (region A) is always present and arises due to the intrinsic instability that we describe below. In the following part we use a model to explain our observations. The motion of a cantilever is modeled by a spring-ball system. The inherent nonlinearity of the cantilever due to its finite dimensions has not been introduced into our calculation, in order to keep things simple. Thus, we write the force balance equation for the static (or quasi-equilibrium) case as

$$k_c d = f_{ts}(h + d), \tag{4.1}$$

The tip-sample interaction force $f_{ts}(h + d)$ is modeled by a combination of attractive van-der-Waals interaction, for a sphere plate geometry (which is close to the real situation) and the repulsive forces arising due to elastic interaction between the tip and the sample. In order to have a definite result Dejarguin-Muller-Toporov (DMT) [15, 16] force between the tip and the surface has been used. The tip-sample force is thus, formally, given by,

$$f_{ts}(h+d) = \begin{cases} -\dfrac{HR_t}{6(h+d)^2} & \text{for } z > a_0, \\ -\dfrac{HR_t}{6a_0^2} + \dfrac{4}{3}E^*\sqrt{R_t}\,(a_0 - (h+d))^{\frac{3}{2}} & \text{for } z \le a_0 \end{cases} \tag{4.2}$$

where H and R_t are the Hamaker constant and the radius of curvature of the tip respectively. The attractive force is the only force present when $h + d >$ the intermolecular distance (a_0), whereas when $h + d < a_0$ the force has a repulsive component, which increases with reducing h. The repulsive component typically ensures that $h + d > 0$. It is interesting to note that, while the repulsive force is essential, the qualitative understanding of the f-h curves, comes even when the repulsive force is taken to be absent. In our analytical calculation, we have ignored the repulsive interaction for obtaining the exact solutions to the equation of motion of the cantilever. This will produce a slight deviation from the actual results, however, this will not change the conclusion.

From eq. 4.1 and eq. 4.2 (in the region $h + d > a_0$), we obtain the equation for the deflection (d) as,

$$\tilde{d}(1+\tilde{d})^2 + \tilde{a} = 0. \tag{4.3}$$

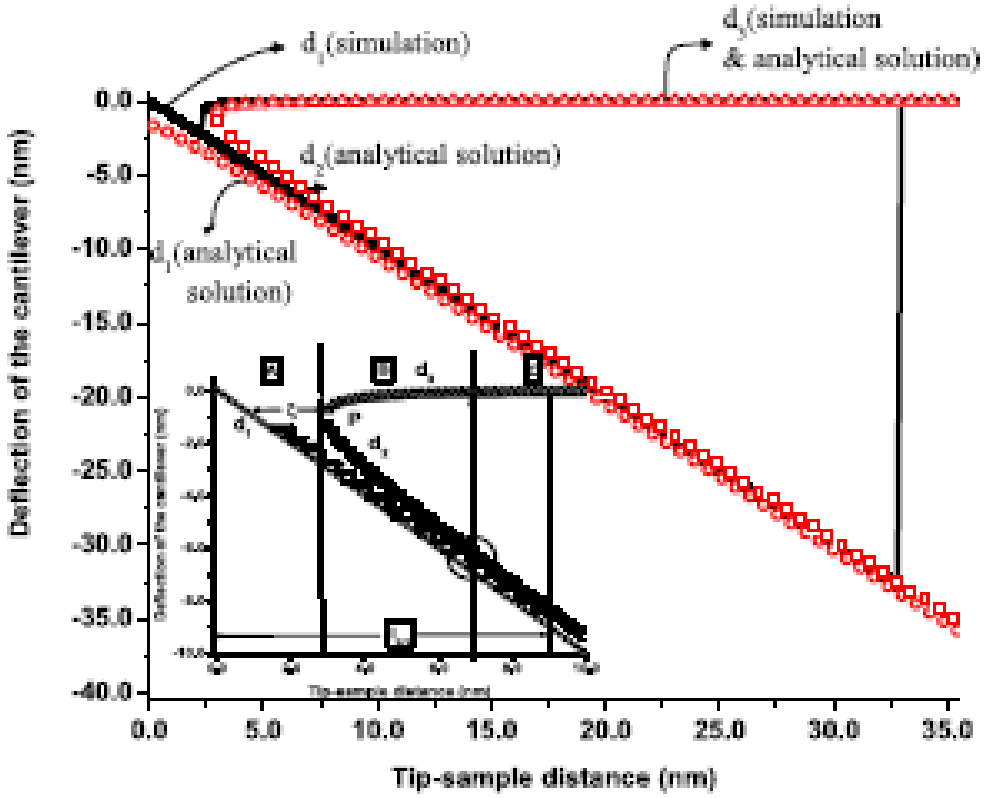

Figure 4.4 Plot of the simulated d-h curves (black line) and the three analytical solutions (red symbols) of eq. 3 as a function of tip-sample distance (h) for the parameters mentioned in the text. For analytical solutions, the open circles ($\tilde{d}_1=d_1.h$) and open triangles ($\tilde{d}_3=d_3.h$) represent stable solutions and the open squares ($\tilde{d}_2=d_2.h$) represent the unstable solution. Three different regions (A, B and C) are shown in the inset.

where $\tilde{d} = d/h$ and $\tilde{a} = HR_t/6k_ch^3$ are dimensionless. The three exact solutions of this equation are already given in chapter three; therefore, we are not mentioning it here.
For further discussion, we will refer these three solutions as $\tilde{d}_1$, $\tilde{d}_2$ and $\tilde{d}_3$. Solution $\tilde{d}_1$ is real while $\tilde{d}_2$ and $\tilde{d}_3$ are either both real and complex conjugate of each other, depending on the parameters of the equation. Fig. 4.4 shows the simulated d-h curves (approach and retract) in presence of both attractive and repulsive part of the tip-sample interactions and also the analytical solutions of eq. 4.3 as a function of the tip-sample distance (h) for $HR_t=2.2 \times 10^{-27}$ N.m^2 (appropriate for our experimental conditions) and $a_0=0.172$ nm. In simulated d-h curves we get realistic d_1 (= $\tilde{d}_1.h$) as in this case both attractive and repulsive part of the tip-sample interactions are present. One can find out from fig. 4.4 that d_1+h, obtained from simulation, is always positive whereas in case of analytical

solution it is negative because the repulsive part of the tip-sample interaction has not been considered. It can be noted that the JIC position also matches quite well in these two cases. The solutions corresponding to d_2 and d_3 approach each other and they meet at a point P (for example, at h ~ 3.0 nm) and as h is reduced below this point they become complex. The distance of point P from the substrate (ξ) is the JIC point, which arises from the intrinsic cantilever instability. Here $\tilde{d}_1$ and $\tilde{d}_3$ are stable solutions, while $\tilde{d}_2$ is unstable. Hence, the tip will either equilibriate to the solution $\tilde{d}_1$ or $\tilde{d}_3$.

We use fig. 4.4 to explain the observed data. Here we assumed that, during the process of data acquisition for the d-h curves, the motion of the cantilever is quasi continuous, i.e., at each point the initial deflection (d) of the cantilever is determined by its final deflection at the previous point. This assumption is not exactly valid. In general, when the tip is in contact with the surface the deflection would actually be larger. However, note that, our argument presented below is to understand the point at which the jump-off-contact occurs. In this context, close to the jump-off-contact, this assumption is not very bad. It is also important to note that the experimental results (fig. 4.2 and fig. 4.3) clearly point out to the fact that step size remains an important parameter irrespective of the ambient conditions and the procedure of varying the step size. In fig. 4.4 (in the inset), we show two examples of the paths traced by the cantilever (shown as steps). In one case (solid line steps), for relatively large step sizes ($\delta h_{c2} < \delta h < \delta h_{c1}$), the intrinsic instability dominates, and the jump from $\tilde{d}_1$ to $\tilde{d}_3$ occurs when the equilibrium position at the point just prior to the jump, takes the cantilever across $\tilde{d}_2$ (marked by a circle in fig. 4.4). In the other case (dotted line steps), for relatively smaller step sizes ($\delta h \sim \delta h_{c2}$), the "snap off" instability dominates and causes a jump across the solution $\tilde{d}_2$. Here, l_{brg} determines the scale at which the water bridge snaps off, causing a jump across the solution $\tilde{d}_2$. If $\delta h \geq \xi$, then, during the retract part, the cantilever tip will jump directly to the stable solution $\tilde{d}_3$ and d^* and h^* both become essentially independent of δh. This corresponds to the region A, where the intrinsic instability is solely responsible for the JOC and which among other things depends on k_c, Hamaker constant (H) and tip radius (R_t). In region A we can thus identify $\xi \approx \delta h_{c1}$. In region B both h^* and d^* increase as δh is decreased. This is the region described above (solid line steps in fig. 4.4). In absence of "snap off" instability, the region B extends all the way down to very small step sizes, as seen on the experiments on hydrophobic surfaces. On the other hand, if the "snap off" instability is present and $\delta h \sim \delta h_{c2}$, the JOC occurs when $h \sim l_{brg}$, as discussed above (dotted line steps in fig. 4.4). This is the region we identify as region C. In this region h^* and d^* are independent of δh and l_{brg} is dependent only on R_H and R_t. Thus the qualitative discussion based on fig. 4.4

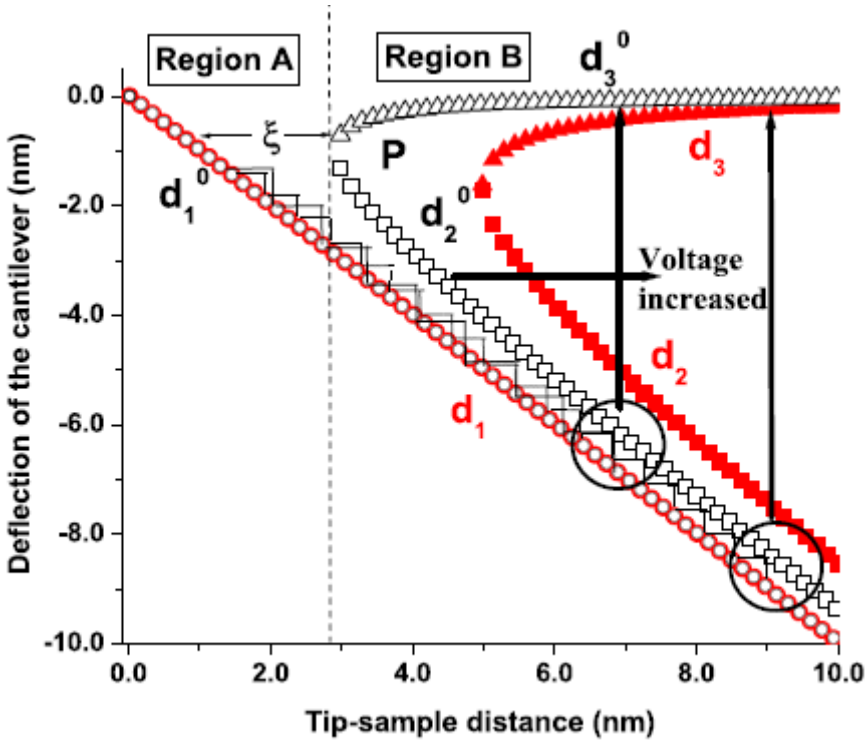

Figure 4.5 Deflection-distance curves for v = 0V (open symbols) and v = 5V (closed symbols) for the parameters mentioned in the text and k = 0.2 N/m. Two different regions (A and B) are shown in the figure.

clearly identifies the regions of the observed curve and the instabilities that give rise to them. Thus in an actual experiment the (d-h) curves need to be taken as a function of δh and the regions corresponding to the two instabilities can be clearly identified. In fig.4.3, we show the data taken in an UHV-AFM, on a hydrophobic surface (which show only intrinsic cantilever instability) and the actual calculated curve based on the method above. The data for the curves taken with water bridges can also be fitted by taking h^*_{max} as an adjustable parameter. It can be seen that the model proposed by us can explain the data in all the three regions.

In this investigation, the "snap-off" occurs due to the instability of the water bridge that forms between the tip and the sample. It is shown earlier [17] that, for sphere-plate geometry, depending on the radius of curvature of the tip, the water bridge configuration becomes metastable for a particular sphere-sample separation when R_t/h becomes ~1.0, where R_t is the radius of curvature of the tip. For the tip used R_t=30 nm, this should happen for h ~ 30 nm which matches very well with the value of h^*_{max} ≈ 26.5 nm observed experimentally. The main proposal of the paper that there is an intrinsic instability of the cantilever can be further tested if we can modify the f_{ts} in a controlled way. In region A, $\xi \approx \delta h_{c1}$ and our model gives $\xi \approx (1.12HR_t/k_c)^{1/3}$. From the experimentally determined H and R_t we find that calculated δh_{c1} ≈ 2.9 nm and experimentally obtained value is ~ 3.0 nm. We have also checked that if we use softer cantilever having k_c = 0.03 N/m (R_t = 25 nm) then δh_{c1} shifts to 4.32 nm (calculated value of δh_{c1} in this case is 4.29 nm).

4.3.2. Electrostatic interaction:

To establish the validity of our hypothesis we used electric field to control f_{ts} and obtained the (d-h) curves with applied electric field. The force due to the applied electric field [18] adds to the force term due to the van-der-Waals force. In presence of electric field eq. 4.2 can be written as [19]

$$f_{ts}(h+d)=\begin{cases}-\dfrac{HR_t}{6(h+d)^2}-\pi\varepsilon_0\dfrac{R_t v^2}{(h+d)^2} & \text{for } z > a_0\\ -\dfrac{HR_t}{6a_0^2}-\pi\varepsilon_0\dfrac{R_t v^2}{a_0^2} & \text{for } z \le a_0\\ +\dfrac{4}{3}E^*\sqrt{R_t}(a_0-z)^{\frac{3}{2}} & \end{cases} \qquad (4.4)$$

We note that since both the attractive terms have $(h+d)^{-2}$ dependence, we can replace the Hamaker constant H with an effective Hamaker constant where $H_{eff} = H + 6\pi\varepsilon_0 R_t v^2$. The enhanced H_{eff} will make ξ larger and will also shift δh_{c1} to a higher value. Variation of the solutions as a function of h is shown in fig. 4.5. The solutions $\tilde{d}$'s are for v = 5V. The solutions for v = 0 are marked as $\tilde{d}^0_1$, $\tilde{d}^0_2$ and $\tilde{d}^0_3$. It is noted that solution $\tilde{d}_1$ is insensitive to v and is mostly decided by the repulsive part. Application of the field shifts the other two solutions to higher values of h as can be seen from the shift of the point P with voltage. The primary effect of the electric field can be seen in fig. 4.6. We see from the

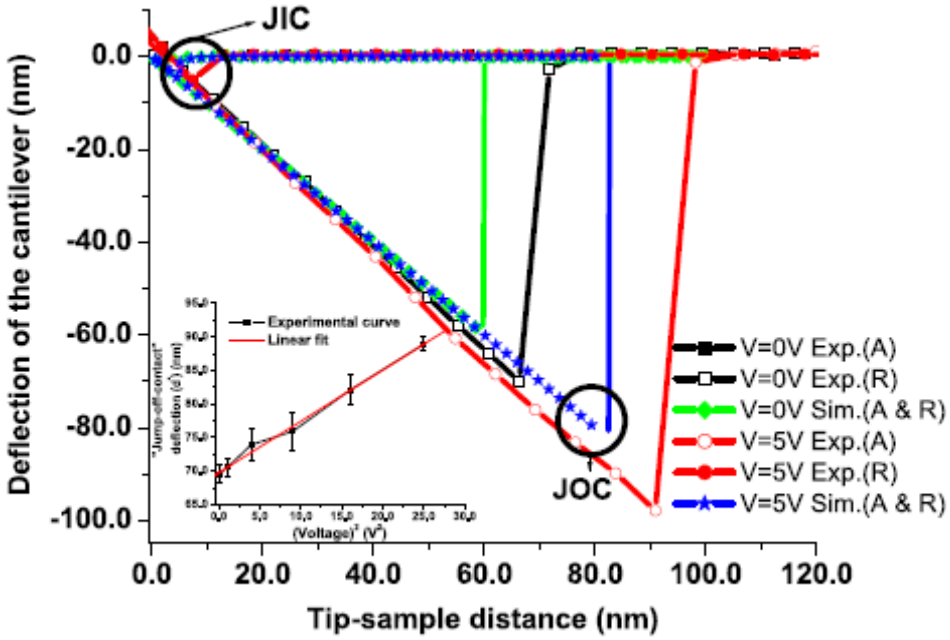

Figure 4.6 Plot of d-h curves for v = 0V and v = 5V (both experimental and simulated curves are shown). The inset shows v^2 dependence of d^*.

d−h curves that h^* and d^* increase with increase of the applied voltage between the tip and the sample. We find that even a moderate v = 5V can shift h^* and d^* by nearly 25% to 30%. The inset in fig. 4.6 shows the quadratic dependence of d^* on v. Therefore, everything remaining constant, the applied voltage can distinctly shift the f-h curves and the JOC points can be tuned by applying an electric field.

The second important observation is shown in fig. 4.7 which shows a set of and d^* (h^*) data plotted as a function of the step size δh for four different applied voltages. The data have been obtained from the typical d−h curves by only using different values of δh keeping other parameters fixed. The data shown in fig. 4.7 have been taken using UHV-AFM, therefore, there are two regions (no region C) in the data. In region A, occurring at higher step size, we find that for $\delta h \geq \delta h_{c1}$, d^* (h^*), reaches a limiting value which is independent of δh as already has been discussed earlier in this chapter. In region B, d^* (as well as h^*) keep on increasing as δh is reduced. The step size for which the cross over from region A to B occurs is marked as δh_{c1}. These figures clearly show that the applied field not only increases the d^* and h^*, it also sifts the value of δh_{c1} to a higher value.

To show the effect of the field, we present an important observation that all the curves shown in the fig. 4.7 can be merged uniquely to a single curve (see the inset) using a voltage dependent shift. We have shown the merged plot of d^* as a function of δh. We have applied two shift relations - i) to scale the deflection of the cantilever d^* at different voltages and ii) to scale the step sizes for different voltages. The cross over step-size δh_{c1} was found to have clean $v^{2/3}$ dependence. To scale d^* and δh_{c1} for $v \neq 0$, the data files have been divided by a factor Av^2 and $Bv^{2/3}$ respectively, where A and B are proportionality constants. It can be seen that ξ shifts to higher value as v is increased and $\xi \propto v^{2/3}$ as $\delta h_{c1} \sim \xi$ in region-A. We confirm this also from experiment. Using the equations and the procedure described above, we can simulate the d − h curves and compare them with experiment. This is shown in fig. 4.6. The parameters of the simulation are $(HR_t)_{eff}=10.2\text{x } 10^{-27}$ N.m^2 and a0=0.25 nm.

The simulated d − h curves agree very well with the observed curves and show the shift of d^* and h^* to higher values as v is increased. The d^* as a function of v is shown in fig. 4.6 (in the inset) and the observed quadratic dependence thus can be explained. Shift of d^* and h^* to higher values on application of v happens essentially due to shift the solutions $\tilde{d}_2$ and $\tilde{d}_3$ to higher h.

We have also simulated the variation of the d^* as a function of δh and shown in fig. 4.7. It matches quite well with our experimental data as shown in fig. 4.7. The shift of d^* (and h^*) for a given δh has v^2 dependence as shown before. Thus to make all curves coincide a shift is used. The shift of the δh_{c1} to make the curves coincide has $v^{2/3}$ dependence. This can be explained as follows. The quantity δh_{c1} is ~ ξ. Thus the shift of P to higher value for $v \neq 0$ makes ξ and hence δh_{c1} larger. From the solution of the equations we find that $\delta h_{c1} \approx \xi \approx (1.12H_{eff}R_t/k_c)^{1/3}$. Since $H_{eff} \propto v^2$, one would expect that $\delta h_{c1} \sim H_{eff}^{1/3} \sim v^{2/3}$. A plot of δh_{c1}^3 vs. V^2 in the inset of fig. 4.8 shows that this dependence indeed exists.

This also explains the experimental data and also the shifting used in fig. 4.7. The essential physics can be explained in the following way. The force due to the applied electric field adds to the force term due to the van-der-Waals force and gives rise to an enhanced effective Hamaker constant H_{eff}. The positions of the instabilities (i.e, JOC and JIC) are determined by the solutions $\tilde{d}$'s which are shifted to higher h on enhancement of

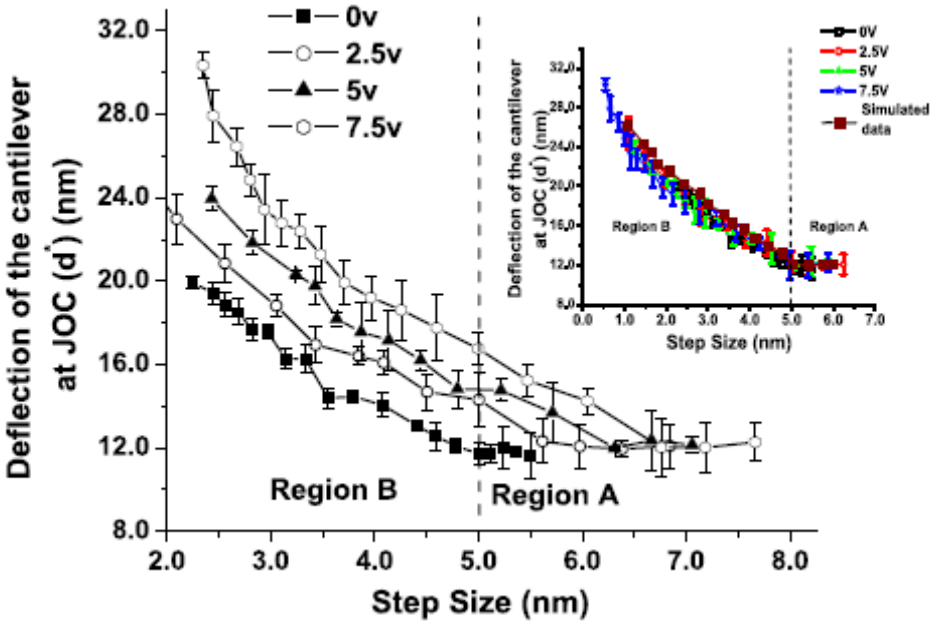

Figure 4.7 Variation of d^* with step size as a function of bias voltages is shown. All the curves merge to a single one (as shown in the inset) after doing the proper shifting mentioned in the text. The simulated curve (closed symbol) is also shown in the inset.

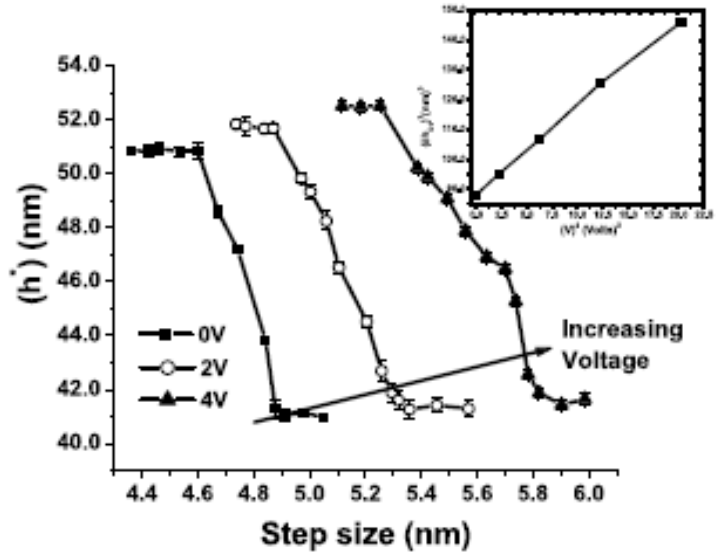

Figure 4.8 Variation of h^* with step size as a function of bias voltage. The closed squares show the curve for v=0V, the open circles for v=2V and the closed triangles for v=4V. Variation of δh_{c1} as a function of applied voltage (v) is shown in the inset.

H_{eff}. The enhanced H_{eff} will thus make JIC and JOC distance larger and will also shift δh_{c1} to higher values.
We have also checked the behaviour of h^* (d^*) as a function of δh in presence of electric field using AFM in ambient condition. The observed behaviour is shown in fig. 4.8. In this case we have seen all the three regions (A, B and C) as mentioned earlier in case of data taken in absence of electric field. We also observe a shift of δh_{c2}, h^*_{max} and d^*_{max} to higher values on application of electric field. This instability is related to water bridges [20]. It has been seen recently that water bridges become more stable in an applied electric field. The stability of the water bridge will be reflected in enhancement of l_{brg} in an applied electric field leading to enhancement of the attractive force as shown in [20].

4.4 Conclusions:

In summary, we have shown that the static d-h curves for an AFM, depends on the intrinsic instability of the microcantilever of the AFM. The phenomena like JIC and JOC occur even in absence of water bridge snap off as in an UHV-AFM and on hydrophobic surface. At larger step sizes, the intrinsic instability dominates over the "snap off" instability, leading to erroneous results in the calculation of these forces. The instabilities due to "snap-off" forces dominate at smaller step sizes. We have also shown experimentally that the intrinsic instability due to cantilever can be controlled by an applied electric field. The applied field shifts the instability points. We show how to tune and quantitatively evaluate the effective tip-sample interaction when the electric field is applied.

Bibliography

[1] F. Chen, G. L. Klimchitskaya, V. M. Mostepanenko and U. Mohideen, Phys. Rev. Lett. 97 170402 (2006).
[2] Mykhaylo Evstigneev, Andr´e Schirmeisen, Lars Jansen, Harald Fuchs and Peter Reimann, Phys. Rev. Lett. 97 240601 (2006).
[3] Sergey N. Medyanik, Wing Kam Liu, In-Ha Sung and Robert W. Carpick, Phys. Rev. Lett. 97 136106 (2006).
[4] T. Trevethan, M. Watkins, L. N. Kantorovich and A. L. Shluger, Phys. Rev. Lett. 98 28101 (2007).
[5] Ferdinand K¨uhner, Matthias Erdmann and Hermann E. Gaub, Phys. Rev. Lett. 97 218301 (2006).
[6] Nolan C. Harris, Yang Song, and Ching-Hwa Kiang, Phys. Rev. Lett. 99 68101 (2007).
[7] G. Binning, H. Rohrer, Ch. Gerber, and E. Weibel, Phys. Rev. Lett. 49 57 (1982).
[8] B. Cappella and G. Dietler, Surface Science Reports 34, 1 (1999).
[9] B. Cappella, P. Baschieri, C. Frediani, P. Miccoli and C. Ascoli, Engineering in Medicine and Biology Magazine IEEE 16, 58 (1997).
[10] H. H. Wen, A.M. Bar´o and J.J. S´aenz, Jour. Vac. Sci. Tech.B 9, 1323 (1991).
[11] M. He, A.S. Blum, D.E. Aston, C. Buenviaje, R.M. Overney and R. Luginb¨uhl, Journal Of Chemical Physics 114, 1355 (2001).
[12] J. Grobelny, N. Pradeep, D.-I. Kim and Z.C. Ying, Applied Physics Letters 88, 091906 (2006).
[13] Veeco Instruments Inc. Corporate Headquarters 100 Sunnyside Blvd. Ste. B Woodbury New York 11797-2902.
[14] Omicron NanoTechnology GmbH. Limburger Str. 65232 Taunusstein.
[15] J. Israelachvili, Intermolecular and Surface Forces (Academic Press, London) (1991).
[16] Derjaguin B V, Muller V M and Toporov Y P, Jour. Colloid Interface Sci., 53, 314 (1975).
[17] D. Andrienko, P.Patr´ıcio and O.I. Vinogradova, Journal Of Chemical Physics 121, 4414 (2004).
[18] S. Hudlet, M. Saint Jean, C. Guthmann, and J. Berger, Eur. Phys. J. B 2, 5 (1998).
[19] G.M. Sacha, A. Verdaguer, and M. Salmeron, J. Phys. Chem. B 110, 14870 (2006); G.M. Sacha, J. J. S´aenz, M. Calleja and R. Garc´ıa, Phys. Rev. Lett. 91 056101-1 (2003).
[20] S. Hudlet, M. Saint Jean, C. Guthmann, and J. Berger, Eur. Phys. J. B 2 5 1998.

Chapter 5

Effects of Nonlinear Forces on Dynamic Mode Atomic Force Spectroscopy

In previous chapters, the effect of nonlinear tip-sample forces on static mode atomic force spectroscopy has been discussed. In this chapter, we describe the effects of nonlinear tip–sample forces on dynamic mode atomic force microscopy and spectroscopy. Dynamic atomic force microscopy is a standard technique for imaging and the analysis for surfaces at the nanometer scale. In order to estimate material properties from the microscope data it is important to understand the nonlinear dynamics in the tip-sample interaction. In dynamic mode force spectroscopy one measures the vibration amplitude (A) as a function of tip-sample distance (h). The jumps and hysteresis observed in the vibration amplitude (A) versus tip–sample distance (h) curves have been traced to bistability in the resonance curve. A numerical analysis of the basic dynamic equation was used to explain the hysteresis in the experimental curve. It has been found that the location of the jump (mentioned below as jump I) occurs at higher tip-sample separation in the A–h curve depends on the frequency of the forced oscillation relative to the natural frequency of the cantilever. This jump is always a consequence of the existence of two oscillation states for the same conditions. In the other case, the jump (mentioned below as jump II) occurs at smaller tip-sample separation arises because of inherent instability of the cantilever moving in a non-linear force field as has been observed in case of static mode spectroscopy also.

5.1 Introduction

Atomic force microscopy (AFM) has emerged as a powerful tool for the study of material surfaces, particularly in the case of non-conducting materials [1]. The dynamic force microscope (DFM) has turned out to be a major improvement over the original static mode AFM. DFM methods offer three main advantages with respect to static (contact) AFM. First the tip motion is sensitive to both forces and force gradients. Suitable experimental setups may allow simultaneous force and interatomic potential mapping. Second, in contact AFM the tip-sample interaction is measured following the cantilever's deflection. In dynamic AFM the oscillation amplitude, the frequency, and the phase shift, as well as the cantilever deflection, may be recorded. This opens several channels for simultaneous data acquisition, each of them describing a different property. Third, the forces required to obtain a stable signal in contact AFM may involve some sort of sample damage that prevents high resolution imaging. This applies, in particular, to image

compliant materials (biomolecules and polymers) in air or semiconductors in ultrahigh vacuum. DFM methods may substantially reduce the sample damage. The above advantages are being exploited by using different dynamic AFM modes [2-8]. The DFM is generally operated in two modes:

(a) The intermittent contact (tapping) mode, in which the probe microcantilever intermittently touches the sample surface. This occurs when the probe microcantilever is very close to the sample surface and is in the repulsive regime of the atomic forces in part of its oscillation cycle. While this is in itself a very powerful technique, it has the disadvantage of not being completely non-destructive.

(b) The other mode is the non-contact mode in which the microcantilever never touches the sample surface since the DFM is operated in the attractive regime of the atomic forces, which is quite far off from the sample surface with respect to the distances in the tapping mode.

This method has the advantage of being non-destructive and hence can be used to study soft materials, e.g., biomolecules but precise alignment is needed for this mode so it is better to go for the justified one. The quantity that is generally measured in dynamic force spectroscopy (DFS) is the variation of the amplitude (A) of a vibrating microcantilever as a function of distance (h) between the microcantilever and the sample. In DFS, as the cantilever tip approaches the sample, it starts moving in nonlinear force field. This particular aspect shows up in the (A–h) curve and as shown in this chapter, can contribute to such effects as hysteresis. A schematic diagram of the (A-h) curves is shown in fig. 5.1.

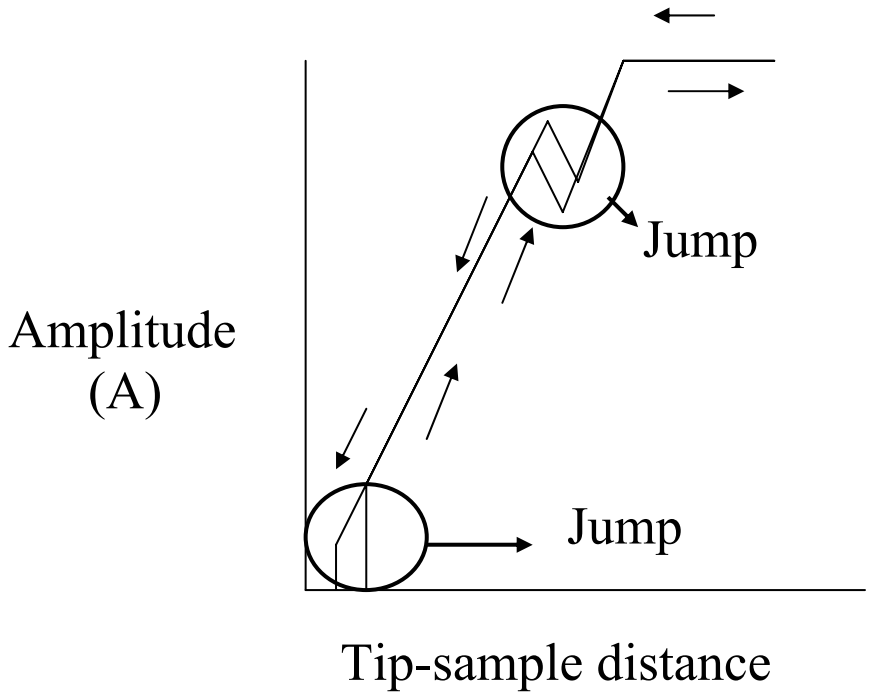

Figure 5.1 Schematic diagram of the amplitude versus distance curve in dynamic mode AFM. The arrows show the direction of motion of the cantilever.

One of the biggest challenges in the study of surfaces using DFS comes directly from the principles on which the DFS operates. Since, the DFS is a probe driven by atomic forces, which are intrinsically non-linear, a very careful analysis of the behavior of the microcantilever is required in order to interpret the DFS data. The microcantilever, vibrating in flexure, itself has a nonlinear response. Numerous attempts have been made in this direction over the past several years, to understand the effect of the non-linear atomic forces on the response of the microcantilever [9].

Gleyces et al. [10] were the first to describe non-linear dynamic effects in scanning probe microscopy experiments. They measured the oscillation amplitude as a function of the excitation frequency for an STM tip vibrating in the proximity of a surface. They observed that for some frequencies two different values of the amplitude could be obtained. Anczykowski et al. [11] invoked bi-stability to explain hysteresis effects in amplitude versus distance curves. On the other hand, Aime and co-workers [12] proposed a non-linear dynamics analysis to explain the dependence of the hysteresis on the strength of the attractive interaction. Furthermore, the contributions of Garcia and San Paulo [13, 14, 15], Wang [16], Nony et al. [17] and Marth et al. [18] have emphasized the intrinsic non-linear character of the tip motion in AM-AFM.

Earlier works have already established the basic equation that governs the tip motion [8, 19]. Martin, Williams and Wickramasinghe explained the motion of a vibrating tip (cantilever) and its response to tip-surface forces in terms of a linear (harmonic) model [20]. The gradient of the force between tip and sample modifies the compliance of the cantilever, hence including a change in the oscillation amplitude due to the shift of the tip resonance, $\Delta\omega/\omega_0 = - \partial F_{ts}/\partial z/2k_c$, where F_{ts} is the tip-sample interaction force and k_c is the spring constant of the cantilever. The linear approximation has been improved and extended by several authors to consider the tip motion as described by a weakly disturbed harmonic oscillator [3]. In the process, linearized models have become the effective paradigm encompassing different dynamic AFM modes.

In spite of the very extensive experimental use of the tapping-mode AFM, a detailed understanding of the observed tip's motion as a function of tip-sample separation is still emerging. This lack of understanding makes it difficult to interpret tapping mode AFM images in terms of topographic variations. Initially, it was assumed that at one end of the oscillation the tip established mechanical contact with the sample surface [6]. Repulsive forces were thought to be the main mechanism to control the amplitude, although several experimental [13, 16, 17] and theoretical [13, 18] results pointed out that long-range attractive forces could also contribute to the reduction of the amplitude.

In most situations, the amplitude decreases with the tip-sample proximity as shown in fig. 5.1. However, a sharp jump (mentioned as jump I in fig.5.1) in the amplitude curves has been reported by experiments and simulations [13, 16]. This jump has been attributed to the onset of repulsive regime, i.e., the oscillation switches from a purely noncontact (long-range attractive forces) to tapping mode (attractive and repulsive) [21]. However, it has been found that a steplike discontinuity in the amplitude curve is not an exclusive characteristic of the noncontact to intermittent contact transition. It has also been shown that a discontinuity is always a consequence of the existence of two oscillation states [22]. The transition between the attractive and repulsive regime may be smooth or steplike, depending on free amplitude and material properties. The amplitude reduction is solely controlled by the attractive regime [22].

In this chapter, we revisit the issue of the effect of nonlinearity on the cantilever dynamics in details. We present a numerical solution of the equation of motion of the cantilever in the DFS that includes the non-linear aspect of the probe–surface interaction. We have shown that the amplitude of oscillation of the microcantilever depends strongly on the distance (h) between the mean position of the microcantilever and sample surface. We have also shown that the amplitude decreases rapidly once the cantilever reaches the attractive regime of the atomic forces and goes to zero at very small distances, corresponding to the repulsive regime of the atomic forces. The amplitude decreases smoothly as the tip is brought closer to the sample until it shows a sudden jump at a point (henceforth referred to as jump I). If the probe–sample separation (h) is reduced, the vibration amplitude (A) of the cantilever undergoes a change. We have shown here that the changes in slope of the amplitude (A) versus h curves can be understood in terms of the shift in resonance frequency of the cantilever due to the atomic forces. It is shown here that nonlinearity can lead not only to shift in the resonance frequency but can also dramatically change the shape of the resonance curves. The numerical solution has been used to calculate the A–h curves. The experimental data (A versus h curves) have been used to estimate the forces which have been used as input into the simulation to calculate the various properties of the cantilever dynamics. Use of the specific interaction force in understanding interaction of the tip with the substrate is very important. However, some of the observed features are qualitatively similar irrespective of the force of interaction. In our calculation, we have used a combination of van-der-Waals force and the Derjaguin-Muller-Toporov (DMT) forces [23, 24].

Beyond the point of jump I, the amplitude again decreases smoothly [4] until there is another jump (henceforth referred to as jump II) observed at very small tip-sample distance both in the approach and the retract curve. Though there are several studies available to understand the reason behind jump I in (A-h) curves but almost no attention has been paid to understand the second jump (jump II) observed in DFS curve. Here we have shown that this jump (jump II) is observed in the experimental (A-h) curves as well as in the simulated curves. The position of this jump is dependent on the Hamaker constant (H) of the tip-sample assembly, radius of curvature of the tip (R_t), spring constant of the cantilever (k_c) (in case of approach path) and also on the step size of data collection (in case of retraction path). It has been shown that these jumps are related to the features seen in static mode spectroscopy – e.g., “jump-into-contact” and “jump-off-contact”. We have also explained here why this jump occurs in (A-h) curves at very small tip-sample separation.

The chapter is arranged as follows: In Section II, we present the experimental data for the amplitude (A) versus h curves. In Section III, we introduce the model for calculating the amplitude versus distance curves and the resonance curves. In Section IV, we discuss the results. In Section V, we conclude.

5.2 Experimental Results

The experiments were performed using a CP-II scanning probe microscope (Veeco Instruments Inc. [25]) on a silicon substrate with native oxide layer on it (in air). The silicon wafers were cleaned in an ultrasonic cleaner with Acetone, Propanol (Isopropyl

alcohol) and Milli-Q-grade water. Presence of the native oxide makes the Si hydrophilic. The cantilever used for DFS had a tip made of phosphorus doped silicon.

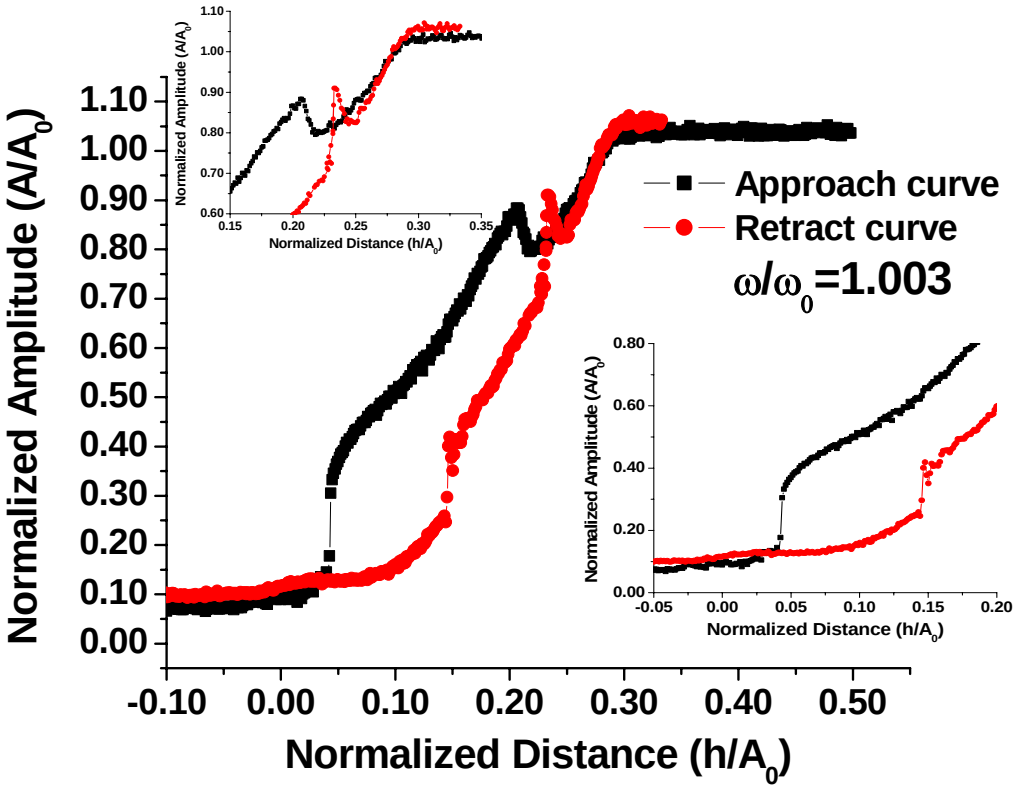

Figure 5.2 Amplitude versus distance curves (approach and retract) on silicon in air (experimental data). The free vibration amplitude A_0 = 75 nm, spring constant of the cantilever k_c = 20 N/m, resonance frequency of the cantilever ω_0 = 320.10 kHz, set frequency ω= 321.06 kHz (ω/ω_0 = 1.003). In the upper (left hand side) inset of the figure the region around jump I has been magnified and in the lower inset (right hand side) the region around jump II has been magnified.

The spring constant of the cantilever was 20 N/m (Manufacturer's value) and the free vibration resonance frequency ω_0 of the cantilever was 320.1 kHz. This is derived from the resonance curve of the cantilever for the experiments. The cantilever was initially fixed at a height of about 3.75 μm above the sample and the driving frequency (ω) was set at 321.06 kHz (i.e. slightly above the free vibration resonance frequency of the cantilever, ω = 1.003 ω_0) for obtaining the (A-h) curves. In the experiment, this shift in frequency is necessary in order to keep the system in the non-contact mode. The cantilever was then made to approach the sample while data was taken for the distance of the cantilever from the sample (h) and the corresponding amplitude. After the cantilever had hit the surface of the sample it was retracted back to the distance of 3.75 μm and data

were taken on the return path also. We have also taken the amplitude vs. distance curves for $\omega = 0.997\ \omega_0$ (slightly below the free vibration resonance frequency of the cantilever). The rate of data collection was 0.5 Hz for all the data presented here.

The amplitude (A) versus h curves was taken on the samples for free amplitude 75 nm. Figure 5.2 shows a typical set of data obtained for the above mentioned starting amplitude for the silicon at $\omega = 1.003\omega_0$. Note that the tip–sample distance is obtained from the relative displacement of the piezo positioner, on which the sample is kept and the distances are calculated relative to the "set point" (i.e., the tip–sample distance set before the experiment is performed). In order to get the correct tip–sample distance one has to know the "zero-level" i.e., the position of the sample surface. This is generally a difficult task.

It has been discussed in detail in chapter three. Hence, it is the usual practice to assume that the sample surface (h = 0) is defined by the point at which the amplitude becomes zero during the approach of the cantilever.

The amplitude versus distance curve shows two characteristic jumps and hysteresis around the jumps. The jump I occurs both for the approach curve and the retract curve where the output amplitudes of the cantilever is approximately 57.0 nm and 65.25 nm respectively. In the upper (left hand side) inset of the figure 5.2 we show the region around the jump I to clearly display the hysteresis and

in the lower (right hand side) inset we show the region around jump II. From figure 5.2, we can see that jump II occurs at h = 3.0 nm for the approach curve and at h = 11.25 nm for the retract curve.

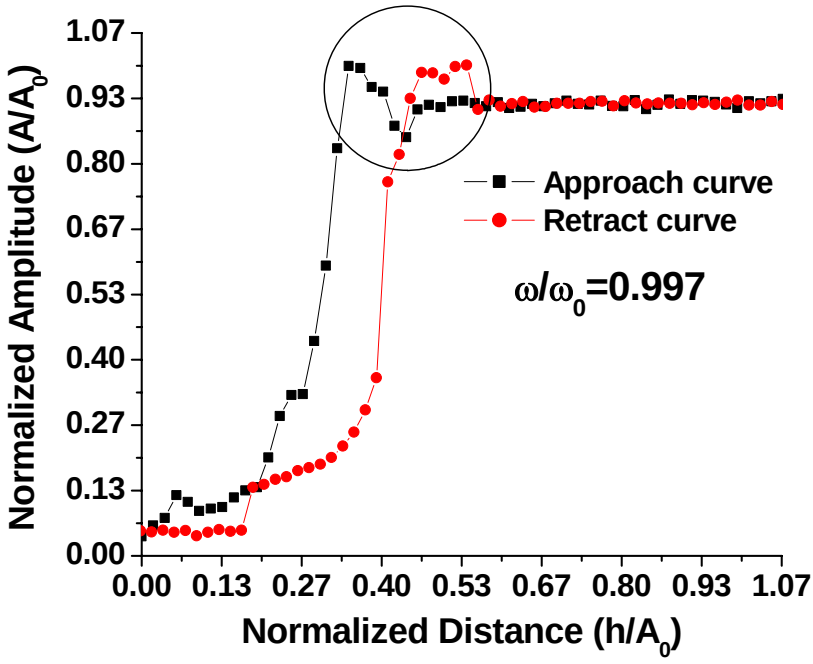

Figure 5.3 Amplitude versus distance curves (approach and retract) on silicon in air (experimental data). The free vibration amplitude A_0 = 75 nm, spring constant of the cantilever k_c = 20 N/m, resonance frequency of the cantilever ω_0 = 320.10 kHz, set frequency ω= 319.14 kHz ($\omega/\omega_0 = 0.997$).

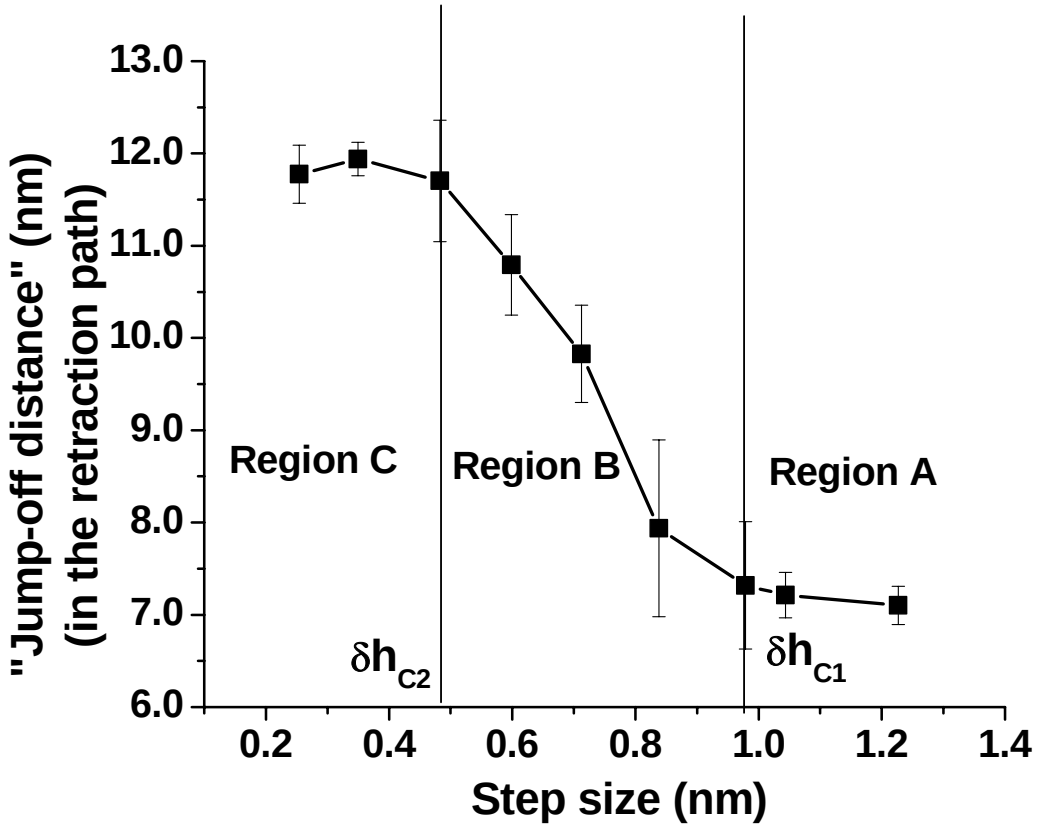

Figure 5.4 Variation of the position of jump II in the retract path of (A-h) curves with step size (experimental data).

Figure 5.3 shows the (A-h) curves for $\omega = 0.997\omega_0$. The other parameters are same as for the (A-h) curves taken at $\omega = 1.003\omega_0$. From fig. 5.3 we can see that position of jump I has been shifted to higher tip-sample separation and higher amplitude values compared to the position of the jump occurred in the (A-h) curves for $\omega = 1.003\omega_0$.

We have also studied the effect of step size on the DFS curves. In chapter four we have shown that "jump-off-contact" position in the static mode spectroscopy curve (occurs in the retract path) depends strongly on the step size (δh) of the data collection. We have defined the step size as follows. If the maximum distance between the cantilever and the surface is h_{max} and the number of data points acquired is N, then $h_{max} = N\delta h$. In case of our experiments N has been kept fixed at 500 (in one direction) and hence δh can be varied by varying h. In case of (A-h) curves in dynamic mode we have found that the position of jump II in the retract path also depends on the step size of data collection. In figure 5.4 we have shown the variation of the position of jump II in the retract path of the (A-h) curves with the step size. From the figure we can see that the position of jump II (in the retract path) shifts to higher tip-sample separation as δh is reduced (referred as region B in figure 5.4) and we can also see two saturation regions for $\delta h \geq \delta h_{c1}$ (for larger step

sizes, region A in figure 5.4) and for $\delta h \leq \delta h_{c2}$ (for smaller step sizes, region C in figure 5.4). In these two regions the position of jump II (in the retract path) reaches a limiting value which is independent of step size. All these features are exactly similar with that observed in case of the variation of "jump-off-contact" position with step size for the static mode spectroscopy curves. The data shown here are representative of a large number of data collected in the controlled experiment. It is important to mention here that jump II in the approach curve does not depend on step size for a particular value of H, R_t and k_c. Later on we show that jump II has the same physical origin as similar features in static AFS curve. We note that this is the first time that such a clear connection between these two types of force spectroscopy curves have been established.

5.3. Model Calculation

The aim of this section is to provide the fundamental concepts needed to understand the tip motion in AM-AFM. The description of the tip dynamics is performed for a tip-surface interaction potential with long-range van-der-Waals forces and contact repulsive forces. Even with simplified assumptions, those forces have power law dependencies on the tip-surface separation. The non-linearity of the interactions has deep implications in the resulting tip motion. It also makes difficult to find analytical solutions.

The equation that describes the tip motion is sensitive to both tip-surface and tip-environment interactions. Technical details of the operation of a dynamic AFM depend on the medium. Operation in air and liquids is usually performed with an amplitude modulation feedback (AM-AFM) while operation in vacuum requires a frequency modulation feedback. Here we focus our study on atmospheric pressure environments, i.e., AM-AFM systems with a quality factor (q) between 50 and 1000.

The equation of motion of the microcantilever is generally very complex, since one has to take into account not only the motion of the tip in presence of a medium (air or water) but also the bending of the beam of the microcantilever. In this calculation, we will, however, restrict ourselves to the motion of the tip. While a more sophisticated calculation is necessary to get a better fit for the experimental curves, we find that the approximation of treating only the motion of the tip captures all the generic features obtained in the experiments. The dominant contributions considered in the equation of motion of the cantilever are its elastic response, the hydrodynamic damping with the medium, the tip-sample interaction, and the excitation force. The resulting nonlinear, second-order differential equation of motion of the tip of the cantilever, whose mass is taken to be concentrated at the tip is given by,

$$m\ddot{d}(t) + \eta \dot{d}(t) + k_c d(t) = f_{ts}(h + d(t)) + F\cos(\omega t) \qquad (5.1)$$

where m is the effective mass of the cantilever, d(t) denotes the position of the tip at time t relative to its equilibrium position, η is the friction coefficient, k_c is spring constant of the cantilever, f (d(t)+h) is the instantaneous force acting on the microcantilever tip when its fixed end is at a distance h from the surface, F is the amplitude of the oscillating driving force on the microcantilever and ω is the frequency of the oscillating force. $\dot{d}$ and

$\ddot{d}$ are the first and second derivatives of the position d(t) with respect to time t. The free oscillation frequency of the microcantilever is given by

$$\omega_0 = \sqrt{\frac{k}{m}} \tag{5.2}$$

Equation (5.1) can be rewritten as,

$$\ddot{d}(t) + \lambda \dot{d}(t) + \omega_0^2 d(t) = \frac{1}{m} f_{ts}(h + d(t)) + \frac{1}{m} F\cos(\omega t) \tag{5.3}$$

where $\lambda = \eta/m$.

The solution of a harmonic oscillator with damping has a transient term and a steady solution as shown in figure 5.5. Initially, both motions are prominent, however, after a time $2q/\omega_0$, the transient term is reduced by a factor of 1/e, from then on the motion is dominated by the steady solution. The steady term is a sinusoidal function (harmonic) with a phase lag with respect to the excitation force.

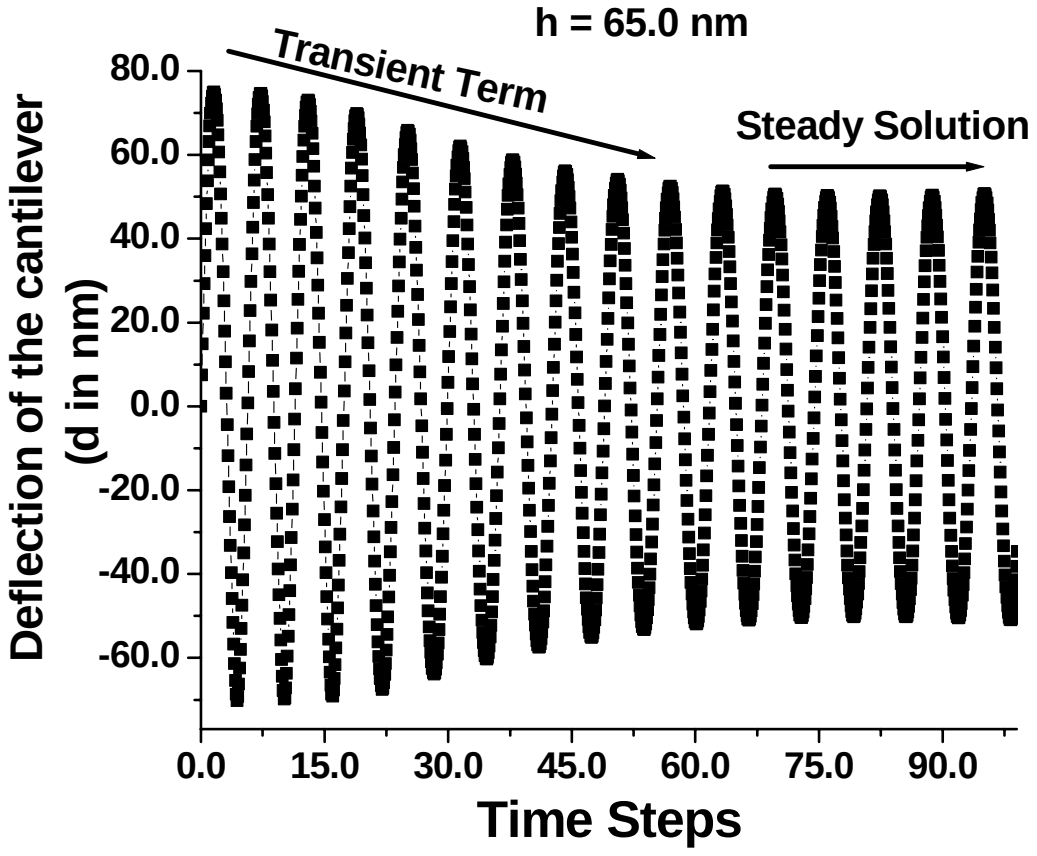

Figure 5.5 It shows the solution of a harmonic oscillator with damping having a transient term and a steady solution.

The general solution of (5.3) is complicated, due to the presence of the nonlinear atomic force $f_{ts}(d+h)$. The complication arises because $f_{ts}(d+h)$ is a function of d(t). If the atomic forces are absent (e.g., when the microcantilever is far away from the sample surface), equation (5.3) reduces to the well known equation of a harmonic forced damped oscillator. At small times, this system shows a transient behavior, but at large times, it oscillates with the frequency of the harmonic forcing term i.e., ω. The interaction in principle can have a velocity [d(d(t))/dt] dependent frictional force term. For simplicity we club all the velocity dependent frictional forces into one term. The above equation implies several assumptions. (i) It considers the cantilever-tip ensemble as a point-mass spring. (ii) The q factor used here is independent of tip-sample separation. The first assumption ignores the contribution to the cantilever motion of the higher flexural modes of the lever [26]. The second one neglects changes in the hydrodynamic damping of the cantilever during its motion [27].

As the microcantilever approaches the surface of the sample, the nonlinear terms begin to make appreciable contribution to the solution of the equation of motion of the microcantilever. As long as the microcantilever is not too close to the surface, the dominant physical effect of the nonlinear forces is to introduce higher harmonics into the motion of the microcantilever. Here we have solved eq. (5.3) numerically and presented the results below.

We solve the equation of motion (5.3) exactly by numerical techniques. The tip-sample interaction contains attractive and repulsive forces. Long range attractive forces are derived from the non-retarded van-der-Waals energy for two atoms in vacuum. Assuming additivity, for a sphere-flat geometry the van-der-Waals force is

$$F_{TS}(z) = -\frac{HR_t}{6z^2} \quad \text{for } z > a_0 \tag{5.4}$$

where H is the Hamaker constant and R_t is the tip radius and z= d(t)+h where d(t) is the instantaneous deflection of the cantilever and h is the tip–sample distance. a_0 is an intermolecular distance. For separations $z < a_0$, the resulting van-der-Waals force is identified with the adhesion force given by the Dejarguin-Muller-Toporov (DMT) theory, [23, 24]

$$F_a = 4\pi R_t \gamma = \frac{HR_t}{6a_0^2} \tag{5.5}$$

where γ is the surface energy.

In addition to the adhesion force, during the contact ($z < a_0$) there are repulsive forces arising from Pauli and ionic repulsion. The repulsive force and the sample deformation are modeled by using the DMT contact mechanics,

$$F_{TS} = -\frac{HR_t}{6a_0^2} + \frac{4}{3}E^*\sqrt{R_t}(a_0 - z)^{\frac{3}{2}} \tag{5.6}$$

$$\frac{1}{E^*} = \frac{(1-\nu_t^2)}{E_t} + \frac{(1-\nu_s^2)}{E_s} \tag{5.7}$$

where E_x, υ_x are the tip (sample) elastic modulus, the Poisson coefficients, respectively and E* is the effective elastic modulus between the tip and the sample.
The numerical simulation has been performed for silicon dioxide (SiO_2) E =70 GPa, γ =31 mJ/m^2, H =1.2× 10^{-20} J [22]. A Poisson coefficient of 0.3 has been used for the materials. For the cantilever-tip system we have used a radius R_t = 50 nm, q = 50, k_c = 20 N/m. For our calculation the operating frequency (ω) is taken to be equal to $1.003\omega_0$. The simulated (A-h) curve is shown in figure 5.6 for $\omega = 1.003\omega_0$. In the upper (left hand side) inset of the figure the region around jump I has been magnified and in the lower inset (right hand side) the region around jump II has been magnified. We have also calculated the (A-h) curves for $\omega = 0.997\omega_0$ as shown in figure 5.7. Here also we can see that the position of jump I has been shifted to higher tip-sample separation for $\omega = 0.997\omega_0$ as has been observed for experimental data.

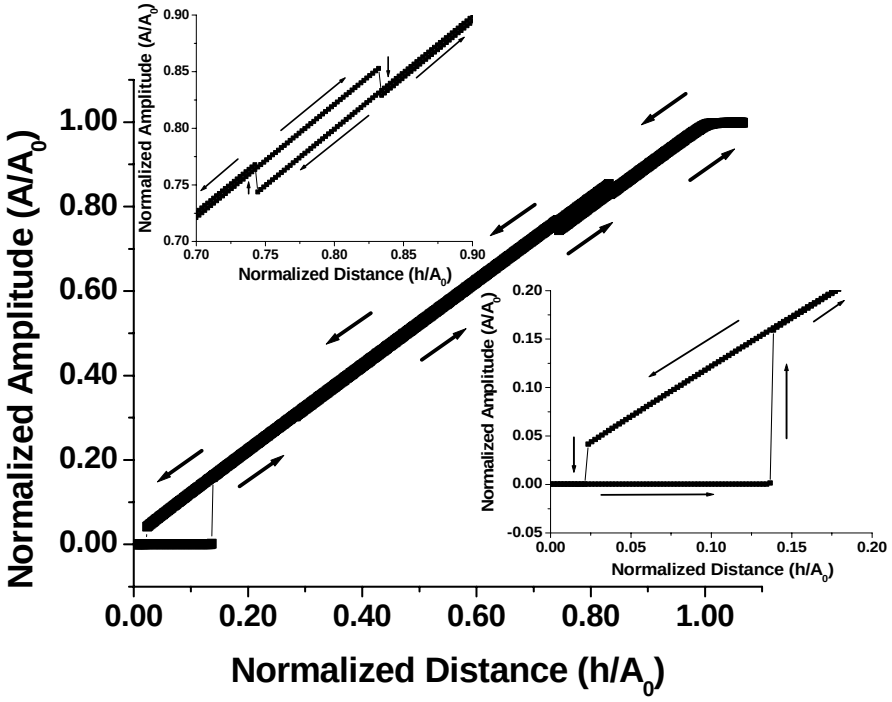

Figure 5.6 Amplitude versus distance curves (approach and retract) on silicon in air (simulated data). The free vibration amplitude A_0 = 75 nm, spring constant of the cantilever k_c = 20 N/m, ω/ω_0 = 1.003. In the upper (left hand side) inset of the figure the region around jump I has been magnified and in the lower inset (right hand side) the region around jump II has been magnified.

5.4 Discussions

As can be seen from figure 5.6 a prominent outcome of our numerical result is the presence of two jumps in the amplitude distance curve as the cantilever approaches the sample and retracts back. Both experimental curves (fig. 5.2) and simulated curve (fig.

5.6) show these features. We have studied this aspect in detail, using van-der-Waals forces with adhesion forces and the observed features originate from the nonlinear nature of the interaction. The simulated results give us a quantitative way to understand the observed features in DFS curves. We note the following features. First, there is a flat region for large tip-sample separation in the amplitude versus distance curves (both in experiment and simulation). Second, when the cantilever starts to sense the long-range attractive force it reduces the effective

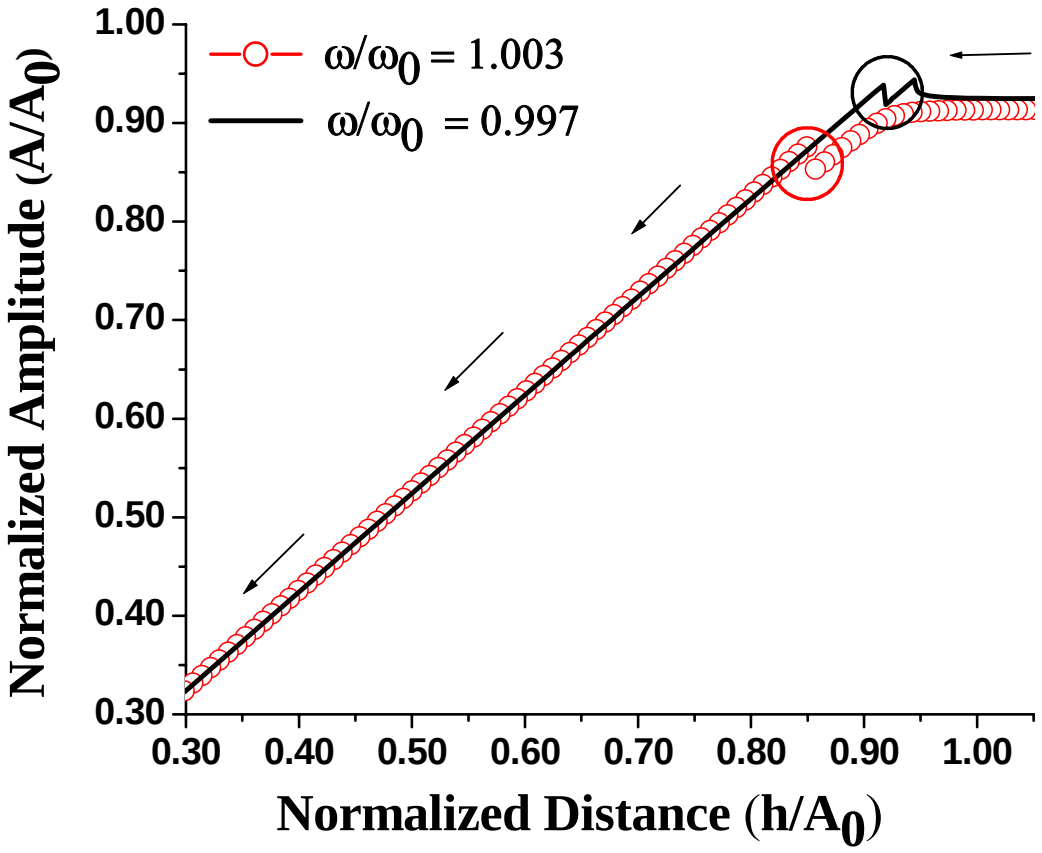

Figure 5.7 Calculated amplitude versus distance curves for ω/ω_0 = 0.997 (black) and ω/ω_0 = 1.003 (red).The free vibration amplitude A_0 = 75 nm, spring constant of the cantilever k_c = 20 N/m. Circles in the figure shows the positions of the jump I.

spring constant and hence the resonance frequency. Third, there is a transition region (jump I) (h/A_0 = 0.74) where the amplitude shows an increase [4]. Fourth, after the transition the amplitude decreases again linearly. Hysteresis loop is observed in the approach-retract curves around this region for the experimental curve and as well as for the calculated curve. Again we observe another jump in the (A-h) curves just before the amplitude becomes zero both in the approach and the retract part.

The first nontrivial region is the transition region (jump I) First and second regions are easy to understand. We will try to understand jump I that occurs at comparatively higher tip-sample separation. To understand the features seen in (A-h) curves we have calculated the resonance curves for the same system for different tip-sample separations (h), as shown in figure 5.8. The resonance curves for large tip-sample distances are Lorentzian in nature. As we reduce the tip-sample distance (h), the resonance curves begin to distort away from a Lorentzian [22]. It has been shown that a sideways deformation in the resonance curve is associated with a dominant attractive force while the stretching of the curve to higher frequencies reflects the dominance of repulsive interactions [22]. The nature of this distortion depends on the direction of the frequency sweep. In figure 5.9 we show the resonance curves for h = 56 nm (corresponding to the jump height of the approach curve) as the frequencies are changed from low to high frequencies (upward sweep) (indicated in the figure by (a) curves) and from high to low frequencies (downward sweep) (indicated in the figure by (r) curves). In Figure 5.10 we show the resonance curves for h = 62.26 nm (corresponding to the jump height of the retract curve)

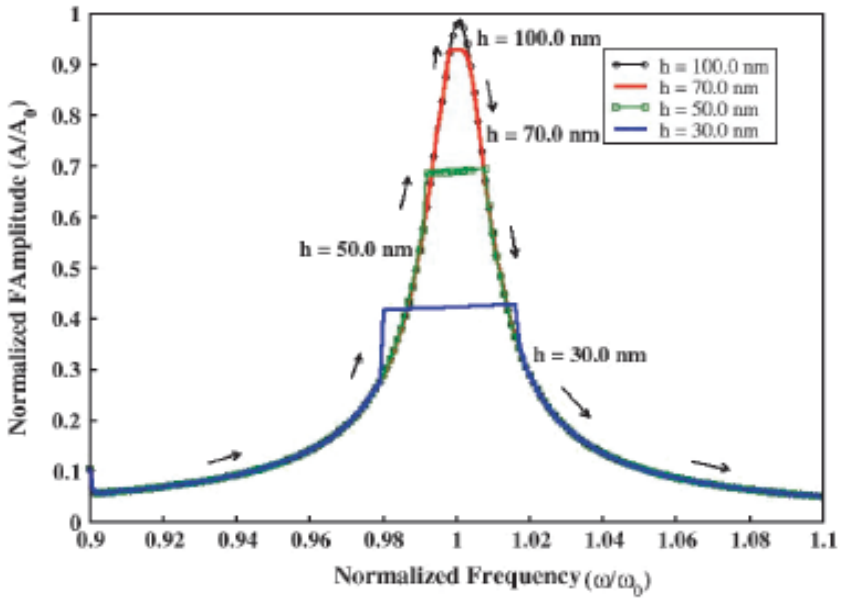

Figure 5.8 Calculated resonance curves for different tip–sample separations. The arrows indicate the direction of the frequency sweep.

as in figure 5.6. The resonance curve show a bistability in a range of frequencies, which has been studied extensively earlier [28]. The nature of the resonance curves also indicates the basic reasons behind the jump in the A–h curves. We explain this briefly below.

In the resonance curves obtained at height 56 nm, we observe that at $\omega/\omega_0 = 1.003$, the value of the amplitude (55.7 nm) is nearly equal to value of the amplitude given by the downward sweep curve (or the (r) curve). We find that at tip–sample distances slightly larger than 56 nm, during approach, the value of the output amplitude is given by the corresponding downward sweep resonance (r) curve for that height. At tip–sample distances slightly smaller than 56 nm, during approach, the output amplitude is given by

the corresponding upward sweep resonance (a) curve. Thus, at about h = 56 nm, there is a sudden jump in the amplitude from the downward sweep curve to the upward sweep curve. For the retract curve, the same pattern is repeated except that the jump occurs from

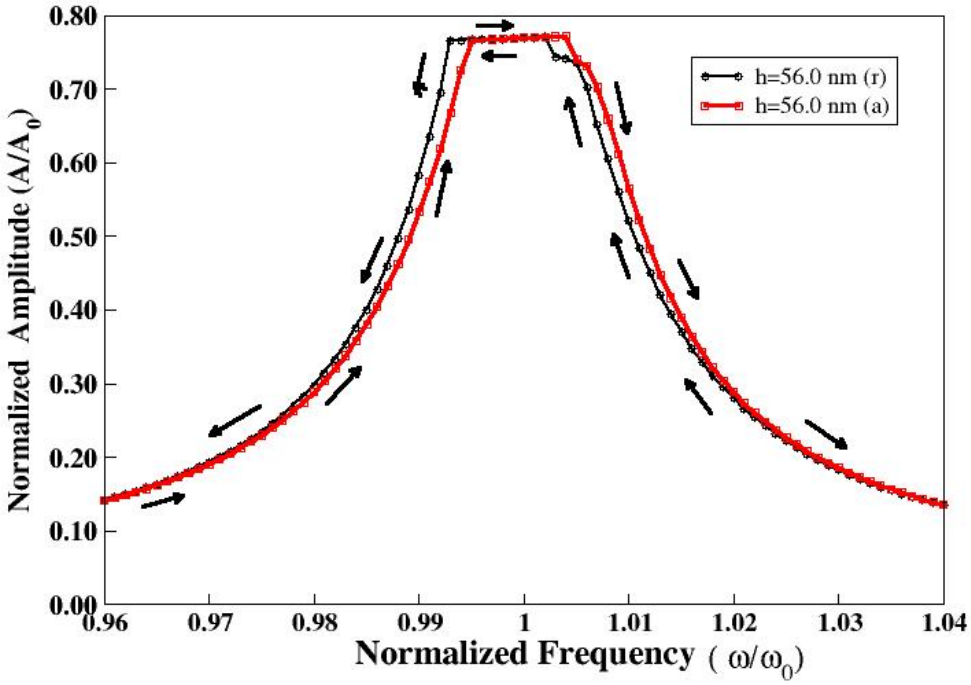

Figure 5.9 Calculated resonance curves for tip–sample distance h = 56 nm (upward sweep and downward sweep).The upward and downward sweeps are labeled as (a) and (r), respectively and are indicated by arrows.

the upward sweep resonance (a) curve to the downward sweep resonance curve (r) across h = 62.26 nm. Thus the approach and retract curves show a hysteresis behaviour [5] as well as a jump in the A–h curves as can be understood from the upward and the downward sweep of the resonance curves.

The present numerical analysis for the (A–h) curve has important implication for imaging in DFM. We note that the position, where the jump (jump I) in the (A–h) curves occurs, depends on the parameters of the force and the set frequency. In fact, when $\omega<\omega_0$, then the jump point actually shifts to larger tip-sample distances. When $\omega >\omega_0$, the jump point shifts to smaller tip–sample distances. This is shown in figure 5.7. In figure 5.7, we have plotted the amplitude versus distance curves (A–h) for $\omega = 0.997\omega_0$ and $\omega= 1.003\omega_0$ keeping the other parameters fixed. This is precisely why, we use $\omega>\omega_0$ for the non-contact mode DFM measurements—this makes sure that the hysteresis region shifts to lower values of tip–sample distances, thus making sure that we are always in one of the bistable branches. Similarly, in case of tapping mode DFM, where the tip–sample distances have to be small, we avoid the hysteresis region by shifting the jump (jump I) to higher values of tip–sample distances (by choosing $\omega<\omega_0$).

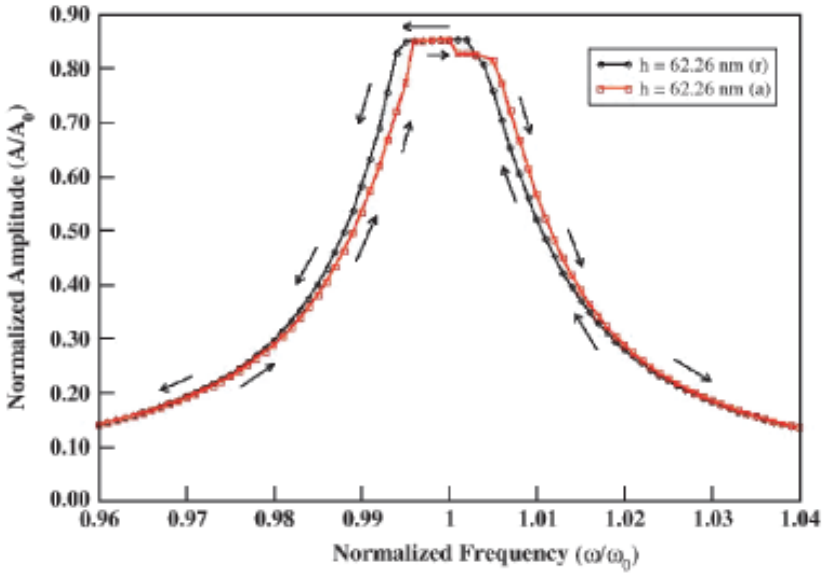

Figure 5.10 Calculated resonance curves for tip–sample distance h = 62.26 nm (upward sweep and downward sweep).The upward and downward sweeps are labeled as (a) and (r), respectively and are indicated by arrows.

It is an established practice in probe microscopy to attribute noisy or unstable data to a contaminated tip or a changing tip shape. However, the above example shows that in some cases noisy or unstable data only reflects the intrinsic structure of the tip motion. It also explains the manipulation of the observer with the driving frequency or set point amplitude as a process that modifies the tip's motion to reach a configuration where a single solution is available.

Now to understand the second jump (jump II) in the (A-h) curves as can be seen both in the experimental curve as well as in the simulated curve near smaller tip-sample separation we have to revisit the equation of motion of the cantilever given by eq. 5.3. At very small tip-sample separation, the amplitude of oscillation of the cantilever becomes very small (A~ 0). In that case, the forcing term of equation 5.3, i.e. $F\cos(\omega t)$ will be ~ 0 because $F = (A.k_c)/q$ and A is ~ 0. Therefore, at very small tip-sample separation equation 5.3 will effectively be reduced to the equation of motion of the cantilever in case of static mode spectroscopy as the forcing term is ~0. At small tip-sample separation the instability in the (A-h) curves arises solely because of the non-linear tip-sample interaction force. Figure 5.11 shows the average value of the deflection (normalized) of the cantilever as a function of the tip-sample distance (normalized) and also the simulated deflection-distance (d-h) curves in static mode for the same parameters. From the figure we can see that the mean deflection of the cantilever in dynamic mode shows all the features seen in the static mode (d-h) curves, that is, the "jump-into-contact" and "jump-off-contact". This is because if we take the average of the eq. 5.3, the last term in the equation, that is, $\langle F\cos(\omega t)\rangle$, will average out to be zero. Then eq. 5.3 will actually

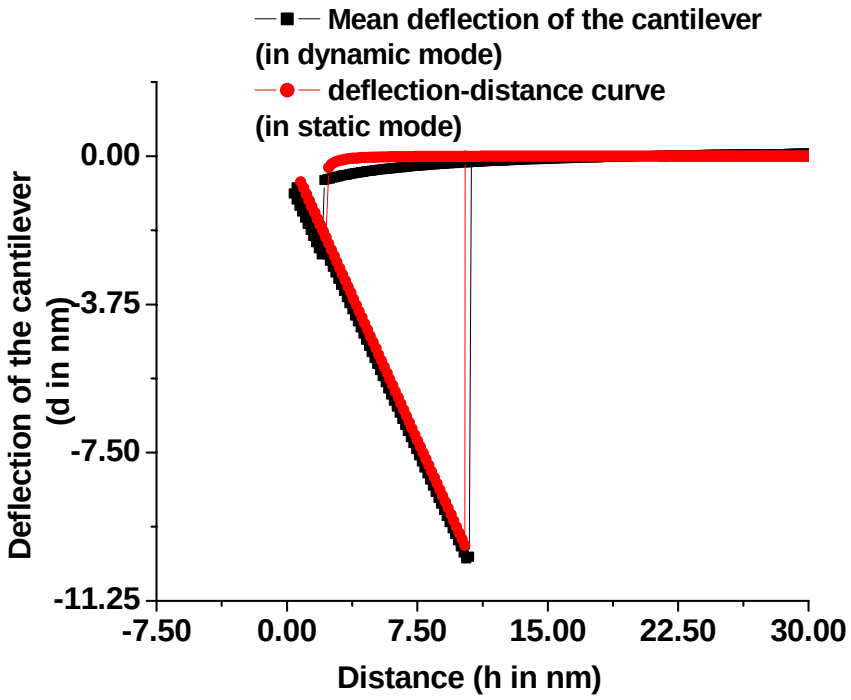

Figure 5.11 Deflection vs. distance curves both in static mode as well as dynamic mode (mean deflection of the cantilever) has been shown. Both the curves match quite well.

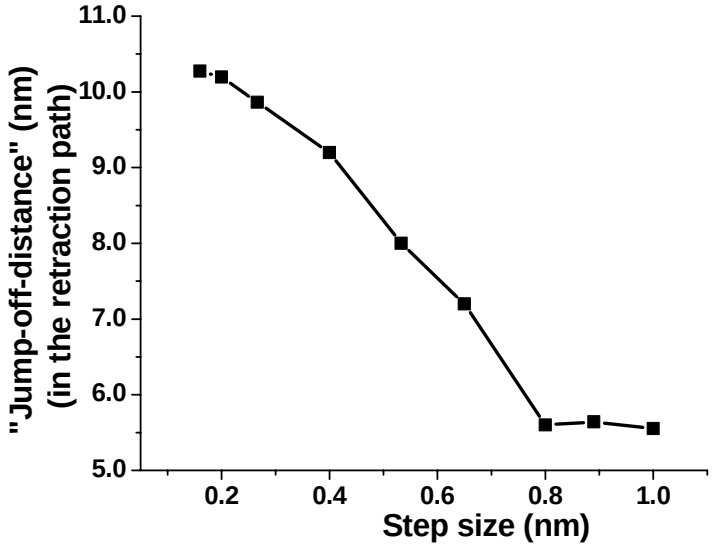

Figure 5.12 Variation of the position of jump II in the retract path of (A-h) curves with step size (simulated data).

represents the equation of motion of the cantilever in static mode (discussed in chapter 3 and 4), where the cantilever is not vibrated using an external sinusoidal signal. As we have discussed in chapter 3 and 4 that the origin of the "jump-into contact" and "jump-off-contact" mainly occurs because of inherent instability of the cantilever moving in a non-linear force field. This instability also shows up in the (A-h) curves of the dynamic mode AFM. From figure 5.11 we can see that the "jump-into-contact" and "jump-off-contact" positions match exactly with the second jump positions in the approach and retract part of the (A-h) curves. We have also simulated the variation of the position of jump II as a function of step size as shown in figure 5.12. We have observed that the position of the jump shifts to larger tip-sample separation as step size is reduced. This feature is also seen in the experimental data. The reason behind this shift of the position of jump II with step size has already been discussed in chapter 4 in great detail. The results presented here clearly show that the DFS curve if done completely can also encompass the same information from jump II as has been obtained from static AFS. The JIC and JOC seen in DFS curve as seen in static AFS curve also give us quantitative information on the parameters of the tip-sample interaction.

5.5 Conclusions

In summary, we find that the amplitude versus distance curve shows two distinct jumps as the cantilever approaches the sample surface. These features are very clearly seen both in experimental curve and simulated curve. The average value of the interaction force introduces characteristic features both in the amplitude–distance curves and resonance curves. In case of amplitude versus distance curve, the presence of an abrupt change in the amplitude (jump I) can be explained from the resonance curves. These features can be observed whenever there is nonlinearity in the potential in which the vibrating microcantilever is placed. The second jump observed in the (A-h) curves can be correlated with the features seen in static mode spectroscopy – e.g., "jump-into-contact" and "jump-off-contact" instabilities.

The model considered here is in some respects an over simplification. In particular, the tip-cantilever is considered as a single –mass model, thus neglecting any higher modes of vibration of the cantilever. It also does not include any internal degree of damping (viscosity) or tip-sample inelastic interactions. Despite all these simplifications, the model yields amplitude vs. distance and amplitude vs. frequency curves that reproduce the experimental features. This reinforces the validity of the model to describe dynamic mode operation and supports the results of the simulations for situations to be explored experimentally.

Bibliography

[1] G.Binning, C.F .Quate, and Ch.Gerber, Phys. Rev. Lett. 56, 930, 1986.
[2] Y. Martin, C.C. Williams, and H.K. Wickramasinghe, J. Appl. Phys. **61**, 4723 (1987).
[3] T. R. Albrecht, P. Grütter, D. Horne, and D. Rugar, J. Appl. Phys. **69**, 668 (1991).
[4] F.J. Giessible, Science **267**, 68 (1995); Phys. Rev. B **56**, 16010 (1997).
[5] M. Guggisberg, M. Bammerlin, R. Lüthi, Ch. Loppacher, F. Battiston, J.L.A. Baratoff, E. Meyer, and H.-J. Güntherodt, Appl. Phys. A: Mater. Sci. Process. **66**, S245 (1998).
[6] Q. Zhong, D. Imniss, K. Kjoller, and V.B. Elings, Surf. Sci. **290**, L688 (1993).
[7] R. Pérez, Y. Stich, M. Payne, and K. Terakura, Phys. Rev. B **58**, 10835 (1998).
[8] J. Tamayo and R. Garcia, Langmuir **12**, 4430 (1996).
[9] S.I. Lee, S.W .Ho well, A. Raman, and R. Reifenberger, Phys. Rev. B 66, 115409-1 2002.
[10] P. Gleyces, P.K. Kuo, A.C. Boccara, Appl. Phys. Lett. 58, 2928, 1991.
[11] M.B. Anczykowski, D. Kruger, and H. Fuchs, Phys. Rev. B 53, 15485 1996.
[12] R. Boisgard, D. Michel and J.P. Aimé, Surf. Sci. 401, 199, 1998.
[13] Ricardo Garcia and Alvaro San Paulo, Phys. Rev. B 60, 4961 1999.
[14] Ricardo Garcia and Alvaro San Paulo, Phys. Rev. B 61, R13381-R 2000.
[15] A. San Paulo, R. García, Phys. Rev. B 66, 041406(R), 2002.
[16] L. Wang, Surf. Sci. 429, 178 1999.
[17] L. Nony, R. Boisgard and J.P. Aimé, J. Chem. Phys. 111, 1615, 1999.
[18] M. Marth, D. Maier, J. Honerkamp, R. Brandsch and G. Bar, J. Appl. Phys. 85, 7030, 1999.
[19] J. Chen, R. Workman, D. Sarid, and R. Höper, Nanotechnology 5, 199, 1994.
[20] Y. Martin, C.C. Williams, and H.K. Wickramasinghe, J. Appl. Phys. 61, 4723, 1987.
[21] B. Anczycowsky, D. Kruger, and H. Fuchs, Phys. Rev. B 53, 15485 (1996).
[22] R. Garcia and A. San Paulo, Phys. Rev. B 60, 4961, (1999).
[23] J. Israelachvili, Intermolecular and Surface Forces, Academic, Orlando 1991.
[24] B.V. Derjaguin, V.M. Muller, and Y.P .Toporov, J. Coll. Interf. Sci.53, 314 1975.
[25] Veeco Metrology Inc.,112 Robin Hill Road, Santa Barbara, CA 93117.
[26] U. Rabe, J. Turner, and W. Arnold, Appl. Phys. A: Mater. Sci. Process. **66**, S277 (1998).
[27] G. Chen, R. Warmack, A. Huang, and T. Thundat, J. Appl. Phys. **78**, 1465 (1995).
[28] Franz J. Giessibl, Phys. Rev. B 56, 16010 1997.

Chapter 6

Controlled manipulation of nano-objects using Atomic Force Microscope

In previous chapters we have mainly discussed about the microcantilever dynamics moving in a non-linear force field in atomic force microscope and its impact on static mode spectroscopy as well as on dynamic mode spectroscopy. In this chapter we will concentrate on the utilization of the tip of the microcantilever for doing controlled manipulation of nano-objects using atomic force microscope. Here we have presented the experimental results that provide new insights into nanomanipulation phenomena. Reliable and accurate positioning of colloidal nanoparticles on a surface is achieved by pushing them with the tip of an atomic force microscope under control of software that compensates for instrument errors. We have used two different nano-objects (Polystyrene spheres of 100 nm and silica spheres of 150 nm) for our experiments. We have shown that better control over the forces can be achieved during manipulation of nano-objects using AFM if we use an external electric field between the tip and the sample. We have also demonstrated how the inherent properties of the cantilever (like mass, resonance frequency) can be changed if the particle gets attached to the tip during nanomanipulation using AFM. We have also shown manipulation of nano-objects inside the trenches created by E-beam lithography followed by chemical etching on silicon surface to investigate pushing on uneven substrates, which might lead to applications in three-dimensional manipulation.

6.1 Introduction

One milestone on the roadmap of nanotechnology is the fabrication of new materials with improved properties due to specially designed nanometer-scaled features, which directly implies the characterization, change, and control of surfaces at the nanometer scale. Two different approaches are available for nano-structuring and modifying properties of surfaces. In the “bottom-up” approach, molecular self assembly processes involving non-covalent bonding are used for nano-structuring. The second approach, denominated “top-down”, downscales the structuring of surfaces into the nanoscale by using currently available methods, usually high end lithography processes applied in the semiconductor industry. Although the “bottom-up” approach is quite interesting since it leads to completely new structures, it lacks of a real spatial control of the patterning process and requires additional characterization methods.

The most versatile “top-down” approach to get access to the nanoscale is the lithography of surfaces by scanning probe microscopy (SPM), which relies on the modification of chemical, electrical or mechanical properties of a surface by using a proximal probe. SPM based lithography achieves a high fabrication control over both direction and position. Additionally, SPM offers the possibility of in situ ultra-high resolution characterization of the fabrication process and resulting surface structure. The success of SPM also relies on the fact that its application for imaging is not only restricted to topography measurement, but also offers a plethora of possibilities to characterize different surface properties, including the local acquisition of spectroscopy data reaching the single-molecular level.

The first member of the SPM family was the scanning tunneling microscope (STM) [1], invented by Gerd Binnig and Heinrich Rohrer in 1981.The STM measures surface topography using the tunneling current flowing through a nanometer-wide gap between a conductive sharp tip and a conductive sample. However, the STM has some severe limitations, the most important of them being the fact that it is only applicable on conducting surfaces. Another prominent member of the SPM family is the atomic force microscope (AFM), invented by Binnig et al. in 1986 [2]. The working principle of the AFM relies on the measurement of the contact force between the apex of a sharp tip attached at the free end of a microcantilever and the sample surface. The main advantages of the AFM are: (i) it can image almost any flat surface, i.e. there is no need for the sample to be conductive; (ii) it can work in different environments including liquids; (iii) it offers a direct measurement of the interaction forces, facilitating the control and characterization of the lithography process. Due to these adventages, the AFM has become the preferred scanning probe microscope in a wide range of scientific and technological applications both for imaging and lithography. This versatility also translates into its application to lithography, allowing for a wide variety of different physical and chemical surface modifications.

The pioneering work of Eigler [3], Lyo [4], Beton [5] Jung [6], and others has shown that it is possible to precisely position atoms and molecules on a surface by using a scanning probe microscope (SPM). These are remarkable achievements. However, manipulation of particles with dimensions of a few to a few tens of nanometres is likely to have a greater impact in nanometre-scale science and technology in the near future. Patterns of colloidal nanoparticles can be constructed by SPM manipulation, and have several potential applications that are worth investigating. They can be used to efficiently store digital information, to build single electron transistors, as suggested in [7]; or as templates for building nanostructures that can function as components of nano electromechanical systems (NEMS). For example, Au nanoparticles can be linked by dithiols [8], and the resulting structures can (potentially) be used to construct more complex objects in a bottom-up fashion.

Reliable and accurate manipulation of nanoparticles has been difficult to achieve in the past. This is due largely to a lack of understanding of the underlying phenomena, and to a lack of suitable control software. Detailed experimental studies of tip/particle/sample interactions during manipulation are very few [9]. Instrument errors such as creep, hysteresis, and thermal drift, lead to a manipulation environment with high spatial uncertainty, especially in ambient air and at room temperature. These errors must be physically eliminated (e.g. by operating at low temperatures), which leads to elaborate

and costly procedures and equipment, or the control software must compensate for them, which is the approach taken in our work.
In this work, we have mainly concentrated on how to achieve better control over the forces during manipulation. From the previous studies on nanomanipulation using AFM it has been observed that nano-objects can be moved only by few tens of nanometers by pushing the object with the tip of the cantilever. Here, we have shown that the results can be drastically improved by applying an electric field between the tip and the sample during manipulation. Externally applied electric field provides a better control over the forces during nanomanipulation. This report presents experimental results that provide new insights into nanomanipulation phenomena. It also shows that nanoparticle manipulation operations can be executed reliably with an AFM in ambient conditions. We have also shown manipulation of nano-objects inside the trenches created by E-beam lithography followed by chemical etching on silicon surface to investigate pushing on uneven substrates, which might lead to applications in three-dimensional manipulation.

6.2 Experimental Procedure

6.2.1 Sample Preparation: Preparation of Silicon surface

The first and crucial step of sample preparation is the cleaning of the substrate and the surface treatment according to the need of sample preparation. For our experiments we have mainly used silicon substrates. Here we will first mention about the cleaning procedure of silicon surface and then the surface treatment to make it hydrophilic. The silicon wafer has been cleaned in the following way. Firstly, the silicon wafer was ultrasonicated in Tri-chloro-ethylene (TCE), acetone and propanol (Iso-propyle alcohol) at room temperature for 5 min, to remove contamination from organic grease. Then, the degreased silicon substrate was heated in boiling Piranha solution (4:1 (v/v) H_2SO_4/H_2O_2) and RCA solution (1:1:5 (v/v/v) $NH_3/H_2O_2/H_2O$) for 1 hour each. Subsequently, the silicon substrate was rinsed several times with MQ water. Another function of the Piranha solution is to increase the thickness of the oxide layer on top of the silicon surface which makes the surface hydrophilic.

Patterning silicon surface using Ebeam lithography:

Next step is to make patterns on the cleaned silicon surfaces. We have used Scanning Electron Microscope from FEI [10] (Model No. Quanta 200) for electron beam lithography. We have used two positive photoresists PMMA (350K) and PMAA (950K) for our work. First we have spin cast PMAA (350K) at 3000 r.p.m. for 40 seconds on cleaned silicon surface and baked it at 180^0C for 3 mins. Then on top of it we have spin cast PMMA (950K) at 6000 r.p.m. for 40 seconds and baked it at120^0C for 1 hour. Figure 6.1 shows the SEM image of the patterned generated by E-beam lithography. The parameters for writing the patterns using electron beam are mentioned below:

Filament voltage: 30 KV

Filament current: 50 μAmp

Area dose: 300 μAmp/cm^2

Spot size: 1 pico Amp.

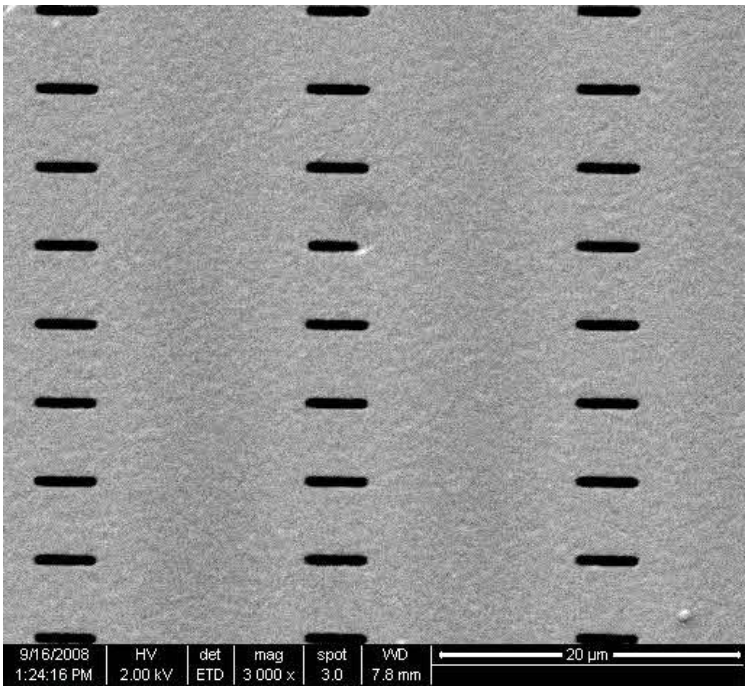

Figure 6.1 SEM image of the pattern generated by E-beam lithography

The dimensions of the pattern are 5 μm (L) X 500 nm (W).

Catalytic Etching for making patterned surface

Now to make trenches we have used the process of catalytic etching. This technique is actually a deposition of metal plus wet chemical etching method [11]. Metal particles are usually deposited on the silicon wafer with oxide layer on it, and then silicon substrates covered with metal clusters are immersed into the etching solution. An etching mixture consisting of MQ water, HF, and H_2O_2 was used at room temperature. The detailed experimental procedure is given below.
(100)-oriented silicon wafers were used in the experiments. This dry deposition plus wet chemical etching method mainly consists of four steps:
(1) Silicon wafers were sequentially cleaned with acetone (5 mins), ethanol (5 mins), MQ water and boiling Piranha solution (H_2SO_4:H_2O_2 = 4:1; V/V, 1 h), rinsed thoroughly with MQ water and then RCA solution (1:1:5 (v/v/v) $NH_3/H_2O_2/H_2O$) for 1 h. Subsequently, the silicon substrate was rinsed several times with MQ water.

(2) Metal films (thickness ~ 30 nm) were deposited via thermal evaporation onto the clean silicon surface in a vacuum evaporator with degree of vacuum 1×10^{-6} mbar.
(3) Silicon wafers covered with metal clusters were immersed into the etching solution of mixed MQ water, HF and H_2O_2 in a sealed Teflon vessel, and treated for a certain time (room temperature). The concentrations of HF and H_2O_2 were 4.6 and 0.44 M, respectively.
(4) Finally, the silver film was removed by immersion in boiling aqua regia (3:1 (v/v) HCl/HNO_3) for 15 mins.
However, the role of the metal (Ag) particles and the exact mechanism of the catalytic etching process are still unclear and controversial but it is believed that microscopically local anode (Si) and cathode (metal) sites form on the etched surface with local cell currents flowing between the sites during etching. In analogy with the pioneering studies of Si etching, [12, 13] the following mechanism is proposed:
Cathode reaction (at metal):
$H_2O_2+2H^+ \rightarrow 2H_2O+2H^+$,
$2H^++2e^- \rightarrow H_2\uparrow$,
Anode reaction:
$Si+4H^++4HF \rightarrow SiF_4+4H^+$,
$SiF_4+2HF \rightarrow H_2SiF_6$,
Overall reaction:
$Si+H_2O_2+6HF \rightarrow 2H_2O+H_2SiF_6+H_2\uparrow$.
A critical feature of this reaction scheme is the generation of H^+ from H_2O_2 and the reduction of H^+ to form H_2, both of which are facilitated by the metal particles. The observation of much higher etching rates for Ag suggests a catalytic role. Finally, it is well to note that H_2O_2 is but one possible oxidant, and others may work as well or better—the key feature being the ability to generate mobile holes at the metal-solution interface.

We have used this technique to make periodic trenches on silicon surface. For this, we have first written the pattern on silicon surface by e-beam lithography as described before. After developing the resist was present everywhere on the substrate except on the patterns. Then a thin silver film (~ 30 nm) has been evaporated on top of it. We have used evaporation system from Hind High Vacuum Co. (P) LTD. [14] (Model – 12" MSPT) to evaporate silver on silicon substrate. Then the substrate has been immersed into the chemical etching solution to get the trenches. The depth of the trenches depends on the concentration of echants and how long the substrate has been immersed into the solution. Finally the silver film has been removed as stated above. Fig. 6.2(a) shows a SEM image of these trenches made on silicon surface by the abovementioned technique and fig. 6.2(b) shows the magnified SEM image of one of such trenches.

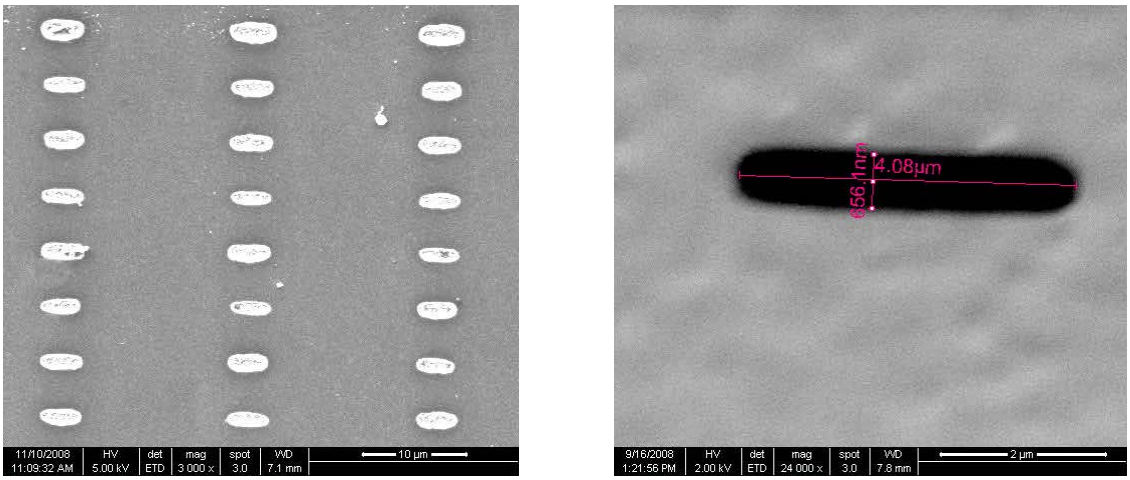

Figure 6.2 (a) SEM image of the trenches made on silicon surface. (b) Magnified SEM image of one of such trenches made on silicon surface.

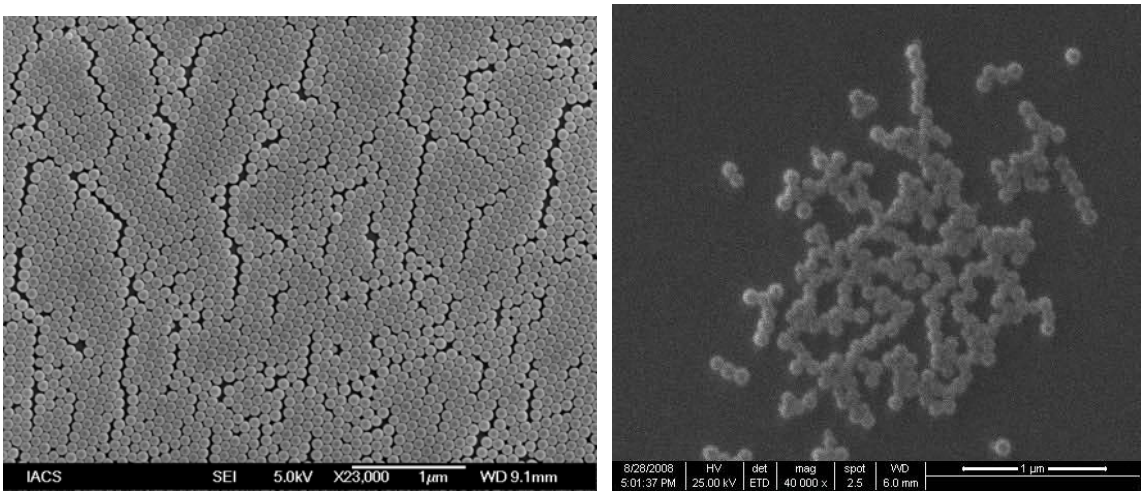

Figure 6.3 (a) and (b) show the SEM images of monolayer of Polystyrene spheres deposited on silicon substrate by spin coating.

Spin coating:

Then we have used spin-coating technique for preparing monolayer of latex spheres of 100 nm Polystyrene spheres and 150 nm of silica spheres purchased from Bangs Laboratories [15] onto the Si substrate (both plain and patterned surfaces) using a spin coater. The speed of the spin-coater was 4000 r.p.m for 100 nm Polystyrene spheres and 7000 r.p.m. for 150 nm silica spheres. The spin coating time was 30 seconds for both the cases. The concentration of the solution was 0.2 wt% and it was mixed with ethanol in 1:1 (V:V) ratio. The amount of the solution used for spin coating was 10 µl. We have used spin-coating technique because in this case most of the area of the substrate is covered by single or by few numbers of spheres and in rest multilayer is formed. This is well-suited for doing nanomanipulation of single sphere using Atomic Force Microscope.

Fig. 6.3 (a) and (b) show the SEM images of monolayer of Polystyrene spheres deposited on silicon substrate by spin coating.

6.2.2 Nanomanipulation:

The final step of the experiment is nanomanipulation. Nanomanipulation is generally done in dynamic mode. The manipulation mechanism, that is generally used, is based on the mechanical pushing of an object by the tip. Since the imaging mode is based on the opposite mechanism, that is, a feedback loop that works to prevent mechanical contact between the tip and sample, the software takes control of the imaging process by using various manipulation protocols. These manipulation protocols differ in their approach to achieve physical contact between the tip and the object. All the protocols are based on dynamic mode operation, but some work in contact mode as well. Each of these mechanisms can be used independently; however a combination of two may be used in some cases (some combinations are not allowed by the software due to logical conflicts).
The process of nanomanipulation involves control of a number of forces. The main two forces are the force of adhesion (F_a^{tp}) between the AFM tip and the adsorbate particle which will be manipulated and that between the particle and the substrate (F_a^{ps}). These forces are mediated by the surface forces [16] and depend on the formation of meniscus on the substrate. While F_a^{ps} stabilizes the particle on the substrate, F_a^{tp} makes the particle stick to the tip. The contact force between the tip and the particle F_c makes the particle move. The movement of the cantilever from its equilibrium position and the force constant of the cantilever determine the contact force in turn. In addition, since the experiments are carried out in air ambient, there are capillary forces between the tip and the particle as well as the van-der-Waal forces between the tip and the particle and that between the particle and the substrate. It is the balance of these forces that determines the final dynamics of the particle movement.
As a simple model it is considered that $F_a^{tp} \approx 4\pi R_{eff} \gamma_{sv}$ and $F_a^{ps} \approx 4\pi R_p \gamma_{sv}$ where R_t = Radius of curvature of the tip and R_p= Radius of curvature of the particle and $R_{eff} = (1/R_t+1/R_p)^{-1}$. γ_{sv} = surface energy at the solid vapour interface. In order to move the particle from one place to other it is important to ensure (1) that the particle does not adhere to the tip and also (2) the component of the contact force between the tip and the particle parallel to the surface ($F^c_{||}$) is larger than the force of friction so that the particle can be moved. As a rough estimate of the force of friction is $F^{ps}_{friction} \approx \mu^{ps} (F_a^{ps} + F^{ps}_{load})$ where F^{ps}_{load}= loading force and μ^{ps} is the coefficient of friction between the particle and the substrate. The tip will "ride" smoothly along the surface of the particle when the tangential component of F_c on the surface of the particle is larger than the frictional force between the two which is determined by F_a^{tp} and the μ^{tp}, the coefficient of friction between the particle and the tip. To meet condition (1), i.e, to ensure the particle does not stick to the tip, one should minimize F_a^{tp}, which for a given γ_{sv} happens for a minimum R_t. This can be achieved by a tip of long aspect ratio. When the tip and the particle have similar size, $R_{eff} \approx R_p/2$ and $F_a^{tp} \approx F_a^{ps}/2$ and the particle is not likely to adhere to the tip. Condition (2) would imply that there is minimum contact force that is needed to move the particle. In order to have a substantial contact force that can make $F^c_{||} > F^{ps}_{friction}$. This would imply that one would need a stiff cantilever (one with a large

spring constant typically > 10 N/m) for the manipulation. In fig.6.4 (a) a tentative force diagram for the nanomanipulation is shown.

The scheme to do nanomanipulation can be roughly described as below. Generally noncontact mode mage of the substrate is first taken to mark the particles to be manipulated and the trajectory of its movement. The noncontact mode ensures that $F^{c}_{||} \approx 0$. The cantilever vibrating at amplitude *A* is then lowered near the particle to be moved. At this stage, the feed back loop of the AFM is put to a hold mode so that the change in vibration amplitude does not make the feed back circuit adjust the tip - particle distance. The contact to the particle is detected by reduction in *A* and an increase in the static deflection. The cantilever carrying the tip is then moved along the desired trajectory. This movement would require a closed loop X-Y scanner for the AFM. At the stop position the tip is again pulled out and the feed back is enabled to start the noncontact mode imaging process again. Sufficient $F_a^{ps} > F_a^{tp}$ will ensure that the particle is parked at the desired spot as described before. This can be made sure by the cantilever oscillating at its previous amplitude again. A schematic of the manipulation process described above is given in figure 6.4(b). The description given above of the nanomanipulation process as well as the important forces is a simplification of the process that occur which in reality is rather involved.

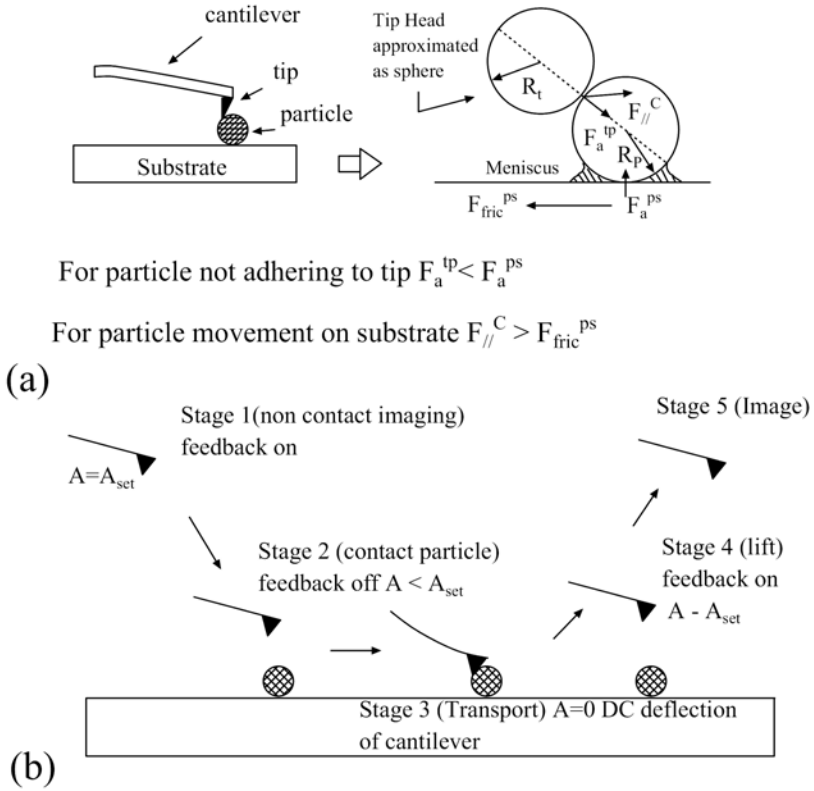

Figure 6.4 (a) Schematic of the forces involved in the nanomanipulation. (b) The scheme for the nano manipulation.

6.3 Experimental Results:

The AFM used for the experiments is a commercial AutoProbe CP II from Veeco [17]. The manipulation software is provided by the same company. We have used two different types of cantilevers for nanomanipulation. For manipulating the Polystyrene spheres and the silica spheres in absence of electric field we have used phosphorus doped silicon cantilevers. The spring constant (k_c) of the cantilever was 3 N/m (Manufacturer's value). The radius of curvature of the tip was ~ 70 nm as measured from the SEM images. For manipulating the silica spheres in presence of electric field we have used conducting cantilever. A Si cantilever (k_c~0.2 N/m) with tip coated with PtIr was used. A d.c. bias of 1.5 Volts was applied to the tip from an external source and the sample was grounded. The sample has been imaged in non-contact mode, and a tilt correction is performed to ensure that the tip moves parallel to the substrate surface even with the feedback disabled. The user chooses the desired pushing path by drawing an arrow with the mouse over the previously acquired image. The control software automatically executes single line scans along the specified line segment and displays the corresponding topography. The operator translates the arrow until the displayed topography indicates that the path is centred over the particle to be pushed. (The latest version of our software automates this procedure by tracking the centroid of the selected particle.) This ensures that the pushing operation is successful, and corrects for creep of the piezo and thermal drift. The last step before actual pushing is to select on the line scan the points where the manipulation starts and ends. For the data reported here, the pushing protocol consists of disabling the feedback between the start and the endpoints, and is similar to a procedure published by Junno et al [18].

We have shown the results below. Fig. 6.5 (a) and (b) show the 5 μm X 5 μm AFM image of 100 nm Polystyrene spheres deposited on silicon surface before manipulation and after manipulation respectively. Fig.6.6(a) shows the AFM image of silica spheres deposited on silicon substrate (with native oxide layer on it) by spin coating before manipulation and fig. 6.6(b) shows the same after manipulation. Fig. 6.7(a) and (b) show the AFM images of silica spheres deposited on silicon substrate before and after manipulation respectively (in presence of electric field). We have also shown that nano-objects can be moved within a trench created on silicon surface as shown in fig.6.8(a) and (b). Fig.6.9(a) shows the stacking of silica spheres within the trench before doing the manipulation. We have moved the sphere, marked by a circle in fig.6.9(a), by the tip inside the trench in presence of electric field. Fig.6.9 (b) shows the AFM image after manipulation.

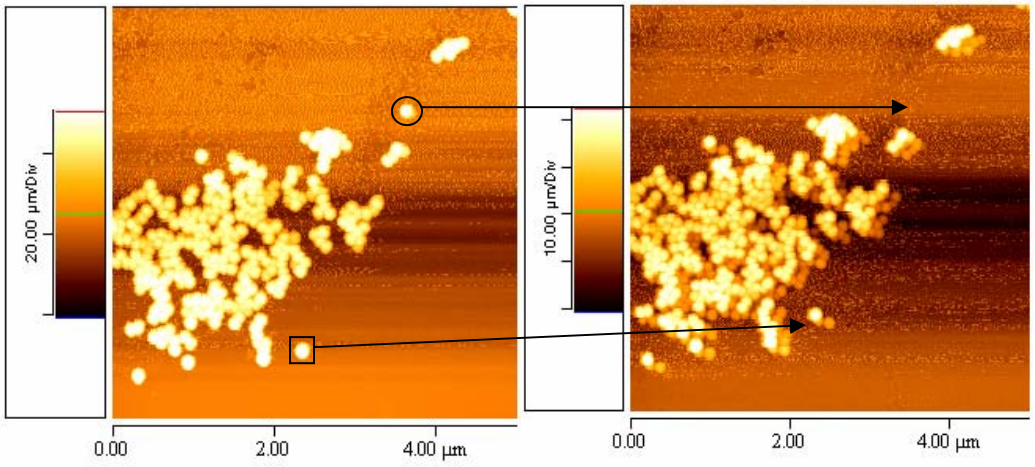

Figure 6.5 (a) It shows the 5 µm X 5 µm AFM image of 100 nm Polystyrene spheres deposited on silicon surface before manipulation and (b) shows the same after manipulation.

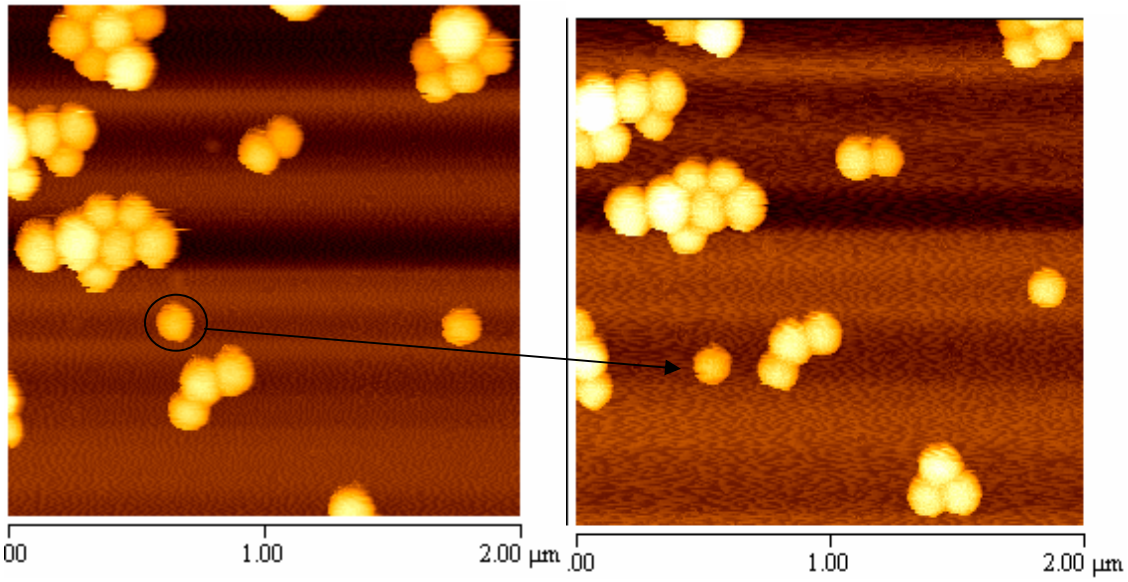

Figure 6.6 (a) It shows the AFM image of silica spheres deposited on silicon substrate by spin coating before manipulation (2 µm X 2 µm) and (b) shows the same after manipulation.

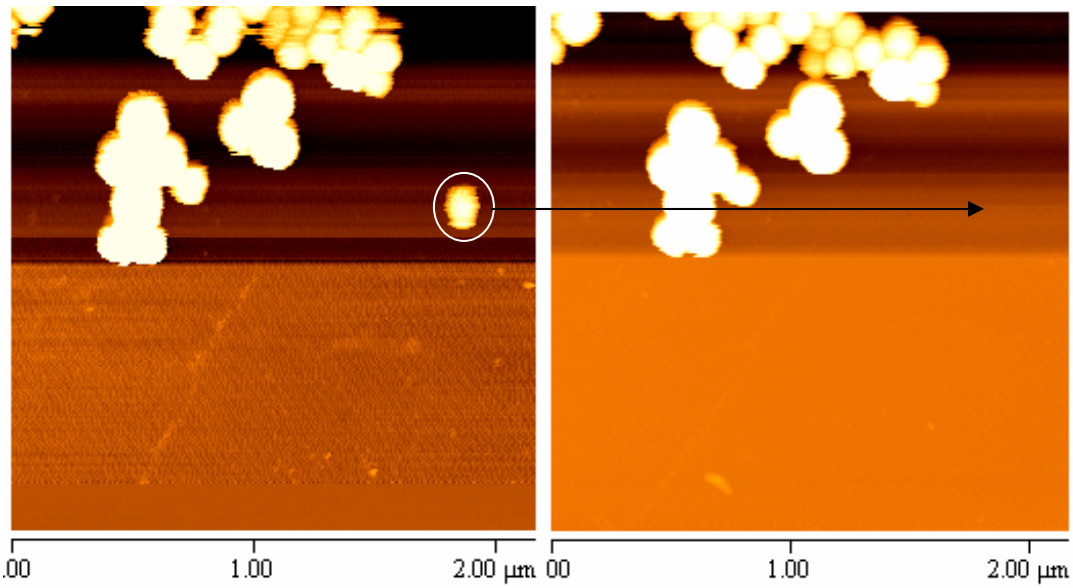

Figure 6.7(a) It shows the AFM images of silica spheres deposited on silicon substrate before manipulation and (b) after manipulation (in presence of electric field).

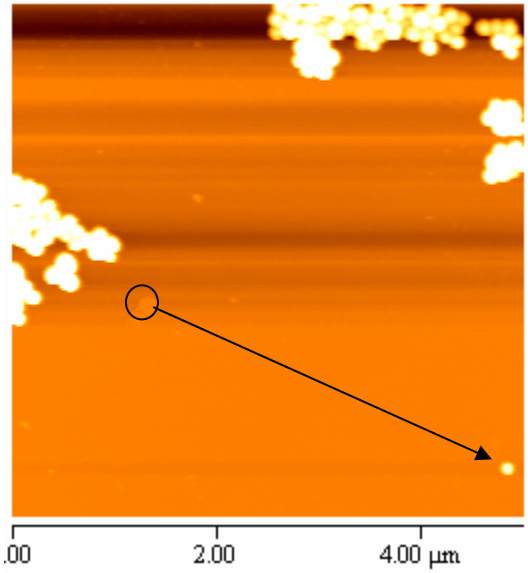

Figure 6.7(c) It shows the AFM images of silica spheres deposited on silicon substrate after manipulation (in presence of electric field). Scan area 5 µm X 5 µm.

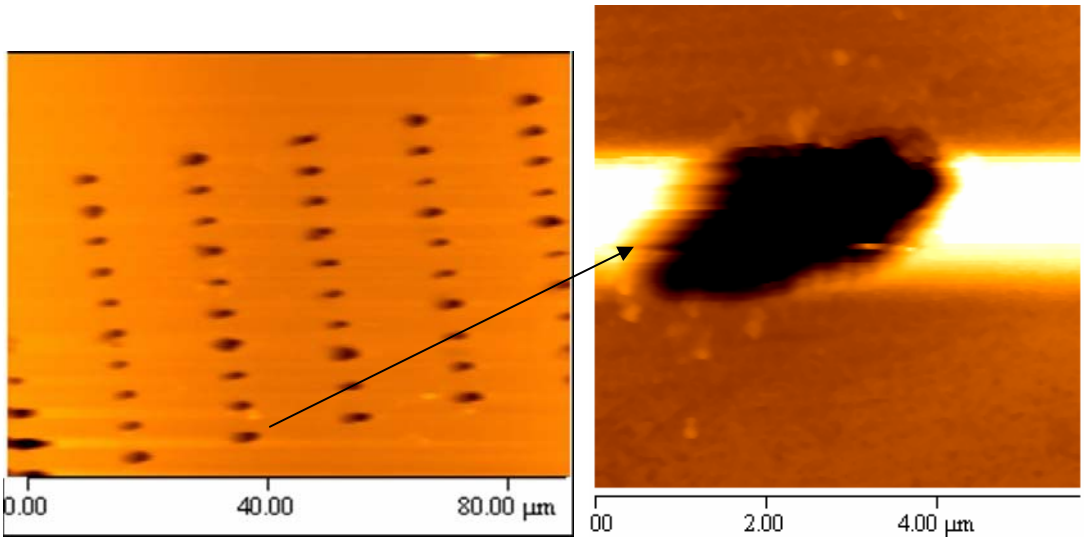

Figure 6.8 (a) AFM image of the trenches made on silicon surface (b) magnified image of one of the trenches.

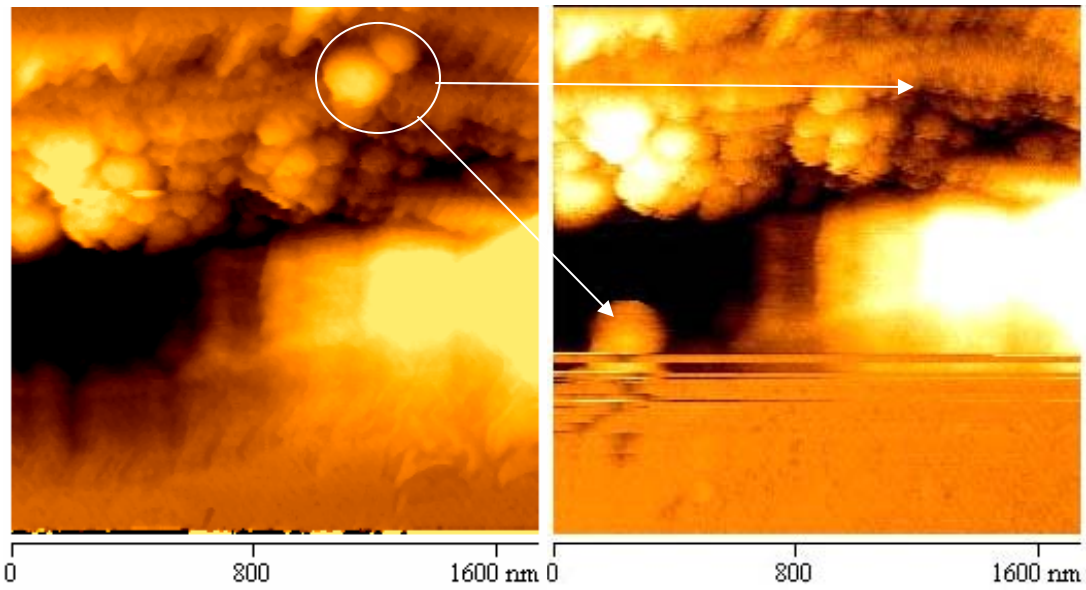

Figure 6.9(a) shows the stacking of silica spheres within the trench before doing the manipulation and (b) shows the AFM image after manipulation in presence of electric field.

6.4 Discussions:

First we have tried to manipulate Polystyrene spheres (100 nm) deposited by spin coating on silicon substrate (having native oxide layer on it). Fig. 6.5 (a) shows the 5 µm X 5 µm AFM image of these spheres deposited on silicon surface before manipulation and fig.

6.5 (b). shows the image of the same area after doing the manipulation. We have found that after manipulation one sphere (marked by square in fig.6.5(a)) has been moved upwards as can be seen from fig. 6.5(b). It is also noticed that another sphere (marked by circle in fig. 6.5(a)) is missing from its previous position and all the Polystyrene spheres have been imaged twice in fig.6.5(b) (after manipulation). To understand the reason behind it we have imaged the tip of the cantilever that has been used for manipulation using SEM. The SEM images of the tip before and after manipulation are shown in fig. 6.10 (a) and (b) respectively. From the image it is clear that the Polystyrene sphere (marked by circle in fig. 6.5(a)) actually gets attached to the tip of the cantilever. We have also checked the resonance frequency of the cantilever before and after doing the manipulation. Fig.6.11 shows the resonance curves of the same cantilever before (black curve) and after (red curve) manipulation. One can see from the figure that after manipulation the resonance frequency of the cantilever has been reduced. We have found out change in resonance frequency of the cantilever after manipulation. The resonance frequency of the cantilever before doing the manipulation was 12.047 KHz and after doing the manipulation it has been reduced to 11.978 KHz. We have found

$$\omega_0 = \sqrt{\frac{k_c}{m}} \qquad (6.1)$$

out that after doing the manipulation the mass of the cantilever has been increased by $1.6X10^{-11}$ gm by using the equation (6.1) where ω_0 is the resonance frequency of the

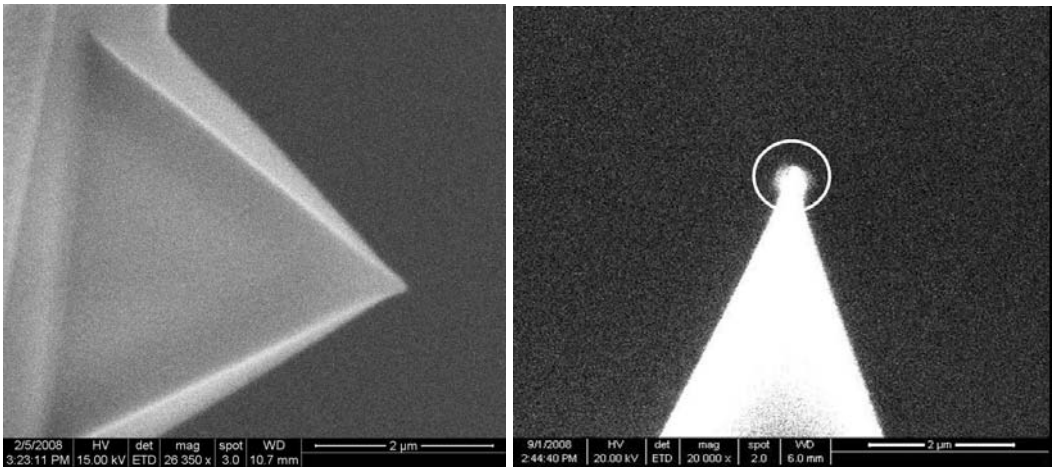

Figure 6.10 (a) The SEM images of the tip before manipulation and (b) after manipulation.

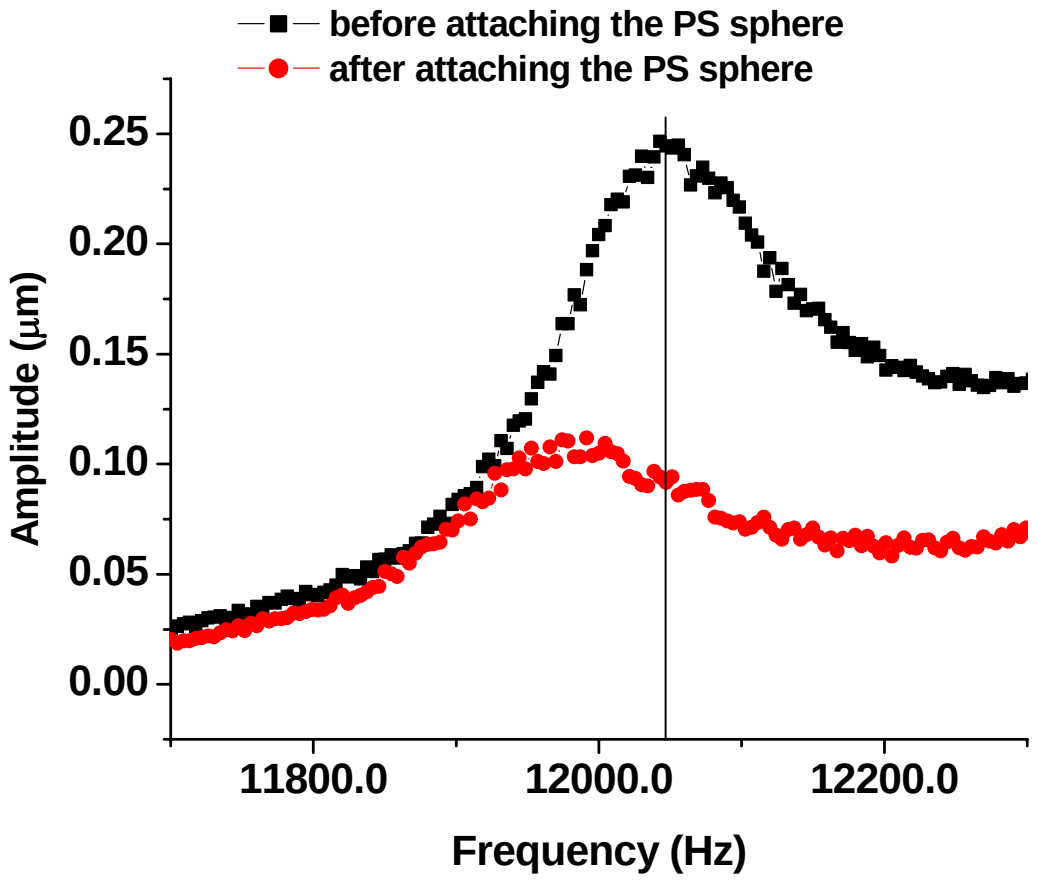

Figure 6.11 The Resonance curves of the cantilever before (black) and after (red) doing the manipulation.

cantilever, k_c is the spring constant of the cantilever and m is mass of the cantilever.
We have found that if we try to move the Polystyrene spheres using the tip of the cantilever, in most of the cases it gets attached to the tip. Therefore, we have tried to manipulate silica spheres (150 nm) using AFM tip as shown in fig.6.6. Fig.6.6(a) shows the AFM image of silica spheres deposited on silicon substrate (with native oxide layer on it) by spin coating before manipulation and fig. 6.6(b) shows the same after manipulation. From fig.6.6(b), we can see that the sphere marked by circle has been moved downward ~ 500 nm. In case of silica sphere we have found that it does not get attached to the tip during manipulation as it has happened in case of Polystyrene spheres. It is important to mention here that the sphere has been moved (~ 500 nm) to the final position in three consecutive steps and not in a single step. Then we have tried to move the particle (silica spheres) using the tip in presence of an externally applied dc electric field.
Fig. 6.7(a) and (b) show the AFM images of silica spheres deposited on silicon substrate before and after manipulation (in presence of electric field) respectively. One can see that after manipulation the sphere (marked by a circle in fig.6.7(b)) is missing from its

previous position. Then we have taken a bigger scan of the surface (5 μm X 5 μm) and found that the silica sphere has been moved ~ 3 μm by the tip (fig.6.7(c)). It is important to mention here that it is done in a single step. In this case there is an extra force, arising from the applied dc bias between the tip and the sample, acting on the tip which provides a better control over forces during manipulation. We have shown that in absence of electric field the sphere only moves by a distance of ~ 500 nm whereas in presence of electric field it is possible to move it ~ 3 μm. It immediately reflects the fact that the externally applied electric field can act as a very good control parameter during manipulation. Though there are several literatures available on how to do nanomanipulation using the tip of AFM but almost no report has been found on the manipulation of nano-objects in presence of electric field.

We have also shown that nano-objects can also be moved within a trench created on silicon surface as shown in fig.6.8(a) and (b) in presence of electric field. Fig.6.9(a) shows the stacking of silica spheres within the trench before doing the manipulation. We have moved the sphere, marked by a circle in fig.6.9 (a), by the tip inside the trench in presence of electric field. Fig.6.9 (b) shows the AFM image after manipulation. So far, it has been demonstrated that the nano-objects can be manipulated on planar surface. All of the mechanical positing and pushing work with an AFM or STM reported by other research groups until now has been limited to two dimensions, and steps of the substrate have been used mainly for alignment. Here we have shown that it is also possible to do nanomanipulation in three-dimensions.

6.5 Conclusions:

In conclusion, we have shown that nanomanipulation can be done in presence of electric field and it provides a very good control over the forces during manipulation. We have also demonstrated that the nano-spheres can be moved within the trench created on silicon surface in presence of electric field which opens up the possibility to do nanomanipulation in three-dimensions. However, the research on controllability and the extension of the capabilities of AFM still have many unresolved issues. The main restrictions to AFM performance in the modification of surfaces include its limited field of operation to areas of some tens of micrometers in diameter, the necessary contact between probe and sample either for imaging or manipulation, and the lack of knowledge about how system dynamics really affects the lithography process.

Bibliography

[1] G. Binnig, H. Rohrer, C. Gerber, and E. Weibel, Phys. Rev. Lett., vol. 50, pp. 120-123, 1983.
[2] G. Binnig, C. F. Quate, and C. Gerber, Phys. Rev. Lett., vol. 56, pp. 930–933, 1986.
[3] J A Stroscio and D M Eigler , Science 254**,** 1319, 1991.
[4] I W Lyo and P Avouris , Science 253**,** 173, 1991.
[5] P H Beton, A W Dunn and P Moriarty, Appl. Phys.Lett. 67**,** 1075, 1995.
[6] T A Jung, R R Schlittler, J K Gimzewski, H Tang and C Joachim, Science 271, 181, 1996.
[7] H Ahmed, J. Vac. Sci. Technol. B 15, 2101,1997.
[8] R P Andres *et al,* J. Vac. Sci. Technol. A 14**,** 1178, 1996.
[9] T R Ramachandran *et al,* Nanotechnology,1998.
[10] North America Nnaoport, 5350 NEDawson Creek Drive, Hillsboro, Oregon, 97124, USA.
[11] Z. Huang, H. Fang, and J. Zhu, Adv. Mater., 19, 744–748, 2007.
[12] X. Li and P. W. Bohn, Appl. Phys. Lett., 77, 2572, 2000.
[13] T. Unagami, J. Electrochem. Soc. 127, 476, 1980.
[14] Hind High Vacuum Co. (P) LTD. Bangalore, India.
[15] Bangs Laboratories, Inc., 9025 Technology Dr., Fishers, IN.
[16] M. Sitti and H. Hashimoto, Proc. IEEE/ASME 1999, Int. conference on Adv. Intelligent Mechanotronics, September 19-23, 1999 Athens, USA. pp 13-20.
[17] Veeco Metrology Inc.,112 Robin Hill Road, Santa Barbara, CA 93117.
[18] T Junno, K Deppert, L Montelius and L Samuelson , Appl. Phys. Lett. 66 3627, 1995.

Chapter 7

Concluding remarks on this thesis

7.1 A summary of the work done

This thesis focuses on two specific aspects as stated below. First, to understand the dynamics of microcantilever of Atomic Force Microscope (AFM) moving in a non-linear tip-sample interaction. Second, to modify the interaction by applying an electric field between the tip and the sample to achieve an external control on tip-sample interaction and finally to utilize this understanding for nanomanipulation with precise control in presence of electric field.

Atomic force microscope (AFM) is one of the most widely used tools in nanoscience and nanotechnology. Since the time of the discovery of AFM by Binning et. al., many attempts have been made to explain some of the non-intuitive features seen in these systems. For example, the force versus distance (f-h) curves depend on whether the cantilever is approaching towards the sample or retracting away from it, leading to a hysteresis like behavior. The hysteresis has traditionally been attributed to adhesion due to the layer of water existing on the surface of the sample, or ruptures of molecular bonds, and has indeed been used to measure the “snap off” force. It is shown here that the static force spectroscopy curve is severely modified due to presence of intrinsic cantilever instability. This instability acts in tandem with such instabilities like water bridge or molecular bond rupture and makes the static force spectroscopy curve (including “jump-off-contact”) dependent on the step-size of data collection. A theoretical model has been proposed for the first time to explain the data. This has been further validated by applying an electric field between tip and substrate which modifies the tip-substrate interaction.

Further, the effects of nonlinear tip–sample forces on dynamic mode atomic force spectroscopy have also been studied both experimentally and by theoretical calculations. The jumps and hysteresis observed in the vibration amplitude (A) versus tip–sample distance (h) curves have been traced to bistability in the resonance curve. A numerical analysis of the basic dynamic equation was used to explain the hysteresis in the experimental curve. It has been found that the location of the hysteresis in the A–h curve depends on the frequency of the forced oscillation relative to the natural frequency of the cantilever. Apart from the abovementioned jump there is a second jump observed at very small tip-sample separation in the (A-h) curves which is related to the static mode spectroscopy curves.

Next we have utilized the tip of the microcantilever of AFM for manipulating nano-objects. The capability to fabricate or modify nanoscale structures using nanomanipulation is a fundamental step toward realizing the promise and potential of nanotechnology. To achieve better control, nanomanipulation is done in presence of electric field. To start with, PS spheres of 100 nm and silica spheres of 150 nm are used to make a periodic array on silicon substrates (with native oxide layer on it) with the help of standard techniques. In the next step AFM tip has been used to manipulate a particular sphere (or spheres) in presence of an electric field applied between the tip and sample. The presence of the electric field creates a controllable tip surface interaction that then can be utilized for nanomanipulation.

In chapter 1, we have first discussed about the various forces that play crucial role in Atomic Force Microscope (AFM). Then we have given a compact review of previous investigations on static mode atomic force spectroscopy, dynamic mode atomic force spectroscopy and nanomanipulation using AFM. Also the major aspects of this thesis discussed in the subsequent chapters have been summarized.
In the first section of chapter 2, we describe about the mathematical model that we have developed to understand our experimental data. The interaction between the tip of an AFM and the sample is modeled as van-der-Waals force. Solutions of the equation of motion of the cantilever in static mode and also in dynamic mode atomic force spectroscopy have been derived. In case of static mode both analytical solution as well as numerical simulation has been done to obtain the cantilever deflection whereas in dynamic mode only numerical simulation has been done. The second part of this chapter presents the experimental techniques used to study the tribology and mechanics at the nanometer scale. A specific emphasis is dedicated to the atomic force microscope, as it is the central pillar for data acquisition in this work. Other tools for probing or imaging the surfaces have been reviewed. This section focuses on the technique of Atomic Force Microscopy (AFM) and Spectroscopy (AFS), sample preparation procedure and other techniques that have been used for sample characterization.
In chapter 3, we show that the "jump-into-contact" and "jump-off-contact" of the cantilever in AFM is caused by an inherent instability in the motion of the AFM cantilever. We have also discussed how to evaluate the interaction parameters of van-der-Waals force using the atomic force spectroscopy curves in static mode.
Chapter 4 mainly focuses on the effect of intrinsic instability of cantilever on static mode atomic force spectroscopy. A quantitative understanding of the effect of meniscus force and van-der-Waals force on force-distance curves along with the effect of electric field on static mode spectroscopy has also been discussed in detail in this chapter.
In chapter 5, we describe the effects of nonlinear tip–sample forces on dynamic mode atomic force microscopy and spectroscopy. We have also established a connection between the dynamic mode spectroscopy curve and the static mode spectroscopic curves which has not been reported before.
In chapter 6, we will concentrate on the utilization of the tip of the microcantilever for doing controlled manipulation of nano-objects using atomic force microscope. We have also used an external electric field during manipulation to achieve better control over the forces during manipulation.

7.2 Summary of main results

7.2.1 A new method to quantitatively evaluate the Hamaker constant using the jump-into-contact effect in atomic force spectroscopy

We have shown that the "jump-into-contact" and "jump-off-contact" of the cantilever in the atomic force microscope (AFM) is caused by an inherent instability in the motion of the AFM cantilever. We have also shown that the "jump-into-contact" distance can be used to find the interaction of the cantilever tip with the surface. A model has been

proposed to explain the data. In the specific context of the attractive van-der-Waals interaction, this method can be realized as a new method of measuring the Hamaker constant for materials. The Hamaker constant is determined from the deflection of the cantilever at the "jump-into-contact" using the force constant of the cantilever and the tip radius of curvature, all of which can be obtained by measurements. The results have been verified experimentally on a sample of cleaved mica, a sample of Si wafer with natural oxide and a silver film, using a number of cantilevers with different spring constants. We emphasize that the method described here is applicable only to surfaces that have van-der-Waals interaction as the tip–sample interaction. We also find that the tip to sample separation at the 'jump-into-contact' is simply related to the cantilever deflection at this point, and this provides a method to exactly locate the surface.

7.2.2 Effect of intrinsic instability of cantilevers on static mode Atomic Force Spectroscopy

We have shown that the static force spectroscopy curve is significantly modified due to presence of intrinsic cantilever instability. This instability acts in tandem with such instabilities like water bridge or molecular bond rupture and makes the static force spectroscopy curve (including "jump-off-contact") dependent on the step-size of the motion of the cantilever. A model has been proposed to explain the data. This has been further validated by applying an electric field between tip and substrate which modifies the tip-substrate interaction. We have investigated the role of cantilever instabilities in determination of the AFS curves in an Atomic Force Microscope (AFM) working in Ultra-High vacuum (UHV). We have also showed how an electric field applied between tip and the sample shifts the observed deflection (or force) –vs.-distance curves in the AFM. We explained the experiment using a model and quantitatively established a relation between the observed AFS curves and the electric field which modifies the effective tip-sample interaction in a controlled manner. The investigation establishes a way to quantitatively evaluate the electrostatic force in an AFM using the static AFS curves.

7.2.3 Effects of Nonlinear Forces on Dynamic Mode Atomic Force Spectroscopy

We have described the effects of nonlinear tip–sample forces on dynamic mode atomic force microscopy and spectroscopy. Dynamic atomic force microscopy is a standard technique for imaging and the analysis of surfaces at the nanometer scale. In order to estimate material properties from the microscope data it is important to understand the nonlinear dynamics in the tip-sample interaction. In dynamic mode force spectroscopy one measures the vibration amplitude (A) as a function of tip-sample distance (h). The jumps and hysteresis observed in the vibration amplitude (A) versus tip–sample distance (h) curves have been traced to bistability in the resonance curve. A numerical analysis of the basic dynamic equation was used to explain the hysteresis in the experimental curve. It has been found that the location of the jump (mentioned below as jump I) occurs at higher tip-sample separation in the A–h curve depends on the frequency of the forced

oscillation relative to the natural frequency of the cantilever. This jump is always a consequence of the existence of two oscillation states for the same conditions. In the other case, the jump (mentioned below as jump II) occurs at smaller tip-sample separation arises because of inherent instability of the cantilever moving in a non-linear force field as has been observed in case of static mode spectroscopy also.

7.2.4 Controlled manipulation of nano-objects using Atomic Force Microscope

We have shown that better control over the forces can be achieved during manipulation of nano-objects using AFM if we use an external electric field between the tip and the sample. We have presented the experimental results that provide new insights into nanomanipulation phenomena. Reliable and accurate positioning of colloidal nanoparticles on a surface is achieved by pushing them with the tip of an AFM under control of software that compensates for instrument errors. We have shown that much better results can be achieved if we use an electric field of moderate value during the time of manipulation. We have also demonstrated how the inherent properties of the cantilever (like mass, resonance frequency) can be changed if the particle gets attached to the tip during nanomanipulation using AFM. We have also shown manipulation of nano-objects inside the trenches created by E-beam lithography followed by chemical etching on silicon surface to investigate pushing on uneven substrates, which might lead to applications in three-dimensional manipulation.

7.3 Main deficiencies of this work

In this thesis, a systematic study has been done to understand the basic physics of atomic force spectroscopy both in static mode as well as in dynamic mode through experiment and simulation. Though the simulated results match quite well with the experimental results but we want to mention here that we have used a simple model which only describes the tip motion. The equation of motion of the microcantilever is generally very complex, since one has to take into account not only the motion of the tip in presence of a medium (air or water) but also the bending of the beam of the microcantilever. In this calculation, we will, however, restrict ourselves to the motion of the tip. Here we have considered the cantilever-tip ensemble as a point-mass spring. The assumption ignores the contribution to the cantilever motion of the higher flexural modes of the lever. Secondly, the tip-sample interaction in principle can have a velocity dependent frictional force term. For simplicity we club all the velocity dependent frictional forces into one term. The q factor used here is assumed to be independent of tip-sample separation. The second assumption neglects changes in the hydrodynamic damping of the cantilever during its motion.

We have also shown in this thesis that we can achieve better control over the forces during manipulation using AFM by applying an electric field between the tip and the sample. Though this point has been established by our experimental results but a modeling is needed to understand the exact process and also to quantify it. This may also help us to do manipulation in more controlled way.

7.4 Future scope of the work

Modeling the interaction between the tip and the sample in AFM during manipulation both in presence and absence of electric field will be a very useful addition to this work. This will not only quantify the process but also help us to understand the effect of different forces present at the time of manipulation. It will also provide a good control over this process which is still very much needed in this field. In this thesis we have studied only the effect of dc electric field on nanomanipulation. It will also be interesting to study the effect of ac electric field on manipulation of nano-objects using AFM.

Appendix A

Growth of atomically smooth films of metal-arachidates by Langmuir-Blodgett technique

In this chapter, we report synthesis of atomically smooth Ni-arachidate films using Langmuir-Blodgett technique. The interaction between arachidic acid monolayer and nickel ion has been investigated as a function of subphase pH by measuring the compression isotherms at the air/water interface. As the pH is increased, the compressible liquid (L_2) phase is observed over a smaller range of surface pressure (π) and area/mol (A) until at high enough pH the L_2 phase is altogether absent. A further increase in pH does not result in any additional change in the isotherm. This is a general trend observed for all bivalent cations but the disappearance of L_2 phase occurs at different pH values for different ions. The atomically smooth monolayers are deposited when the pressure is beyond the L_2 phase (typically ~ 35mN/m). Along with the isotherms, monolayer of nickel arachidate deposited on mica, were studied thoroughly using Atomic force Microscopy. Atomic force microscope images show atomically smooth and defect free surface of nickel arachidate transferred on mica substrate. The images allow proper determination of the lattice vectors.

A.1 Introduction

The Langmuir-Blodgett (LB) technique is a room-temperature deposition process that may be used to deposit monolayer and multilayer films of organic materials. This method permits the manipulation of organic molecules on the nanometer scale, thereby allowing intriguing superlatice architectures to be assembled [1]. Multilayer Langmuir-Blodgett (LB) films were used as a metal-organic precursor matrix and quasi-two-dimensional reaction media for the synthesis of semiconductor [2-5] and metallic [6] nanoparticles. In recent years there has been considerable interest in the production of metallic nanoparticles and nanoparticulate films due to their unique optical properties [7] and potential applications [8] in the fields of catalysis, electronic/magnetic components, and as biological sensors. Convenient and effective organization of nanomaterials into one-, two-, and three-dimensional structures is the key to the realization of nanodevices [9-11]. The LB technique is one of the most promising methods for producing well-organized 2-D monolayers of surfactants, polymers and nanoparticles, because it provides fine control of the thickness and homogeneity of the monolayer and multilayers.

While pure fatty acids film growth is very well studied the growth of metal-arichidates is a relatively less investigated field. Long chain fatty acids and their divalent salts of Cd, Mn and Ba have been extensively studied model LB systems both as Langmuir monolayers as well as LB multilayers [12-15] but almost no attention has been paid to

Ni^{2+}. The sensitivity of the fatty acids toward metal ions present in the subphase is thought to be coupled with the ability of the carboxyl group to ionize and to further react chemically with the subphase ions. The experimental indications are that most divalent metal ions interact with the carboxyl head groups in the proportion of 1:2 [16-18]. The composition, structure and stability of the monolayer are known to be sensitive to the type and concentration of the metal ion and the pH of the subphase which controls the extent of metal ion complexation with the acid head group [19]. These interactions are of major importance in facilitating the manufacture of high quality LB multilayers with potential applications in thin film technology, since LB films containing metal ions may have interesting electric and magnetic properties [20]. The presence of minute amounts of di- or even trivalent metal ions enhances the stability of the monolayer [21] and condenses the monolayer over a pH range which is different for different metal ions. The interaction is largely dependent on the physical and chemical properties of the metal ion. Thus it is necessary to determine the pH dependence of the interaction for each metal ion separately. LB films can be used as a precursor for synthesizing metal nanoparticles or metal oxide, for example, CdO, ZnO had been prepared from Cd arachidate and Zn arachidate LB films respectively [22, 23]. A novel approach to make such thin films is through the pyrolysis of LB deposited films. The most prevalent compounds used in LB work form metal carboxylate films which, when pyrolysed, result in oxide thicknesses ranging from 0.05 to 0.1 nm per LB monolayer. This technique would thus find application in areas requiring very thin films or well-controlled film thicknesses. Similarly, Ni arachidate can be used for synthesizing nickel nanoparticles and NiO film which is an antiferromagnet and is a promising material for use in spintronics. The physical and chemical properties of synthesized nanoparticles and film depend on the subphase pH of the LB film. Therefore, the pH dependence of the precursor LB films needs to be studied thoroughly.

Probably, most important utilization of nickel-arachidate film lies in functionalizing of biomolecules. Ultrathin metal-organic films formed by the Langmuir-Blodgett technique can be extremely useful in designing of model biological membranes due to possibility of having well-defined molecular orientation and ordering in these films. Immobilization of individual biomolecules and their complexes is an important requirement for a number of biophysical and biochemical experiments. It is already shown that LB film of Ni arachidate is a very good substrate for immobilizing Histidine tagged (Histagged) proteins and protein-DNA complex at the molecular level, using a LB film of Ni (II)-Arachidate (NiA), utilizing the well-known Ni-Histidine interaction [24].

Langmuir-Blodgett films are formed by transferring molecular monolayers of amphiphilic molecules from a liquid surface onto a solid substrate. There are several techniques like x-ray [25], or electron [26] diffraction, spectroscopic (infrared or Raman) [27] and neutron [28] reflectivity to characterize the physical properties of the LB films. It must be emphasized, however, that these techniques only give access to spatially averaged information. In particular, the structural defects within the films that can be evidenced this way are only macroscopic. However, Atomic force microscope (AFM) has been shown to be promising technique for the elucidation of the structure of LB films at the molecular level [29-31]. The Atomic force microscopy provides a nondestructive way to image atomically smooth LB films to determine film quality at length scales from nanometers to micrometers.

A.2 Experimental Details

Sample Preparation

a. Materials: Arachidic (eicosanoic) acid (99%), $NiSO_4$, $7H_2O$ (99.999%), were purchased from Sigma Aldrich [32]. Tris buffer (pure AR) solution used to adjust the subphase pH was obtained from SRL [33]. NaOH and HCl used to adjust the pH of the buffer solution were purchased from Merck [34]. The spreading solution (1mg/ml) was prepared using chloroform (HPLC grade). All the chemicals were used without further purification. The water was purified with a Millipore Milli-Q filtering system yielding a water resistivity > 18 MΩ cm. The concentrations of the salt solutions were $0.2X10^{-3}$ M. Arachidic acid was spread from chloroform solution on a $NiSO_4$ solution. The pH was adjusted between 4.0 and 7.5 (± 0.1) using the buffer solution.

b. Method: The surface pressure-mean molecular area (π-A) isotherms were recorded with a computerized Langmuir trough manufactured by Apex Instruments Co. [35]. The experiments were carried out at 22 ± 0.2^0C using a thermostated Teflon trough (190X70 mm^2). The compression was started 5 min after spreading using a constant barrier speed of 5 mm/min. The precision of the instrument was ±0.05mN/m. One molecular layer of Ni arachidate at pH 7.5 was transferred to mica substrates by vertical lifting at 2 mm/min while the monolayer was held at constant surface pressure (π = 35 mN/m). For all the arachidates the transfer ratios were nearly 1.0 at pH 7.5. Mica substrates were freshly cleaved immediately before use.

Films were dried in desiccator for almost one hour before imaging using AFM. Imaging was performed using a CPII atomic force microscope from Veeco [36] under ambient conditions using silicon cantilever with spring constant 0.9 N/m. The resonance frequency of the cantilever was 20-23 KHz. Both contact and tapping mode images were acquired on all the samples. For contact mode imaging softer cantilever was used with spring constant 0.03 N/m and the set force was 2 nN. For tapping mode images the set frequency was 22.65 KHz. Images were obtained from at least five macroscopically separated areas on each sample. Representative images are presented below.

A.3 Results and Discussions

The surface pressure-area/mol (π-A) isotherms of Ni^{2+} as a function of subphase pH (fig. A.1) show qualitatively similar variation like other bivalent ions. At low pH the fatty acids are un-ionized and the isotherms are indistinguishable from an isotherm of arachidic acid on pure water (with no cation present). The region of intermediate slope between about 0.26 and 0.20 nm^2/mol for nickel arachidate corresponding to the L_2 phase, [37] ends at a kink at about 35 mN/m which signals a transition to the solid-like (LS) phase as shown in fig.A.1. In the surface pressure vs. area/mol (π-A) isotherm, L_2 is a low pressure phase and it is fairly compressible. In the L_2 phase, the alkyl chains are tilted towards the nearest neighbours whereas in LS phase the molecules are upright and

it is less compressible than L_2 phase. It is important to mention here that the area per molecule (A) of a LB

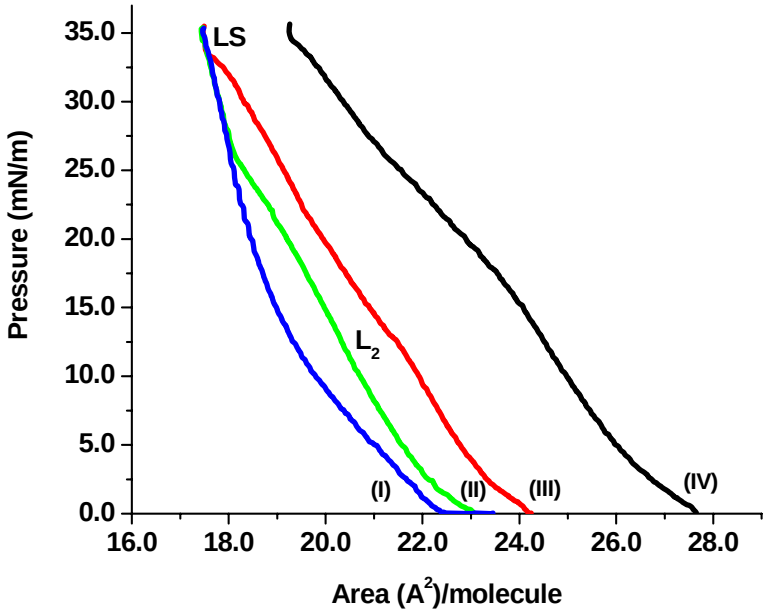

Figure A.1 Surface pressure vs. area/mol isotherms of nickel arachidate at different subphase pH. Starting from right (I) is for pH=7.5, (II) for pH=6.0, (III) for pH=5.4 and (IV) for pH=4.4. This figure clearly shows the L_2 to LS phase transition as a function of subphase pH.

monolayer mainly depends on two factors – the ionic radius and the electronegativity of the cation. It is also evident from fig.A.1 that as the pH is increased, the L_2 phase is observed over a smaller range of π and area/mol until at high enough pH the L_2 phase is altogether absent. A further increase in pH does not result in any additional change in the isotherm. This evolution occurs for nickel arachidate over a pH range of 4.5 – 7.5 (fig.A.1) which is higher than zinc and cadmium arachidate as can be seen from Table I. This could be understood if we consider the nominal pKa (The pKa of the fatty acid-subphase salt system is defined as follows – it is the pH at which half of the fatty acid heads are dissociated (pKa value of arachidic acid is 5.5)) values of the fatty acid salt system for different cations. At low pH values acidic carboxylic groups are protonated and metal cataions do not bind and affect the monolayer [38, 39]. Due to the metal cation binding with monolayer under increasing in subphase pH the fractions of free acid and soap coexist in monolayer what results in characteristic changes in monolayer compression isotherms due to phase behaviour of a mixed monolayer [38-41]. At high enough pH values dependent on the metal cation nature the fatty acid monolayer is condensed and converted completely to the salt form what is manifested by characteristic compression isotherm without L_2/LS phase transition [42].

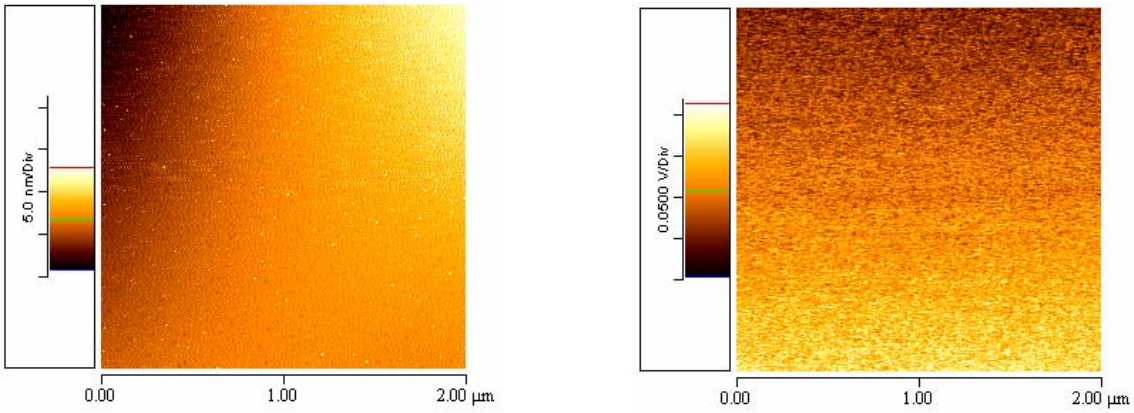

(a) (b)

Figure A.2 Tapping mode AFM image of one layer of nickel arachidate deposited on mica (a) topography (b) phase image.

Figures A.2(a) and (b) show the tapping mode topographic and phase image of Ni arachidate LB film (single layer) deposited on the mica substrate after one cycle of vertical substrate lifting respectively. Transfers were made in the LS phase. If transfers are made in L_2 phase one does not get uniform coverage. The AFM images of films transferred in LS phase show macroscopically flat structure. The variation of r.m.s. roughness with the scan size is shown in fig.A.3. As can be seen from fig.A.3, for smaller scan sizes the r.m.s. roughness is very low which is because of the resolution limit of the instrument. As the scan size is increased the r.m.s. roughness value increases to ~ 2.6 nm. This value is in good agreement with the length of the fully extended arachidic acid molecule which is 2.7 nm long. All the AFM images were acquired after drying the samples in the desiccator for almost one hour. Two types of scan heads were used: one for large area scan (90X90 μm^2 scan range) and another one for molecular-resolution images (5X5 μm^2 scan range). All images presented here were obtained with a cantilever

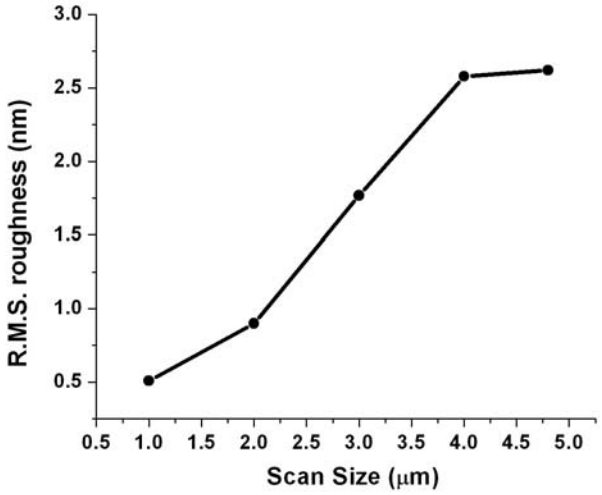

Figure A.3 Variation of r.m.s. roughness of one layer nickel arachidate film deposited on mica with scan size.

of spring constant k=0.9 N/m for tapping mode images and k=0.03 N/m for contact mode images. Typical values of forces used in these experiments were in the range of nN for contact mode imaging.

Bi-valent ions	Area/mol (nm^2/mol) (in between L_2 phase and LS phase)	pH range of L_2 to LS (complete salt formation) phase transfer	Comparison of pKa values of the bi-valent ions
Ni^{2+}	0.26-0.20	4.5-7.5	Ni>Cd≈Zn [42]
Cd^{2+}	0.21-0.18	4.5-6.0	Cd≈Zn<Ni
Zn^{2+}	0.20-0.16	4.5-6.0	Zn≈Cd<Ni

Table A.1 Comparison of different parameters of Ni, Cd and Zn arachidate salts formed by LB technique.

Finally, we also achieved high-resolution images which allowed us to obtain the 2D crystallographic structure of the nickel arachidate LB film. Atomic resolution images of films deposited on mica can be obtained when the pH is more than the pKa values showing a complete salt formation has been achieved. Figure 4(a) shows atomic resolution image of one-layer nickel arachidate film. The molecules are arranged regularly as evident from fig.A.4. The intermolecular distances are 0.328±0.03 nm and 0.643±0.04 nm along the two lattice vectors. The variation in the unit cell dimensions is related to the degree of covalent bonding between the metal ion and the carboxylic acid group, and to specific interactions with the mica substrate. The role of the interface (substrate or free surface) in determining molecular ordering is only to allow or disallow the adjacent head-group-head-group stabilization. The structure and extent of positional correlations of the monolayer films are dramatically affected by a change in cation and are related to a strong interaction with the mica substrate. Theses distances can be deduced from the two-dimensional fast Fourier transform of the data as shown in fig. A.4(b). In FT's, the vertical and horizontal streaks are due to noise generated by the discrete raster pattern of the AFM. AFM images (figs. A.4(a) and (b)) of one-layer NiA film show a different spacing along the two in-plane vectors, indicating an orthorhombic or monoclinic crystal structure. This difference could originate from a distortion of the molecules or the lattice by the scan process. From measurements of molecular spacing, one gets an area per molecule, $A_{AFM} \approx 0.22$ nm^2, which is in good agreement with area/mol deduced from isotherms, $A_{iso} \approx 0.23$ nm^2. This suggests that the films are homogeneous and they maintain the order after the transfer. Nickel counterion determines the area per molecule of the LB film and that the alken packing adjusts to find the optimal structure given this constraint.

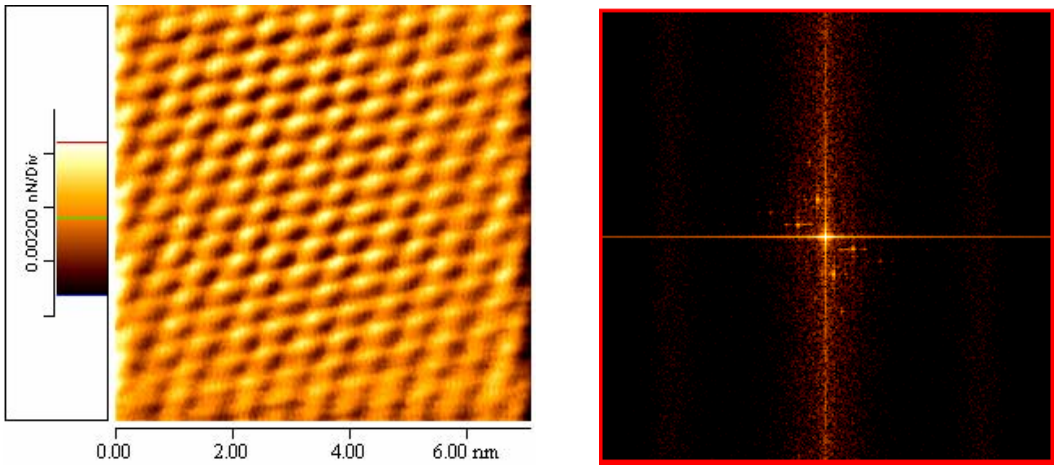

(a) (b)

Figure A.4 Molecular resolution image of nickel arachidate film on mica substrate is shown. The scan area is 7 nm X 7 nm (a). Fourier transform of the molecular resolution image shows the rectangular lattice structure (b).

During the measurements we observed no damage of the films caused by the probing tip. The force of 10^{-9} N that we used is an upper limit; at higher loadings, plastic deformation of the film has been reported [43].
Difficulties that must be considered include damage to the sample by the AFM tip, image drift due to thermal variations and hysteresis of the piezoelectric scanners, and both gross and subtle variations between AFM tips. The degree of drift in the image was evaluated by comparing Fourier transforms of images scanned in opposite directions (up and down).

A.4 Conclusions

In summary, the interaction between arachidic acid and Ni^{2+} has been investigated as a function of subphase pH. From surface pressure-area/mol (π-A) isotherms, it reveals that for higher pH (> 7.0), fully condensed monolayer was obtained which corresponds to a 100% conversion of the acid to the metal arachidate form. AFM images of one layer NiA films deposited on mica substrate show atomically smooth surface. We have also obtained molecular resolution images and high resolution Fourier transforms of LB films of NiA. In combination with careful calibration and evaluation of errors, we determined the lattice symmetry with good precision. This ability is a necessary first step to any experimental work on two-dimensional lattices. The AFM images show that the essential factor in determining order and stability in the alkyl chains in NiA films is the presence of an adjacent head-group-head-group interface stabilized by nickel ions. Thin LB films can develop long-range order which suggests that the driving force for ordering in these films is strong and is controlled by interactions between adsorbed molecules. The monolayer stability behaviour and molecular packing arrangement in all the metal arachidates studied in this work are significantly affected by subphase pH. These results point out the limited nature of the correlation between metal ion electronegativity and the molecular packing arrangement in the monolayer and multilayer of divalent fatty acid

salts. It also implies that the complex nature of the relationship between the properties of the monolayer on water surface and the structure of transferred multilayers need to be explored.

Bibliography

1. M.C. Petty, Langmuir-Blodgett Films, Cambridge University Press: Cambridge, (1996).
2. E.S. Smotkin, C. Lee, A.J. Bard, A. Campion, M.A. Fox, T.E. Mallouk, S.E. Webber, J.M. White, Chem. Phys. Lett. 152, 265-268, (1988).
3. V. Erokhin, L. Feigin, G. Ivakin, V. Klechkovskaya, Y.U. Lvov, N. Stiopina, Macromol. Chem. Macromol. Symp. 46, 359, (1991).
4. A.V. Nabok, A.K. Ray, A.K. Hassan, J.M. Titchmarsh, F. Davis, T. Richardson, A. Starovoitov, S. Bayliss, Mat.Sci. Eng. C 89, 171, (1999).
5. R.S. Urquhart, C.L. Hoffmann, D.N. Furlong, N.J. Geddes, J.F. Rabolt, G. Franz, J. Phys. Chem. 99, 15987, (1995).
6. S. Ravaine, G.E. Fanucci, C.T. Seip, J.H. Adair, D.R.Talham, Langmuir 14, 708, (1998).
7. C.K. Preston, M.J. Moskovits, J. Phys. Chem. 97, 8405, (1993).
8. M. Haruta, T. Koyabashi, H. Sano, N. Yamada, Chem. Lett. 405, (1987).
9. G. Schmid, Nanoparticles: From Theory to Application, Wiley-VCH: Weinheim, Germany, (2004).
10. A.K. Boal, F. Ilhan, J.E. DeRouchey, T. Thurn-Albrecht, T.P. Russell, V.M. Rotello, Nature, 404, 746, (2000).
11. Y. Maeda, H. Tabata, T. Kawai, Appl. Phys. Lett. 79, 1181, (2001).
12. G.L. Gaines, Insoluble Monolayers at Liquid-Gas Interface, Interscience, New York, (1966).
13. A. Dhanabalan, N. Prasanth Kumar, S. Major, S.S. Talwar, Thin Solid Films, 327-329, 787-791, (1998).
14. D.J.M. Linde′n, J.P.K. Peltonen, J.B. Rosenholm, Langmuir, 10, 1592-1595, (1994).
15. M.L. Kurnaz, D.K. Schwartz, Langmuir, 12, 4971-4975, (1996).
16. Roberts, G.G., Ed. Langmuir-Blodgett Films, Plenum Press, New York, (1990).
17. J.G. Petrov, I. Kuleff, D. Platikanov, J. Colloid Interface Sci., 88, 29, (1982).
18. M.R. Buhaenko, M.J. Grundy, R.M. Richardson, S.J. Roser, Thin Solid Films, 159, 253, (1988).
19. B.P. Binks, Adv. Colloid Interface Sci. 34, 343, (1991).
20. R. Aveyard, B.P. Binks, N. Carr, A.W. Cross, Thin Solid Films, 188, 361, (1990).
21. J. W. Ellis, J.L. Pauley, J. Colloid Sci. 19, 755, (1964).
22. N. Matsuura, D.J. Johnson, D.T. Amm, Thin Solid Films, 295, 260-265 (1997).
23. D.M. Taylor, J.N. Lambi, Thin Solid Films, 243, 384-388, (1994).
24. L.K. Brar, P. Rajdev, A. K. Raychauhuri, D. Chatterji, Langmuir, 21, 10671, (2005).
25. H.G. Hansma, S.A.C. Gould, P.K. Hansma, H.E.Gaub, M.L. Longo, J.AN. Zasadzinski, Langmuir, 7, 1051, (1991).
26. M. Seul, P.M. Eisenberger and H.M.McConnell, Proc. Natl. Acad. Sci. U.S.A. 80, 5795 (1983).
27. A. Fisher and E. Sackmann, J. Colloid Interface Sci., 112, 1, (1986).
28. M. Pomerantz and A. Segmuller, Thin Solid Films, 68, 33, (1980).

29. S. Garoff, H.W. Deckmann, J. Dunsmuir, M.S. Alvarez, J.M. Bloch, J. Physique, 47, 701-709, (1986).
30. E. Meyer et al., Nature (London), 349, 398, (1991).
31. M. Egger et al., J. Struct. Biol., 103, 89, (1990).
32. Sigma Aldrich, St. Louis, Missouri, USA.
33. SRL Ranbaxy Limited, USA.
34. Merck & Co., Inc., Whitehouse Station, NJ, USA.
35. Apex Instruments Co., Jadavpur, Kolkata, India.
36. Veeco, Santa Barbara, California, USA.
37. A.L. Weisenhorn et al., Langmuir 7, 8, (1991).
38. C.M. Knobler, R.C. Desai, Annu. Rev. Phys. Chem. 43, 207, (1992).
39. J.A. Spink, J.V. Sanders, Trans. Faraday Soc., 51, 1154, (1955).
40. M.L. Kurnaz, D.K. Schwartz, J. Phys. Chem., 100, 11113, (1996).
41. J.A. Spink, J. Coll. Interf. Sci., 23, 9, (1967).
42. H. Reigler, K. Spratte, Thin Solid Films, 210-211, 9, (1992).
43. G.S. Blackman, C.M. Mate, M.R. Philpott, Phys. Rev. Lett., 65, 2270-2273 (1990).

Appendix B

Study of large area patterned arrays of gold nanoparticles using Atomic Force Microscope

I) Two-dimensional arrays of uncapped gold nanoparticles on silicon substrates

In this section we have described the study of two-dimensional arrays of uncapped gold (Au) nanoparticles spin-coated on silicon substrate by atomic force microscopy (AFM). Firstly, we have mentioned the method of preparing large area patterned 2D arrays of uncapped Au nanoparticles on silicon substrate. The pattern has been formed using self-assembly of uncapped Au nanoparticles. The Au nanoparticles were synthesized via toluene/water two phase systems using a reducing agent and colloidal solution of Au nanoparticles was produced. Analysis by AFM showed discrete Au nanoparticles of 4 nm average diameter. TEM analysis also showed similar result. The AFM studies also showed these nanoparticles formed self-assembled coherent patterns with dimensions exceeding 500 nm. Spin coating on silicon substrate by suitably adjusting the speed can self-assemble these nanoparticles to lengths exceeding 1 μm.

I a. Multiscale array formation of gold-nanoparticles using spin coater

Au sol was prepared by following the procedure by Drake et. al. [1]. The synthesis process of such small particles does not use any kind of capping agent and it is achieved only by controlling the rate of the reaction. The process is described in detail in [2]. Next part of this work is to make large area periodic arrays of these small particles. It has been shown before that the nanoparticles fabricated without cross-linking agents can from arrays whose dimension can approach ~500nm [3-5]. We have investigated whether by using simple techniques we can form a pattern where these smaller arrays (which we now call islands) are arranged in an array of larger dimensions. The concentration of the Au-sol used was 2.54 mg/ml. About 400-500 μl of solution was spread on silicon substrate by a micropipette. We have investigated two different spin-coating speeds – i) 1000 r.p.m. and ii) 7000 r.p.m. For 7000 r.p.m., the pattern so generated has two scales. In one scale we have individual islands (of approximate size 500 nm) of nanoparticles (size ~few nm) and in the other scale these islands themselves are arranged in an ordered pattern in the scale of few μm. This is thus a multi-scale pattern which can be formed by

a single step process of spin–coating once the stable sol of Au nanoparticles is formed. The islands (few micron size) formed by spin-coating are not strictly 2D in nature. In some places the islands contain agglomeration of the Au nanoparticles that lead to 3D pilling of the nanoparticle in regions. On the other hand, the ordered pattern formation occurs with the Au-sol at a critical speed of spin coating. The critical speed itself depends on the solution characteristics. Typical critical speed for the ordered pattern formation is ~1000 r.p.m. An optical microscope image of the pattern is shown in fig. B.1.

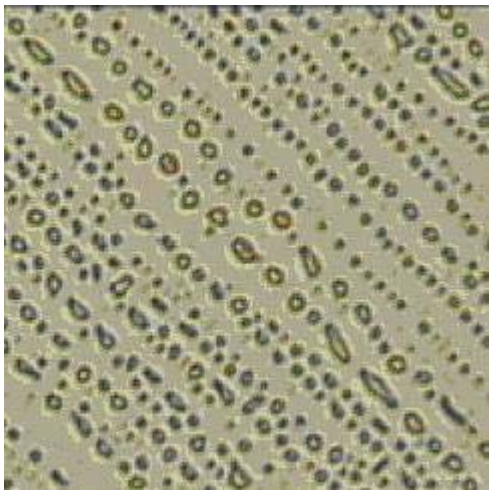

Figure B.1 Optical microscopic image (magnification 10X) of large periodic array formed on hydrophilic silicon substrate. Spin coating speed was 1000 r.p.m.

Figure B.2 shows a cartoon to demonstrate the types of pattern formed at different speeds. It can be seen that a pattern with regular spacing of the islands can be formed only at a critical speed. At other speed one observes larger spherical agglomerations of gold nanoparticles or finger like patterns. The pattern formation depends on the hydrophilic nature of the substrate. If the native oxide layer was etched out using HF and the substrates are made hydrophobic no regular pattern formation occurs. The re-growth of an oxide layer on the Si substrate makes the patterns reappear.

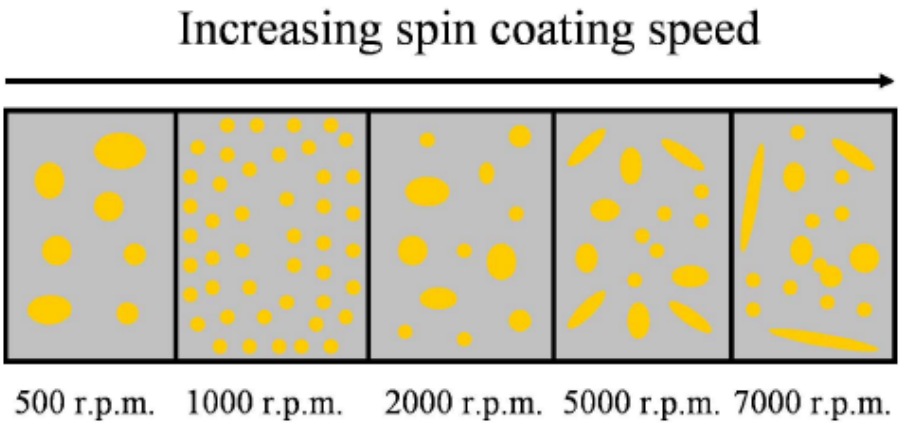

Figure B.2 A cartoon of the effect of spin coating speed on pattern formation.

I b. Analysis of gold self assembled islands by atomic force microscope (AFM)

To assess the state of the Au nanoparticles we used an atomic force microscope (AFM). However, imaging of nanoparticles of such sizes is not very straightforward due to the finite size of the tip used. The convolution of tip shape on sample topography can introduce significant inaccuracy in an AFM image, when the tip radius is comparable to the typical dimension of the sample features to be observed [6]. One should also be very careful about the instrumental noise also to obtain reliable data. For this a good amount of statistics is generated from AFM line scans to find the state of Au nanoparticles. For this a good amount of statistics is generated from AFM line scans to find out the state of Au nanoparticles. The particle size was calculated from noncontact mode AFM data. AFM images were taken using CP II from Veeco [7]. Noncontact mode images were taken using a silicon tip having spring constant, 0.9 N/m and resonance frequency 22.83 kHz. The set frequency was 22.80 kHz. Figures B.3a and b show both the tapping mode topography and phase images (with line scan) of Au nanoparticles spin coated on silicon substrate at 7000 rpm for 30 s. Substrates were cleaned by well known RCA cleaning. The concentration of the solution was 2.54 mg/ml. The images were taken on an island formed by assembly of such nanoparticles. Most of the islands are closer to circular shape. The average particle size calculated from AFM data is 4.26 ± 1.31 nm (calculated from noncontact mode data) which is in good agreement with the TEM data. The average particle size calculated from TEM images is 3.97 ± 0.45 nm [2]. The particle size was calculated from contact mode AFM (LFM) data for further confirmation and it came out to be 4·28 ±1·26 nm. Figure B.4 shows the particle size distribution from tapping mode AFM data.

The spin coating of Au sol on the silicon substrate does not lead to one kind of structure. It has been noticed that two different types of structures were formed on silicon substrate because of spin coating at 7000 rpm. The surface of the substrate was hydrophilic. At the centre of the substrate spherical agglomeration of Au nanoparticles (size ranging from 30 nm to 400 nm) were found. Further imaging inside these bigger islands reveals smaller islands of gold nanoparticles which are < 30 nm in size as shown in figures B.5 (a, b) and B.6 (a,b). At the corner of the substrate we noticed long structures (size ~ 4 μm) as shown in figures B.7(a, b), respectively. These long structures, known as 'fingers'[8], are believed to be formed because of imperfect wetting behaviour during spin coating at the expanding front.

Here both the topographical and phase images are shown and it can be easily seen that the contrast is much more in phase images than topographical images. Both types of structures have the Au nanoparticles in similar state of assembly. However, the long types can grow up to sizes as large as 4 μm. The observed self-assembly depends on hydrophilic nature of the substrate. By making the substrates hydrophobic (by HF etching) does not lead to such self-assembly.

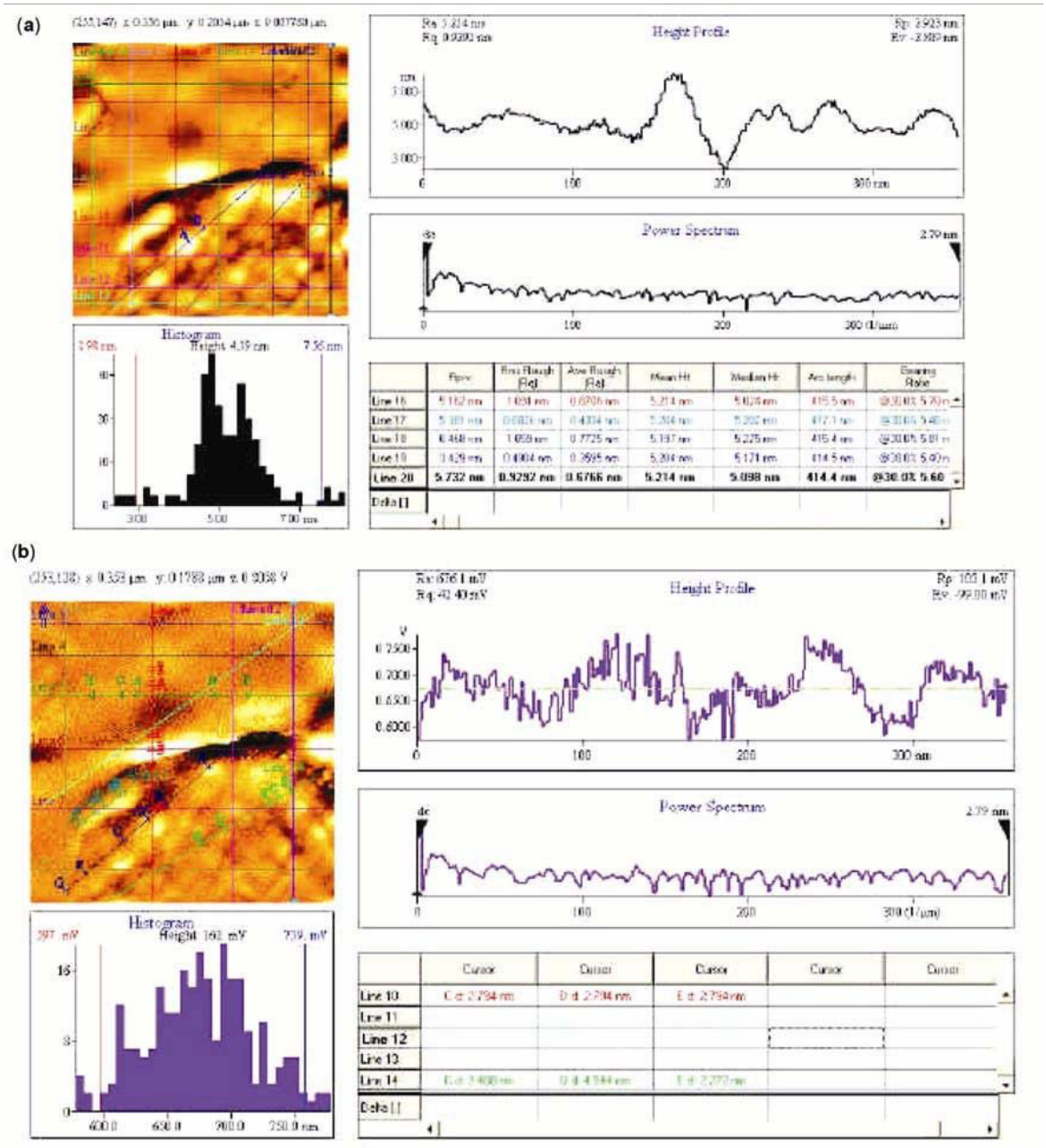

Figure B.3 a. Topographical image (tapping mode) of gold nanoparticles (with line scan) spin coated on silicon substrate (7000 rpm). Scan size 367 × 367 nm. b. phase image (tapping mode) of gold nanoparticles (with line scan) spin-coated on silicon substrate (7000 rpm). Scan size 367 × 367 nm.

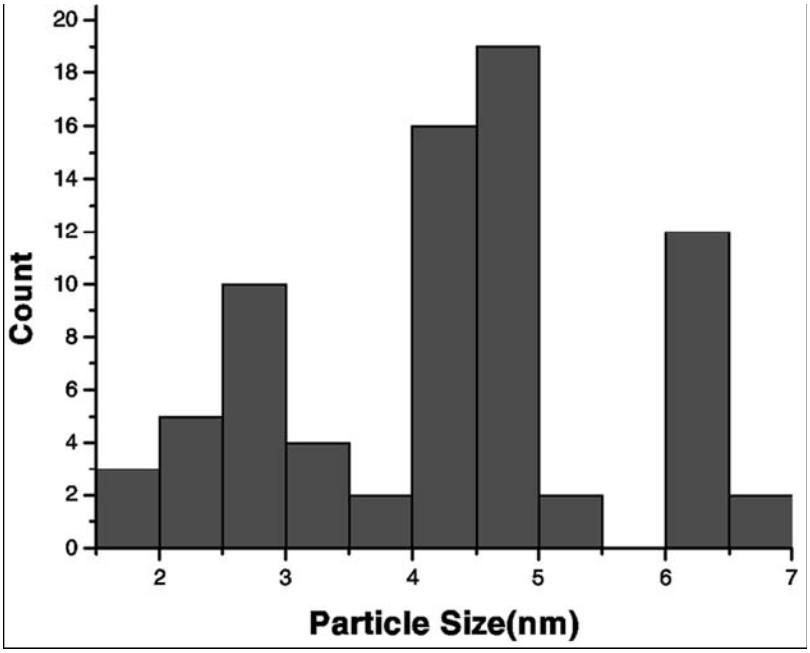

Figure B.4. Particle size distribution from tapping mode AFM data.

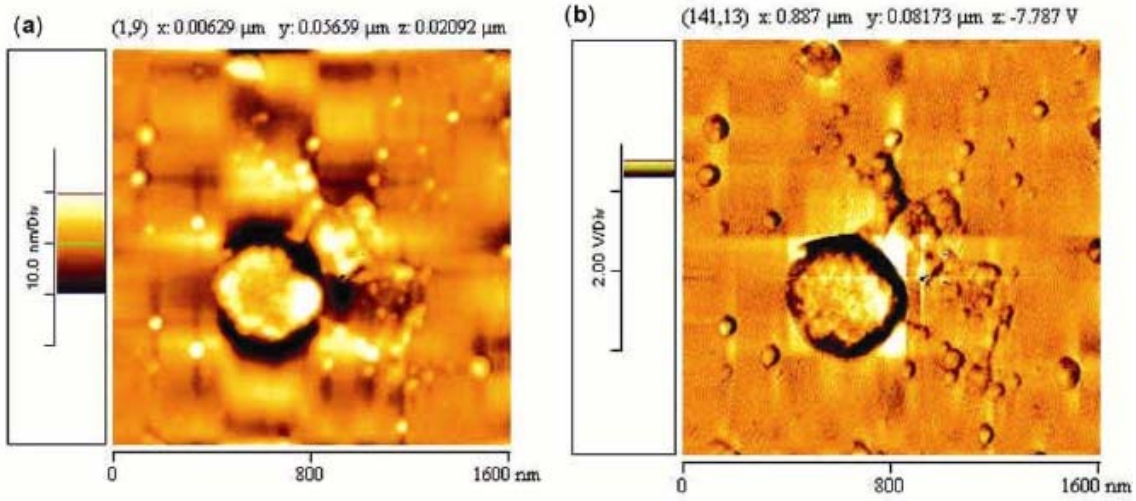

Figure B.5 a. Topographical image of gold nanoparticles spin coated on silicon substrate (7000 rpm). Spherical agglomeration (size ranging from 30 to 400 nm) at the middle portion of the substrate. Scan size, 1.6 × 1.6 µm and b. phase image of gold nanoparticles spin coated on silicon substrate (7000 rpm). Spherical agglomeration (size ranging from 30 to 400 nm) at the middle portion of the substrate. Scan size, 1.6 × 1.6 µm.

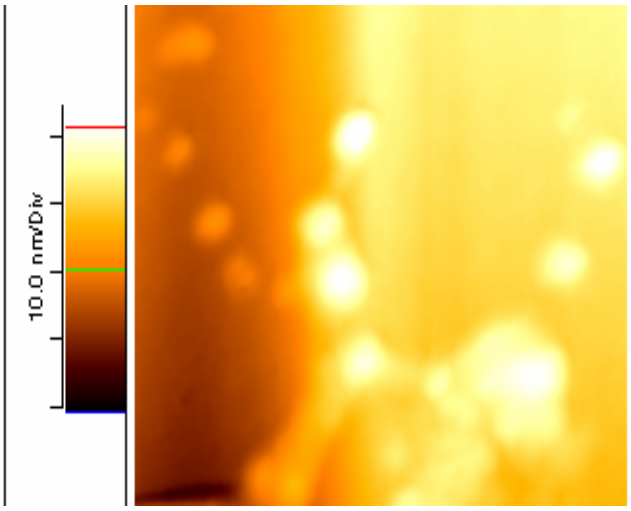

Figure B.6a Topographical image (noncontact mode) of gold nanoparticles spin-coated on silicon substrate (7000 r.p.m). Scan size 610 nm X 610 nm.

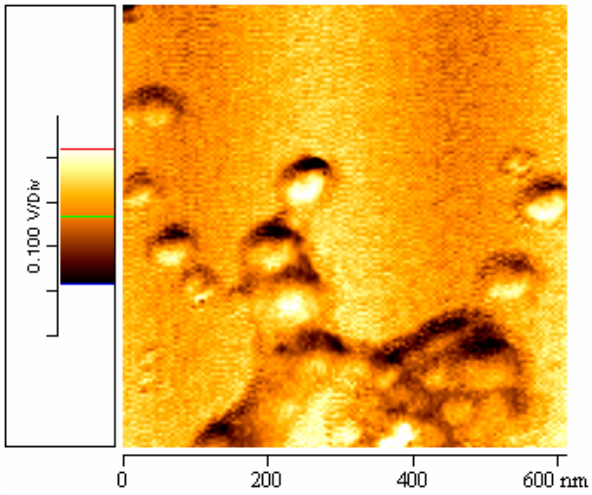

Figure B.6 b. Phase image (tapping mode) of gold nanoparticles spin coated on silicon substrate (7000 r.p.m). Scan size 610 nm X 610 nm.

Briefly we explain the pattern formation as follows. The sol containing the Au nanoparticles spreads due to wetting. Its thickness is controlled (thinned) due to spin-coating thinning rate $\propto h^3\omega^2$, h being film thickness and ω is the spinning speed. At later stages solvent evaporation contributes to the thinning process. The centrifugal force makes the liquid accumulate at the rim. At a critical thickness $h=h_c$ (typically ~50nm) the film so formed becomes hydrodynamically unstable and produces a reproducible pattern of water drops (islands). The periodicity is controlled by the thickness and the contact angle (θ) and is given by wavelength $\approx (4\pi h / \theta)$ of the most rapidly growing instability.

Spin coating is a simple and effective technique to deposit thin, uniform films across planar substrates. The film solution generally consists of volatile solvents in solution with

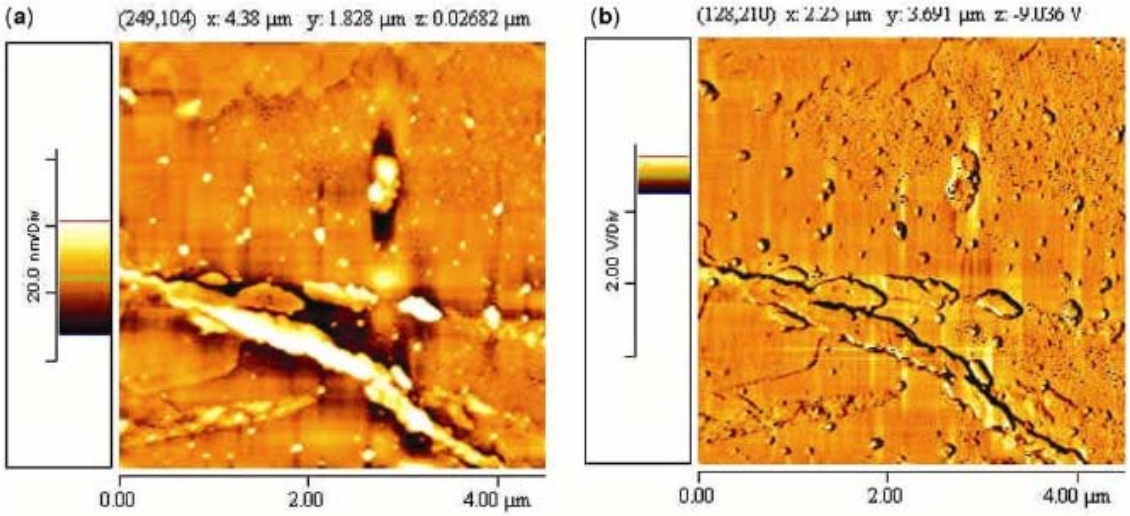

Figure B.7. a. Topographical image of gold nanoparticles spin coated on silicon substrate (7000 rpm). Long structure (size, ~ 4 µm) at the corner of the substrate. Scan size, 4.5 ×4.5 µm and b. phase image of gold nanoparticles spin coated on silicon substrate (7000 rpm). Long structure (size, ~ 4 µm) at the corner of the substrate. Scan size, 4.5 × 4.5 µm.

effectively non-volatile solutes. This solution is dispersed onto a planar surface that is then accelerated to a predetermined rotation rate. Evaporation of the volatile constituents occurs from the top surface of the solution, while simultaneously the rotation (centrifugal force) forces the fluid to flow uniformly outward. Typically, fluid flow considerations dominate the early part of spinning while solvent evaporation controls the behaviour at later stages. The thinning rate of solution which is attributed to viscous flow varies as the cube of solution thickness (and the square of spin speed), so this dominates the early stage of spinning. The thinning rate of solution contributed by solvent evaporation is independent of solution thickness because it occurs only at the top surface and is limited by diffusion of the evaporated solvent molecules through a laminar vapour boundary layer above the solution/air interface.

II Study of uncapped gold nanoparticle filled polymer thin films on patterned surface by atomic force microscope

The detailed structural study of uncapped gold nanoparticles (diameter ~ 3–4 nm) filled thin polymer (polystyrene) film on patterned surface by atomic force microscopy has been discussed in this section. It shows that the final dewetted morphology comprises of an isotropic array of nearly equal sized droplets. Force modulation atomic force microscopy reveals the detailed core–shell structure of each individual dewetted droplet.

While the outer core comprises of the dewetted polymer, the core is constituted due to self origination and aggregation of the nanoparticles present in the film.

II a. Preparation of gold nanoparticle filled Polystyrene films

Here also we have used the Au nanoparticles prepared by the procedure by Drake et. al. as mentioned above for preparing Au nanoparticle filled polystyrene films on patterned surface. Toluene is one of the most common solvents for polystyrene and therefore bids of Mono-dispersed PS (Sigma Aldrich [9], molecular weight: 280K, Poly Dispersity Index (PDI) <1.1) were added directly to the gold sol stabilized in toluene for making PS solution containing gold nanoparticles. The concentration of the particles was calculated as the ratio of the weight of gold nanoparticles present in the system to that of the polymer added. The PS solution in the toluene sol is directly spin coated on cleaned single side polished n–type commercial grade silicon wafer (Wafer World Inc.[10]) pieces. Films having thicknesses of 12 ± 0.3 nm, 17 ± 0.6 nm, 23 ± 0.8 nm and 30 ± 0.2 nm, with nanopartcile loadings of 0.04%, 0.1%, 1.0 %, 2.0 %, 4.0 % and 8.0 % as well as 0% (PS films without any nanoparticle) for each thickness have been prepared. The detailed description of the sample preparation is given in [11, 12]. It does not come under the scope of this thesis.
The film thicknesses are controlled by varying the concentrations of the PS solution and the spin speed, and the duration of spinning to a lesser extant. The dewetting of the films is triggered by exposure to toluene vapor in a closed glass chamber pre-saturated with toluene vapor. Exposing a polymer film to its solvent vapor effectively reduces the glass transition temperature due to penetration of the solvent molecules into the film matrix. The absorption of solvent into the polymer matrix leads to increase in its free volume, resulting in reduced cohesion between the polymer molecules, which in turn aids to their mobility. Thus, the molecules become free to reorganize, and depending on the thermodynamics of the system, can lead to the rupture and dewetting of the thin film. Minimization of the excess free energy is the key motivation for the self organization. The shapes of the final dewetted structures are governed by the equilibrium contact angle (θ_E) of the polymer on the substrate material and the length scale of the structures is a function of the film thickness as well as the surface and interfacial tensions of the film and the substrate materials.

II b. Study of detailed structure of a single dewetted Droplet

In order to understand how the gold nanoparticles orient themselves within the dewetted polymer structures, Force Modulation Atomic Force Microscopy is performed on a single droplet forming due to dewetting of a 15 nm thick PS film, with 0.1 % nanoparticle concentration. Figure B.8 (a, b) shows the tapping mode amplitude and phase image of the patterned surface with polystyrene embedded gold nanoparticles. The image (figure B.9a) reveals that each droplet has a core–shell structure. This is further verified by the contrast in the phase image, shown in figure B.9b. The inner core is constituted of an aggregate of gold nanoparticles that have phase

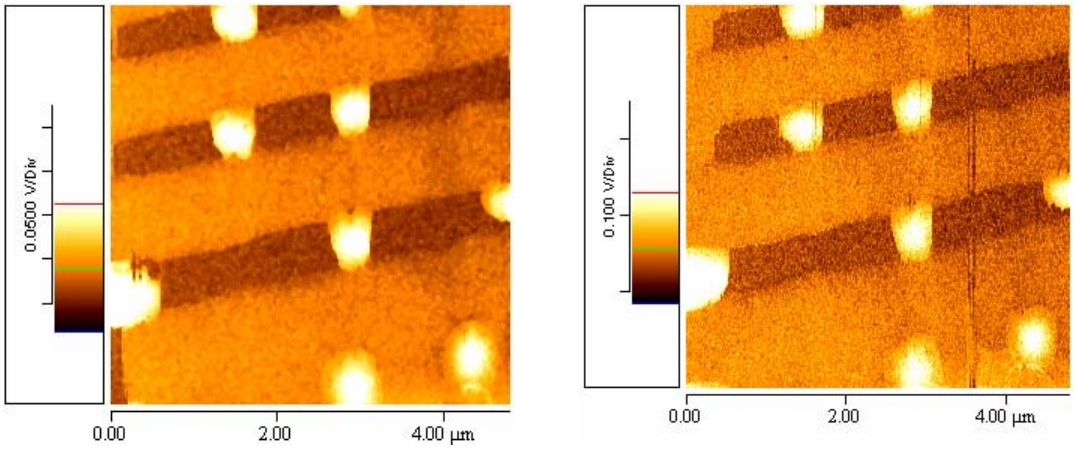

(a) (b)

Figure B.8a Amplitude image of the patterned surface with polystyrene embedded gold nanoparticles. Scan size 4.8 X 4.8 µm. b Phase image of the same.

separated from the polymer and accumulated at the centre of the droplet. A lower particle – particle cohesive energy penalty, in comparison to a higher particle–polymer adhesive energy is probably the reason for accumulation of the uncapped nanoparticles. The core is surrounded on all sides by a shell of dewetted polystyrene. Thus, incorporation of nanoparticles result in formation of novel core–shell type dewetted structures, which is otherwise difficult to fabricate by the existing top down lithography or even most other self organized patterning techniques.

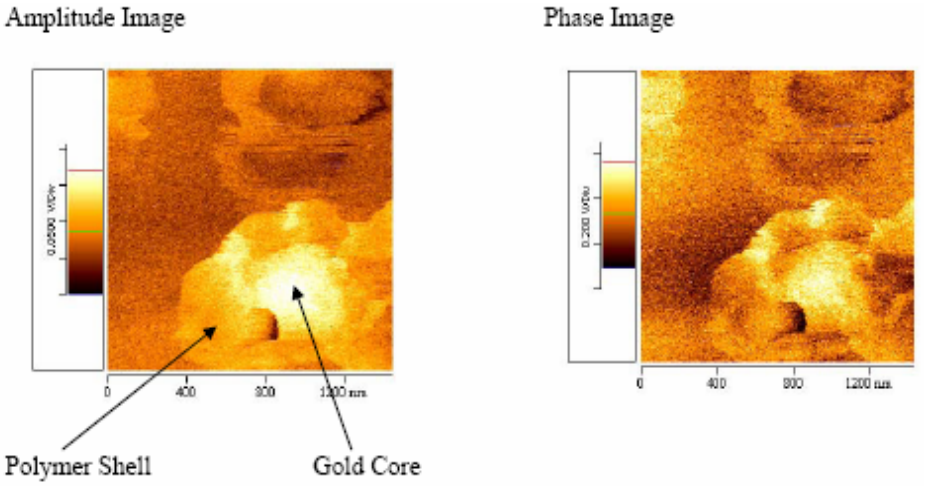

(a) (b)

Figure B.9 a Amplitude and b Phase contrast image of Force Modulation Atomic Force Microscopy, revealing the detailed core – shell structure of each individual polymer droplet, from dewetting of a nanoparticle filled film.

Bibliography

[1] Drake P and Youngs I, Mat. Sci. Technol. 18**,** 772, 2002.
[2] Anindya Das, Soma Das and A.K. Raychaudhuri, Bull. Mater. Sci., 31, 1-6, 2008.
[3] Kodama H, Momose S, Ihara N, Uzumaki T and Tanaka A, Appl. Phys. Lett. 83, 5253, 2003.
[4] Cho Y S, Choi G S, Hong S Y and Kim D, J. Cryst. Growth, 243, 224, 2002.
[5] Choi G S, Cho Y S, Son K H and Kim D J, Microelectron. Eng., 66, 77, 2003.
[6] D Tranchida, S Piccarolo and R A C Deblieck, Meas. Sci. Technol,. 17, 2630, 2006.
[7] Veeco Instruments Inc. Corporate Headquarters 100 Sunnyside Blvd. Ste. B Woodbury New York 11797-2902.
[8] Schwartz L W and Roy R V, Phys. Fluids, 16, 569, 2004.
[9] Sigma Aldrich, U.K.
[10] Wafer World Inc., U.S.A.
[11] Ashutosh Sharma, Manoj Gonuguntla, Rabibrata Mukherjee, Subash A. Subramanian, and Ravindra C. Pangule, Journal of Nanoscience and Nanotechnology, 7, 1744–1752, 2007.
[12] Rabibrata Mukherjee, Manoj Gonuguntla, and Ashutosh Sharma, Journal of Nanoscience and Nanotechnology, l.7, 2069–2075, 2007.

Appendix C

Programs

Static mode

```
ampl = 0.0; h = 80.0; q = 33.3; k = 0.1;
amplit = ampl;
npts = 200;
step = (80.0 - 0.1) / npts;
noutfile = OpenWrite["d200.dat"];
ampfile = OpenWrite["vel03.dat"];
forcefile = OpenWrite["forcevan300.dat"];
outfile = OpenWrite["quick.in"];
Write[outfile, step];
Write[outfile, h];
Close[outfile];
xval1 = 0.0;
xpr = 0.0;
For [fcount = 1, fcount ≤ 2.0 * npts, fcount += 1,
    (*f=0.5*(ampl+amplit)*1.0/q; *)
  Clear[t];
  a = 2.2; a0 = 0.122; b = 580.0;
  fext2[z_] := -1.0 * a / (6.0 * z^4) /; z > a0;

  fext2[z_] := -1.0 * a / (6.0 * a0^4) + b * (a0 - z)^1.5 /; z ≤ a0;

  fext = Evaluate[fext2[z] /. z → (x[t] + h)];
  xval1 *= 0.7;
  sol =
    NDSolve[
     {D[x[t], {t, 2}] ==
        -(x[t] - fext / k + 1.0/q * D[x[t], t]), x[0] == xval1,
     x'[0] == xpr}, x[t], {t, 0.0, 1500.0},
    MaxSteps → 1000000];
       t = 1500.0;
     xval1 = Evaluate[x[t] /. sol[[1]]];
     t = 1499.999;
     xval2 = Evaluate[x[t] /. sol[[1]]];
     xpr = (xval2 - xval1) / 0.001;
       Write[noutfile, FortranForm[h],
  OutputForm["        "], FortranForm[xval1]];
  Write[ampfile, FortranForm[h], OutputForm["        "],
   FortranForm[xpr]];
  Write[forcefile, FortranForm[h], OutputForm["        "],
   FortranForm[fext2[h]]];
  If[fcount ≤ npts,
   h1 = h - step,
   h1 = h + step;
  ];
  h = h1;
 ];
Close[noutfile];
Close[ampfile];
Close[forcefile];
```

Dynamic mode: Amplitude

```
h = 100.001; q = 100.0; k = 40.0;
ampl = 75.0;
amplit = ampl;
fil = "a.0.dat";
step = 100.0 / 650.0;
om = 1.0;
noutfile = OpenWrite["appret3.dat"];
ffile = OpenWrite["force.dat"];
Write[noutfile,
  "# d=0.8 a=20.14 q=1.0 ampl=1.5"];
outfile = OpenWrite["quick.in"];
Write[outfile, step];
Write[outfile, h];
Close[outfile];
xval1 = h;
xpr = ampl * om;
For [fcount = 1, fcount ≤ 1300, fcount += 1,

    f = 0.5 * (ampl + amplit) * 1.0/q;
  Clear[t];
  a = 1.42; a0 = 0.164;
  fext2[z_] := -1.0 * a / (6.0 * z^2) /; z > a0;

  (*fext2[z_]:=-1.0*a/(6.0*a0^2)+7.7943*(a0-z)^1.5/;
      z≤a0;*)
  fext2[z_] := -1.0 * a / (6.0 * a0^2) + 7.7943 * (a0 - z)^1.5 /;
    z ≤ a0;
  fext = Evaluate[fext2[z] /. z → (x[t] + h)];
  If[fcount ≤ 650,
   h1 = h - step;,
   h1 = h + step;
  ];
  h = h1;
  sol =
    NDSolve[
     {D[x[t], {t, 2}] ==
        -(x[t] - fext / k + 1.0/q * x'[t] - f * Cos[om * t]),
     x[0] == xval1, x'[0] == xpr}, x[t], {t, 0.0, 1500.0},
    MaxSteps → 100000];

      xvalmin = 1000.0;
     xvalmax = -1000.0;
     For [t = 1490.0, t < 1500.0, t += 0.01,
         xval = Evaluate[x[t] /. sol[[1]]];
         xvalmin = Min[{xvalmin, xval}];
         xvalmax = Max[{xvalmax, xval}];
     ];
     t = 1500.0;
     xval1 = Evaluate[x[t] /. sol[[1]]];
     t = 1499.999;
     xval2 = Evaluate[x[t] /. sol[[1]]];
     xpr = (xval2 - xval1) / 0.001;
        amplit = (xvalmax - xvalmin) / 2.0;
        If[fcount == 1, amplit0 = amplit];
       Write[noutfile, FortranForm[h],
   OutputForm["        "], FortranForm[amplit]];
  Write[ffile, FortranForm[h], OutputForm["        "],
   FortranForm[fext2[h]]];

 ];
Close[noutfile];
Close[ffile];
```

Dynamic mode: Resonance curves

```
h = 68.547; q = 100.0; k = 40.0;
ampl = 75.0;
amplit = ampl;
fil = "a.0.dat";
step = 0.01 / 100.0;
noutfile = OpenWrite["ret.res.1.003.r21.dat"];
Write[noutfile, "# d=0.8 a=12.0 q=1.0 ampl=0.012"];
outfile = OpenWrite["quick.in"];
Write[outfile, step];
Write[outfile, h];
Close[outfile];
om = 1.0 + step * 100.0;
xval1 = 0.0;
xpr = ampl * om;
For [fcount = 1, fcount ≤ 200, fcount += 1,
  f = 0.5 * (ampl + amplit) * 1.0 / q;
   Clear[t];
  a = 1.42; a0 = 0.164;
  fext2[z_] := -1.0 * a / (6.0 * z^2) /;
    z > a0;
  fext2[z_] := -1.0 * a / (6.0 * a0^2) + 7.7943 * (a0 - z)^1.5 /;
    z ≤ a0;
  fext1 = Evaluate[fext2[z]];
  fext = Evaluate[fext1 /. z → (h + x[t])];
  sol =  NDSolve[
     {D[x[t], {t, 2}] ==
       -(x[t] - fext / k + 1.0 / q * x'[t] - f * Cos[om * t]),
      x[0] == xval1, x'[0] == xpr}, x[t], {t, 0.0, 1500.0},
     MaxSteps → 100000];
  xvalmin = 1000.0;
  xvalmax = -1000.0;
   For [t = 1490.0, t < 1500.0, t += 0.001,
    xval = Evaluate[x[t] /. sol[[1]]];
    xvalmin = Min[{xvalmin, xval}];
    xvalmax = Max[{xvalmax, xval}];
  ];
   t = 1500.0;
  xval1 = Evaluate[x[t] /. sol[[1]]];
  t = 1499.999;
  xval2 = Evaluate[x[t] /. sol[[1]]];
  xpr =  (xval2 - xval1) / 0.001;
  amplit =  (xvalmax - xvalmin) / 2.0;
  If[fcount == 1, amplit0 = amplit];
  Write[noutfile, FortranForm[om],
   OutputForm["       "], FortranForm[amplit]];
  om1 = om - step;
   om = om1;
   ];
Close[noutfile];
```